Search for new resonances decaying to a Standard Model Vector boson (W/Z) and Higgs boson in the $\ell\ell b\bar{b}$, $\ell\nu b\bar{b}$ & $\nu\nu b\bar{b}$ channels in pp collisions at $\sqrt{s} = 13$ TeV with the ATLAS detector

Stephen Paul William Jiggins
University College London

Submitted to University College London in fulfilment
of the requirements for the award of the
degree of **Doctor of Philosophy**

February 20, 2018

Declaration

I, Stephen Paul William Jiggins confirm that the work presented in this thesis is my own. Where information has been derived from other sources, I confirm that this has been indicated in the thesis.

Stephen Jiggins _____

Abstract

The following thesis presents the result of a Beyond the Standard Model search for heavy resonances (V'/A) decaying into a Standard Model W or Z boson, and a Higgs (h) boson with a final state signature $l^+l^-b\bar{b}$, $l^{\pm}\nu b\bar{b}$, or $\nu\nu b\bar{b}$, where $l^{\pm} = e^{\pm}/\mu^{\pm}$, in proton-proton collisions at a center of mass energy of $\sqrt{s} = 13$ TeV. The data is collected using the ATLAS detector at the Large Hadron Collider, during the data periods of 2015+2016, amounting to 36.1 fb^{-1}.

The search is conducted using the (transverse) invariant mass spectrum of the reconstructed Standard Model W/Z boson and Higgs boson system, $W/Z + h$, ($m_{Vh}^{(T)}$) to search for excesses using the CL$_s$ binned profile likelihood test statistic. No excess is observed, therefore the results are interpreted in terms of constraints on $\sigma_{V'/A} \times BR(h \to b\bar{b})$, for heavy vector bosons predicted by Heavy Vector Triplet models (HVT), W'/Z', or the CP-odd scalar boson A predicted by Two-Higgs Doublet Models ($2HDM$). The upper limits on the production cross-sections are then used to assign constraints to the model parameter space.

For the HVT interpretation, limits on two benchmark models corresponding to fermiophobic and fermiophilic extensions, labelled A and B, of the heavy resonances are set: $m_{V'} = 2800(2930)$ GeV. For 2HDMs, limits on the production cross-section for mediator masses ranging from 220-2000 GeV are set: 5.5×10^{-3} pb $\to 2.4 \times 10^{-1}$ pb for $gg \to A$ production, and $3.4 \times 10^{-3} \to 7.3 \times 10^{-1}$ pb for bbA associated production.

Acknowledgements

I would like to thank first and foremost my parents, without their continued support over the last 4 years I would not have been able to finish my PhD.

I would also like to say thank you to Kristian Gregersen for his insightful perspectives, and guidance throughout the last 2 years. Furthermore, his expertise in coding and the CxAOD framework, on which I could draw on instantly, have been invaluable. As such, I am doubtful that I will ever be able to pay the debt that I owe you, in time or patience. Thank you again.

A big thank you goes to Alex Martyniuk, with whom I shared an office and regularly interrupted with small irritating questions. Your knowledge of the ATLAS trigger system, and the detector have been invaluable throughout my PhD, and only wish to repay the kindness you have shown, in due time.

To those that I shared an office with at CERN, Andrew Bell and Laurie McClymont, thank you. The many insightful discussions we had over the course of my stay, helped resolve many questions and problems that I have had over the course of my PhD. The ability to borrow your expertise was also greatly appreciated, and so I wish you the best.

A big thanks goes to Eric Jansen, thank you for your training on the event display, and despite your departure from ATLAS, you spent many late hours over skype assisting me with problems and issues. I fear I will never be able to repay your generosity in this regard, but will endeavour to do so.

It goes without saying that the academics at UCL, along with the UCL departmental staff, have been a critical component necessary for the completion of this thesis. Thank you to you all, and I wish you the best of luck in the future.

This leaves the analysis members of the HVT/AZh $Vhbb$ team and Gavin Hesketh. First, to the HVT/AZh $Vhllbb$ analysis team, without your hard work, guidance, expertise, time, and unwavering resolve, the work presented here would not be possible. It was a privilege working with you all, and I can only apologise for any late nights incurred as a result of my skype calls and emails. In no particular order, Hannah Arnold, Garabed

Halladjian, Spyridon Argyropoulos, Forrest Philips, Wade Cameron, Natalia Kondrashova, Ruth Jacobs, Tatjana Lenz, Andreas Hoenle, Felix Mueller, and Valerio Dao. A special thanks goes to Valerio for producing a plot following my request, especially considering that the plot was only for my thesis. Thank you for doing this, it was much appreciated.

Finally, I'd like to give a special thank you to Gavin Hesketh, my supervisor. Without his continued guidance and supervision I would not have been able to finish my PhD. You have suffered first hand from my worrisome nature, and survived. Thank you.

Author Contributions

Due to the vast scale of the LHC scientific program, and complexity of the ATLAS detector, collaboration amongst several if not dozens of personnel is often required when performing an analysis. This does not include the 1000's of engineers, physicists, computer scientists, and logistics personnel that work unobserved from the analysis perspective on calibrations, detector construction, GRID computing architecture, and more.

Therefore, given the collaborative nature of the work conducted at the LHC and within the ATLAS Collaboration, the work presented within the following thesis is not entirely the work of the *author* of this document. Therefore, in good faith and honesty the authors contributions to the following thesis and the LHC program are outlined.

Heavy Flavour Overlap Removal

The author of this thesis was tasked with the development of a matrix element and parton shower merging tool for the MadGraph5+Pythia8 generator setup. The purpose of this tool was to combine under a 4-flavour PDF scheme, V+Jets Monte Carlo samples involving heavy flavour quarks (b/c-quarks) in the final state, that are either produced in the hard interaction and so are calculated at the matrix element level, or via gluon splitting using the parton shower approximation. This tool was commited to the ATLAS generator SVN repository on 09/11/14 for general use by the collaboration.

Measurement of b-hadron pair production with the ATLAS detector in proton-proton collisions at $\sqrt{s} = 8$ TeV

The author of this thesis was a member of an analysis aimed at measuring the differential cross-section of $J/\Psi + \mu$ production, where the J/Ψ decayed to two muons, thereby yielding a final state of three muons. The overall goal of the analysis was to measure the differential production cross-section for said process as a function of variables sensitive to gluon splitting to b-quarks, $g \to b\bar{b}$. The involvement of the author in this analysis primarily involved estimating the background from pile-up, implementation of systematics, development of the

fitting code, and truth muon definitions used by the analysis. This analysis was published in Ref. [1].

Search for heavy resonances decaying to a Standard Model Vector Boson Z/W and Higgs boson, in the llb$\bar{\text{b}}$, lνb$\bar{\text{b}}$, and $\nu\nu$b$\bar{\text{b}}$ decay signatures.

The author of this thesis was the lead 1-lepton analyst for the analysis presented in Part IV, which was published here [2]. Consequently, the following thesis will concentrate on the 1-lepton analysis, on which the author predominantly worked.

The author was responsible for merging the 1-lepton analysis code base of an earlier version of this analysis presented in [3] (of which said author was a member), with the SM $Vh \to l^+l^-/l^\pm\nu/\nu\nu + b\bar{b}$ analysis CxAOD framework. As such, the author is one of the original developers of the 1-lepton analysis code (CxAODReader) used to produce the results published in [2]. This was done in conjunction with *Felix Mueller* [1] and the *CxAODFramework* developers.

Specific contributions of the author to the aforementioned analysis include: the study/development of the 1-lepton event selection summarised in Chapter 15, and the study/implementation of a variety of reconstruction schemes for the 1-lepton channel summarised in Chapter 12. The author was also responsible for deriving all V+Jets, $t\bar{t}$, and single top-quark systematics detailed in Chapter 18, for the 0-/1-/2-lepton channels,.

The author worked collaboratively with Forrest Phillips [2] on the production, validation, and testing of the 1-lepton inputs to the Binned Profile Likelihood fit, used to produce the final results summarised in Chapter 19. The author was also involved collaboratively with Garabed Halladjian [3], on running the fit performance studies designed to assess the importance of the various signal and control regions used by the 1-lepton HVT analysis. This was done via the production, testing, and validation of the input data provided to the Binned Profile Likelihood fit, derivation of the modelling systematics and discussion on how to implement them within the analysis, or via studies using the statistical fitting framework. The results are summarised in Chapter 9 and Section 18.4.2.

The author also assisted with the technical implementation and validation of the 1-lepton Multijet estimate procedure outlined in Chapter 16, with the 1-lepton analysis code base. This procedure was developed by *Andreas Hoenle* [4] and *Felix Mueller* [5]. As such this

[1] Max Planck Institute for Physics, Munich
[2] Michigan State University (US), supervised by Wade Cameron Fisher (Michigan State University (US))
[3] Michigan State University (US), analysis contact
[4] Technische Universität München, Munich, Institut für Kern-, Teilchen- und Astrophysik
[5] Max Planck Institute for Physics, Munich

chapter is presented due to its importance to the 1-lepton analysis, however the related physics studies were conducted by the aforementioned analysis members, not the author of this thesis.

In summary, the author produced all plots presented in this thesis unless stated explicitly in the caption or if a reference is given. The former is done when the plot was produced by another person, but is not publicly available, as such the author gives credit to the creator where applicable. The later is done when the plot or image is published.

Contents

List of figures

List of tables

Part I.

Overview

Chapter 1.

The *Standard Model* is the product of the scientific work of thousands of experimental and theoretical physicists, spanning dozens of experiments and more than half of the 20th century. Despite all of its successes, the Standard Model is still known to be an incomplete theory, and so in the 21st century the field of *High Energy Particle Physics* is tasked with studying this model, and its possible extensions. The **L**arge **H**adron **C**ollider (LHC) is one of a long line of collider experiments designed to probe the small distance scales of the universe with the intention of studying the fundamental forces of the universe, and thus the Standard Model, using proton-proton collisions accelerated to a center of mass energy ranging from 900 GeV to 14 TeV.

With this in mind the following thesis will describe an analysis of the data collected by the ATLAS (**A** **T**oroidal **L**HC **A**pparatus) detector during the 2015+2016 proton-proton data collection periods operating at a center of mass energy of $\sqrt{s} = 13$ TeV. This analysis is designed to search for new heavy Z'or W'resonances predicted by a number of *Beyond the Standard Model* theories, such as *Heavy Vector Triplet Models* (HVT) and *2-Higgs-Doublet Models* (2HDM). Chapters 2–5 present a brief overview of the Standard Model and some of its failings, in addition to introducing the HVT model and the *Simplified Model Strategy*. A discussion of Monte Carlo phenomenology is also presented due to the influence of Monte Carlo simulation on the aforementioned analysis, and how it limits the analysis performance.

Following this an overview of the LHC complex and the ATLAS detector is given by Part III. Chapters 8–19 detail the analysis strategy used to process the collected proton-proton data from the LHC and quote the final results. These chapters will cover the configuration of the data and Monte Carlo samples, analysis strategy, statistical fitting framework, systematic considerations, and model interpretations.

Part II.

Theoretical Framework

Chapter 2.

Introduction

The Standard Model (SM) is a theoretical framework that describes the interactions of the fundamental particles of the universe. It is the result of scientific collaboration between experimental and theoretical physics spanning most of the 20th, and the entire 21st century. Its major successes include predicting the W/Z, gluon, Higgs, bottom, top, and charm quarks, and being able to precisely predict several SM parameters such as the anomalous magnetic dipole moment of the electron ($|a_e^{\text{exp}} - a_e^{\text{theory}}| = 0.91(\pm 0.82) \times 10^{-12}$) [4, 5].

Nevertheless the SM is not without its faults. It predicts that neutrinos are massless, now known to be incorrect following the discovery of neutrino oscillations in atmospheric neutrinos [6] and solar neutrinos [7] in 1998 & 2001, respectively. Furthermore, the SM does not provide a viable candidate for Dark Matter/Energy, which constitutes approx 27%/68% of the observed universe; an inference made after galaxy rotation curves, gravitational lensing [8], and the accelerated expansion of the universe [9, 10], indicated that majority of the matter and energy of the universe is unobserved.

The most relevant shortcoming is the *Hierarchy Problem* (described in detail in Section 3.4.1), which states that there must be a finely tuned cancellation of the radiative corrections with the Higgs bare mass, in order for the observed Higgs mass of $m_h = 125.09 \pm 0.24$ GeV [11] to be manifested physically. This problem is the motivation behind HVT models, as will be described in Chapter 4.

The following chapter will provide a brief overview of the theoretical concepts that motivate the HVT search presented in Part IV, in addition to the foundations of the SM, and Monte Carlo phenomenology.

Chapter 3.

Standard Model

The Standard Model is based on an $SU(3)_c \otimes SU(2)_L \otimes U(1)_Y$ gauge symmetry and is an example of a quantum field theory. The $SU(3)_c$ group describes Quantum Chromodynamics (QCD), whilst Quantum Electrodynamics (QED) and the Weak force are embedded in the chiral electroweak $SU(2)_L$ and hypercharge $U(1)_Y$ sector.

Table 3.1 and Table 3.2 summarise the particle content of the SM, where all particles are considered to be point-like and elementary, with an intrinsic spin, which is used to categorise each particle into one of two categories; those with integer spin are known as *bosons* and those with half-integer spin are known as *fermions*. For each particle there exists an exact duplicate known as its anti-matter partner, which has the same mass, but opposite quantum numbers [12].

Fermions of the SM can be sub-divided further into either *quarks* or *leptons*, based on whether they interact via the strong force ($SU(3)_c$ sector) or not. Those that do are referred to as quarks, of which there exist 3 colour variants.

Those that do not interact via the strong force are referred to as leptons, and interact via the electromagnetic and weak forces of the SM in the case of the charged leptons, and via the weak force exclusively in the case of the neutrinos [12].

3.1. Quantum Electrodynamics (QED)

Quantum Electrodynamics (*QED*) is the simplest implementation of a quantum field theory within the SM. Based on the $U(1)_Q$ Abelian Lie group, QED models the electromagnetic force of the SM and predicts, due to the Abelian nature of the group, that the QED gauge boson, or photon, has no self-interaction [12].

	Leptons			Quarks		
	Particle	Mass	Charge	Particle	Mass	Charge
I	electron e	0.511 MeV	-1	up u	2.3 MeV	$+\frac{2}{3}$
I	e neutrino ν_e	< 2 eV	0	down d	4.8 MeV	$-\frac{1}{3}$
II	muon μ	105.658 MeV	-1	charm c	1.275 GeV	$+\frac{2}{3}$
II	μ neutrino ν_μ	< 2 eV	0	strange d	95 MeV	$-\frac{1}{3}$
III	tau τ	1776.82 MeV	-1	top t	173.07 MeV	$+\frac{2}{3}$
III	τ neutrino ν_τ	< 2 eV	0	bottom b	4.18 GeV	$-\frac{1}{3}$

Table 3.1.: The predicted and experimentally observed SM fermions, with their corresponding masses and electromagnetic charge [11].

Particle	Mass	Charge	Spin
Photon γ	0	0	1
$W^\pm$	80.385 ± 0.015 GeV	$\pm$ 1	1
Z^0	91.1876 ± 0.0021 GeV	0	1
gluon	0	0	1
Higgs	125.09 ± 0.24 GeV	0	0

Table 3.2.: Predicted and experimentally observed SM bosons, with their corresponding masses, electromagnetic charge and spin [11].

The QED Lagrangian can be constructed at a fundamental level by imposing **local gauge invariance** on the Dirac Lagrangian defined as:

$$\mathcal{L}_{\text{Dirac}} = \mathrm{i}\bar{\psi}\gamma^\mu\partial_\mu\psi - m\bar{\psi}\psi, \tag{3.1}$$

where under a local $U(1)_Q$ gauge transformation of the form $\psi(x) \to \psi'(x) = e^{\mathrm{i}\alpha(x)}\psi(x)$ and $\bar{\psi} \to \bar{\psi}' = e^{-\mathrm{i}\alpha(x)}\bar{\psi}(x)$ (x represents the space-time position & $\alpha(x)$ is space-time dependent) the Dirac Lagrangian does not remain invariant:

$$\mathrm{i}\bar{\psi}\gamma^\mu\partial_\mu\psi - m\bar{\psi}\psi \to \mathrm{i}\bar{\psi}\gamma^\mu\partial_\mu\psi - \bar{\psi}\gamma^\mu\psi\partial_\mu\alpha(x) - m\bar{\psi}\psi. \tag{3.2}$$

To be precise, the $\partial_\mu\alpha(x)$ term violates local gauge invariance. The solution is to introduce what is referred to as the **Covariant Derivative**, which is designed to transform in exactly the same manner as the Dirac spinor $\psi(x)$. In this sense it is a 'covariant'

derivative of $\psi(x)$:

$$D_\mu \psi(x) \rightarrow D'_\mu \psi'(x) = e^{\mathrm{i}\alpha(x)}(D_\mu \psi(x)) \tag{3.3}$$

This only holds if the covariant derivative is defined as:

$$D_\mu = \partial_\mu + \mathrm{i}eA_\mu, \tag{3.4}$$

where e is the electric charge, and A_μ is a new gauge field that transforms as:

$$A_\mu \rightarrow A'_\mu - \frac{1}{e}\partial_\mu \alpha(x) \tag{3.5}$$

With these two components the Dirac Lagrangian can be altered to be gauge invariant under the previously defined local transformations, giving rise to the form:

$$\mathcal{L}' = \mathcal{L}_{\text{Dirac}} - e\bar{\psi}\gamma^\mu \psi A_\mu = \mathrm{i}\bar{\psi}\gamma^\mu D_\mu \psi - m\bar{\psi}\psi \tag{3.6}$$

Realising that the Lagrangian now contains a new gauge field A_μ, of which there is no kinetic term, a kinetic term of of the form $-\frac{1}{4}F_{\mu\nu}F^{\mu\nu}$ can be defined. $F_{\mu\nu}$ is known as the field strength tensor taking the form:

$$F_{\mu\nu} = \partial_\mu A_\nu - \partial_\nu A_\mu \tag{3.7}$$

Adding this to the gauge invariant Lagrangian given by equation 3.6, the QED Lagrangian is defined:

$$\mathcal{L}_{\text{QED}} = \mathrm{i}\bar{\psi}\gamma^\mu D_\mu \psi - \frac{1}{4}F_{\mu\nu}F^{\mu\nu} - m\bar{\psi}\psi \tag{3.8}$$

In summary, by taking the Lagrangian for free Dirac fields and imposing local gauge invariance, a new massless gauge field intrinsic to the $U(1)_Q$ group is spawned. This new Lagrangian describes all freely propagating Dirac particles, and their electromagnetic interactions.

3.2. Quantum Chromodynamics (QCD)

Quantum Chromodynamics on the other hand is structurally more complex. Based on the non-Abelian Special Unitary group of dimension N_c ($\mathrm{SU}(N_c)$), where N_c is experimentally known to be $N_c = 3$, QCD differs from QED as a result of a self interacting gauge boson.

Composed of a *gauge invariant*, *gauge fixing* and *ghost* term, the QCD Lagrangian takes the form [13, 14]:

$$\mathcal{L}_{\text{QCD}} = \mathcal{L}_{\text{invar}} + \mathcal{L}_{\text{ghost}} + \mathcal{L}_{\text{gauge fixing}}$$

Where:

$$\mathcal{L}_{\text{invar}} = -\frac{1}{4}G_i^{\mu\nu}G^i_{\mu\nu} + \bar{\Psi}(x)(\mathrm{i}\partial\!\!\!/ - m_q)\Psi(x) + g\bar{\Psi}\gamma_\mu T^a \Psi A^\mu_a$$

$$\mathcal{L}_{\text{ghost}} = \left(\partial_\mu \bar{c}_a\right)\left(\partial^\mu \delta_{ad} - gC_{abd}A^\mu_b\right)c_d$$

$$\mathcal{L}_{\text{gauge fixing}} = -\frac{\lambda}{2}\sum_{a=1}^{N_c^2-1}\left(\partial_\mu A^\mu_a\right)^2 \quad 1 < \lambda < \infty$$

where the spin-1/2 matter fields of this theory are represented as a triplet (3-dimensional vector) representing the 3 colour states of the fermion for a given quark flavour:

$$\Psi(x) = \begin{pmatrix} \Psi^1(x) \\ \Psi^2(x) \\ \Psi^3(x) \end{pmatrix} \tag{3.10}$$

Aptly named the *gauge invariant* term, the first term of the QCD Lagrangian is analogous to the QED Lagrangian. It remains invariant under a SU(3) local gauge transformation of the form:

$$U(x) = \exp(\mathrm{i}\sum_{i}^{N_c^2-1}\alpha_i(x)T_i), \tag{3.11}$$

where $\alpha_i(x)$ are the familiar space-time dependent functions that drive the phase variation, and $T_i = \frac{\lambda_i}{2}$ are the group generators. These group generators follow the group algebra:

$$[T_i, T_j] = \mathrm{i}c_{ijk}T_k, \tag{3.12}$$

where c_{ijk} are the **structure constants** of the group. For an Abelian group the generators commute, so the structure constants in all cases satisfy $c_{ijk} = 0$, whilst for the SU(3) group $c_{ijk} \neq 0$ [13, 14]. To maintain invariance under this gauge transformation, the covariant derivative is defined:

$$D^\mu = \partial^\mu - \mathrm{i}g\sum_{i}^{N_C^2-1}A^\mu_i T^i \tag{3.13}$$

Whilst the field strength tensor, or kinematic term for the SU(3) gauge boson is given by:

$$G_i^{\mu\nu} = \partial^\mu A_i^\nu - \partial^\nu A_i^\mu + g f_{ijk} A_j^\mu A_k^\nu \tag{3.14}$$

The *gauge fixing* term represents the removal of the redundant degrees of freedom of the gluon field observed during quantisation of the field theory, and the *ghost* term is introduced to maintain the *unitarity* of the S-matrix prescription [13, 14].

Note that due to the non-Abelian property of the SU(3) generators, which manifests itself in the field strength tensor, the term $-\frac{1}{4}G^{\mu\nu}G_{\mu\nu}$ in equation 3.9 gives rise to 2 terms corresponding to the self-interaction of 3 & 4 gluon vector fields. This self-coupling of the gluon (thus gluons carry colour) results in what is known as *asymptotic freedom* and *confinement*.

3.2.1. Renormalisation and Asymptotic Freedom

When calculating particle interactions, the matrix element $\mathcal{M}$ which represents the transition amplitude from a set of initial to final quantum states, is calculated. For a process like $gg \to gg$, the matrix element can be expanded perturbatively in terms of the strong coupling constant α_s (infinite number of terms):

$|\mathcal{M}|^2 =$ 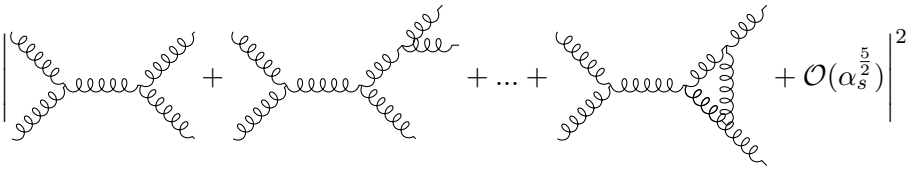 $+ \mathcal{O}(\alpha_s^{\frac{5}{2}})$ (3.15)

Unfortunately, virtual terms (e.g. the third term) in the series involve loop integrals of 4-momenta that often diverge (become infinite). Fortunately, the higher order terms $\mathcal{O}(\alpha_s^{\frac{5}{2}})$, should cancel these infinite loops, thus yielding a finite result. However, when truncating the series to a given order in perturbation theory, e.g. NLO in QCD, the loop integrals are no longer cancelled by the higher order terms, and so *ultraviolet divergences* ruin the predictive capability of QCD. This is overcome by *renormalising* the quantum field theory.

By requiring a field theory to be renormalisable, a renormalisation scale μ_R, which is not predicted by the QCD Lagrangian, is introduced to the field theory. This non-physical parameter controls how much of a calculation stems from non-loop Feynman diagrams versus the remaining finite components of loop Feynman diagrams [13, 15]. Considering that the QCD Lagrangian does not mention by construction μ_R, no physical observable

should ever depend directly on this scale; rather the strong coupling constant absorbs this parameter, $\alpha_s \to \alpha_s(\mu_R^2)$, such that it now runs with the choice of the scale (see Figure 3.1) [11, 13, 15].

The evolution of the $\alpha_s(\mu_R^2)$ can be conveniently expressed via the renormalisation group equation:

$$\mu_R \frac{\partial \alpha_s(\mu_R^2)}{\partial \mu_R^2} = \beta(\alpha_s(\mu_R^2)), \tag{3.16}$$

where the *beta function*, $\beta(\alpha_s)$, encodes the higher order loop corrections to the bare QCD vertices, and so formulates the dependence of the coupling constant on the scale μ_R [11]. In QCD $\beta(\alpha_s)$ has a perturbative expansion:

$$\beta(\alpha_s) = -b\alpha_s^2 + b'\alpha_s^3 + b''\alpha_s^4 + O(\alpha_s^5), \tag{3.17}$$

where the coefficients of the β function are extracted from the higher-order corrections to the aforementioned bare vertices of the theory. Considering only the leading order term $(-b\alpha_s^2)$, the renormalisation group equation (equation 3.16) can be solved for α_s, yielding the result:

$$\alpha_s(\mu_R^2) = \frac{\alpha_s(\mu_0^2)}{1 + \alpha_s(\mu_0^2) b \ln\left(\frac{\mu_R^2}{\mu_0^2}\right)} \tag{3.18}$$

where $b = 11 - \frac{2}{3}f$, and f is the number of flavours in the theory [15]. It is therefore obvious from the form of equation 3.18, that for the SM ($f = 6$) the strong coupling constant decreases as the scale of the interaction increases ($\mu_R = Q$). Here we have equated the renormalisation scale to the scale of the physical process Q, since the choice of the renormalisation scale is not defined *a priori* [11, 13, 15]. This behaviour of the strong coupling constant is what is referred to as asymptotic freedom.

3.3. Electroweak Unification

The unification of the electromagnetic and weak force was first proposed in 1961 by Sheldon Glashow [16], a model based on $SU(2) \times U(1)$ gauge invariance. The model was reliant on the presence of massive gauge mediating bosons ($W^{\pm}$ & Z^0) in order to explain the disparity in the electromagnetic and weak strength. Forbidden under local gauge invariance, this issue was not resolved until 1967-68 when Steven Weinberg and Abdus Salam imposed Spontaneous Symmetry Breaking (*SSB*).

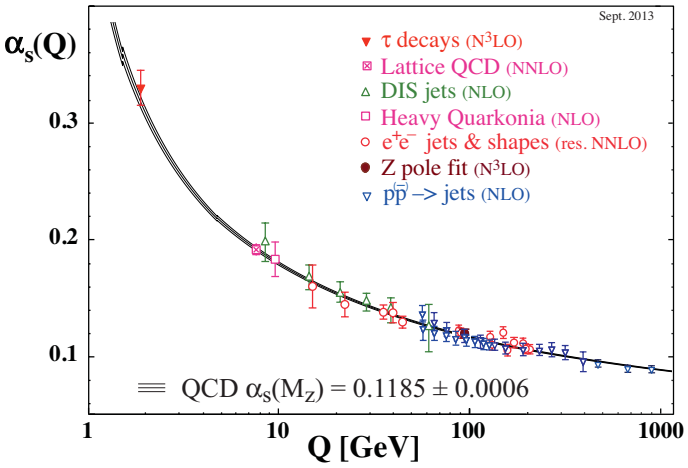

Figure 3.1.: Summary of the α_s measurements as a function of the scale of the interaction Q [11].

Formally based on the gauge invariant group $SU(2)_L \times U(1)_Y$, the $SU(2)_L$ weak isospin group is used to construct the weak current which only couples to left-handed fermions. $U(1)_Y$ is the group of weak hypercharge Y related to the $U(1)_Q$ Abelian QED subgroup by the relation $Y/2 = Q - I_3$, where Q is the electric charge and I_3 is the third component of weak isospin. As a result of imposing this chiral symmetry, the fermion fields are represented as left-handed weak isospin doublets and right-handed weak isospin singlets:

$$L_L(x) = \begin{pmatrix} \nu_L^e \\ e_L \end{pmatrix}, \begin{pmatrix} \nu_L^\mu \\ \mu_L \end{pmatrix}, \begin{pmatrix} \nu_L^\tau \\ \tau_L \end{pmatrix}, \quad L_R(x) = e_R, \mu_R, \tau_R \tag{3.19}$$

$$Q_L(x) = \begin{pmatrix} u_L \\ d_L \end{pmatrix}, \begin{pmatrix} c_L \\ s_L \end{pmatrix}, \begin{pmatrix} t_L \\ b_L \end{pmatrix}, \quad U_R(x) = u_R, c_R, t_R \tag{3.20}$$

$$D_R(x) = d_R, s_R, b_R \tag{3.21}$$

A necessity given that only the left-handed neutrinos have been experimentally observed, and weak leptonic currents take a *Vector-Axial* $(V - A)$ form. By imposing this coupled $SU(2)_L \times U(1)_Y$ local gauge invariance on the Dirac Lagrangian given by equation 3.1 (like the technique presented in Section 3.2) we arrive at the electroweak Lagrangian:

$$\mathcal{L}_{\text{EW}} = \mathcal{L}_{\text{Gauge Fermion,L}} + \mathcal{L}_{\text{Gauge Fermion,R}} - \frac{1}{4} B_{\mu\nu} B^{\mu\nu} - \frac{1}{4} W^a_{\mu\nu} W^{a\,\mu\nu} \tag{3.22}$$

The first two terms represent the left-handed and right-handed Gauge-Fermion interaction:

$$\mathcal{L}_{\text{Gauge Fermion,L}} = \bar{Q}_L(\mathrm{i}\gamma_\mu \boldsymbol{D}^\mu - m)Q_L + \bar{L}_L(\mathrm{i}\gamma_\mu \boldsymbol{D}^\mu - m)L_L \tag{3.23}$$

$$\mathcal{L}_{\text{Gauge Fermion,R}} = \bar{U}_R(\mathrm{i}\gamma_\mu D^\mu - m)U_R + \bar{D}_R(\mathrm{i}\gamma_\mu D^\mu - m)D_R + \bar{L}_R(\mathrm{i}\gamma_\mu D^\mu - m)L_R, \tag{3.24}$$

where $\frac{1}{4}B_{\mu\nu}B^{\mu\nu}$ represents the $U(1)_Y$ hypercharge gauge boson kinetic term, and $\frac{1}{4}W^a_{\mu\nu}W^{a\,\mu\nu}$ represents the kinetic term of the $SU(2)_L$ gauge bosons (a is a free index summing over the 3 gauge fields of the $SU(2)_L$ group). The covariant derivatives in this case takes the form:

$$\boldsymbol{D}_\mu = \partial_\mu + \mathrm{i}g_w T^a W^a + \mathrm{i}\frac{g'}{2}Y_i B_\mu \tag{3.25}$$

$$D_\mu = \partial_\mu + \mathrm{i}\frac{g'}{2}Y_i B_\mu \tag{3.26}$$

Here T^a represents the generators of the $SU(2)_L$ group, and g_w/g' represent the coupling strength of each gauge field with the fermion fields. It should be noted that by plugging equation 3.25 into the EW Lagrangian, the gauge fields W^a_μ and A_μ are massless. As will become apparent in the following section (Section 3.4), the massive weak gauge fields and massless photon are linear combinations of the weak and hypercharge gauge fields, taking the form:

$$W^\pm_\mu = \frac{1}{\sqrt{2}}(W^1_\mu \mp \mathrm{i}W^2_\mu) \tag{3.27}$$

$$Z^0_\mu = \cos\theta_W W^3_\mu - \sin\theta_W B_\mu \tag{3.28}$$

$$A_\mu = \sin\theta_W W^3_\mu - \cos\theta_W B_\mu, \tag{3.29}$$

where θ_W is the weak mixing angle.

3.4. Spontaneous Symmetry Breaking

By enforcing local gauge invariance on the three symmetry groups, it has been possible to construct a large part of the SM Lagrangian. However, by conforming to local gauge invariance a series of massless bosons have been introduced, which mediate the strong (gluons) and EW (W^i & B) forces.

Experimentally we know that the gluon and photon are massless, but W/Z bosons are known to be *massive*. This problem was rectified in 1964 when Peter Higgs, Robert

Brout and Francois Englert, and Gerald Guralnik, C. R. Hagen, and Tom Kibble [17–19], introduced the concept of Spontaneous Symmetry Breaking (SSB).

In the case of the EW sector, an $SU(2)$ doublet of complex scalar fields can be modelled by the Lagrangian:

$$\mathcal{L}_\phi = (D_\mu \Phi)^\dagger (D_\mu \Phi) - \mu^2 \Phi^\dagger \Phi - \lambda |\Phi^\dagger \Phi|^2, \tag{3.30}$$

which conforms to the $SU(2) \times U(1)$ gauge symmetry (so the covariant derivative is given by equation 3.25). The scalar fields, corresponding to a doublet of complex scalar fields takes the form:

$$\Phi = \begin{pmatrix} \phi^+ \\ \phi^0 \end{pmatrix} = \begin{pmatrix} \frac{1}{\sqrt{2}}(\phi_1 + \mathrm{i}\phi_2) \\ \frac{1}{\sqrt{2}}(\phi_0 + \mathrm{i}phi_3) \end{pmatrix}, \tag{3.31}$$

where the doublet has weak isospin $\frac{1}{2}$, weak hypercharge $Y_\phi = 1$ and the complex field ϕ^+ has $I_3 = +\frac{1}{2}$ and ϕ^0 has $I_3 = -\frac{1}{2}$. Recalling that a Lagrangian is defined as $\mathcal{L} = T - V$ (T = kinetic energy, V = potential energy), the potential of the above Lagrangian has the form $V(\Phi^\dagger \Phi) = \mu^2 \Phi^\dagger \Phi + \lambda |\Phi^\dagger \Phi|^2$. By assuming $\mu^2 < 0$, and thus substituting $\mu^2 = -|\mu^2|$, the Lagrangian becomes:

$$V(\Phi^\dagger \Phi) \rightarrow V(\Phi^\dagger \Phi) = -|\mu^2| \Phi^\dagger \Phi + \lambda |\Phi^\dagger \Phi|^2 \tag{3.32}$$

The minimum of this potential can then be defined as $|\Phi_{min}| = \sqrt{-\frac{\mu^2}{2\lambda}} = \frac{v'}{\sqrt{2}}$, a state with an infinite number of degenerate minima states or *vacuum expectation values* (vev). Therefore without loss of generality we can select a minimum for the corresponding scalar field of the form:

$$\Phi_{min} = v = \begin{pmatrix} 0 \\ \frac{v'}{\sqrt{2}} \end{pmatrix} \tag{3.33}$$

With this minimum being one of an infinite number of degenerate vev, and working under the assumption that our universe resides within a vacuum point, the scalar field is re-parameterised to be equivalent to the vev plus a series of field fluctuations:

$$\Phi = \frac{1}{\sqrt{2}} \begin{pmatrix} \phi_1' + \mathrm{i}\phi_2' \\ v' + h + \mathrm{i}\phi_3' \end{pmatrix}, \tag{3.34}$$

where $\phi_1', \phi_2', \phi_3'$ are massless Goldstone Bosons, whilst h is the massive Higgs field. To simplify the entire process, the quantum fluctuations can be represented as a variation in the modulus ($|\Phi|$ or radial component) and 'phase' of the field, thus equation 3.34 can be written in the form:

$$\Phi = \frac{1}{\sqrt{2}} e^{\mathrm{i}(w^a T^a - w^3 \frac{Y_\phi}{2})} \begin{pmatrix} 0 \\ v' + h \end{pmatrix} \tag{3.35}$$

Here T^a are the $SU(2)$ group generators, $w^a(x)$ are space-time dependent phase terms and Y_ϕ is the $U(1)_Y$ group generator. It is at this point that the phase variation or field fluctuations can be *gauged/rotated away* by making a gauge choice. Specifically, by performing an $SU(2) \times U(1)$ gauge transformation of the form $U(x) = e^{-\mathrm{i}(w^a T^a - w^3 \frac{Y_\phi}{2})}$ (the generators of the broken symmetries), the scalar field becomes:

$$\Phi \to \Phi' = U(x)\Phi = \frac{1}{\sqrt{2}} \begin{pmatrix} 0 \\ v' + h \end{pmatrix} \tag{3.36}$$

Substituting equation 3.36 into the scalar Lagrangian given by equation 3.30, we end up with:

$$\begin{aligned} \mathcal{L}_\Phi = \frac{1}{2}(\partial_\mu h)(\partial^\mu h) - \mu^2 |h|^2 + \frac{1}{8} g_w^2 v'^2 (W_\mu^1 W^{1\,\mu} + W_\mu^2 W^{2\,\mu}) \\ + \frac{v'^2}{8}(g_w W_\mu^3 - g' B_\mu)(g_w W^{3\,\mu} - g' B^\mu) \\ + (\text{higher orders}) + (\text{kinetic terms for } W,\, B \text{ fields}) \end{aligned} \tag{3.37}$$

Recalling the re-definition of the gauge vector fields given by equation 3.29, we obtain:

$$\mathcal{L}_\Phi = \frac{1}{2}(\partial_\mu h)(\partial^\mu h) - \mu^2 |h|^2 \tag{3.38}$$

$$+ \frac{g_w^2 v'^2}{4} W_\mu^\pm W^{\pm\,\mu} \tag{3.39}$$

$$+ \frac{v'^2}{8}(g_W^2 + g'^2) Z_\mu Z^\mu \tag{3.40}$$

$$+ (\text{higher orders}) + (\text{kinetic terms for } W,\, B \text{ fields}) \tag{3.41}$$

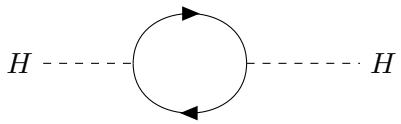

Figure 3.2.: Illustration of a SM fermion loop correction to the Higgs bare mass.

From equation 3.41, you can see that there are 3 massive vector bosons, $W^{\pm}_{\mu}$ and Z^{0}_{μ}. Where the corresponding masses are given by:

$$M_{W^{\pm}} = \frac{g_w v'}{2}, \quad M_Z = \frac{(g_w^2 + g'^2)^{\frac{1}{2}}}{2} = \frac{M_W}{\cos\theta_W}, \tag{3.42}$$

where θ_W is the weak mixing angle. Consequently, by selecting a vacuum expectation value and by imposing local gauge invariance, it is possible to generate a series of massive vector bosons. In the SM, this process gives rise to the massive $W^{\pm}$ & Z^0 bosons, but the photon (A^{μ}) remains massless. Furthermore, an additional scalar field, h, has also acquired a mass of $m_h = \mu^2 = -\lambda\nu'^2$, which represents the Higgs boson.

Similarly, the fermion masses are also generated by their coupling to the Higgs boson. Specifically, a series of Yukawa-type couplings between the fermions and Higgs boson can be added of the form:

$$\mathcal{L}_{\text{Yukawa}} = -\mathcal{Y}_L \bar{L}^i_L \Phi_i L_R - \mathcal{Y}_D \bar{Q}^i_L \Phi_i D_R - \mathcal{Y}_U \epsilon_{ij} \Phi^{C\,j} \mathcal{U}_R + h.c., \tag{3.43}$$

where i/j are indices that refer to the $SU(2)_L$ weak isospin components of the lepton (quark) isospin doublets $\bar{L}^i_L$ ($\bar{Q}^i_L$) and Higgs doublet Φ^i. L_R, D_R, and U_R are the lepton, down-quark, and up-quark singlets, whilst $\Phi^C = \frac{1}{2}(\nu' + h(x), 0)^T$. The constants $\mathcal{Y}_L$, $\mathcal{Y}_D$, and $\mathcal{Y}_U$ correspond to the Yukawa-coupling constants to the leptons, down-quarks, and up-quarks, respectively. It should be noted that the Yukawa couplings are related to the fermion masses, $\mathcal{Y}_f = \sqrt{2} m_f / \nu'$.

3.4.1. Hierarchy Problem

Despite the predictive capabilities of the Standard Model it is clear that it is still work in progress. Certainly a new theoretical paradigm will be needed at the reduced Planck scale $M_P = (8\pi G_{\text{Newton}})^{-1/2} = 2.4 \times 10^{18}$ GeV, where the effects of gravity become important, and thus the predictive performance of the Standard Model breaks down. It is therefore clear that some new physics must arise in between the electroweak scale, $m_W \sim 100$ GeV, and the Planck scale [20].

This introduces the infamous 'hierarchy problem'. If we consider the electrically neutral part of the Higgs, then the classical potential of the complex scalar SM Higgs field, as given by equation 3.32, requires a non-vanishing vacuum expectation value. This arises when $\lambda > 0$ and $\mu^2 < 0$, however the 2012 discoveries of the SM Higgs boson (see Ref. [21] and Ref. [22]) at a mass of $m_h = 125.09 \pm 0.24$ GeV implies that $\lambda \approx 0.126$ and the Higgs bare mass $\mu \sim m_H \approx 92$ GeV [20].

The problem is that the Higgs bare mass receives large quantum corrections from virtual effects of every particle or phenomenon that couples to the Higgs field. For example, as shown by Figure 3.2, the Higgs has 1-loop corrections involving fermions f of mass m_f. Given that within the Standard Model the Higgs couples to fermions according to a term of the form $-\lambda_f H \bar{f} f$, then the Feynman diagram above adds a correction to the bare mass of the form:

$$\Delta m_h^2 = -\frac{n' |\lambda_f|^2}{8\pi^2}[\Lambda_{\mathrm{UV}}^2 - 2m_f^2 \ln(\Lambda_{\mathrm{UV}}/m_f) + ...] \tag{3.44}$$

Here n' depicts the multiplicity of the fermion states (colours in QCD for example), and Λ_{UV} represents the ultraviolet cut-off used to regulate loop integral induced divergences [20]. The largest correction comes from the top-quark loop, where $\lambda_t \approx 0.94$. Therefore, if $\Lambda_{\mathrm{UV}} = M_{\mathrm{P}}$, then the quantum corrections to m_h^2 must be some 10^{34} orders of magnitude larger than the bare mass itself. In order to yield the observed SM Higgs mass, finely tuned cancellations between the higher order virtual corrections must be precise to 10^{17} orders of magnitude.

Naturally one can choose a smaller ultraviolet cut-off, however this represents the scale at which some new physics must arise. In this situation, whatever extension to the Standard Model is chosen, this extension must not only alter the propagators in the loop, but also cut-off the UV divergence. This remains problematic for the Standard Model which contains only two derivatives, and higher-derivative Lagrangian theories violate unitarity and causality arguments [20, 23].

This finely tuned aspect of the current Standard Model prediction is coined the 'hierarchy problem'. It should be noted that the term 'problem' is a poor description of this phenomenon, since it is not a fundamental flaw in the Standard Model, rather its sensitivity to any imaginable extension of the Standard Model at higher mass scales. Furthermore, it is not inconceivable that the Standard Model and nature are finely tuned.

Chapter 4.

Heavy Vector Triplet Models

Several extensions to the Standard Model attempt to resolve the hierarchy problem by introducing a new strong interaction at a higher scale. Such extensions often predict the existence of new heavy resonances that decay to SM particles, for example a SM vector boson (V) and Higgs boson (h). Examples of such models are Minimal Walking Technicolor [24–26], Little Higgs [27] or composite Higgs [28, 29]. However, due to the plethora of theoretical models currently in circulation a *Simplified Model* strategy can be employed. This is discussed in the following section.

4.1. Simplified Models and Bridge Method of Phenomenological Lagrangians

For any given theoretical framework, whether it be *Extra-Dimensions* or some *New Symmetry*, several models can be constructed within this umbrella. Each model makes some educated assumptions on the nature of new physics Beyond the Standard Model (BSM). From a practical perspective, attempting to compare all these models to LHC data is simply impossible, because not only does each model often depend on a vast array of parameters, thereby requiring a multi-dimensional scan of some parameter space, the vast array of models in current circulation makes the task impractical.

To overcome this limitation the Simplified Model strategy can be used. For resonance searches, only the parameters of the underlying theoretical model related to the mass of the resonance and field interaction terms driving the production and decay modes are experimentally observable. In this situation a phenomenological Lagrangian can be constructed where these relevant parameters are retained and the rest dropped. The 'aggregate' phenomenological Lagrangian parameters are then related to the free parameters of the 'fundamental' Lagrangian by a series of parameter relations, $\vec{c}(\vec{p})$, where $\vec{p}$ =

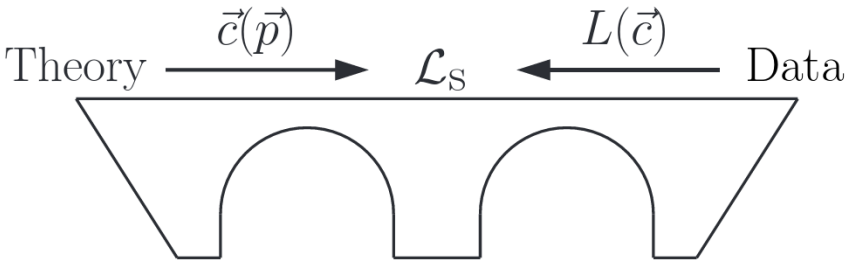

Figure 4.1.: Illustration of the 'Bridge Method' used by Simplified Model strategies [30].

$\{p_1, p_2, ..., p_m\}$ represents the vector of m free parameters within the fundamental model, and $\vec{c}$ represents the parameters of the phenomenological Lagrangian.

Consequently, whether the analysis quotes a discovery or sets an exclusion limit on the production cross-section, a multi-dimensional scan of the reduced set of phenomenological parameters can be performed, and the predictions compared with the data. The compatibility of various phenomenological parameter configurations with the observed result can thereby be set using confidence level intervals, $L(\vec{c})$. This procedure can be depicted via a two-span bridge, as shown by Figure 4.1, where the central pillar is the Simplified Model, and the two arches represent the fundamental/phenomenological parameter relations (left) and phenomenological parameter comparisons with data (right). This methodology is coined the 'Bridge Method' [30].

4.2. Iso-triplet extensions to the Standard Model

Following this 'Simplified Model' prescription, a generic phenomenological Lagrangian incorporating an iso-triplet of vector fields, V_μ^a for $a = \{1, 2, 3\}$ in the adjoint $SU(2)_L$ representation with vanishing hypercharge can be constructed. The iso-triplets form one charged and one neutral heavy spin-one particle with charge eigenstate fields of the familiar form [30]:

$$V_\mu^\pm = \frac{V_\mu^1 \mp \mathrm{i}V_\mu^2}{\sqrt{2}}, \; V_\mu^0 = V_\mu^3 \tag{4.1}$$

The additional vector fields V_μ^a do not represent the mass eigenstates, since they mix with the electroweak $SU(2)_L$ sector vector bosons after electroweak symmetry breaking (EWSB). The dynamics of the new vector fields are described by a phenomenological

Lagrangian of the form [30]:

$$\begin{aligned}\mathcal{L}_{\mathcal{V}} = &-\frac{1}{4}[D_\mu V_\nu^a - D_\nu V_\mu^a][D^\mu V^{\nu a} - D^\nu V^{\mu a}] + \frac{m_V^2}{2} V_\mu^a V^{\mu a} \\ &+ \mathrm{i} g_V c_H V_\mu^a H^\dagger \tau^a \overleftrightarrow{D}^\mu H + \frac{g^2}{g_V} c_F V_\mu^a J_F^{\mu a} \\ &+ \frac{g_V}{2} c_{VVV} \epsilon_{abc} V_\mu^a V_\nu^b D^{[\mu} V^{\nu]c} + g^2 c_{VVHH} V_\mu^a V^{\mu a} H^\dagger H - \frac{g}{2} c_{VVW} \epsilon_{abc} W^{\mu\nu a} V_\mu^b V_\nu^c,\end{aligned} \tag{4.2}$$

where $D^{[\mu}V^{\nu]a} = D^\mu V^{\nu a} - D^\nu V^{\mu a}$ which transforms according to $D^\mu V^{\nu a} = \partial^\mu V^{\nu a} + g\epsilon^{abc} W^{\mu b} W^{\nu c}$, $\tau^a = \sigma^a/2$ are the familiar Pauli matrices, $\alpha \overleftrightarrow{D}^\mu \beta = (D^\mu \alpha)\beta + \alpha(D^\mu \beta)$, and g denotes the $SU(2)_L$ coupling in the typical SM electroweak sector. The third term of equation 4.2 contains the $V' \to Vh$ interaction components relevant to the following HVT analysis, meaning that the parameter c_H controls the strength of the iso-triplet interactions with the SM Higgs and SM vector bosons (V); particularly the bosonic decays of the heavy resonances. The parameter c_F is the strength parameter controlling the decay of V' to the SM left-handed fermions, where $J_F^{\mu a} = \sum_f \bar{f}_L \gamma^\mu \tau^a f_L$ represents the SM fermionic current. The choice of a generic c_F for all SM fermions is made for simplicity, however different current couplings can exist for the lepton, light quarks, and heavy quarks:

$$c_F V_\mu^a J_F^{\mu a} \to c_l V_\mu^a J_l^{\mu a} + c_q V_\mu^a J_q^{\mu a} + c_3 V_\mu^a J_3^{\mu a} \tag{4.3}$$

The parameter g_V, in equation 4.2, represents the typical strength of the V' interactions with the SM bosons and fermions, meaning that the dimensionless c coefficients parameterise the departure of the fermion and SM boson couplings from the generic coupling strength. It should be noted that the third line of equation 4.2 contains only $V'V'V'$, $V'V'\,HH$, and $V'V'\,W$ vertices, i.e. no terms involving light SM fields and a single V'. Therefore, they do not directly contribute to the process $V' \to VV/Vh/ff$, but rather contribute to these decays processes via the mixing of V_μ^a with the SM W_μ^a fields during EWSB. This mixing is typically small, and so these terms are irrelevant in the following search.

The parameter m_V does not coincide with the masses of the new heavy vector fields, but rather their masses are obtained after the new V_μ^a vector fields mix with the SM W_μ^a vector fields post-EWSB. Therefore, post-EWSB the masses of the V^0 and $V^\pm$ heavy vector bosons are given by:

$$\begin{aligned} M_0 &= \hat{m}_Z^2 - m_Z^2 + \hat{m}_V^2 \\ M_\pm &= \hat{m}_W^2 - m_W^2 + \hat{m}_V^2 \end{aligned} \tag{4.4}$$

where $m_{Z/W}$ is the SM prediction of the Z/W-boson mass, and $\hat{m}_V^2 = m_V^2 + g_V^2 c_{VVHH} \hat{v}^2$. The vacuum expectation value of the Higgs field within this model, $\hat{v} = 2\langle H^\dagger H \rangle$, differs significantly from the physical EWSB scale predicted by the SM of $v = 246$ GeV. This leaves $\hat{m}_Z = \frac{1}{2}(g^2 + g'^2)^{\frac{1}{2}}$ and $\hat{m}_W = g\hat{v}/2$ (g' is the familiar $U(1)$ gauge coupling), which essentially represent the SM Z/W-bosons masses at a higher EWSB scale.

In the mass ranges of interest, specifically the situation when the $V^0/V^\pm$ masses are substantially heavier than the SM Z/W-bosons (order of 1 TeV), to $< 1\%$ precision $\hat{m}_{Z/W} \to m_{Z/W}$. In short, the masses of the Z/W-boson are unchanged by the presence of the additional iso-triplet sector and thus the V'resonances; this is also true for the rest of the SM parameters. A consequence of this convergence at large masses, is that the new neutral (V^0) and charged ($V^\pm$) heavy resonance masses become degenerate:

$$M_\pm^2 = M_0^2(1 + \mathcal{O}(\%)) \tag{4.5}$$

This last feature of the iso-triplet extension is one fundamental assumption made when deriving the combined $W'^\pm$ and Z' exclusion limits given in Section 19.2.2.

This phenomenological model is known as the 'Heavy Vector Triplet' model (HVT), which is designed to encompass fundamental theoretical models like Extended Gauge Models (EGM) or Composite Higgs Models (CHM).

4.3. Benchmark Models

Two specialised forms of the HVT model are used as *benchmark* models during the analysis; HVT models A and B. Model A represents an extended gauge symmetry with a symmetry breaking pattern $SU(2)_1 \otimes SU(2)_2 \otimes U(1)_Y \to SU(2)_L \otimes U(1)_Y$ [31]. Model B describes a SO(5) global symmetry spontaneously broken symmetry to a SO(4) subgroup; for example the *Minimal Composite Higgs Model* (MCHM) [32].

These two models impose specific constraints on the generic HVT model parameters:

$$\textbf{Model A: } c_H \sim -g^2/g_V^2 \text{ and } c_F \sim 1 \tag{4.6}$$

$$\textbf{Model B: } c_H \sim c_F \sim 1, \tag{4.7}$$

meaning that since the V'coupling to SM vector bosons is given by $g_V c_H$, and the fermionic coupling is $g^2 c_F/g_V$ (see equation 4.2), under Model A the coupling of fermions and bosons is equivalent. However, for Model B, the fermionic coupling is suppressed for any value that satisfies $g_V > 1$; in this specific model $g_V = 3$.

Chapter 5.

Proton-Proton Collisions & Monte Carlo Phenomenology

Whether it be a SM precision measurement or a BSM search, being able to simulate a physical process is often necessary for many analyses. This is often due to the unavailability of a data-driven estimate for the process of concern. Simulating a process is achieved via the use of the *Monte Carlo* method, a process of random sampling to obtain a numerical result. Specifically, the Monte Carlo method is primarily used in the areas of *numerical integration* (e.g. *importance sampling*) to solve complex integrals originating from phase space integrations of a matrix element calculation, and randomly drawing from a probability distribution to replicate the random generation of a specific type of event [33].

As a result of constructing these MC events from an underlying theoretical model, not only can they be produced on demand, but the full event record of the proton-proton collision is available. As such, these events serve as powerful analysis tools for optimising event selections, studying the behaviour of scientific methodologies, running performance studies, or assessing systematic uncertainties.

In searches, MC predictions are typically used in hypothesis testing when deriving model-dependent exclusion limits or quoting the statistical significance of a new physical process. This is in fact the very use of MC generated signal samples for the following HVT and 2HDM analysis presented in the next chapter. Within this analysis SM processes like $t\bar{t}$ and V+jets form a large part of the background. These processes are estimated using MC simulated events, and are used in the hypothesis-testing stage of the analysis.

Therefore, the following sections will outline the key components of Monte Carlo simulations and the phenomenology related to it.

5.1. Monte Carlo Event Structure

Figure 5.1 shows a representation of a $t\bar{t}H$ event as seen from the perspective of a Monte Carlo event generator (MC EvGen). This chaotic process is simulated by factorising the event into several phases, each produced via different techniques and occupying a unique region of phase space.

In general the dark red central blob represents the hard process which is calculated to some fixed order using perturbation theory via the *matrix element* prescription. If QCD partons are produced in the final state (as in this process), then the hard scale (Q^2_{hard}) produced coloured partons are evolved down to the non-perturbative regime, $\Lambda_{\text{QCD}} \sim 0.5$ GeV [34], via the *parton shower* model; this is depicted via the light red lines. At this stage the quarks and gluons within the event undergo hadronisation, which refers to the formation of hadrons from quarks and gluons due to colour confinement. This is achieved through the use of empirical *Hadronisation* models, which produce colourless hadron final states at scales below Λ_{QCD} (light green ellipses and dark green blobs).

The purple lines represent a combination of *Multiple Parton Interactions* (MPI), and *Underlying Event* (UE), which are non-perturbative, and the blue lines represent the incident partons extracted from the proton that initiated the hard process, and the associated *Initial State Radiation* handled by the parton shower model.

5.1.1. Hard Scatter - Proton-Proton Cross-section

For the high-energy interactions taking place at the LHC, the production cross-section for any $pp \to X$ process, where X represents an n-body final state (e.g. $t\bar{t}$ production), can be calculated according to the formula:

$$\sigma = \sum_{a,b} \int_0^1 dx_a dx_b \int f_a(x_a, \mu_{\text{F}}) f_b(x_b, \mu_{\text{F}}) \times \frac{1}{2\hat{s}} |\mathcal{M}_{\text{ab}\to\text{n}}|^2(\Phi_n; \mu^2_{\text{R}}, \mu^2_{\text{F}}) d\Phi_n, \tag{5.1}$$

where a/b represent the partons extracted from proton, $\sum_{a,b}$ is the sum over all parton combinations that lead to the final state X, $x_{a/b}$ corresponds to the momentum fraction of the parton with respect to its parent hadron, and $f_{a/b}(x_{a/b}, \mu_{\text{F}})$ correspond to the parton density functions (*PDF*) for partons [a,b] at a factorisation scale μ_{F} [11, 34, 36]. Φ_n denotes the Lorentz invariant space phase for the n-body final state, and $d\Phi_n$ is the differential Lorentz invariant phase space element [11, 34, 36]. This leaves $|\mathcal{M}_{ab\to n}|^2(\Phi_n; \mu_{\text{R}}, \mu^2_{\text{F}})$ which corresponds to the squared matrix element for the scattering of two partons a/b to the set of X (n-bodies) final states, evaluated at a renormalisation scale μ_{R}.

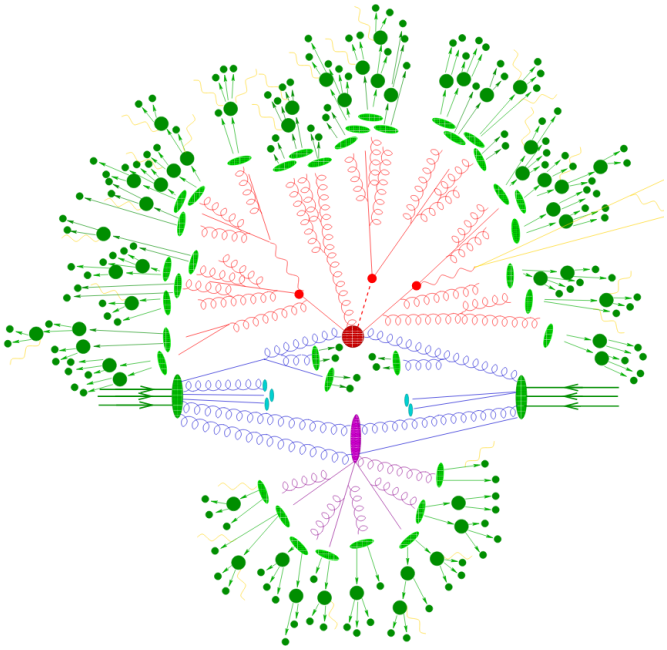

Figure 5.1.: Pictorial representation of a $t\bar{t}H$ event as generated from a Monte Carlo Generator [35].

Here, the assumption that the partonic interaction is independent of the PDF is made by invoking the *factorisation theorem* [37], which separates the process into the perturbative partonic cross-section $\hat{\sigma}_{ab} = \int |\mathcal{M}|^2/F \; d\Phi_n$ (F is the flux factor), calculable using QCD, and the non-perturbative distribution of partons within the proton (PDF). Figure 5.2 illustrates this factorisation diagrammatically.

Parton Distribution Functions The PDFs, parameterised as $f_a(x_a, \mu_\mathrm{F})$, correspond to the probability of finding a parton of type a with momentum $p_a = x_a P$, where the parton extracted from the proton has the momentum fraction x_a. Calculated by fitting experimental data under some hypothesised proton structure, they are measured at some scale Q^2_PDF, where the *Dokshitzer-Gribov-Lipatov-Altarelli-Parisi* (DGLAP) [38, 38, 39] equations model how to transform a PDF from one scale to another; the distribution of partons within the proton differs as a function of Q^2. In the above notation this scale is depicted as μ_F, which is known more formally as the *factorisation scale*. This phenomenological parameter represents the separation of the long- and short-distance physics, where long-distance interactions are absorbed into the PDF (soft/collinear emissions), and short-distance interactions are calculated within the matrix element (hard wide angled emissions resolvable in the final state).

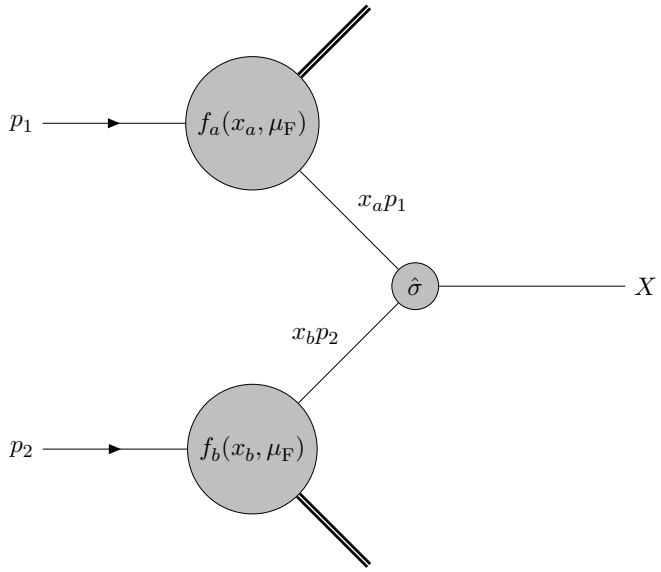

Figure 5.2.: Schematic diagram of the parton model of a hard scattering process.

Matrix Element Generation

Matrix element generators are concerned with not only evaluating the matrix element, $\mathcal{M}$, which corresponds to the squared scattering amplitude for a set of initial momentum eigenstates to a series of final momentum eigenstates, mediated by the interaction Lagrangian of the field theory, but also the Monte Carlo integration/sampling of the phase space element ($\int d\Phi_n$).

The $\mathcal{M}$ can be evaluated in a number of different ways, for example the summation of *pre-computed matrix elements*, the evaluation of the individual amplitudes using *helicity amplitudes*, or *recursive construction techniques* [34]. Following the evaluation of each matrix element, the integral over the initial and final state particles must be performed. This is performed by what is referred to as a phase space integrator, which are essentially complex Monte Carlo integrand sampling algorithms (the reader is directed to Ref. [33] and Ref. [34]).

5.1.2. Parton Shower Model

The parton shower approximation stems from the factorisable nature of QCD. If one considers a hard scatter of two partons $[a, b]$ into an n-body final state, where the squared matrix element is denoted as $|\mathcal{M}|_n$ (Figure 5.3a), then the $(n+1)$-body final state matrix element denoted as $|\mathcal{M}|_{n+1}$ (figure 5.3b), can be seen as a splitting of a parton into two

(a) $gg \to ggg$ **(b)** $gg \to ggg$

Figure 5.3.: Example of a $gg \to gg$ process and $gg \to ggg$ process.

new partons ($\alpha \to \beta\epsilon$). In this situation, the $(n+1)$-body final state matrix element can be expressed in the *soft and collinear* limit as [15]:

$$|\mathcal{M}|_{n+1} \sim \frac{4g^2}{p_\alpha^2} \mathcal{C} \hat{P}_{\beta\epsilon}(z) |\mathcal{M}|^2, \tag{5.2}$$

where the soft and collinear limit is defined as the emission of a new QCD parton ϵ from a parent parton α (four-momentum p_α), that either has a small relative transverse momentum or a small angle of separation with the parent. In analysing equation 5.2 it is therefore obvious that the $(n+1)$-body matrix element can be expressed using a factor $4g^2/p_\alpha^2$ that represents an additional QCD vertex ($\alpha \to \beta\epsilon$), $\mathcal{C}$ is a generic QCD colour factor, and $\hat{P}_{\beta\epsilon}(z)$ represents the regularised DGLAP parton splitting kernels [15, 34, 40]. These splitting kernels represent the probability that a parton α splits into two partons β and ϵ, when parton β has $z = E_\beta / E_\alpha$.

This unique factorisation of the matrix element is the foundation of the parton showering scheme, because any $n+m$ parton final state process in the soft and collinear phase space, can be seen as the n-body process with m additional partons originating from a series of parton splittings. Therefore, by using the parton splitting kernels and what is referred to as the *Sudakov Form Factor* [15, 34, 40], any n-body final state matrix element calculated process can be showered by iteratively splitting a final state parton from one scale $t_1 = |p_\alpha^2| = Q^2_{\text{hard}}$ to a lower (higher) $t_2 = t_1 - dt$ scale (timelike (spacelike) evolution). This is shown diagrammatically by Figure 5.4.

Hadronisation This process is necessary for calculating observables, because only the hadronised components of QCD partons are observable. Therefore, by iteratively splitting final state partons, the hard matrix element final state partons produced at a Q^2_{hard} scale, are slowly reduced to the non-perturbative regime Λ_{QCD}. Once at the non-perturbative

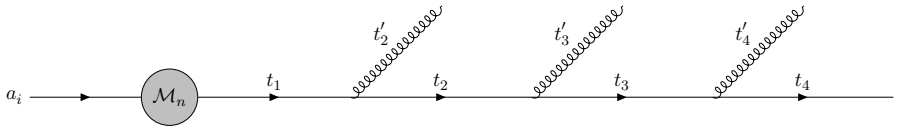

Figure 5.4.: Schematic diagram of an evolving final state parton from the hard scattering process. Where the scale of each parton follows $t_1 > t_2 > t_3 > t_4$, and $t_i > t_i'$.

boundary empirical hadronisation models, typically the *Lund String model* or *Cluster model*, simulate the conversion of the final state partons to colourless bound states, or hadrons.

5.1.3. Merging & Matching

Parton showers apply approximate higher-order real-emission corrections to a n-body final state hard process using the universal soft and collinear factorisation properties of perturbative QCD [40]. The resulting process is an $(n+m)$-body final state, where the additional m partons populate the soft/collinear regime. Unfortunately, higher-order perturbative calculations are often needed to accurately describe an observable, O; in this situation fixed-order calculations for some given power of the strong coupling constant replace the equivalent parton shower approximation [40].

For example, in measuring the cross-section of Z + 2-jets, the partonic cross-section $\hat{\sigma}_{Z+2\,\text{jets}}$, is inclusive of an infinite number of final state partons, i.e. it contains the terms $\hat{\sigma}^{incl}_{Z+2\,\text{jets}} = \sum_{n=2}^{\infty} \hat{\sigma}_{Z+n}$, where n represents the number of final state partons calculated perturbatively in a matrix element calculation. However, when passing the n^{th} calculation to a parton shower it is dressed by m partons, $\hat{\sigma}_n \to \hat{\sigma}_{n+m}$. Depending on the scale of this m^{th} splitting, the $n+1$ matrix element calculation may now overlap with the $n+m$ dressed final state.

In order to prevent double counting of phase space regions when calculating an observable, the *matrix element* (fixed order perturbative) calculation must be combined with the all-order approximation of the *parton shower* using either a *Merging* or *Matching* algorithm [40, 41].

- **Merging:** A separate tree-level calculation is performed for each parton multiplicity, where soft and collinear divergences of the matrix element calculation are prevented by adequate phase space cut-offs. The final state processes are then showered, but double counting is prevented by vetoing specific types of branchings. In short, the matrix element calculation will allow additional partons with a scale $t^2 > Q^2_{\text{cut}}$, however the parton shower will allow parton splittings with a scale $t^2 < Q^2_{\text{cut}}$. Examples of these types of algorithm include the MLM and CKKW-L matching algorithms.

- **Matching:** At NLO in QCD, an observable $\mathcal{O}$ is comprised of three main components, a *Born* configuration $\mathcal{B}$ which has no emissions, a real-emission term $\mathcal{R}$ involving one and only one emission, and virtual loop corrections $\mathcal{V}$ [40, 41]:

$$\langle \mathcal{O}^{\mathrm{NLO}} \rangle = \int \mathrm{d}\boldsymbol{\phi}_n \mathcal{O}(\boldsymbol{\phi}_n) \left[\left(\frac{d\sigma}{d\boldsymbol{\phi}_n} \right)_{\mathcal{B}} + \left(\frac{d\sigma}{d\boldsymbol{\phi}_n} \right)_{\mathcal{V}} \right] + \int \mathrm{d}\boldsymbol{\phi}_{n+1} \mathcal{O}(\boldsymbol{\phi}_{n+1}) \left(\frac{d\sigma}{d\boldsymbol{\phi}_{n+1}} \right)_{\mathcal{R}}, \tag{5.3}$$

  where $\boldsymbol{\phi}_n$ and $\boldsymbol{\phi}_{n+1}$ depict the n-body and $(n+1)$-body final state phase space configurations, respectively. In order to prevent overlap between the perturbatively calculated $(d\sigma/d\boldsymbol{\phi}_{n+1})_{\mathcal{R}}$ hard emission ($n+1$ partons), and the soft/collinear parton shower higher-order corrections applied to the Born configuration (n partons), the parton-shower expression at fixed-order is computed and subtracted from the higher-order calculation. The parton shower is then used to *fill-in* or complete the calculation, when a NLO calculated event is passed to a parton shower. This is known as the *Subtraction method* [40, 41].

Part III.

The Large Hadron Collider and the ATLAS Detector

Chapter 6.

LHC

The LHC is a 27 km circumference ring designed to accelerate protons and heavy ions in two counter rotating beamlines at an operational frequency of 40 MHz (25 ns bunch spacing). Divided into eight arcs, each section utilises superconducting radio-frequency cavities operating at a frequency of 400 MHz to accelerate the proton/heavy ion bunches with a net gain in particle energy of 485 keV per turn during the acceleration phase. The beam is then bent between these eight segments using superconducting dipole magnets capable of generating an 8.3 T magnetic field, where additional quadrupoles, sextupoles, octupoles, and decapoles are used to adjust the beam properties or trajectory.

In 2011 a maximum beam energy of 3.5 TeV was achieved resulting in a center of mass of energy of $\sqrt{s} = 7$ TeV. This was increased in 2012 to $\sqrt{s} = 8$ TeV, and in 2015/2016 to $\sqrt{s} = 13$ TeV. The first two energies were grouped into the 2010, 2011, and 2012 data taking period referred to as *Run 1*, and the latter is referred to as *Run 2*.

To achieve these energies, an accelerator chain comprised of a linear accelerator known as the Linear Accelerator 2 (LINAC 2), and three circular accelerators, the Proton Synchrotron Booster (PSB), Proton Synchrotron (PS), and Super Proton Synchrotron (SPS), are used. Starting from bottled hydrogen, protons are produced by stripping electrons from the hydrogen atom, which are fed to the LINAC 2 and accelerated to an energy of 50 MeV. The protons are then injected into the PSB and accelerated to an energy of 1.4 GeV, followed by the PS which pushes the beam energy to 25 GeV, and accelerated to a final beam energy of 450 GeV by the SPS before being injected into the LHC, where they are brought to a beam energy of 6.5 TeV. Figure 6.1 summarises this injection chain.

During the *Run 2* period each beam was built from $\approx$ 2600–2800 proton bunches spaced at 25(50) ns intervals for the 2016(2015) data collection years. Each bunch contained $\sim 1.3 \times 10^{11}$ protons, yielding an instantaneous luminosity of $L \approx 10^{34}$ cm^{-2}s^{-1}. The beams are brought to collision at 4 interaction points, coinciding with the ATLAS, CMS,

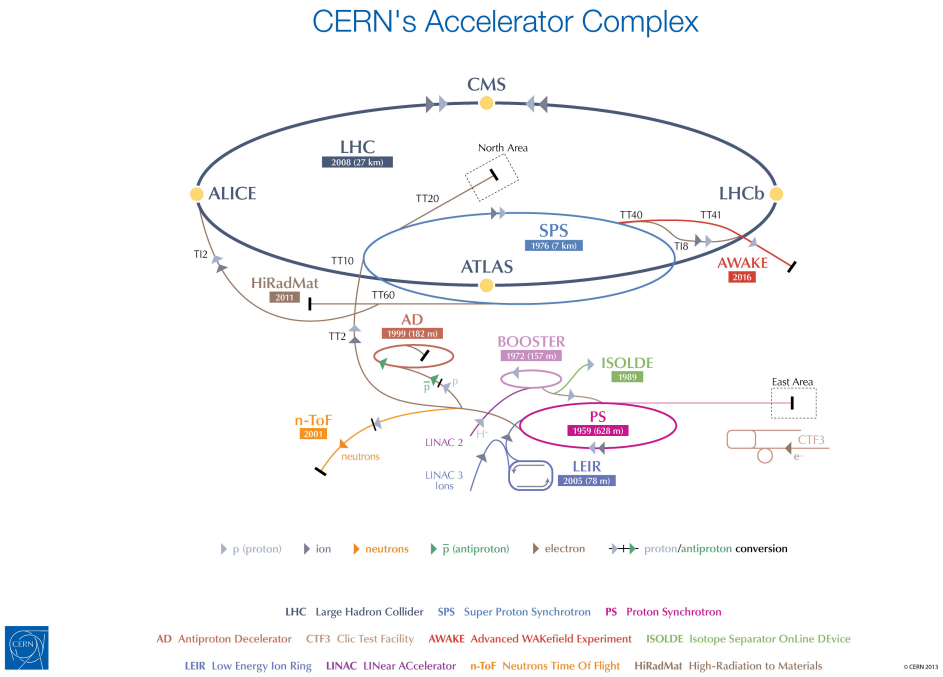

Figure 6.1.: CERN accelerator complex, showing the LINAC 2, PSB, PS and SPS injector chains to the LHC [44].

ALICE and LHCb detectors, with a crossing angle ranging from $145 - 250$ μrad [42, 43], where at the ATLAS interaction point the beams cross with an angle of 145 μrad.

6.1. Luminosity

The number of events generated at the LHC is given by the product of the integrated luminosity multiplied by production cross-section:

$$N_{\text{event}} = \sigma_{\text{event}} L = \sigma_{\text{event}} \int_{t_0}^{t_1} \mathcal{L} dt, \tag{6.1}$$

where $\mathcal{L}$ represents the instantaneous luminosity provided by the LHC machine. Dependent on several beam specific parameters, parameters that encapsulate the confinement and kinematic distribution of the protons within each bunch, the instantaneous luminosity can be calculated according to the formula:

$$\mathcal{L} = \frac{N_b^2 n_b f_{\text{rev}} \gamma_r}{4\pi \epsilon_n \beta *} F, \tag{6.2}$$

where N_b is the number of particles within each bunch, n_b is the number of bunches per beam, f_{rev} is the revolution frequency of the beam, γ_r is the relativistic gamma factor, ϵ_n is the normalised transverse beam emittance, $\beta*$ is the beta function at the collision point, and F is the geometric luminosity reduction factor needed to account for the small crossing angle of the two beams at the interaction point [42].

Determining the delivered luminosity during a run period is therefore critical for any analysis, since the expected number of events for any given physical process, e.g. BSM processes, is dependent on the integrated luminosity.

Therefore, ATLAS continually measures the delivered luminosity by using several different detectors and counting algorithms to measure the rate of inelastic collisions, in conjunction with beam-separation scans, or *van der Meer* (νdM) scans. The latter are used to determine the horizontal and vertical convolved beam widths (the beam specific parameters $\beta*$ and ϵ_n), but also to calibrate the visible interaction rate of each of the specific detector/algorithm measurements [45]. The ATLAS specific measurements include the Inner Detector (see Section 7.3), Minimum Bias Trigger Scintillators (MBTS) [46], Beam Conditions Monitor (BCM), Luminosity measurement using Cherenkov Integrating Detector (LUCID), Tile Calorimeter (see section 7.4.2), and Forward LAr End-cap Calorimeter (see section 7.4.4). For full details the reader is directed to Ref. [45].

Chapter 7.

ATLAS Detector

7.1. Co-ordinate System

ATLAS utilises a right-handed coordinate system with reference to the LHC ring. The nominal interaction point defines the origin, and the beam line defines the z-axis. The x-axis points to the center of the LHC ring, and the y-axis points upward towards the surface.

Side A of the detector is defined to be positive in z, whilst side C is negative. The azimuthal angle ϕ is measured around the z-axis in the x–y plane, and the polar angle θ defines the angular separation from the beam line (z-axis).

Consequently, a 3-momentum vector $\vec{p} = (p_x, p_y, p_z)$, can be separated into its longitudinal and transverse components, $p_z = |\vec{p}|\cos(\theta)$ and $p_T = |\vec{p}|\sin(\theta)$. The 3-momentum vector can then be expressed as:

$$\vec{p} = (p_T \cos(\phi), p_T \sin(\phi), p_z) \tag{7.1}$$

The *rapidity*, or relativistic velocity between the particles rest frame and the lab frame, can be defined as:

$$y = \frac{1}{2} \ln \left(\frac{E + p_z}{E - p_z} \right), \tag{7.2}$$

where E is the particle energy. In the massless limit, $E = |\vec{p}|$, rapidity simplifies to a quantity referred to as *pseudo-rapidity*:

$$\lim_{E \to |\vec{p}|} y = \frac{1}{2} \ln \left(\frac{|\vec{p}| - p_z}{|\vec{p}| + p_z} \right) = -\ln \left(\tan \left(\frac{\theta}{2} \right) \right) \tag{7.3}$$

The significance of this variable is its lack of dependency on the particle energy, making it the preferred variable for depicting the angular position of observed objects in the ATLAS detector.

7.2. Magnetic System

The magnetic system of ATLAS [47] is one of many fundamental components of the detection system; necessary for determining the momentum of charged particles, it follows a hybrid design philosophy composed of a *Central Solenoid* (CS) surrounding the *Inner Detector* (ID), and three air-core toroids that generate the magnetic field for the muon chambers. Totalling 26 m in length and 22 m in diameter the magnetic system stores 1.6 GJ of energy [47].

Spanning 5.3 m in length with a diameter ranging from 2.46 m to 2.56 m (inner to outer), the CS provides a central magnetic field of 2 T for the ID. The *Barrel Toroid* (BT) forms a cylindrical envelope around the beam line of axial length 25.3 m and inner(outer) diameter of 9.4(20.1) m. Formed from eight coils encased in stainless steel vacuum vessels, the BT provides a magnetic field strength ranging from 0.2-2.5 T in the muon chambers. The two *End-Cap Toroids* (ECT) produce a magnetic field strength ranging from 0.2-3.5 T for the muon spectrometer system in the end-cap regions. Totalling 5.0 m in axial length and inner(outer) diameter of 1.65(10.7) m, the ECTs contain eight coils each offset in azimuthal angle (ϕ) by 22.5° to the BT coils in order to provide radial overlap in the magnetic field between the two coil systems. An illustration of the magnetic system is given by figure 7.1.

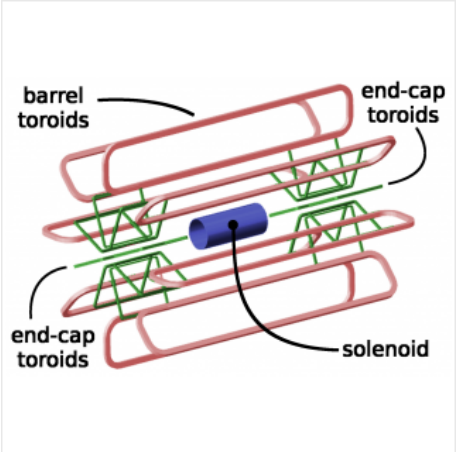

Figure 7.1.: Illustration of the Central Solenoid, Barrel Toroid and End-Cap toroids used by ATLAS for magnetic field production [47].

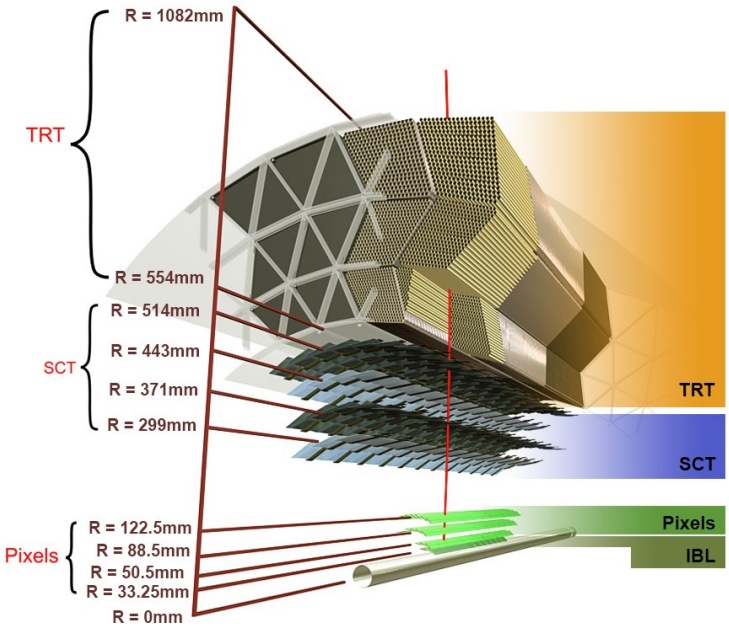

Figure 7.2.: Sketch of the ATLAS inner detector showing all its components, including the new insertable B-layer (IBL). The distances to the interaction point are also shown [48].

7.3. Inner Detector

The ATLAS Inner Detector [47] is designed to provide hermetic coverage of the beam line in order to provide robust pattern recognition of incident charged particles, high momentum resolution, primary/secondary vertex determination of charged particle tracks with $p_T > 0.5$ GeV in a pseudorapidity range of $|\eta| < 2.5$, and electron/pion identification over $|\eta| < 2.0$. The combined system is capable of reconstructing track momenta with a designed resolution of $\sigma_{p_T}/p_T = 0.05\%\ p_T/GeV \oplus 1\%$ [1], and transverse impact parameter with resolution $\sigma_{d_0} \approx 0.015$ mm for tracks with $p_T > 10$ GeV (deriving using low $\langle\mu\rangle$ minimum-bias 2016 data) [2].

Forming a cylindrical envelope of length ±3512 mm and radius 1150 mm, the ID is engulfed by the 2 T magnetic field of the CS, and is comprised of three sub-detectors; the Pixel detector, the **S**ilicon Semi**c**onductor **T**racker (SCT), and the Transition Radiation Tracker (TRT). The exact layout of the ID can be seen by Figure 7.2 and many of the key characteristics of the detector are summarised in Table 7.1 [48].

[1] The notation $a \oplus b$ denotes the quadratic sum of the two errors a and b according to $\sigma = \sqrt{a^2 + b^2}$

[2] Minimum-bias is obtained through the use of the MBTS system [46]. This system consists of eight 2 cm thick polystyrene scintillator disks positioned in the $2.08 < |\eta| < 3.86$ region. Events are collected when a at least 1 MBTS disk registers a charged pulse exceeding typical electronic noise; this minimal activity yields a dataset that has little to no trigger bias.

System	Position	Resolution σ (μm)	Channels (10^6)	η coverage	Radius/Length (mm)
Pixel	IBL	$R-\phi = 10$, z = 72	12	± 2.58	$R = 33.25$, $0 < \|z\| < 330.15$
	B-Layer	$R-\phi = 10$, z = 115	13.2	± 2.5	$R = 55.5$, $0 < \|z\| < 400.5$
	2 Barrel Layers	$R-\phi = 10$, z = 115	54	± 2.5	$88.5 < R < 122.5$, $0 < \|z\| < 400.5$
	2× 3 End-Cap Disks	$R-\phi = 10$, $R = 115$	2× 6.6	$\pm 1.7 - 2.5$	$88.5 < R < 149.6$, $495 < \|z\| < 650$
Silicon Strips	4 Barrel layers	$R-\phi = 17$, z = 580	2×6.3	± 1.5	$255 < R < 549$, $0 < \|z\| < 805$
	2×9 End-Cap Disks	$R-\phi = 17$, $R = 580$		$\pm 1.5 - 2.5$	$251 < R < 610$, $810 < \|z\| < 2797$
TRT	Axial barrel Straws	$R-\phi = 130$	0.351	± 2.0	$563 < R < 1066$, $0 < \|z\| < 712$
	Radial End-Cap Straws			$\pm 2.0 - 2.5$	$644 < R < 1004$, $848 < \|z\| < 2710$

Table 7.1.: Inner Detector specifications and coverage within the ATLAS coordinate system [47,49].

The Pixel detector makes up the the innermost part of the ID, and is constructed from four layers of silicon pixel detectors: the Insertable B-Layer (IBL) and three Pixel layers. These pixels are segmented in R–ϕ and z with a granularity of 50×250 μm at its finest to 50×400 μm at its most coarse, with the IBL closest to the beam pipe at a radius of $R = 33.25$ mm and the second pixel layer at a radius of $R = 122.5$ mm.

The SCT forms the second layer of the ID, consisting of four barrel layers and nine end-caps. Each sensor in the barrel region runs parallel to the beam-axis, and is composed of two silicon sensors rotated around the geometric center by ± 20 mrad, and is divided longitudinally into silicon strips with an average separation of 80 μm. This arrangement allows for the determination of the hit position along the length of the module. Totalling eight layers, a maximum of four space-points are generated for each incident charged particle.

The TRT is the final component of the ID, and is constructed from 4 mm diameter Polyimide drift straws arranged parallel to the beam-axis in the barrel region, and radially in the end-caps, offering track coverage up to $|\eta| < 2.0$. Each straw is filled with a 70% Xe, 27% CO_2 and 3% O_2 mixture pressurised at 5–10 mb, with a 31 μm diameter tungsten gold plated filament wire running down the center. This gas mixture is ionised when charged particles pass through, giving rise to negative charges that drift towards to the central anode wire, providing a measurement with a spatial resolution of 130 μm. The spaces between the straws are filled with polypropylene fibres/foils (barrel/end-cap) designed to generate transition radiation. This radiation deposits additional energy via Xe atom excitation and emission, leading to higher readout signals that can be used to discriminate between electrons and pions [11].

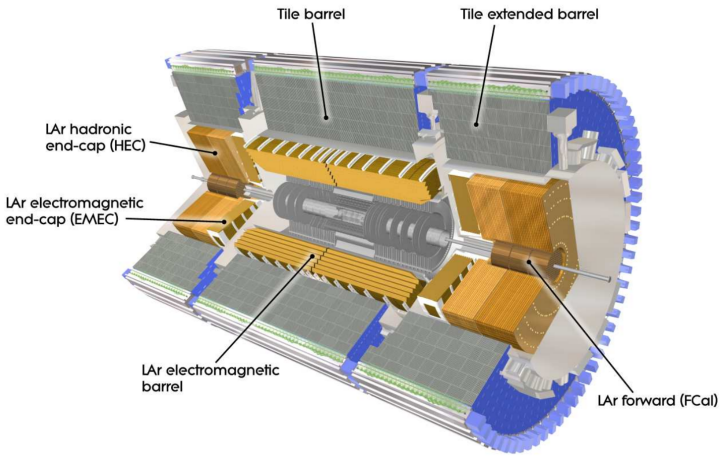

Figure 7.3.: Schematic view of the ATLAS EM and hadronic calorimeters [47].

7.4. Calorimeters

The ATLAS calorimeters [47] are designed to measure the energy of both charged and neutral particles originating from the interaction point, covering $|\eta| < 4.9$ and offering hermetic coverage in ϕ. Termed *sampling* calorimeters, the detector system is composed of alternating elements of passive and active material, where the passive material is designed to initiate a particle shower, whilst the active material measures energy deposits.

Due to the flexibility in segmenting the layers longitudinally and laterally, sampling calorimeters offer superior spatial resolution over other techniques such as *homogeneous* calorimeters [11], and perform better at particle identification. However, the energy resolution of sampling calorimeters suffers from a larger stochastic term due to the interleaving of active and passive material; the energy deposited in the active medium fluctuates event by event more than homogeneous calorimeters. Therefore enhanced sampling fluctuations limit the energy resolution of sampling calorimeters [47].

The fine granularity of the EM calorimeter is suited towards electron and photon precision measurements, whilst the coarser granularity of the hadronic calorimeter is suited towards reconstructing jets from hadrons and E_T^{miss} measurements. Figure 7.3 summarises the relative layout of the EM and hadronic calorimeters of the ATLAS detector.

7.4.1. Liquid Argon (LAr) Electromagnetic Calorimeter

The EM calorimeter is formed from two barrel components covering $|\eta| < 1.475$, and two end-caps covering $1.375 < |\eta| < 3.2$. The barrel calorimeter consists of two identical half

barrels, separated by a small gap of 4 mm at $z = 0$, each 3.2 m in length with an inner and outer radius of 2.8 m and 4 m, respectively. To incident particles/radiation the total thickness of the barrel region is 22-33 radiation lengths (X_0) depending on η.

Each end-cap is divided into an outer wheel covering $1.375 < |\eta| < 2.5$ and an inner wheel that covers $2.5 < |\eta| < 3.2$, with a thickness of 63 cm and an internal/external radius of 330/2098 mm. The thickness of the end-caps to incident EM particles/radiation ranges from 24 X_0 to 38 X_0 as η increases.

In the region $|\eta| < 1.8$, and so covering both the barrel and part of the two end-caps, a 1.1 cm (0.5 cm) thick LAr layer exists in front of the EM calorimeters inner surface. Referred to as the *presampler*, this layer is designed to sample the energy of photons and electrons in order to determine the energy lost by the photon/electron as a result of the upstream material prior to the EM calorimeter (ID, CS, ...).

Constructed using liquid-argon and lead plates, for the active and passive material respectively, the layers in the barrel and end-cap regions form an accordion shape with copper electrodes placed in the middle of the gaps between the lead absorber plates. An illustration of the geometry is presented in Figure 7.4, where the waves propagate parallel to the z-axis and run in ϕ for the barrel sections, but are parallel in the radial axis and run in the z-axis for the end-caps.

This design provides uniform performance in terms of resolution and linearity as a function of ϕ, but varies as a function of η. It has a design energy resolution of $\sigma_E/E = 10\%/\sqrt{E/\text{GeV}} \oplus 0.7\%$ [47].

7.4.2. Tile Hadronic Calorimeter

The tile sampling calorimeter is comprised of three components, a 5.8m in length barrel which covers the $|\eta| < 1.0$ region, and two extended barrels 2.6m in length that cover the region $0.8 < |\eta| < 1.7$ [47]. The central barrel and extended barrels both have an inner radius of 2.28 m and outer radius of 4.25 m. Constructed from steel absorber plates and scintillating tiles (98.456% polystyrene, 1.5% PTP and 0.044% POPOP) as the active medium, ionising particles crossing the scintillating blocks produce ultraviolet light in the base polystyrene material which is wavelength shifted by the PTP/POPOP fluors to the visible spectrum [47]. The two sides of a scintillating block are then read out by wavelength-shifting fibre optics that feed into two separate photo-multiplier tubes (PMTs) [47]. This design has a single particle energy resolution of $\sigma_E/E = 50\%/\sqrt{E/\text{GeV}} \oplus 3\%$ [47].

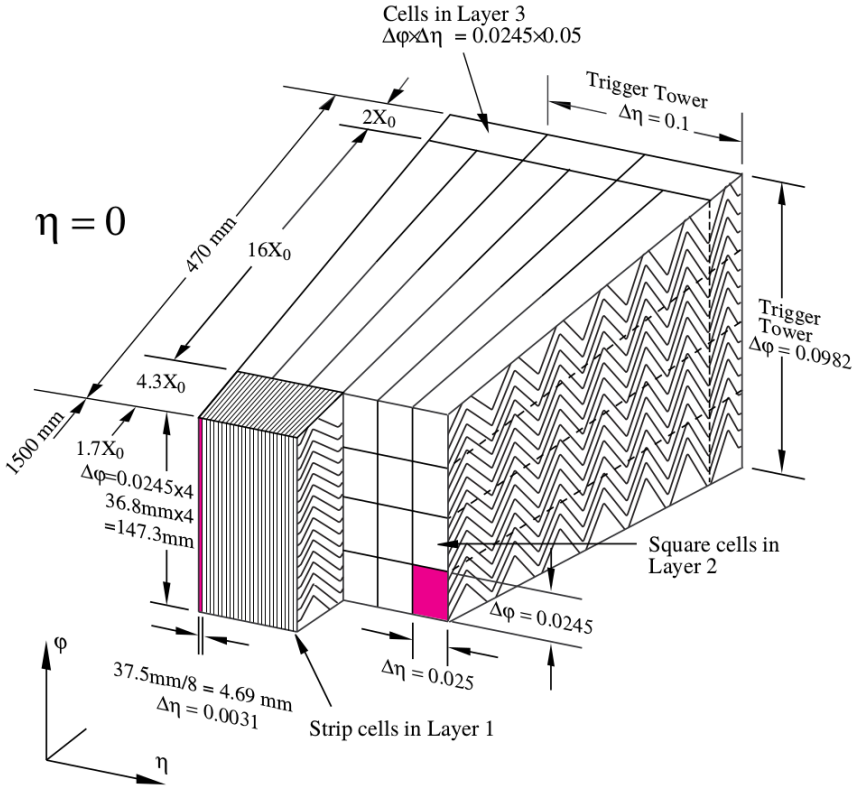

Figure 7.4.: Illustration of the lead absorber plate geometry and liquid-argon active material for the EM calorimeter barrel sections.

The central and extended barrels are divided into 64 modules in ϕ, in order to provide uniform acceptance in the azimuthal direction. The central barrel is constructed from three layers of approximately 1.5, 4.1, and 1.8 interaction lengths (λ) spanning radially, whilst the extended barrels are divided into 1.5, 2.6, and 3.3 λ layers [47]. Figure 7.5 shows schematically the module construction as previously defined.

7.4.3. LAr Hadronic End-cap Calorimeter

The hadronic end-cap calorimeter (HEC) is a copper/LAr sampling calorimeter using a flat-plate design consisting of two independent wheels per side, the front wheel (HEC1) and rear wheel (HEC2), covering the region $1.5 < |\eta| < 3.2$. Each wheel is constructed from 32 identical wedge-shaped segments, which are shown schematically by Figure 7.6. The modules of the front wheels are made of 24 copper plates each 25 mm thick plus a 12.5 mm

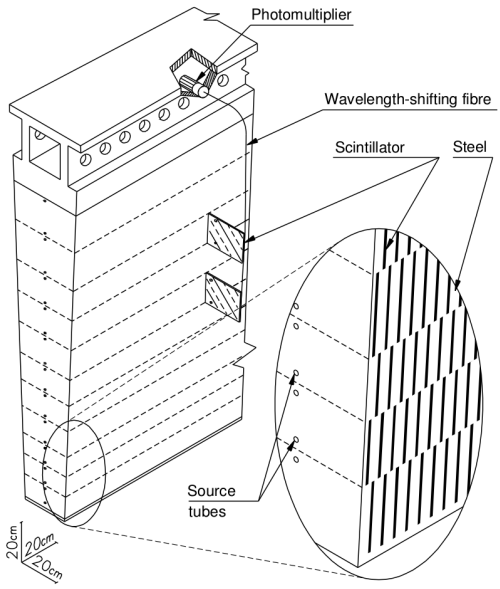

Figure 7.5.: Schematic diagram of the assembly of the electronic read out, active/passive sampling materials, and support structure modules used to form the 64 modules of the tile calorimeter [47].

thick front plate, whilst the rear wheels are constructed using 16 copper plates of 50 mm thickness plus a 25 mm front plate.

Each copper plate is separated by an 8.5 mm gap, which serves as the LAr cavity. Each gap is further sub-divided by three electrodes giving rise to four LAr drift zones of 1.8 mm in width. The central/middle electrode carries a pad structure covered by a high-resistivity layer, which serves as the read-out electrode.

7.4.4. Forward LAr End-cap Calorimeter

The forward calorimeters (FCAL) provide coverage in the $3.1 < |\eta| < 4.9$ range, and are divided into three 45 cm deep modules. The first (FCAL1) uses a series of stacked copper plates with holes drilled through them in order to allow electrodes to run longitudinally (parallel to the beam-axis) through the plates. Each electrode consists of a co-axial copper rod and tube separated by a gap of 0.269 mm that serves as the LAr cavities, wound in a radiation-hard plastic fibre. The FCAL1 is optimised for electromagnetic measurements.

The second and third modules (FCAL2 & FCAL3) correspond to the hadronic modules and are constructed using two copper plates of 2.35 cm width, whilst the remainder of the plates are composed of tungsten (the main absorbing material); tungsten limits the lateral

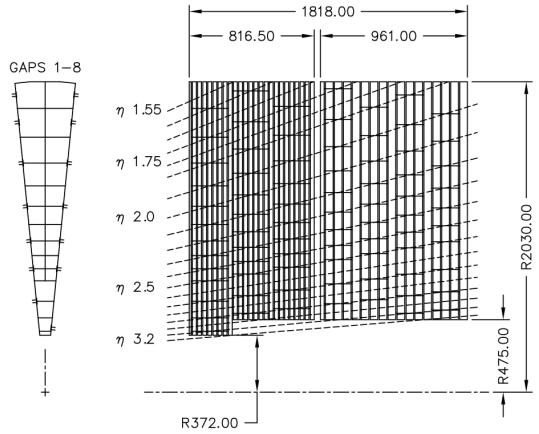

Figure 7.6.: Schematic of HEC wedge modules for the R–ϕ (left) and R–z (right) planes. The $\eta - \phi$ read out cell segments form a semi-pointing layout structure as shown by the dashed lines for a fixed η [47].

spread of the hadronic shower. The electrodes follow the same design as the first layer of the FCAL, however instead of copper, tungsten is used, and the LAr gaps between the anode and cathode of each electrode are 0.376 mm and 0.508 mm for the FCAL2 and FCAL3 modules, respectively. Figure 7.7 schematically illustrates the FCAL modules within the end-cap cryostat. The forward calorimeter is designed to have a single particle energy resolution of $\sigma_E/E = 100\%/\sqrt{E/\text{GeV}} \oplus 10\%$ [47].

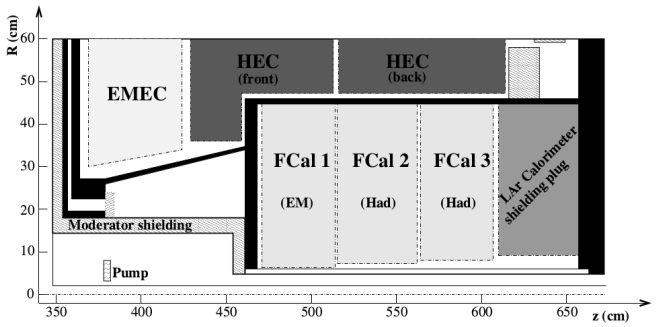

Figure 7.7.: Schematic diagram showing the FCAL modules within the end-cap cryostat, and the surrounding EMEC & HEC detectors [47].

7.5. Muon Spectrometer

Forming the outer layer of the ATLAS detector [47], the Muon Spectrometer (MS) is designed to measure escaping charged particles from the EM and hadronic calorimeters

within the $|\eta| < 2.7$ range to an accuracy of 10% for a particle with momentum of 1 TeV, and to trigger (record the event) on these particles within a smaller fiducial volume given by $|\eta| < 2.4$.

Designed around the toroid magnet system (see section 7.2 for details) the precision-tracking chambers are located between and on the eight coils of the superconducting barrel toroid magnet, while the end-cap chambers reside in front and behind the two end-cap toroid magnets. Therefore the ϕ symmetry of the toroid magnetic system is imposed on the MS, meaning that the barrel and end-cap sub-components are divided into eight octants which are further divided into two sectors in the ϕ direction. This sectioned approach offers overlapping coverage of the MS sub-detectors and thus provides hermetic coverage in ϕ. It should be noted that for $|\eta| < 0.1$ there is a gap in the MS coverage, required to supply cooling and electronic services to the ID and calorimeters.

The cylindrical barrel chambers are layered at radii of 5 m, 7.5 m and 10 m, whilst the end-cap chambers are positioned on the z-axis at 7.4 m, 10.8 m, 14 m, and 21.5 m from the interaction point. Figures 7.8a and 7.8b show schematically the MS in x–y and y–z planes.

Four types of detection element exist within the MS; the Monitored Drift Tubes (MDT) correspond to the precision measurement chambers (tracking chamber) of the MS, covering the $|\eta| < 2.7$ fiducial region. Constructed from three to eight layers of drift tubes, each tube is 29.97 mm in diameter and filled with a Ar/CO_2 gas at a pressure of 3 bar with a 50 μm diameter tungsten-rhenium wire at the center running at a potential of 3080 V. A

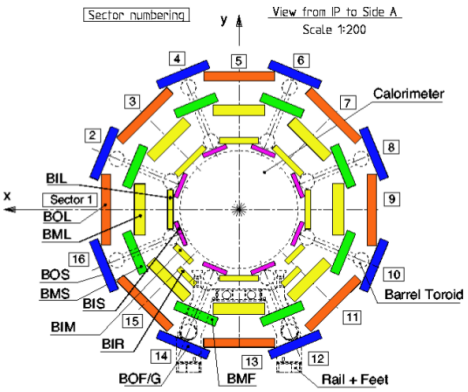

(a) x–y cross-section of the ATLAS detector (non-bending plane) showing the three cylindrical layers of eight ϕ segmented MS chambers [47].

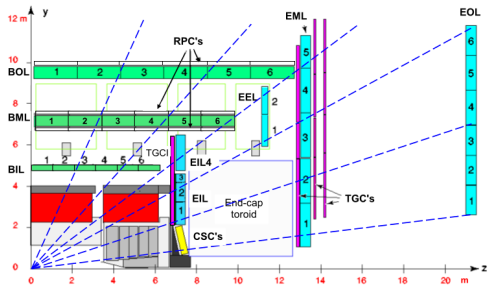

(b) y–z cross-section of the MS (bending plane) showing the three layers of RPC/MDT barrel chambers, and the end-cap wheels constructed using TGC/MDT/CSC chambers [47].

Figure 7.8.: Cross-sections of the muon spectrometer in the x–y (a) and y–z (b) planes.

		Chamber Resolution (RMS)			Measured Hits per Track	
Type	**Function**	z/R	ϕ	time	barrel	end-cap
MDT	Tracking	35 μm (z)	N/A	N/A	20	20
CSC	Tracking	40 μm (R)	5 mm	7 ns	N/A	4
RPC	Triggering	10 mm (z)	10 mm	1.5 ns	6	N/A
TGC	Triggering	2–6 mm (R)	3–7 mm	4 ns	N/A	9

Table 7.2.: MS detector element specifications. The time resolution is the intrinsic response resolution of each chamber, to which the signal-propagation and electronics contributions must be added. The spatial resolution does not include alignment uncertainties [47].

single MDT chamber is capable of achieving an average resolution of 80 μm per tube or 35 μm for the chamber, when reconstructing a charged particle track (see [50] for a detailed overview of the expected MS performance).

The second type of detection element is known as the Cathode Strip Chambers (CSC), which populate the forward region $2.0 < |\eta| < 2.7$ or innermost tracking layer, where the high particle flux requires a higher read out rate and time resolution. Each chamber is constructed of four layers of CSC planes, where each CSC plane is a multiwire anode plane sandwiched by segmented orthogonal cathode plates. The anode wires are orientated in the radial direction, whilst the cathode plates are segmented into strips with one side being perpendicular and the other side being parallel to the anode wires. This orientation of cathode strips and anode wires allows the precision co-ordinate in the ϕ–R plane to be determined and the transverse co-ordinate in the x–y plane to be measured. The precision of the CSC chambers for a track hit in the bending plane is approximately 40 μm and 5 mm in the transverse plane.

The remaining two detection elements used within the MS are the Resistive Plate Chambers (RPC) and Thin Gap Chambers (TGC), which are designed to trigger on muon tracks. As such the RPCs, which complement the MDTs in the barrel region ($|\eta| < 1.05$), and TGCs, which complement the CSC/MDT chambers in the end-caps ($1.05 < |\eta| < 2.5$), are capable of responding and relaying track hit information within the bending (η) and non-bending planes, within 15–25 ns of the passage of a particle. Table 7.2 summarises the specifications of the individual detection elements.

7.6. Trigger and Data Acquisition

With a nominal 40 MHz LHC bunch crossing rate and an approximate event size of 1MB, the amount of data to be recorded by ATLAS exceeds practical limits. Bearing in mind that approximately one W/Z-boson will be produced for approximately every $10^6 - 10^7$ pure-QCD events [51], the need for an efficient triggering system that stores only those events of interest, is paramount.

The ATLAS Trigger and Data Acquisition (TDAQ) system, diagrammatically shown by Figure 7.9, consists of two levels: a hardware-based level 1 (L1) and a software-based high-level trigger (HLT) [52]. The L1 trigger decision is formed by the Central Trigger Processor (CTP), which receives inputs from the L1 calorimeter (L1Calo) and L1 muon (L1Muon) triggers, in addition to the LUCID Cherenkov counter and Zero-Degree Calorimeter (ZDC). The CTP is also responsible for applying preventive dead-time, such as *simple dead-time* (time between accepting and reading L1 data) in order to prevent overlapping read-out windows, and *complex dead-time* (maximum number of L1 accepts in a given number of bunch crossings) in order to prevent the read-out buffers from filling up. The level 1 trigger system reduces the initial 40 MHz data rate to 100 kHz.

The data from the L1 read-out is then stored in the Read-Out-System (ROS) and processed by the HLT. This trigger chain receives Region-Of-Interest (ROI) information from the L1 triggers, and performs regional object reconstruction. These objects are then used to decide whether the full event reconstruction should take place, after which a hypothesis test on the fully built event is made as to whether it should be recorded. If passed, the event is sent to a local storage site at the experiment, which is then exported to the Tier-0 facility at CERNs computing center for offline reconstruction. The HLT reduces the 100 kHz L1 trigger data rate to approximately 1 kHz.

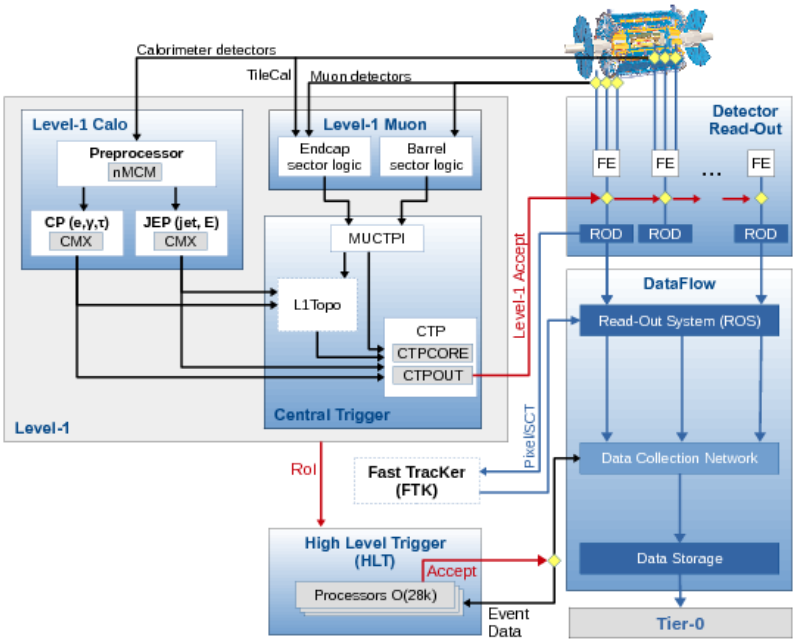

Figure 7.9.: ATLAS TDAQ system schematic used during Run 2 data collection periods of 2015+2016 [52].

Part IV.

Search for Heavy Vector Triplet Resonance Decays Into Standard Model Vh

Chapter 8.

Analysis Overview

8.1. Introduction

The following chapters will present a search for the production of a new heavy resonance that decays to a SM vector boson (V) and SM Higgs boson (h), using the 2015+2016 ATLAS dataset. The search is performed within two BSM paradigms; Heavy Vector Triplet Models as outlined in Chapter 4, and *Two Higgs Doublet Models* (2HDMs) as will be explained below.

8.1.1. Heavy Vector Triplet Model Interpretation

The first analysis is a search for the resonant production of a V and h from the decay of a new heavy vector boson, denoted from here on in as $W' \to Wh$ and $Z' \to Zh$, for resonant masses in the 500–5000 GeV range that are consistent with the HVT paradigm. The final state signature of the analysis is defined by the leptonic decay of the SM vector boson ($V \to \nu\nu, l\nu, ll$), and the bottom quark pair decay of the Higgs boson, $h \to b\bar{b}$. This results in three search channels, $Z' \to \nu\nu b\bar{b}$, $W' \to l\nu b\bar{b}$, and $Z' \to llb\bar{b}$, where Figure 8.1 gives one LO Feynman diagram for each of the three signal topologies.

The resonant mass spectrum of interest to the analysis, defined above as 500–5000 GeV, is bounded from above by the $\sqrt{s} = 13$ TeV center of mass energy supplied by the LHC. The production rate of resonant masses exceeding 5000 GeV are kinematically suppressed, and thus the analysis is insensitive to any excess beyond the Standard Model for an expected integrated luminosity of 100 fb^{-1} during the Run 2 data collection period.

The lower boundary on the other hand, resonant masses below 500 GeV, are excluded via *Electroweak Precision Tests* (EWPT) [30,53]. In these tests, free SM parameters such as the Fermi-constant (G_μ), $h/W/Z$-boson mass ($m_{h/W/Z}$), top-quark mass (m_t), $\alpha_s(m_Z)$, etc, are

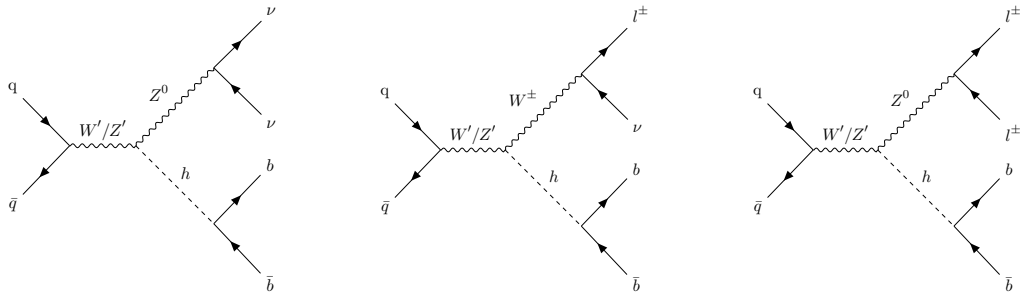

(a) $\nu\nu b\bar{b}$ **(b)** $l\nu b\bar{b}$ **(c)** $llb\bar{b}$

Figure 8.1.: Illustration of HVT signal processes at LO, and the corresponding final state topology of interest to the analysis.

seeded by world averaged experimental results and fitted using a Bayesian approach [54] to those predicted by the SM Lagrangian. The level of compatibility between the electroweak fitted SM parameters and experimentally known values, is then highly dependent on how some new physics attaches to the SM, and thus how the fundamental constants of the SM Lagrangian are altered by its presence.

As an example, within the HVT paradigm the $SU(2)_L$ and $U(1)_Y$ coupling constants can be parameterised as $\tilde{g}_w = g_w + \mathcal{O}(\hat{m}_W^2/\mu_V^2)$ and $\tilde{g} = g + \mathcal{O}(\hat{m}_W^2/\mu_V^2)$ (see Chapter 4 for parameter definitions), respectively, where $\mu_V \propto m_V$, and $\tilde{g}_w/\tilde{g}$ represent the coupling constants under the SM plus HVT hypothesis. In the aforementioned parameterisation, the alterations to g_w/g' are small for resonant masses above 500 GeV, whilst below this, significant deviations from the SM values would be observed. Consequently, other SM parameters that are dependent on these couplings, such as $m_W = vg/2$ and $m_Z = v\sqrt{g^2 + g'^2}/2$, would also differ from experimentally known values, where the latter are known to comply with the SM Lagrangian prediction [30]. Therefore, as a result of the indirect searches using SM electroweak precision measurements of properties like the top-quark mass, Z-boson decay fractions, etc, HVT mediator masses below 500 GeV can be excluded.

Direct searches for localised excesses consistent with HVT signals have also been conducted in the past, with two notable ATLAS publications; a Run 1 analysis using 20.3 fb^{-1} of data at a center of mass energy of $\sqrt{s} = 8$ TeV excluded mediator masses of $m_{Z'} < 1.36$ TeV and $m_{W'} < 1.47$ TeV for benchmark model A at a 95% confidence level [55], whilst an earlier Run 2 analysis using 3.2 fb^{-1} at $\sqrt{s} = 13$ TeV excluded mediator masses of $m_{Z'} < 1.49(1.58)$ TeV and $m_{W'} < 1.75(2.22)$ TeV for benchmark model A(B) at a 95% confidence level [56].

Since each benchmark model represents one possible HVT parameter configuration for a variable mediator mass ($m_{V'}$), limits on the HVT $g^2 c_F/g_V$ (V' coupling to SM fermions) and $g_V c_H$ (V' coupling to SM V-bosons) parameters as a function of the mediator mass, prove a far more useful tool. Therefore, Figure 8.2 shows the parameter exclusion plots for a small collection of mediator masses on a two dimensional $[g^2 c_F/g_V, g_V c_H]$ plane, for the aforementioned Run 1 and early Run 2 ATLAS analyses [55, 56].

It should be noted that whilst the excluded regions of phase space from the Run 1 and early Run 2 analyses are roughly equivalent, the Run 2 analysis was done using a dataset collected from an integrated luminosity that was approximately 10× smaller than the Run 1 version. As such, the Run 2 version was a proof of concept that primarily benefited from the scaling of the production cross-sections for the SM background processes relative to the HVT signal as a function of $\sqrt{s}$; the production rate of SM background processes like $t\bar{t}$ is reduced by a factor of 4, whilst the HVT signal cross-section is halved ($m_{Z'} = 0.5$ TeV at $\sqrt{s} = 8(13)$ TeV is $\approx 1(0.6)$ pb) for $\sqrt{s} = 7$ TeV $\rightarrow$ 13 TeV. However, the Run 2 analysis also benefited from a new substructure technique used to reconstruct the $h \rightarrow b\bar{b}$ decay products, which is capable of reconstructing with higher efficiency larger mediator masses, when compared to the Run 1 reconstruction approach.

With this in mind, the following version of the analysis expands on the early Run 2 version (Ref. [56]) by using the full 2015+2016 ATLAS dataset, thereby increasing the integrated luminosity further by a factor of 10. However, several improvements to the analysis were also made, with particular emphasis on an improved reconstruction technique designed to increase the analysis sensitivity across the entire HVT mediator mass spectrum of interest (Chapter 12), optimised event selection designed to increase the background rejection rate (Chapters 13–15), and increased MC statistics.

8.1.2. Two Higgs Doublet Model Interpretation

The second analysis uses a simple extension of the SM Higgs sector, which is given by the addition of a second complex Higgs doublet. This gives rise to five Higgs bosons; two CP-even scalar fields h and H, one pseudo-scalar A (CP-odd), and two charged fields $h^{\pm}$. Referred to as *Two Higgs Doublet Models* [57–60], the $A \rightarrow Zh$ final state is interpreted within this theoretical framework.

Four types of 2HDMs are tested, corresponding to variations in the coupling strength of the two Higgs scalars to the SM fermions and gauge bosons, which are summarised by table 2 of Ref. [61]. 2HDMs are interesting because they are key ingredients to supersymmetric extensions of the Standard Model, e.g. minimal supersymmetric SM [62–66], that tackle

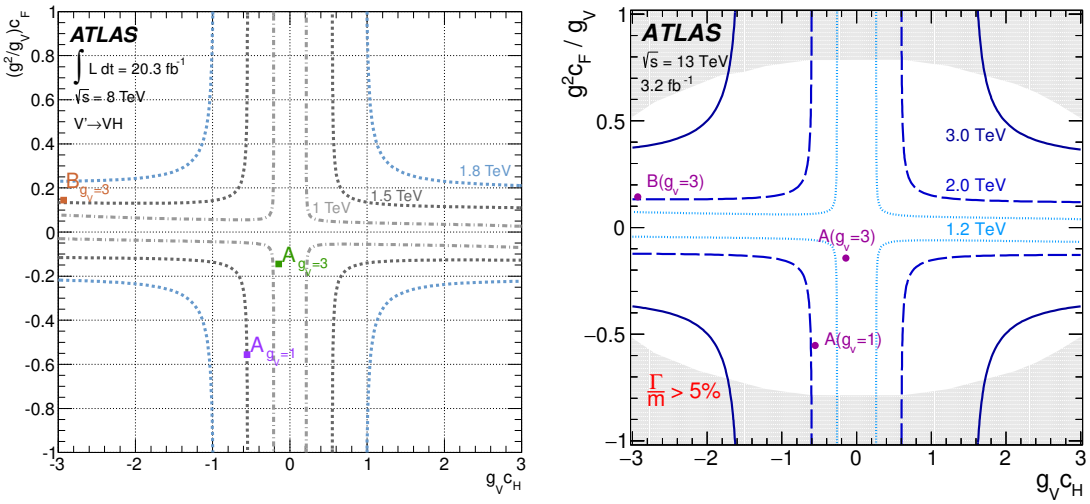

(a) ATLAS Run 1 HVT Vh resonance search using an integrated luminosity of 20.3 fb^{-1} [55]. **(b)** ATLAS Run 2 HVT Vh resonance search using an integrated luminosity of 3.2 fb^{-1} [56].

Figure 8.2.: HVT parameter exclusion plots in the $[g^2 c_F/g_V, g_V c_H]$ plane, for a variety of mediator masses, obtained from the ATLAS Run 1 (a) and early Run 2 (b) direct HVT Vh searches [55, 56].

the problems of baryon asymmetry [67], and are an important ingredient of axion models (dark matter candidates) [68].

In Type I 2HDMs all quarks couple to only one of the Higgs doublets, whilst in Type II 2HDMs the up-type quarks couple to one Higgs doublet, and the down-type quarks couple to the other Higgs doublet. Type III and IV 2HDMs differ from the Type I & II models via their couplings to the leptons. Both the production via gluon-gluon fusion (ggA) and associated b-quark production (bbA) are considered within the following analysis.

For this part of the analysis only the leptonic decays of the SM Z-boson, and bottom quark pair decays of the SM Higgs boson are considered, giving two analysis channels, $A \to \nu\nu b\bar{b}$ (0-lepton) and $A \to llb\bar{b}$ (2-lepton). Figure 8.3 shows the LO Feynman diagrams for the $A \to Zh$ signal.

Two ATLAS and one CMS result have already issued limits on the Type I and Type II 2HDMs, which can be found in Refs [69–71]. A Run 1 CMS result set limits on the production of a light pseudoscalar A boson decaying to Z-boson and h-boson in the $A \to Zh \to e^+e^-(\mu^+\mu^-) + b\bar{b}$ final state signature, using a total of 19.7 fb^{-1} data collected at a $\sqrt{s} = 8$ TeV. This analysis observed no localised excess, and so set upper limits on $\sigma(gg \to A) \times \text{BR}(A \to Zh) \times \text{BR}(h \to b\bar{b}) \times \text{BR}(Z \to e^+e^-(\mu^+\mu^-))$ for mediator masses ranging from 225 GeV $\leq m_A \leq$ 600 GeV, as shown by Figure 8.4a.

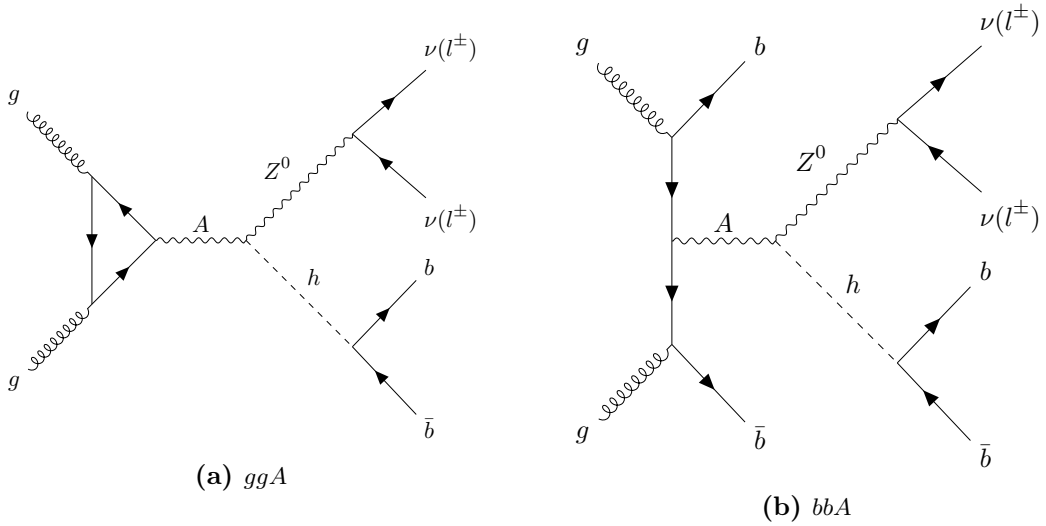

(a) ggA **(b)** bbA

Figure 8.3.: Illustration of AZh signal processes at LO, and the corresponding final state topology of interest to the analysis. For the bbA production mode, the additional b-quarks from gluon splitting typically fall out of the detector acceptance, due to their proximity to the beam-pipe.

For the ATLAS results, a Run 1 analysis using 20.3 fb^{-1} of data at $\sqrt{s} = 8$ TeV, was able to set limits on $\sigma(gg \to A) \times \text{BR}(A \to Zh) \times \text{BR}(h \to b\bar{b}) \times \text{BR}(Z \to ll/\nu\nu)$ for mediator masses in the 220 GeV $\leq m_A \leq$ 1000 GeV range, as shown by Figure 8.4b. Whilst a Run 2 analysis, using 3.2 fb^{-1} of data at a center of mass energy of $\sqrt{s} = 13$ TeV, was able to set limits on the gluon-fusion and associated b-quark production mechanisms for an extended range of mediator masses (220 GeV $\leq m_A \leq$ 2000 GeV) due to the higher center of mass energy obtained in Run 2; Figure 8.4c and Figure 8.4d show these limits on $\sigma(gg(bb) \to A) \times \text{BR}(A \to Zh) \times \text{BR}(h \to b\bar{b}) \times \text{BR}(Z \to ll/\nu\nu)$.

8.2. Analysis Strategy

Regardless of the interpretation, the final state signal topology is a SM vector boson that decays leptonically, paired with a Higgs boson that decays to two b-quarks, as shown by Figures 8.1/8.3.

Many Standard Model processes yield a very similar final state to this signature, and thus constitute the *background* in the following analysis. The two most dominant processes are $t\bar{t}$ and W/Z+jets, for all three lepton channels, and in the 1-lepton channel single-top production is also a key background. Figure 8.5 shows an example production mode for each of the three key backgrounds, and the relevant decays of the top and W/Z bosons

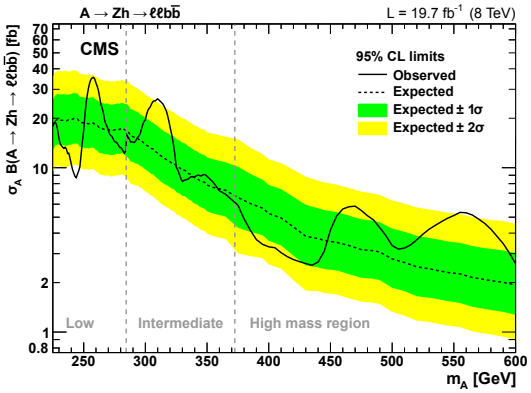

(a) CMS Run 1 $gg \to A \to \nu\nu(l^{\pm}l^{\mp}) + b\bar{b}$

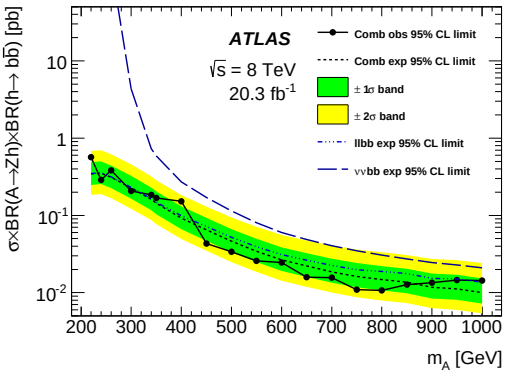

(b) ATLAS Run 1 $gg \to A \to \nu\nu(l^{\pm}l^{\mp}) + b\bar{b}$

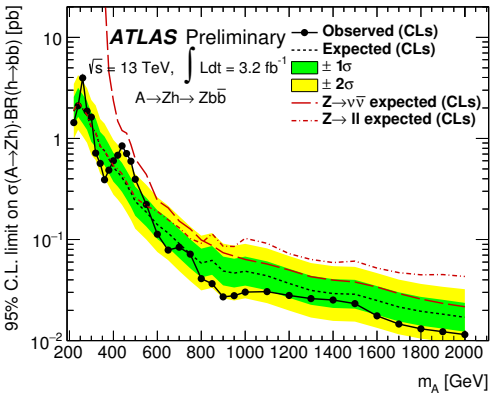

(c) ATLAS Run 2 $gg \to A \to \nu\nu(l^{\pm}l^{\mp}) + b\bar{b}$

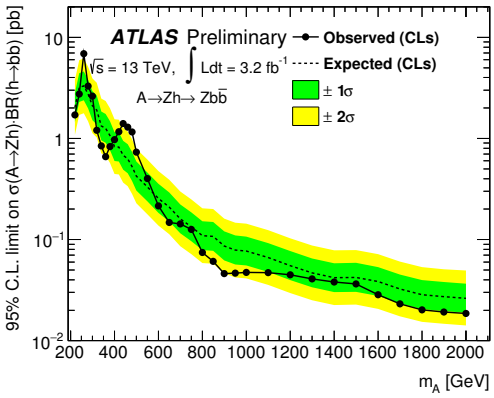

(d) ATLAS Run 2 $bb \to A \to \nu\nu(l^{\pm}l^{\mp}) + b\bar{b}$

Figure 8.4.: Summary of ATLAS and CMS Run 1/2 analyses searching for a pseudoscalar A-boson decaying to a $l^{\pm}l^{\mp}(\nu\nu) + b\bar{b}$ final state [69–71].

that yield the same final state topologies as the signal. Chapter 10 details the Monte Carlo configurations used to simulate these background processes, along with the hypothesised signal.

The goal of the analysis is to identify a localised excess in the collected data that is compatible with the HVT/AZh signal plus SM background hypothesis. This is referred to as the alternative hypothesis $\mathcal{H}_1$, whilst the null hypothesis, $\mathcal{H}_0$, corresponds to the SM background-only scenario. To achieve this goal, the analysis strategy is designed around a *Binned Profile Likelihood* fit (see Chapter 9 for more details) performed using the invariant mass of the SM vector boson and Higgs boson system, m_{Vh}, as the fit discriminant. The m_{Vh} is calculated using the formula:

$$m^2_{V'/A} = m^2_{Vh} = (p^{\mu}_{W/Z} + p^{\mu}_{h})^2 = \left[\sum_{l}^{\text{leptons},\nu} p^{\mu}_{l} + \sum_{b}^{b-\text{quarks}} p^{\mu}_{b} \right]^2 \tag{8.1}$$

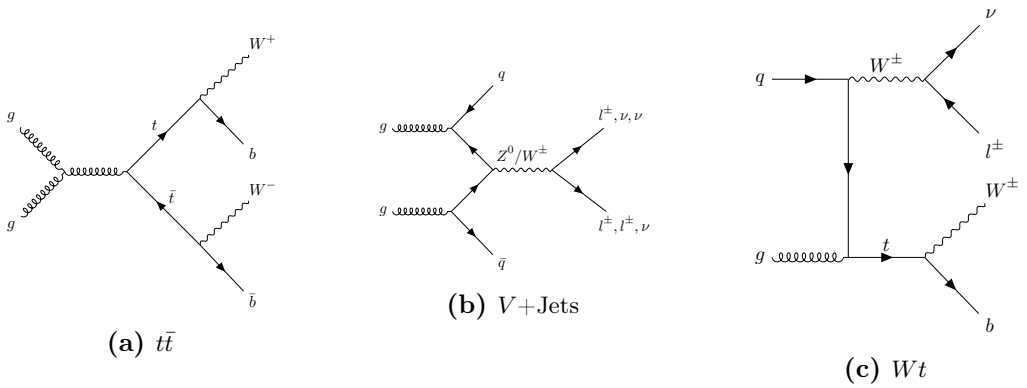

(a) $t\bar{t}$ **(b)** V+Jets **(c)** Wt

Figure 8.5.: Illustration of the dominant Standard Model background processes for HVT/AZh analysis.

As indicated by the above formula, the fit variable is representative of the mediator mass of the underlying resonance $m_{V'/A}$, and is chosen based on theoretical considerations concerning the Simplified Model strategy. Specifically, as previously outlined in Chapter 4, the HVT phenomenological Lagrangian is constructed to only describe *on-shell* resonances; this is because only those parameters of the fundamental model that control the mass of the resonance and its production/decay modes, are kept. Therefore, only on-shell observables that are exclusively sensitive to the resonance formation should be used, in order to mitigate the influence of off-shell effects like extra contact interactions, to the analysis. Furthermore, on-shell observables are easily parameterised in terms of the phenomenological Lagrangian parameters, thereby simplifying the physical interpretation of the upper limits in terms of the underlying parameters of the model [30].

It is easily noticed that the event can be divided into two parts; the leptonic side of the event corresponds to the SM vector boson reconstructed using the typical ATLAS lepton and missing transverse energy (MET) physics objects. The hadronic side of the event corresponds to the reconstruction of the Higgs candidate using the anti-k_T clustering algorithm to form jets seeded by the b-quarks originating from the Higgs decay. The physics objects used to reconstruct the underlying physical process are detailed in Chapter 11. The scheme adopted to reconstruct the hard scatter process is outlined in Chapter 12.

The fit is run using a series of orthogonal fit regions defined by four key event properties; the invariant mass of the reconstructed Higgs candidate (m_h), the number of jets identified as containing a b-hadron (hadron containing a b-quark), the number of leptons, and whether the dilepton system is same or different flavour. These four properties are used to define the various signal and control regions passed to the Binned Profile Likelihood fit. The fiducial phase space of the analysis designed to maximise the signal acceptance and background

rejection is detailed in Chapters 13-15. Details pertaining to the fit regions used by the Binned Profile Likelihood are given by Chapter 17.

If no statistically significant excess is observed then a 95% exclusion limit on the production cross-section of the signal is placed using the CL_s method. The statistical methodology used by the analysis is detailed in Chapter 9. The results from the statistical hypothesis testing are then provided by Chapter 19.

Chapter 9.

Statistical Framework

9.1. Binned Profile Likelihood Fit

To illustrate the Binned Profile Likelihood methodology used within the analysis, a two-bin counting experiment can be considered, one signal and one control region bin. For such a scenario the likelihood function takes the form:

$$\mathcal{L}(\mu) = \mathcal{P}(N|\mu s + b_{\mathrm{SR}}) \times \mathcal{P}(M|b_{\mathrm{CR}}), \tag{9.1}$$

where μ represents the signal strength and the parameter of interest (POI) in the fit, N represents the number of observed data events in the signal region, and M denotes the number of data events in the control region. The nominal signal event yield prediction is given by s, whilst $b_{\mathrm{SR/CR}}$ corresponds to the expected background event yield in the signal or control regions. $\mathcal{P}(...)$ represents the Poisson probability of obtaining $N(M)$ observed data events, given an expected $\mu s + b_{\mathrm{SR}}(b_{\mathrm{CR}})$ number of events in the signal(control) region bin [72].

Generalising to a series of α_{bin} binned measurements ($\vec{n} = \{n_1, n_2, ..., n_\alpha\}$) within the SR and β_{bin} binned measurements ($\vec{m} = \{m_1, m_2, ..., m_\beta\}$) within the CR, for $\alpha_{\mathrm{region}}(\beta_{\mathrm{region}})$ number of signal (control) regions, the likelihood function is the product of Poisson probabilities:

$$\mathcal{L}(\mu, \vec{\theta}) = \left[\prod_{k=1}^{\alpha_{\mathrm{region}}} \prod_{j=1}^{\alpha_{\mathrm{bin}}} \mathcal{P}^{kj}(N|\mu s(\vec{\theta_s}) + b_{\mathrm{SR}}(\vec{\theta_b})) \right] \times \left[\prod_{r=1}^{\beta_{\mathrm{region}}} \prod_{l}^{\beta_{\mathrm{bin}}} \mathcal{P}^{rl}(M|b_{\mathrm{CR}}(\vec{\theta_b})) \right] \tag{9.2}$$

$$= \left[\prod_{k=1}^{\alpha_{\mathrm{region}}} \prod_{j=1}^{\alpha_{\mathrm{bin}}} \frac{(\mu s_{kj}(\vec{\theta_s}) + b_{kj;\mathrm{SR}}(\vec{\theta_b}))^{n_{kj}}}{n_{kj}!} e^{-(\mu s_{kj}(\vec{\theta_s}) + b_{kj;\mathrm{SR}}(\vec{\theta_b}))} \right] \tag{9.3}$$

$$\times \left[\prod_{r=1}^{\beta_{\mathrm{region}}} \prod_{l=1}^{\beta_{\mathrm{bin}}} \frac{(b_{rl;\mathrm{CR}}(\vec{\theta_b}))^{m_{rl}}}{m_{rl}!} e^{-(b_{rl;\mathrm{CR}}(\vec{\theta_b}))} \right], \tag{9.4}$$

where nuisance parameters, $\theta_{s/b}$, have been introduced to encode the uncertainties arising from systematic sources. Each nuisance parameter is parameterised as either a Gaussian or a log-normal distribution, with a width defined as σ_{gauss}. This width, referred to as a *prior*, constrains the nuisance parameters to their nominal values, by penalising the likelihood function for deviations away from the central value. This is done via so-called penalty or auxiliary measurements:

$$\mathcal{L}_{\text{aux}}(\theta) = \prod_{q=1}^{N_\theta} f(\widetilde{\theta}|\theta) \xrightarrow[\text{E.g.}]{\text{Gauss}} \prod_{q=1}^{N_\theta} \frac{1}{\sqrt{2\sigma_q^2}} \exp\left[- \frac{(\widetilde{\theta} - \theta)^2}{2\sigma_q^2} \right], \tag{9.5}$$

where $f(\widetilde{\theta}, \theta)$ represents the distribution of the estimates of the nuisance parameters ($\widetilde{\theta}$) for a given nuisance parameter value θ [72]. Two types of nuisance parameter exist: constrained nuisance parameters have an assigned prior σ_q, and so penalise the likelihood function $\mathcal{L}(\mu, \vec{\theta})$, whilst unconstrained nuisance parameters have a central value of 1 and no prior. The latter are referred to as *freely floating* nuisance parameters, and have no corresponding penalisation term.

The expected number of signal/background events $s/b_{\text{SR/CR}}$ for the signal/control regions are now parameterised as functions of the nuisance parameter $\vec{\theta}$, i.e. $s/b_{\text{SR/CR}} \rightarrow s/b_{\text{SR/CR}}(\vec{\theta_b})$ [73]. Specifically, $s_i(\vec{\theta_s}) = s_{\text{tot}} \int_{\text{bin}\,i} f_s(x; \vec{\theta_s}) dx$ and $b_i(\vec{\theta_b}) = b_{\text{tot}} \int_{\text{bin}\,i} f_b(x; \vec{\theta_b})$ dx, where $f_s(x; \vec{\theta_s})$ and $f_b(x; \vec{\theta_b})$ represent the probability distribution functions (pdf) of the variable x for signal and backgrounds events, and $\vec{\theta}_{s/b}$ parameterise the signal/background shapes of the pdfs [73].

Statistical uncertainties due to the limited Monte Carlo statistics are incorporated into the fit following the recommendations of Barlow and Beeston Lite given by Refs. [74, 75]. Each bin in the $m_{Vh}^{(T)}$ spectrum is assigned a nuisance parameter, γ_i, which are modelled as Poisson priors. As such, a penalty term is introduced to the likelihood function of the form:

$$\mathcal{L}(\gamma_i) = \prod_{i \in \text{bins}} \mathcal{P}(b_i(\vec{\theta_b}) | \gamma_i \tau_i), \tag{9.6}$$

where the predicted event yield for each bin, as given by the MC estimate $b_i(\vec{\theta_b})$, form the Poisson values, and the expected mean for the bin $(\gamma_i \tau_i)$ is a parameter in the fit. It should be noted that γ_i is the parameter, and $\tau_i = (b_i(\vec{\theta_b})/\delta_i)^2$ is a constant that represents the expected background yield. In essence the mean is estimated using the ratio of the estimated event yield $b_i(\vec{\theta_b})$ to the associated MC error δ_i [72].

The full likelihood is therefore given by the product of the above individual terms:

$$\begin{aligned}\mathcal{L}_{tot}(\mu,\vec{\theta},\vec{\gamma}) &= \mathcal{L}(\mu,\vec{\theta})\mathcal{L}_{\text{aux}}(\theta)\mathcal{L}(\gamma_i)\\ &= \left[\prod_{k=1}^{\alpha_{\text{region}}}\prod_{j=1}^{\alpha_{\text{bin}}}\frac{(\mu s_{kj}(\vec{\theta}_s)+\gamma_{kj}b_{kj;\text{SR}}(\vec{\theta}_b))^{n_{kj}}}{n_{kj}!}e^{-(\mu s_{kj}(\vec{\theta}_s)+\gamma_{kj}b_{kj;\text{SR}}(\vec{\theta}_b))}\right]\\ &\times\left[\prod_{r=1}^{\beta_{\text{region}}}\prod_{l=1}^{\beta_{\text{bin}}}\frac{(\gamma_{rl}b_{rl;\text{CR}}(\vec{\theta}_b))^{m_{rl}}}{m_{rl}!}e^{-(\gamma_{rl}b_{rl;\text{CR}}(\vec{\theta}_b))}\right]\\ &\times\prod_{i,u}^{\alpha_{\text{bin}},\beta_{\text{bin}}}\mathcal{P}(b_{i,u}(\vec{\theta}_b)|\gamma_{i,u}\tau_{i,u})\\ &\times\prod_{q=1}^{N_\theta}f(\widetilde{\theta}|\theta)\end{aligned}$$

This is implemented within the analysis through the `HistFactory` tool [72].

9.1.1. Shape Systematics

Systematic uncertainties that impact the $m_{Vh}^{(T)}$ shape for a process P (V+jets, $t\bar{t}$, ...), $h_P(x)$ ($x=[m_{Vh}^T, m_{Vh}]$), are incorporated into the fit by assigning a nuisance parameter $\theta_{k;P}$ to each systematic, where k is the systematic index. Each nuisance parameter is modelled as a log-normal distribution with a mean of 0 and a prior of $\sigma_{k;P}=1$.

For each nominal histogram $h^0_{k;P}(x)$, an up/down variation is defined by varying the underlying systematic within its $\pm1\sigma$ error, giving rise to an alternative histogram $h^{\pm}_P(x)$. For example the Jet Energy Scale (JES) is varied within its $\pm\sigma$ error to give an up/down histogram. The nuisance parameter $\theta_{k;P}$ is then used to modify the nominal prediction, fully correlated across all bins, according to:

$$h^+_{k;P}(x) = h^0_{k;P}(x) + \theta_{k;P}(h^+_{k;P}(x) - h^0_{k;P}(x)) \tag{9.7}$$

$$h^-_{k;P}(x) = h^0_{k;P}(x) + \theta_{k;P}(h^-_{k;P}(x) - h^0_{k;P}(x)) \tag{9.8}$$

9.2. Test Statistic

The nominal fit result, meaning the expected signal strength μ and its corresponding uncertainty σ_μ, given the observed data, is obtained by maximising the likelihood function with respect to all parameters (maximised log-likelihood value (MLL)). A test statistic is

then constructed of the form:

$$q_\mu = -2\ln\left[\frac{\mathcal{L}(\mu,\hat{\hat{\vec{\theta}}})}{\mathcal{L}(\hat{\mu},\hat{\hat{\vec{\theta}}})}\right], \tag{9.9}$$

where $\hat{\mu}$ and $\hat{\vec{\theta}}$ denote the MLL values of the signal strength and nuisance parameters, and $\hat{\hat{\vec{\theta}}}$ are the nuisance parameter values that maximise the log-likelihood function for a given μ value.

This test statistic is then used to measure the compatibility of the background-only hypothesis with the observed data, by extracting the local p-value under the null hypothesis and assuming the observed data has no signal present. This is extracted via the formula:

$$p_\mu = \int_{q_{\mu;\text{obs}}}^{\infty} f(q_\mu|\mu)dq_\mu, \tag{9.10}$$

where $q_{\mu;\text{obs}}$ is the observed value of the test statistic given the data, and $f(q_\mu|\mu)$ is the probability density function of the test statistic. Using the Wald approximation [76] for the test statistic q_μ, and assuming that the maximum likelihood estimator $\hat{\mu}$ is Gaussian-distributed, it can be shown that q_μ follows a *non-central chi-square* distribution of one degree of freedom [73]:

$$\begin{aligned} f(q_\mu|\mu') = \frac{1}{2\sqrt{q_\mu}}\frac{1}{\sqrt{2\pi}}\Bigg[&\exp\left(-\frac{1}{2}\left(\sqrt{q_\mu}+\sqrt{\frac{(\mu-\mu')^2}{\sigma^2}}\right)^2\right) \\ &+\exp\left(-\frac{1}{2}\left(\sqrt{q_\mu}-\sqrt{\frac{(\mu-\mu')^2}{\sigma^2}}\right)^2\right)\Bigg] \end{aligned} \tag{9.11}$$

If no hint of a statistically significant signal contribution to the data is found, then the CL_s method [77] is used to set an upper limit on the signal cross-section. Defined as the ratio of two confidence limits $\text{CL}_{\text{s+b}}$ and CL_b, where $\text{CL}_{\text{s+b}}$ is the confidence interval for the signal-plus-background hypothesis and CL_b is the background-only hypothesis:

$$\text{CL}_\text{s} = \frac{\text{CL}_{\text{s+b}}}{\text{CL}_\text{b}} = \frac{1-p_\mu}{1-p_0} \tag{9.12}$$

This is repeated once for each of the mediator mass points generated by the MC, yielding an exclusion limit curve [72, 73].

9.3. Asimov Dataset

The 'Asimov' dataset is an artificial dataset where all statistical fluctuations are suppressed, and the observed events in all regions and bins (i) are replaced by the expected values, for example:

$$N_i = \mu s_i + b_i, \tag{9.13}$$

$$M_i = b_i \tag{9.14}$$

In practice this means replacing the data with the MC/data-driven background estimates plus the simulated signal, where this signal is multiplied by the parameter of interest μ. Consequently, the estimators of all parameters in the fit should be the true parameter values [73]. This artificial dataset is primarily used for either testing purposes, or calculating the expected sensitivity of the analysis and its fit model to the presence of a HVT/AZh signal.

Chapter 10.

Datasets & Monte Carlo Samples

The following chapter outlines the recorded and simulated data used within the two analyses outlined in Chapter 8. It will summarise the MC setup used to predict both the 2HDM $A \to Zh$ and HVT $V' \to Vh$ signal processes, the SM processes, and the data collected by the ATLAS detector during 2015 and 2016.

10.1. Run 2 Data

The data used within the analysis was collected by the ATLAS detector during the years of 2015 and 2016. The 2015 data was collected during the months of July to November, amounting to a total of 3.21 ± 0.07 fb^{-1} ($\pm 2.1\%$ uncertainty) at $\sqrt{s} = 13$ TeV, operating at a peak luminosity of 5×10^{33} cm^{-2}s^{-1} with an average of 13.7 interactions per bunch crossing ($\langle\mu\rangle$) [45]. The 2016 data was collected during the months of April to November, totalling 32.9 ± 1.1 fb^{-1} ($\pm 3.4\%$ uncertainty) of recorded data, ending at a peak luminosity of 13.8×10^{33} cm^{-2}s^{-1} with $\langle\mu\rangle = 24.9$ [45].

It should be noted that the larger fractional uncertainty on the 2016 integrated luminosity, when compared to the 2015 data, was a direct consequence of beam condition changes; higher $\langle\mu\rangle$ in 2016, increase in particle flux (accelerates calorimeter radiation ageing), and bunch pattern alterations. All these changes gave rise to a larger variance in the luminosity ratio of that measured by the ATLAS TILE/FCAL/EMCAL/Tracker sub-detectors to that measured by LUCID, as a function of the collection runs during 2016 [45]. This run-to-run variance known as 'long-term stability' [45] was calculated to be $\pm 2.5\%$ in early 2017. By late 2017 LUCID was found to systematically over-estimate the measured luminosity in a small portion of the data. Therefore a shift in the LUCID luminosity measurement was applied based on this subset of data, thereby reducing the uncertainty to 1.4%. Amongst further improvements, the final 2016 luminosity was quoted as $\pm 2.2\%$, which falls in line

with the 2015 data; this development was published too late to be used within the following analysis.

In both cases the data is composed of lumi blocks (2-minute data acquisition periods) that meet a set of detector and data quality (DQ) criteria. This is referred to as a Good Runs List (GRL), which ensures that the detector is in good operating condition when the data is analysed. The GRL utilised within the following analysis is referred to as the ATLAS 'All_Good' list.

10.2. Monte Carlo Samples

The following section will give an overview of the default MC configuration used to simulate the $A \to Zh$ & $V' \to Vh$ signal processes (Section 10.2.1), in addition to the SM backgrounds V+Jet, $t\bar{t}$, VV, single top, $t\bar{t}V(h)$, and SM Higgs plus W/Z vector boson production (Vh) processes (see Section 10.2.2). Theoretical uncertainties pertaining to the simulation of these processes are evaluated using alternative MC generators or MC generator configurations; these are summarised in Section 18.3.

10.2.1. Signal Samples

Simulated MC samples for the two signal models are generated using MadGraph5_aMC@NLO 2.2.2 interfaced with the NNPDF2.3LO PDF [78, 79]. The matrix element generated (ME) signal processes are then showered and the final state components are hadronised using the parton shower (PS) generator Pythia 8.186 interfaced with the NNPDF2.3LO PDF set using the A14 parameter tune [79–81].

Samples are generated for a range of mediator masses, from 0.5 TeV to 2 TeV in increments of 100 GeV, from 2 TeV to 3 TeV in 200 GeV increments, and 500 GeV increments for the masses from 3 TeV to 5 TeV. The Higgs boson in the HVT Vh process is produced at a pole mass of 125.5 GeV, with a corresponding width given by the narrow width approximation equivalent to 10% the resonance mass. The Higgs is allowed to decay to all possible quarks, where the $H \to c\bar{c}$ and $H \to b\bar{b}$ relative branching fraction is $BR(h \to c\bar{c})/BR(h \to b\bar{b}) = 0.05$ ($BR(h \to c\bar{c}) = 0.0287$ & $BR(h \to b\bar{b} = 0.569)$) [60].

For the $A \to Zh$ signal, two production modes are considered. The gluon-gluon fusion (ggA) production mode is produced using the ME generator MadGraph5_aMCNLO 2.2.2 using the NNPDF2.3LO PDF set, and the events are showered and hadronised using the PS generator Pythia 8.186 configured to the A14 parameter tune, and using the

NNPDF2.3LO PDF set [78–81]. The b-quark associated production ($b\bar{b}A$) is simulated with MadGraph5_aMCNLO 2.2.3 using next-to-leading order (NLO) matrix elements with massive b-quarks and the CT10F4 NLO PDF set. The parton shower and hadronisation are simulated with Pythia 8.210.

Samples were generated for mediator masses ranging from 220 GeV to 500 GeV in 20 GeV increments, 500 GeV to 1 TeV in steps of 50 GeV, and between 1 TeV and 2 TeV in increments of 100 GeV, assuming a zero natural width of the A boson, but allowed to deviate from this prescription when determining the constraints on the parameters of the 2HDM parameters. The Higgs boson for all signal samples is set to a pole mass of 125 GeV, and the $h \to b\bar{b}$ decay is controlled by the parameters of the 2HDM [82, 83].

10.2.2. Background Samples

The nominal predictions for the SM background processes, except the multi-jet background (MJ), are all estimated via the use of Monte Carlo simulations. The key background processes estimated in this manner are:

- ***V*+Jets:** The production of a SM vector boson (W/Z boson) in association with additional jets.
- ***t*$\bar{t}$:** The production of a SM top anti-top pair.
- ***VV*:** The production of two SM vector bosons, WW, WZ or ZZ.
- **Single Top:** The production of a single SM top quark via the s-channel or t-channel and in association with a SM W boson.
- **SM *Vh*:** The associated production of a SM Higgs boson (h), in association with a SM vector boson $V = W$,Z.
- ***t*$\bar{t}$*V*(*h*)**: Top-quark pair production in association with a SM vector boson or SM Higgs boson.

V+Jets Background

The V+Jets SM process is one of two key backgrounds found within the analysis. The nominal prediction for the V+Jets SM process is produced using Sherpa 2.2.1 [35], where the ME is calculated using the internal ME generators Comix [84] and OpenLoops [85], both of which use the NNPDF3.0NNLO PDF set [51, 84, 85]. The internal Sherpa PS generator (CSShower++) is then used to shower the events under the ME+PS@NLO

merging prescription [86]. This allows the V+Jets process to be predicted to NLO in pQCD for up to two extra partons at the ME level, and three or four extra partons at LO in pQCD at the ME level. For five or more extra partons the resummation of additional real QCD emissions using the PS approach is used. The NLO electroweak corrections are not taken into account.

The SHERPA 2.2.1 sample adopts a 5-flavour scheme, meaning that the bottom and charm quarks are produced as massless partons within the matrix element, but the internal SHERPA 2.2.1 parton shower will treat the b/c-quarks as massive. Massive b/c-quarks can also be produced in the scattering process via the Underlying Event (UE) mechanism.

For both the W+Jet and Z+Jet processes, the cross-sections are known to NNLO in QCD from fixed order perturbative calculations. Therefore, the generator level cross-sections provided by SHERPA 2.2.1 are normalised to these higher order cross-sections [87]. Details on this can be found in Section 18.3.1.

$t\bar{t}$ Background

The production of top anti-top quark pairs ($t\bar{t}$) is the second of two key backgrounds found within these analyses. The $t\bar{t}$ process is modelled using the POWHEG-BOX v2 generator, which provides a NLO calculation in pQCD for the matrix element using the CT10 NLO PDF set [88–91]. The ME is then interfaced with the parton shower generator PYTHIA 6.428 which uses the CTEQ6L1 LO PDF set, for the showering, hadronisation, UE and multiple parton interactions (MPI) [92, 93]. The PYTHIA 6.428 PS generator is configured using the PERUGIA2012 tune, and is interfaced with PHOTOS for the modelling of QED final-state radiation, in addition to TAUOLA for the simulation of τ decays [94–96]. EVTGEN v1.2.0 is used to decay bottom and charm hadrons following the hadronisation step performed by PYTHIA [97].

The ME generator uses a 4-flavour scheme, meaning that the b-quarks within the matrix element calculation are considered massive, and the top quark spin correlations are preserved. The top mass is set to 172.5 GeV, such that the hard process renormalisation and factorisation scales (μ_{R} and μ_{F} respectively), are set to the default POWHEG-BOX v2 values which take the form:

$$\mu_i = \sqrt{m_t^2 + p_T^2}$$

Where m_t is the invariant mass of the top quark, and p_T is the top quark momentum for the Born configuration (before showering). The resummation dampening factor hdamp, which regulates the resummation of additional radiation for the first hardest emission from

the NLO matrix element, is set to m_t in order to obtain good data/MC agreement [98]. The cross-section for the SM $t\bar{t}$ process is known to NNLO in pQCD via fixed order perturbative calculations, as such the $t\bar{t}$ prediction obtained from the aforementioned POWHEG-BOX v2 setup is normalised to the NNLO cross-section. Details of this are given in Section 18.3.2.

Single Top Background

The single top background is simulated using the ME generator POWHEG-BOX v2 utilising the CT10 PDF set for the s-channel and Wt-channel production modes [88–91]. Whilst for the t-channel the POWHEG-BOX v1 ME generator is used [88–91]. Both ME generators are interfaced with PYTHIA 6.428 using the LO CTEQ6L1 PDF set, configured using the PERUGIA2012 parameter tune [92–94]. PYTHIA 6 is further interfaced with PHOTOS in order to model QED final state radiation, and to TAUOLA for the simulation of τ decays [95,96]. The hadronised components of the generated events are then fed to EVTGEN v1.2.0 in order to model the bottom and charm hadron decays [97]. As in the case of the $t\bar{t}$ process the mass of the top quark is set to $m_t = 172.5$ GeV, hdamp is set to the top mass, and top spin correlations are considered in all cases, where for the t-channel production mode the top quarks are decayed using MADSPIN [99].

VV Background

Typically corresponding to the production of two SM vector bosons in the final state, the possible decay permutations of the WW, WZ and ZZ processes can contribute a non-negligible background component to the studied phase space. For example: $Z \to b\bar{b}$ + $Z \to \nu\nu(ll)$ for the 0(2)-lepton channel or $Z \to \bar{b}b$ + $W \to l\nu$ for the 1-lepton channel. Other permutations of mistagged charm jets, for example from the decay of a W boson, can also contribute as well.

With this in mind the diboson process is simulated using the SHERPA 2.1.1 ME generator using the CT10 PDF set [35,91]. For the ZZ process the ME is calculated at NLO accuracy in QCD for 0 or 1 additional partons, and LO accuracy in QCD for 2–3 additional partons. For the WW and WZ processes the ME is calculated at NLO in QCD for 0 additional partons, and 1–3 additional partons at LO. The internal SHERPA 2.1.1 parton shower algorithm is used to shower the final state ME calculation, and is merged with the ME calculation using the CKKW-L merging technique, using a merging scale of $Q_{\text{cut}}^{\text{CKKW-L}} = 20$ GeV [100,101].

SM Higgs Background

The production of a SM Higgs and SM vector boson (Vh) can take place via two production modes. For the quark induced production modes, $q\bar{q} \to Vh$, the background process is simulated using Pythia 8.186 configured using the A14 tune and NNPDF2.3LO PDF set [79, 81, 102]. The gluon fusion induced production mode, $gg \to Vh$, is generated using the Powheg-Box v2 ME generator interfaced with Pythia 8.186 configured to the AZNLO ATLAS tune; both the matrix element and parton shower generators use the CT10 NLO PDF set [88–91, 102, 103].

The Higgs mass is fixed to a value of 125 GeV and the branching fraction for the decay of the Higgs to $b\bar{b}$ is set to 58%. For such a configuration the SM $pp \to Vh$ cross-section, inclusive of the production modes, the production cross-section is known to NNLO(QCD)+NLO(EW) accuracy for both the Wh and Zh processes.

Since the Wh process is exclusively qq initiated, the MC generator predicted cross-section is scaled via a multiplicative factor to the higher order cross-section of 1.38 pb. In the case of Zh production the MC $gg \to Zh$ and $q\bar{q} \to Zh$ processes, calculated at NLO and LO in pQCD respectively, can not be scaled trivially to the fixed order NNLO(QCD)+NLO(EW) cross-section without double counting. Therefore, a fixed order pQCD calculation for the $gg \to Zh$ [104–106] sub-process at NLO+NLL(QCD) accuracy, is subtracted from the inclusive $pp \to Zh$ NNLO(QCD)+NLO(EW) cross-section, in order to yield an estimate of the $q\bar{q} \to Zh$ cross-section contribution at NNLO(QCD)+NLO(EW), referred to as $\sigma_{q\bar{q}}^{\text{NNLO}}$. The $q\bar{q} \to Zh$ sub-process is then scaled to this estimated higher-order cross-section, $\sigma_{q\bar{q}}^{\text{NNLO}}$, using a multiplicative k-factor. Meanwhile the $gg \to Zh$ is scaled to the fixed NLO+NLL(QCD) pQCD accurate cross-section.

$t\bar{t}V$ and $t\bar{t}h$

The $t\bar{t}h$ and $t\bar{t}V$ samples are generated at NLO accuracy with MadGraph5_aMCNLO 2.3.2 interfaced to Pythia 8.210. The NNPDF3.0 NLO PDF set is used in the matrix element calculation while for the parton shower the A14 tune is used with the NNPDF2.3LO PDF set.

Chapter 11.

Object Definitions

The following section details the types of reconstructed physics objects used by the analysis. These physics objects act as proxies for the underlying physical particles produced by the proton-proton collisions, thus enabling the reconstruction of the topology and kinematic characteristics of the event.

11.1. Jets

Due to the asymptotic nature of QCD (Section 3.2.1), *colour-confinement* of quark-antiquark pairs is used to explain the production of colour-singlet final states, mesons and baryons, which are the only observable products of QCD partons. Specifically, as QCD partons become increasingly separated it becomes energetically favourable for the vacuum to spawn a quark-antiquark pair. This process continues eventually yielding a spray of quark-antiquark pairs that become bound to form hadrons. Therefore, the production of energetic partons at the LHC results in a collimated beam of colourless hadrons. This collection of hadrons can be grouped together to form a composite object referred to as a *jet*.

The standard jet reconstruction algorithm used for the following analysis is known as the *anti-k_T* clustering algorithm. Using a distance measure define as :

$$d_{ij} = \min\{k_{Ti}^{-2}, k_{Tj}^{-2}\}\frac{\Delta_{ij}^2}{R^2} \tag{11.1}$$

$$d_{ti} = k_{Ti}^{-2}, \tag{11.2}$$

where for particles $[i, j]$, k represents the momentum vector of the particles, $\Delta_{ij}^2 = (y_i - y_j)^2 + (\phi_i - \phi_j)^2$ is the solid angle between the two particles using the rapidity y and azimuthal angle ϕ of each particle, and R is the constant distance measure used to normalise the equation. d_{ti} represents the distance measure between the i^{th} particle and the beam, whilst d_{ij} is the distance measure between two particles. In the following analysis the jet

width in the y–ϕ plane takes one of three possible values, $R = \{0.2, 0.4, 1.0\}$, depending on the method used to reconstruct the Higgs candidate. A detailed explanation of the algorithm is given by Refs. [107, 108].

11.1.1. Analysis Level Jets

Two types of calorimeter reconstructed jets are used within the following analysis. The first are known as the EM topological clustered anti-k_T $R = 0.4$ jets, referred to as *Small-R* jets from here on in. The *Signal & Forward* jet definitions with their selection criteria are outlined in Table 11.1. To suppress small-R jets arising from pile-up interactions (multiple proton-proton collisions per bunch crossing), signal jets must pass the Jet Vertex Tagger (JVT) requirements outlined in Table 11.1 [109]. Pile-up contamination to the surviving jets is then corrected, and jet energy scale (JES) and jet mass resolution (JMR) calibrations are then also applied according to Ref. [110].

The second type of jet is the *Local Cluster Weighting* (LCW) corrected topological cluster anti-k_T R= 1.0 jet, referred to as a *Large-R* jet from here on in. Local Cluster Weighting is a procedure in which the topological clusters fed to the anti-k_T clustering algorithm are calibrated, prior to jet formation, for hadronic response (non-compensation), out-of-cluster energy loss, and dead material energy loss [111]. These jets are *trimmed* in order to remove energy of clusters originating from initial state radiation (*ISR*), pile-up interactions, and the underlying event [112]. This is achieved by using the anti-k_T clustering algorithm with a distance parameter of $R_{\text{sub}} = 0.2$ on the constituents of the large-R jet. These *sub-jets* are then removed if the fractional contribution of the sub-jet to the large-R jet is $< 5\%$, i.e. $p_T^{\text{sub}}/p_T^{\text{large}-R} < 0.05$ [107, 108, 113]. Table 11.1 summarises the track-jet and large-R jet selection criteria.

To enhance the mass resolution of the large-R, tracks from the ID are *ghost associated* to the large-R jet by reducing the magnitude of the track four-vector to an infinitesimally small value; scale the the vector by a multiplicative factor. The four-vector is then included in the list of calorimeter deposits to be clustered via the anti-k_T clustering algorithm, meaning that each track ends up clustered within a jet. However, due to its infinitesimally small magnitude, a *ghost*, the suppressed four-vector has no impact on the jet properties to which it is *associated*.

By using the track information along with the clustered calorimeter deposits, a correction referred to as the *track-assisted* jet mass is applied [114]. Furthermore the large-R jet mass/energy scale and resolution are calibrated using MC truth comparisons and in-situ top quark measurements [114]. These jets are required to have a $p_T > 250$ GeV and $|\eta| < 2.0$.

Jet Category	Selection Requirements
Forward Jets	$p_T > 30\,\text{GeV}$ $2.5 \leq \lvert\eta\rvert < 4.5$
Signal Jets	$p_T > 20\,\text{GeV}$ $\lvert\eta\rvert < 2.5$ JVT ≥ 0.59 if $\lvert\eta\rvert < 2.4$ and $p_T < 60\,\text{GeV}$
Large-R Jets	$p_T > 250\,\text{GeV}$ $\lvert\eta\rvert < 2.0$ at least one track jet
Track-Jets	$p_T > 10\,\text{GeV}$ $\lvert\eta\rvert < 2.5$ has at least 2 track constituents

Table 11.1.: Selection requirements for all anti-k_T jets.

The analysis also uses a third type of jet known as a *track-jet*; built by clustering ID tracks using the anti-k_T $R = 0.2$ algorithm, each jet must have at least 2 tracks with $p_T > 400$ MeV that are associated with the primary vertex. Each jet must have a total $p_T > 10$ GeV and $|\eta| < 2.5$. These track-jets are ghost associated to the large-R jets when b-tagging the large-R jet for the $h \to bb$ candidate, see Section 11.5.

11.2. Leptons

11.2.1. Isolation Requirements

Suppression of fake electrons and muons resulting from misidentified jets (jets faking electrons) or the non-prompt production of muons via semi-leptonic decays of hadrons, is achieved through the use of the isolation recommendations outlined by the ATLAS Isolation Forum [115, 116].

Two variables with powerful discriminating power are used to separate these types of fake leptons from real leptons: **Calorimeter Isolation**, referred to as the E_T^{cone}, and **Track Isolation**, referred to as the $p_T^{\text{var-cone}}$ variable. The former sums all topological EM calorimeter clusters within a $\Delta R = 0.2$ cone around the lepton, whilst the latter sums all tracks with $p_T > 1$ GeV centered on the electron(muon) track using a variable cone defined

as $\Delta R = \min\{0.2(0.3), 10\ \text{GeV}/p_T^l\}$. The full definition of these variables can be found in Refs. [115, 116].

Two working points are used throughout the following analysis, these are the `LooseTrackOnly` and `FixedCutTight` definitions given by Refs. [115, 116].

11.2.2. Electrons

Electron candidates are reconstructed by matching tracks from the Inner Detector (*ID*) to energy clusters found in the Electromagnetic Calorimeter (*EMCAL*). The EMCAL clusters are reconstructed using the standard ATLAS sliding window algorithms, which cluster calorimeter cells using a fixed-size rectangular window in $\eta \times \phi$ space. Details about the formation of electron energy clusters from the constituent EMCAL cells can be found in Refs. [115, 117–119], whilst an overview of the cluster to track association is found in Ref. [120].

Following the formation of electron candidates, further criteria are applied to the electron candidates giving rise to a variety of different electron quality classifications. These criteria are grouped into 2 main categories, *Isolation* requirements, and *ID quality* requirements. These are described in the following sections.

Inner Detector Identification working points

QCD mediated processes producing multiple jets, called *QCD multijet* background, have a high production cross-section for hadron-hadron colliders. For signal topologies involving *electron+jet* final states, the combination of semi-leptonic decays to electrons and pion decays to photons can generate electromagnetic-like jets which are wrongly reconstructed as an electron. In order to reject this background, three categories of electron identification are defined by the $e^{\pm}/\gamma$ group within ATLAS [121]. These cut based categories use a range of variables sensitive to the shower shape, track quality, particle identification, and track-cluster matching in order to achieve this goal.

The three classifications impose increasingly tighter selections on the aforementioned properties, in order to increase the purity of electrons originating from the hard interaction. These are the `LooseLH`, `MediumLH`, and `TightLH` working points, which are applied to electrons within the central barrel region, $|\eta| < 2.47$. Full definition of these working points can be found in Ref. [121].

Electron Selection	p_T	η	ID	d_0^{sig} [mm]	$\lvert\Delta z_0^{\text{BL}} \sin\theta\rvert$	Isolation
`VHloose`	>7 GeV	$\lvert\eta\rvert < 2.47$	LH Loose	< 5	< 0.5 mm	LooseTrackOnly
`ZHsignal`	>27 GeV	Same as `VHloose`				
`WHsignal`	>27 GeV	$\lvert\eta\rvert < 2.47$	LH Tight	Same as `VHloose`		Tight

Table 11.2.: Electron Selection.

Electron Analysis Categories

The reconstructed electron candidates are then classified according to three analysis level selection criteria, which use the previously defined isolation and identification working points. In addition to this, each category has a unique set of kinematic cuts and track-to-vertex association cuts using the transverse and longitudinal impact parameters (d_0 & $|\Delta z_0 . \sin(\theta)|$).

These categories are referred to as `VHloose`, `ZHsignal`, and `WHsignal`, each applying stricter kinematic, isolation, track identification, and track-to-vertex requirements. These are summarised in Table 11.2.

11.2.3. Muons

Muon candidates can be reconstructed in a number of different ways, where each construction uses to varying degrees the different elements of the ATLAS detector described in Part III; these types of muons will be briefly outlined in section *Types of Reconstructed Muon*. In the following analysis particular emphasis is given to the Combined Muon (*CB*) definition, which is reconstructed using ID tracks (see Refs. [122–124]) and Muon Spectrometer (*MS*) tracks (see Refs. [47, 116, 125, 126]).

Types of Reconstructed Muon

Four complementary types of muons can be defined based on the sub-detectors used to reconstruct the muon candidate. Only two of these muon types are used throughout the following analysis to reconstruct the kinematic properties of the event. These are the **Combined Muon** (CB), which use the ID and MS tracks to form the muon candidate. This is done using either the *inside-out* or *outside-in* algorithm which extrapolates the MS tracks inwards for ID track matching (former case), or extrapolates the ID tracks outwards to the MS hits for the latter case. **Extrapolated** (ME) muons are reconstructed using

Muon Selection	p_T	η	ID	d_0^{sig} [mm]	$\lvert\Delta z_0^{\text{BL}} \sin\theta\rvert$	Isolation
`VHLoose`	>7 GeV	$\lvert\eta\rvert < 2.7$	Loose quality	< 3	< 0.5 mm	LooseTrackOnly
`ZHsignal`	>27 GeV	$\lvert\eta\rvert < 2.5$	Same as `VHLoose`			
`WHsignal`	>27 GeV	$\lvert\eta\rvert < 2.5$	Medium quality	Same as `VHloose`		Tight

Table 11.3.: Muon Selection.

only the MS tracks with some loose requirements on PV association. Full details on these types of muons can be found in Ref. [116].

At the analysis level the ME and CB muons are used exclusively to reconstruct the kinematics of the event, however the categorisation of data and MC events into the 0/1/2-lepton channels will also utilise the *Segment-Tagged* (ST) or *Calorimeter-Tagged* (CT) muon definitions. Specifically, the ST and CT muons are used in the categorisation stage of the analysis, but limited to the $|\eta| < 0.1$ range. Details can be found in Ref. [116].

ID and MS track quality cuts

Three classifications of MS track quality are defined: `Loose`, `Medium`, and `Tight` quality classifications. Each classification is a subset of the preceding looser quality definition, where tighter selections are imposed on the track properties, number of pixel/SCT hits, MDT hits, and χ^2 of the track extrapolation procedure. Full explanation of these classifications can be found in Ref. [116].

Muon Analysis Categories

The reconstructed muons are then assigned three possible analysis level classifications. Utilising the previously defined quality and isolation working points to impose ID/MS track quality cuts and isolate the fake leptons from the hard interaction leptons, additional kinematic cuts are also applied in order to reduce the fake-rate of the QCD mediated processes. These muon analysis level classifications are referred to as the `VHLoose`, `ZHsignal`, and `WHsignal` from here on in, where each category is a sub-set of the preceding due to tighter selection cuts imposed. The ID/MS track quality working points, isolation working points, and additional kinematic cuts used by each analysis category are summarised by Table 11.3.

11.2.4. τ Leptons

Hadronically decaying τ leptons (τ_{had}) are reconstructed from noise-suppressed topological clusters formed from the EM and hadronic calorimeter using the anti-k_T clustering algorithm with a distance parameter $\Delta R = 0.4$ [127]. These jets are passed to the $\tau_{\text{had-vis}}$ reconstruction algorithm outlined in reference [127], if the jets satisfy the $p_T > 10$ GeV and $|\eta| < 2.5$ criteria. The final τ candidates are required to have a $p_T > 20$ GeV, $|\eta| < 2.5$, and must not fall within the barrel/end-cap calorimeter transition region of $1.37 < |\eta| < 1.52$. Furthermore, the τ_{had} candidates must also have one or three associated tracks to the seeding jets previously defined, and must satisfy the BDT `Medium` identification criteria outlined here [127].

11.3. MET Definition

Invisible particles like neutrinos leave no detector signature, therefore these types of particles must be inferred from an imbalance in the transverse energy deposited within the ATLAS detector; from the perspective of the proton-proton center of mass (*CoM*) reference frame, the energy or momentum in the transverse (x–y) plane is negligible[1]. Therefore any missing transverse energy (E_T^{miss}) within the event is possibly the result of invisible particles not interacting with the detection medium.

The reconstruction of E_T^{miss} is characterised by two contributions, the *hard term* corresponds to fully reconstructed and calibrated particles like muons, electrons, jets, photons and tau leptons, whilst the *soft term* is composed of reconstructed charged-particle tracks not associated with a hard physics object [128]. E_T^{miss} is constructed by the negative vectorial sum of the *hard* and *soft* terms, following the form:

$$\mathbf{E}_T^{\text{miss}} = -\sum_{\substack{\text{selected}\\ e^{\pm}}} \mathbf{p}_T^{e^{\pm}} - \sum_{\substack{\text{selected}\\ \mu^{\pm}}} \mathbf{p}_T^{\mu^{\pm}} - \sum_{\substack{\text{selected}\\ \gamma}} \mathbf{p}_T^{\gamma} - \sum_{\substack{\text{selected}\\ \tau^{\pm}}} \mathbf{p}_T^{\tau^{\pm}} - \sum_{\substack{\text{selected}\\ \text{jets}}} \mathbf{p}_T^{\text{jets}} - \sum_{\substack{\text{unused}\\ \text{tracks}}} \mathbf{p}_T^{\text{track}}, \tag{11.3}$$

where $\mathbf{p}_T^i = (p_x, p_y)$ is the transverse momentum vector for one of the physics objects {e,μ,τ,jets,track,γ} [128]. Given that $\mathbf{E}_T^{\text{miss}}$ denotes the vector, the azimuthal angle ϕ^{miss}, and the magnitude of vector E_T^{miss} in the transverse plane can be trivially calculated.

[1] This is ignoring the motion of the colour confined partons intrinsic to the proton driven by the Fermi energy of proton fermion bound states, and the small transverse momentum induced by the crossing angle of the proton beams at the interaction point [34, 47].

11.4. Overlapping Objects

Many of the previously defined physics objects are composite objects constructed from energy deposits or multiple tracks, e.g. jets. To avoid the constituents of these composite objects from being counted multiple times when reconstructing the event, for example by using two or more objects that share a common constituent, an algorithm is defined that iteratively considers pairs of physics objects, i/j, and removes one of the objects in the situation that they are deemed to be overlapping in $\Delta R(i,j)$. The following notation will be used from here on in when referring to the algorithmic steps; $i,j = e,\mu,\tau,j,J,\gamma$ which corresponds to an electron, muon, tau, small-R jet, large-R jet or photon respectively. If i and j overlap then particle i is discarded. The precise overlap removal algorithm used with the following analysis is as follows:

1. $\boldsymbol{\tau/e}$ **:** $\Delta R(\tau,e) < 0.2$
2. $\boldsymbol{\tau/\mu}$ **:** $\Delta R(\tau,\mu) < 0.2$
3. $\boldsymbol{\mu/e}$ **:** Muon is calorimeter-tagged (CT μ) and shares an ID track with the electron
4. $\mathbf{e}/\boldsymbol{\mu}$ **:** Electron shares an ID track with the CB muon
5. $\mathbf{j/e}$ **:** $\Delta R(j,e) < 0.2$ if true then remove small-R jet
6. $\mathbf{J/e}$ **:** $\Delta R(J,e) < 1.2$ if true then remove large-R jet
7. $\mathbf{e/j}$ **:** $\Delta R(e,j) < \min\{0.4, 0.04 + 10 \text{ GeV}/p_T^e\}$ if true then remove electron.
8. $\mathbf{j}/\boldsymbol{\mu}$ **:** $p_T^\mu / \sum_i p_T^{\text{trk}_i} > 0.7$ and $p^\mu/p_T^j > 0.5$ for $p_T^{\text{trk}} > 500\ MeV$, or number of tracks with $p_T^{\text{trk}} > 500$ MeV is less than 3. The muon ID track (CB muon) is also ghost associated to the jet or $\Delta R(j,m) < 0.2$.
9. $\boldsymbol{\mu}/\mathbf{j}$ **:** $\Delta R(\mu,j) < \min\{0.4, 0.05 + 10 \text{ GeV}/p_T^\mu\}$, if true then remove muon.
10. $\mathbf{j}/\boldsymbol{\tau}$ **:** $\Delta R(j,\tau) < 0.2$, if true remove jet.

Steps 7 and 9 use a scaling ΔR cone, based on the relation $1/p_T$. This is done to combat the high rejection rate of electrons and muons when dealing with boosted event topologies, like those found in the following HVT/AZh analysis. It should also be noted that in all pairings the loosest definition of the object is used, i.e. the loosest definitions for the electron, muon, tau, small-R and large-R jet given by Sections 11.2.2, 11.2.3, 11.2.4, and 11.1.1 (small-R and large-R jets), respectively, are considered.

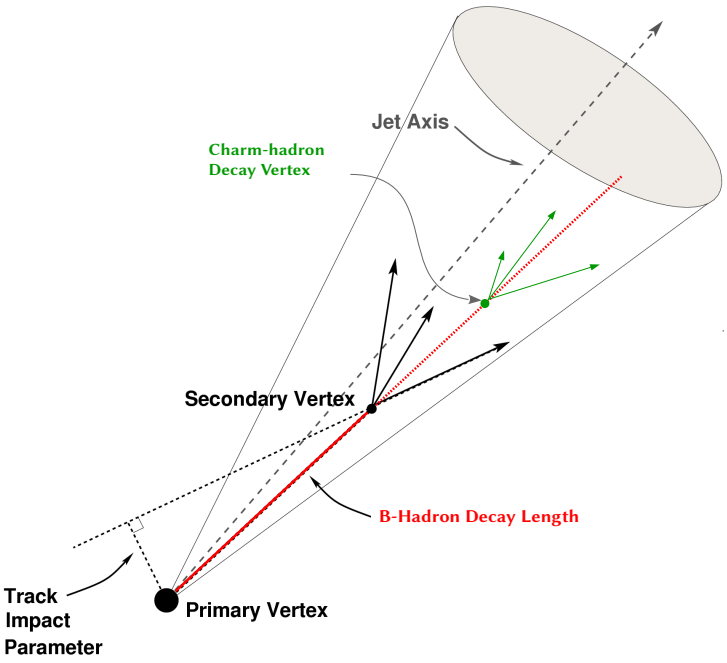

Figure 11.1.: Diagram of the various properties used to reconstruct the b-hadron decay process within a clustered jet.

11.5. b-Tagging

Due to the lifetime of b-hadrons (≈1.5 ps, $c\tau \approx 450$ μm), displaced secondary vertices (SV) from the primary vertex (PV) of the hard scattering process are common for jets that contain a b-hadron [129]. Furthermore, due to the weak decay process of b-quarks, b-hadrons predominantly decay into a charm-hadron, which subsequently decays, giving rise to a tertiary vertex within the same jet. This decay chain process is illustrated by Figure 11.1, which shows how these characteristics can be used as handles to tag a jet as a *b-jet*.

Within ATLAS this is achieved through the use of three algorithms; an impact parameter based algorithm called IP2/3D [130], an inclusive secondary vertex reconstruction algorithm called SV0/1 [129, 131], and a decay chain multi-vertex reconstruction algorithm called `JetFitter` [132].

The first algorithm uses the transverse impact parameter (d_0), which is defined as the distance of closest approach in the r–ϕ plane of the track to the PV, and the longitudinal impact parameter ($z_0 \times \sin(\theta)$), which corresponds to the longitudinal axis location of the closest approach of the track to the PV, to assign some probability that the jet is b-/c-/light-jet like. Figure 11.1 schematically illustrates the use of the track impact parameter within a reconstructed jet. The second algorithm attempts to reconstruct the SVs within the jet,

Jet Type	BDT Cut	b-jet Efficiency [%]	c-jet rejection	Light-jet Rejection	τ Rejection
small-R	0.8244	70	12	381	55
Track-jet	0.7475	70	9.59	253.72	30.99

Table 11.4.: Summary of the reconstruction rejection rates and tagging efficiencies for the 70% working point for the MV2c10 training [129].

whilst `JetFitter` attempts to reconstruct the b-hadron flight path using the secondary and tertiary vertices.

The output from the IP2D/IP3D, SV1, and JetFitter algorithms are combined using a boosted decision tree (BDT) from the ROOT Toolkit for Multivariate Data Analysis ($TMVA$) in order to discriminate b-, c-, and light-jets; this BDT is called *MV2*. In addition to this, the kinematic variables p_T and η of the jets are also fed to the BDT in order to capitalise on the correlation between them and the output variables from the individual b-tagging algorithms previously defined [129, 130].

The training of the MV2 BDT is performed using MC produced $t\bar{t}$ events, with the signal defined as events with a truth flavoured (ghost associated b-hadron within the jet), and the background as c-/light-jets. Various versions of the MV2 algorithm training exist, based on the relative contribution of the c-jets to the total ensemble of training events. These trainings use the notation MV2cXX, where $XX = 00, 10, 20$ representing either 0%, 10% or 20% contribution of c-jets to the total training ensemble.

Figure 11.2, shows the relative performance of the b-jet efficiency vs c-/light-jet rejections for the 2015 and 2016 configurations used throughout Run 2 of the LHC operation. Within the following analysis the recommendation from the b-Tagging working group was to use the MV2c10 training. The fixed-cut working points for the MV2c10 b-tagging algorithm used within the following analysis are summarised by Table 11.4, where the 70% fixed cut working point is used from here on in.

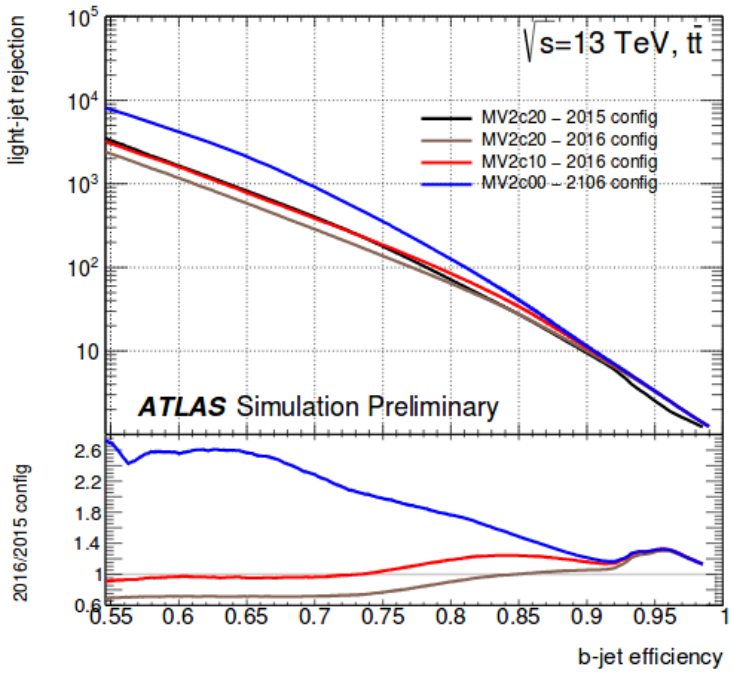

(a) Light-jet rejection vs b-jet efficiency

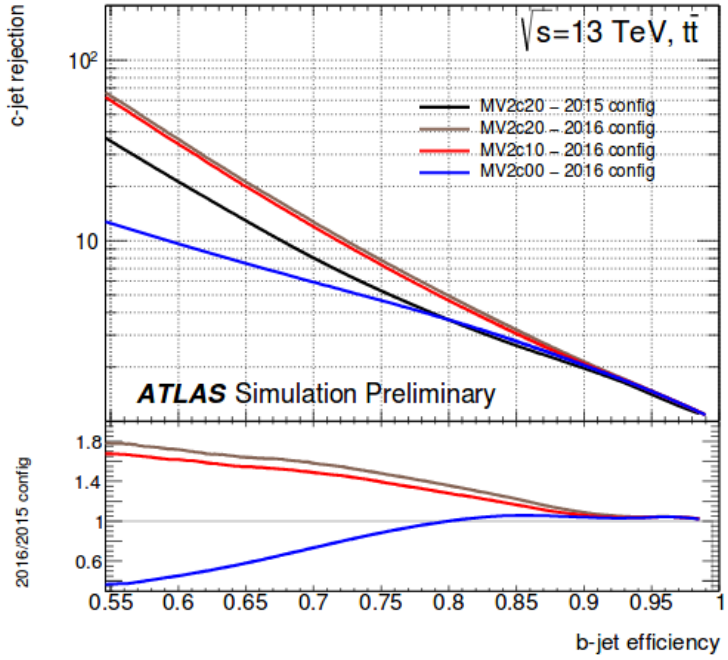

(b) c-jet rejection vs b-jet efficiency

Figure 11.2.: Light flavour (a) and c-jet (b) rejection vs b-jet efficiency for 2016 MV2c00, MV2c10, and MV2v20 configuration compared to the previous MV2c20 2015 configuration [129].

Chapter 12.

Event Reconstruction Scheme

Recalling the form of the fit discriminant used by the Binned Profile Likelihood fit (see Section 8.2):

$$m_{Vh}^2 = (p_{W/Z}^{\mu} + p_h^{\mu})^2 = \Bigg[\underbrace{(\sum_{l}^{\text{leptons},\nu} p_l^{\mu})}_{\text{Leptonic}} + \underbrace{(\sum_{b}^{b-\text{quarks}} p_b^{\mu})}_{\text{Hadronic}} \Bigg]^2, \tag{12.1}$$

the event can be decomposed into two components, a leptonic component and a hadronic component. The former represents the reconstructed SM vector boson that decays to leptons or neutrinos, whilst the hadronic component represents the reconstructed Higgs candidate. The following sections will outline how each term is constructed, and so how the m_{Vh} is formed.

12.1. Leptonic Side Event Reconstruction: V-boson Reconstruction

For the 2-lepton channel the vectorial sum of the four-momentum of the two reconstructed leptons (p^{l_1} & p^{l_2}) is used to construct the four-vector of the dilepton system, and thus the four-vector of the underlying Z-boson.

For the 0-lepton channel the leptonic side of the event is reconstructed using only the E_T^{miss} definition given in Section 11.3. Since the missing transverse energy contains no information about the longitudinal momentum of the neutrinos, only the transverse components of the underlying vector boson can be reconstructed. As such the fit discriminant used by the Binned Profile Likelihood fit in the 0-lepton channel is changed to the transverse invariant mass of the V+h system, $(m_{Vh}^T)^2 = \Big[(\sum_i^{\nu} \boldsymbol{p}_i^T) + (\sum_b^{b-\text{quarks}} \boldsymbol{p}_b^T) \Big]^2$, where $\boldsymbol{p}_j^T$ represents the four-vector in the transverse plane of the detector.

For the 1-lepton channel the single lepton 4-momentum (p^l) is used in conjunction with the E_T^{miss} of the event to reconstruct the $W \to lv$ signature. To reconstruct the 4-momentum of the W-boson candidate in the 1-lepton channel, the z-component of the neutrino must be reconstructed. This is achieved by using the m_W mass constraint to analytically solve the quadratic equation:

$$p_z^\nu = \frac{1}{2(p_T^l)^2}\left[p_z^l X + E_l\sqrt{X^2 - 4(p_T^l)^2)(E_T^{\text{miss}})^2}\right], \tag{12.2}$$

where $X = m_W^2 + 2p_x^l E_x^{\text{miss}} + 2p_y^l E_y^{\text{miss}}$.

12.2. Hadronic Side Event Reconstruction: Higgs Reconstruction

Given the wide range of possible resonance masses predicted by the 2HDM and HVT models, it is expected that for the decay modes $A \to Zh$ and $V' \to Vh$, the decay products will have a wide p_T range. Furthermore, in the decay of the Higgs to two b-quarks, the angular separation between these quarks is highly dependent on the transverse momentum of the Higgs. This separation can be quantified by the ΔR between the two b-quarks (i/j), where under the hypothesis that the two particles originated from a common parent k, $\Delta R(i,j) \approx 2m_k/p_T^k$.

For example, a reconstructed Higgs candidate with $p_T^h > 625$ GeV gives a $\Delta R(b,\bar{b}) \sim 0.4$, meaning that for the typical anti-k_T $\Delta R = 0.4$ radius jet definition used by ATLAS, the hadronised products originating from the b-quarks end up being clustered within the same jet for high momentum Higgs candidates. Consequently, the signal reconstruction efficiency when using a fixed ΔRanti-k_T clustering algorithm to reconstruct the Higgs component of the event, degrades monotonically as a function of the HVT/AZh mediator mass. This was observed from preliminary tests, where for a mediator mass of $m_{V'} = 700$ GeV, 95% of the signal in the 1-lepton channel could be reconstructed when using two anti-k_T $\Delta R = 0.4$ jets to reconstruct the $h \to b\bar{b}$ decay products, however this drops to approximately 11% when $m_{V'} = 3000$ GeV.

Therefore, two reconstruction schemes are used within this analysis. The *Resolved* scheme uses two anti-k_T $R = 0.4$ jets (small-R jets) to reconstruct the Higgs candidate, one for each b-quark initiated jet. These jets are tagged using the MV2c10 70% working point outlined in Section 11.5. The Higgs candidate mass, m_h, is calculated using the squared vectorial sum of the two small-R jets ($p^\mu_{\text{jet }1/2}$), i.e. $m_h = \sqrt{(p^\mu_{\text{jet }1} + p^\mu_{\text{jet }2})^2}$. The resolved signal region (SR) is defined by the window cut 110(100) GeV $< m_h <$ 140(145) GeV

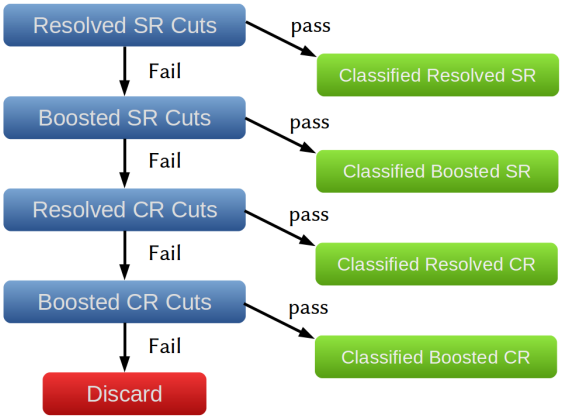

Figure 12.1.: PriorityResolvedSR logic for assigning event categories.

around the Higgs pole mass, whilst the side-bands either side of the Higgs pole mass, 50 GeV $< m_h <$ 110(100) GeV and 140(145) GeV $< m_h <$ 200 GeV, form the control regions for the 0-/1-lepton (2-lepton) channels.

The *Boosted* scheme uses a single anti-k_T $R = 1.0$ jet (large-R jet) to reconstruct a Higgs candidate, where this large-R jet has ghost associated anti-k_T $R = 0.2$ track-jets (see Section 11.1.1). These track-jets, having a smaller ΔR width, are used to reconstruct the sub-structure of the large-R jet. The track-jets are b-tagged using the MV2c10 70% working point outlined in section 11.5. The Higgs candidate mass is then calculated using the trimmed large-R jet mass, $m_h = m_J$, where the Boosted SR is defined as 75 GeV $< m_h <$ 145 GeV. The control regions are defined as 50 GeV $< m_h <$ 75 GeV and 145 GeV $< m_h <$ 200 GeV.

These two reconstruction schemes are then combined using a *combination scheme* called the *Priority Resolved Signal Region* (PRSR), which is designed to maximise the sensitivity of the analysis to as many mediator masses as possible. Under this combination scheme, the event is reconstructed using both the Resolved and Boosted reconstruction schemes, and then tested against all Resolved and Boosted event selection criteria outlined in Chapters 13-15. The event is assigned either success or fail for each test, and is then categorised according to the logic hierarchy shown in Figure 12.1. Based on the logic hierarchy, it should be obvious that the PRSR combination scheme gives priority to the resolved signal regions (SR) over the Boosted signal regions, whilst the SRs are given priority over the control regions (CR).

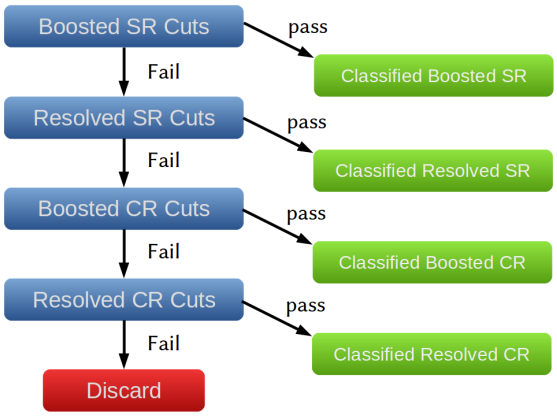

Figure 12.2.: PriorityMergedSR logic for assigning event categories.

12.2.1. Combination Scheme Optimisation

The PRSR combination scheme outlined above (Section 12.2) was designed to maximise the sensitivity of the analysis to lighter mediator masses. This emphasis on lighter mediators was a direct consequence of the smaller mediator mass range of the 2HDM part of the analysis, the pseudoscalar A-boson masses ranges from 220 GeV to 2000 GeV, whilst the HVT analysis was more concerned with mediator masses in the 500 GeV to 5000 GeV range.

However, in arriving at this reconstruction scheme a wide array of alternative schemes were tested. The alternative reconstruction schemes tested were as follows:

- **Resolved :** Requires two or more signal small-R jets, $n_{\text{jet}}^{\text{sig}} \geq 2$, with the lead jet $p_T > 45$ GeV and sub-leading jets with $p_T > 20$ GeV. The event must pass the rest of the event selection outlined by Table 12.1, which is a loosened set of cuts in comparison to the base analysis cuts given in Section 15.

- **Boosted :** Requires at least 1 large-R jet with $p_T > 250$ GeV. Each event is then required to pass the event selection outlined in Table 12.1. This set of criteria corresponds to a looser event selection than those given in Section 15.

- **SimpleMerge500 (SM500) :** Accept event if it satisfies all Resolved criteria for $p_T^V < 500$ GeV, or Boosted selection criteria for $p_T^V \geq 500$ GeV, as given in Table 12.1.

- **PriorityMergedSR :** The event is tested against both the Resolved and Boosted selection criteria outlined in Table 12.1, and assigned either success or fail. The event is then categorised according to the logic shown in Figure 12.2. This recycling scheme therefore gives preference to the Boosted SR over the equivalent resolved regime, where the SRs in both cases takes priority over the corresponding CRs.

In order to test the sensitivity of the analysis to the presence of signal s (AZh /HVT), relative to the abundance of the SM background b, for the aforementioned reconstruction/combination schemes, the radicand of the *Log-Likelihood Ratio* (LLR) [133] is used. The exact functional form used throughout this analysis is given below:

$$\Delta\text{LLR} = \sqrt{\sum_{i}^{\text{regions}} \sum_{j}^{\text{bins}} 2(s_j + b_j)\ln(1 + \frac{s_j}{b_j}) - 2s}, \tag{12.3}$$

where $\sum_i^{\text{regions}}$ represents the sum over analysis regions to be considered in the LLR measure, and $\sum_j^{\text{bin}}$ represents the sum over the bins of the final discriminant (m_{Vh}/m_{Vh}^T) spectrum. During these tests the fiducial phase space used for resolved and boosted regimes is given by Table 12.1, and all signal cross-sections are normalised to 1 pb [1].

Selection	1-lepton Resolved	1-lepton Boosted
Trigger	electron trigger and E_T^{miss} trigger	
1 lepton	exactly 1 `WHloose` electron/muon which should also pass the `WHsignal` criteria	
E_T^{miss}	$E_T^{\text{miss}} > 0$ GeV in electron events $E_T^{\text{miss}} > 30$ GeV in muon events	E_T^{miss} >100 GeV
p_T^W	$p_T(W) > 150$ GeV	
m_h	50 GeV $< m_h <$ 200 GeV	None
Jets	2 or 3 signal jets $\geq$ 0 forward jets	$\geq$ 1 fat jet $\geq$ 1 track-jet associated to leading fat jet
Leading jet p_T	$>$ 45 GeV	large-R jet $p_T >$ 250GeV
Sub-leading jet p_T	$>$ 20 GeV	-
	Veto on events with 3 or more b-jets	-

Table 12.1.: Summary of the event selection in the 1-lepton Resolved and Boosted regime for the Combination Scheme optimisation tests.

Figure 12.3 shows the LLR sensitivity measure for the various combination schemes as a function of the HVT signal mediator mass. It is apparent from this figure that the Resolved scheme loses sensitivity to the HVT signal as the mediator mass increases. This is due to the increasing rate at which the two b-quarks from the Higgs decay become clustered within the same jet, thus violating the requirement of two small-R jets. This happens rapidly at a mediator mass of $\sim$ 1.2 TeV, which corresponds to a Higgs $|\mathbf{p}^h| \approx 600$ GeV and $\Delta R(i,j) \approx 0.4$ between the b-quarks.

[1] The cross-section is irrelevant when attempting to maximise the sensitivity, because it is the relative gain or loss of each combination scheme that matters, not the absolute sensitivity measure of each scheme.

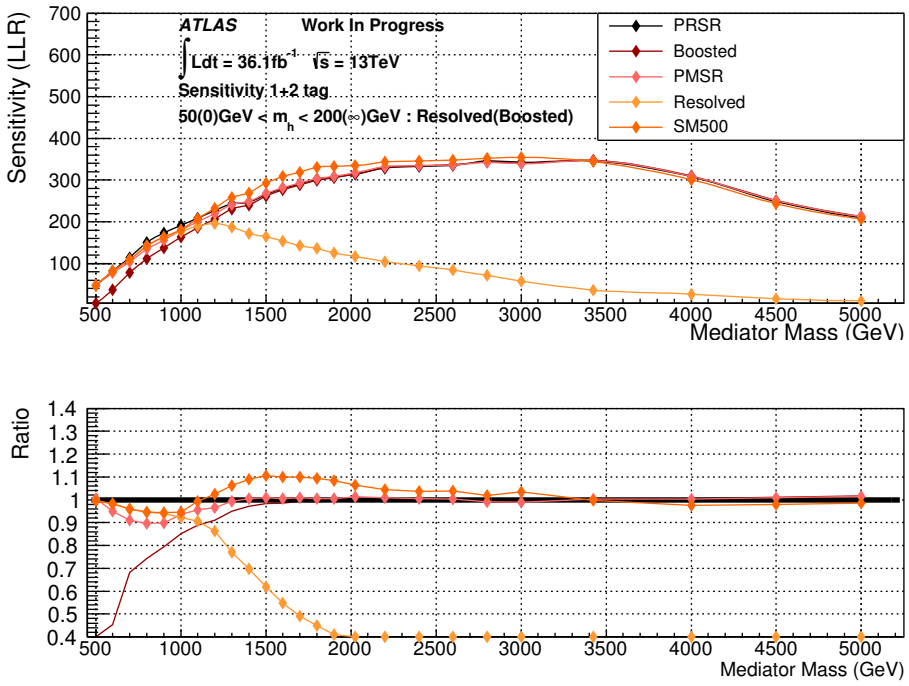

Figure 12.3.: Comparison of the PRSR, PMSR, SM500, combination schemes to the Resolved and Boosted only reconstruction schemes in the 1-lepton channel using the HVT signal models. Comparison is made using the LLR sensitivity measure as given by equation 12.3.

Furthermore, it is immediately obvious from Figure 12.3 that the PRSR and PMSR schemes converge for $m_{V'} > 1.5$ TeV, whilst for the lighter mediator masses, $m_{V'} < 1.5$ TeV, the PRSR scheme is at best 10% more sensitive to the HVT signal. This behaviour is expected because for low mediator masses the b-quarks originating from the Higgs decay are typically back-to-back with an angular separation of $\Delta R > 1.0$, i.e. they are not reconstructed within the same large-R jet. Consequently, in the PMSR scheme, a large percentage of the signal in the low mediator mass regime is assigned to the boosted 1-tag 1+ add. tag m_h SR category; the large-R jet captures one of the b-jets, whilst an unassociated track-jet captures the remaining b-jet (hence the 1+ add. tag assignment). By dividing the signal over multiple fit regions the sensitivity to a signal excess is suppressed.

Furthermore, Figure 12.3 also demonstrates that the PRSR scheme is at best 5% more sensitive to the HVT signal for low mediator masses, $m_{V'} < 1.1$ TeV, when compared to the SM500 scheme. However, the SM500 scheme is at its peak 10% more sensitive for mediator masses in the 1.1 TeV $< m_{V'} <$ 3.5 TeV range. This behaviour stems from the fact that the SM500 scheme splits the resolved and boosted regime into 2 histograms separated by a $p_T^V = 500$ GeV cut. When looking at the distribution of the SM background in p_T^V, the

majority of the SM background resides in the $p_T^V < 500$ GeV regime, for both the Resolved and Boosted reconstruction schemes. Table 12.2 summarises the SM background and HVT signal event yield distribution amongst the low $p_T^V < 500$ GeV and high $p_T^V > 500$ GeV regimes.

Consequently, under the SM500 scheme heavy mediator masses are primarily reconstructed and assigned to the boosted category, but the bulk of the SM background is reconstructed using the Resolved scheme and thus is assigned to a separate binned histogram. This separation of the SM background and HVT signal in the boosted regime drives this performance gain over the PRSR scheme for mediators masses in the 1.1 TeV $< m_{V'} <$ 3.5 TeV range.

Process	**0 GeV $< p_T^V <$ 500 GeV**		**500 GeV $< p_T^V$**	
	Resolved	**Boosted**	**Resolved**	**Boosted**
$t\bar{t}$	99.7%	96.75%	0.3%	3.25%
Single Top ($Wt + t + s$)	99.7%	86.9%	0.3%	13.1%
Wbb	99.4%	93.7%	0.6%	6.3%
Wbl	99.3%	93%	0.7%	7%
HVT WH $m_{V'} = 700$ GeV	99.9%	99.89%	0.1%	0.11%
HVT WH $m_{V'} = 1$ TeV	91.3%	88%	8.7%	12%
HVT WH $m_{V'} = 2$ TeV	25.8%	6.7%	74.2%	93.3%
HVT WH $m_{V'} = 3$ TeV	28.6%	2.6%	71.4%	97.4%

Table 12.2.: Summary of event yield distribution above and below a cut of $p_T^V = 500$ GeV for key SM background and HVT mediator mass points in the resolved 1+2 b-tag combined resolved regime inclusive of m_h, and for the 1+2 b-tag Boosted regime inclusive of m_h for the 0 additional unassociated track-jets outside the large-R category.

However, this effect can be mimicked in the PRSR scheme by splitting events reconstructed according to the Resolved or Boosted schemes, into two separate histograms. Events within the low p_T^V regime, $p_T^V < 500$ GeV, and those in the high p_T^V regime, $p_T^V \geq 500$ GeV, are each assigned to a separate histogram, thereby increasing the number of binned histograms provided to the Binned Profile Likelihood fit ($\sum_i^{\text{regions}}$) by a factor of 2, this is referred to as *PRSR-SplitPtv*. The effect of this splitting is shown by Figure 12.4, which shows the nominal SM500 and PRSR schemes, and the PRSR-SplitPtv scheme. The result of this test indicates that by implementing a $p_T^V = 500$ GeV cut, the difference between the SM500 and PRSR schemes for large mediators can be recovered when using the PRSR scheme.

In summary, for the 1-lepton channel the SM500 and PRSR schemes each offered superior sensitivity to the HVT signal when compared to all other reconstruction schemes. The SM500 favoured the higher mediator masses, whilst the PRSR scheme favoured the lower

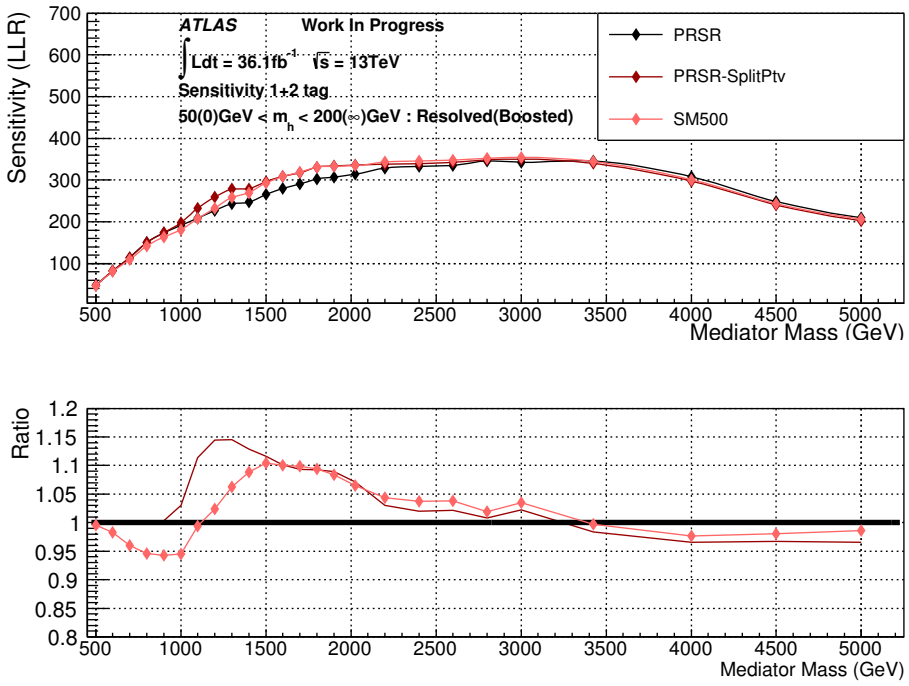

Figure 12.4.: Comparison of the PRSR, SM500, and PRSR-SplitPtv combination schemes in the 1-lepton channel using the HVT signal models. Comparison is made using the LLR sensitivity measure as given by equation 12.3.

mediator mass regimes. However, the PRSR scheme could be adapted to match the SM500 scheme in the high mediator mass regime by implementing the same $p_T^V = 500$ GeV cut as that used in the SM500 scheme. Bearing this in mind, and recalling that the HVT analysis is searching for both a W' and Z' heavy resonance, and the AZh analysis typically predicts smaller mediator masses, the performance of the 0-/2-lepton channels to the alternative reconstruction schemes must also be considered. It was found that for the 0-/2-lepton channel the PRSR scheme offered the best sensitivity improvement when considering all options, therefore it was adopted as the analysis reconstruction scheme.

Chapter 13.

Triggers & Common Event Selection

The following chapter details the data collection triggers used in the analysis to record the proton-proton collisions provided by the LHC, this is given by Section 13.1. Furthermore the chapter also details the event selection common to all lepton channels, which is used to define the fiducial phase space for the resolved and boosted regimes of the analysis, see Section 13.5. It should be noted that the following sections may make reference to previously defined terms relating to either object definitions (Chapter 11) or reconstruction schemes (Chapter 12).

13.1. Missing Transverse Energy Triggers (MET)

For the 2015 data collection period the online triggering threshold was 70 GeV for all 2015 runs, however in the 2016 data collection periods, the trigger thresholds were increased. This was due to an increase in the triggering rate of the MET triggers, caused by an increase in the average number of interactions per bunch crossing during the 2016 data collection period. This effect is demonstrated best by Figure 13.1 [1]. Consequently, during the 2016 data collection period the threshold was raised to 90 GeV and then 110 GeV. See Table 13.1 for details relating to the MET triggers used by the 0-/1-lepton channel.

Trigger Name	Period	Threshold (GeV)	Description
HLT_xe70_mht_L1XE50	2015	70 GeV	Seeded using the level L1_XE50 LAr and Tile calorimeter triggers, calibrated at the EM scale, with a threshold of 50 GeV.
HLT_xe90_mht_L1XE50	2016	90 GeV	
HLT_xe110_mht_L1XE50	2016	110 GeV	

Table 13.1.: MET triggers used during the 2015 & 2016 data period taking.

[1] Courtesy of *Missing Transverse Energy Trigger Signature Group.*

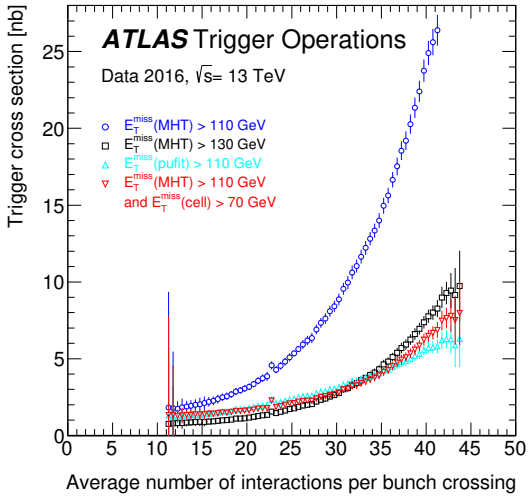

Figure 13.1.: Trigger cross-section as a function of the average number of interactions per bunch crossing for the 2016 data period taking, demonstrating the monotonically increasing relation between the rate and $\langle\mu\rangle$ [134].

13.2. Single Electron Triggers

For the 2015 data runs the lowest unprescaled single electron triggers are used, with a lower p_T threshold of 24 GeV. For the 2016 data periods, the higher instantaneous luminosity saw the lowest p_T threshold rise to 26 GeV, and isolation requirements on the calorimeter cell clusters were imposed. Additional triggers with p_T thresholds above 60 GeV dropped these isolation requirements, and have increasingly looser track ID criteria requirements, in order to recover efficiency for high p_T electrons. Table 13.2 summarises the single electron triggers used by the 1-/2-lepton channels of the following analysis.

13.3. Single Muon Triggers

For the 2015 data periods the lowest unprescaled muon trigger with a p_T threshold of 20 GeV was used, whilst for the 2016 data period the lowest muon trigger threshold was raised to 24 GeV, due to the increase in instantaneous luminosity. Furthermore, for the lowest p_T threshold triggers of 2016, loose isolation requirements were placed on additional radiation around the reconstructed muon of fixed cone $\Delta R = 0.2$, requiring that the ratio of the scalar sum of track p_T within the cone to the muon p_T be less than 0.12. For higher threshold triggers and for the latter months of 2016, the isolation requirements are increased to the

Trigger Name	Period	Threshold (GeV)	Description
HLT_e24_lhmedium_L1EM20VH	2015	24 GeV	Seeded using L1EM20VH level 1 trigger calibrated at the EM scale with a threshold of 20 GeV, and require medium ID quality.
HLT_e60_lhmedium_L1EM20VH	2015	60 GeV	Seeded using L1EM20VH level 1 trigger calibrated at the EM scale with a threshold of 20 GeV, and require medium ID quality.
HLT_e120_lhmedium_L1EM20VH	2015	120 GeV	Seeded using L1EM20VH level 1 trigger calibrated at the EM scale with a threshold of 20 GeV, and require loose ID quality.
‘ HLT_e26_lhtight_nod0_ivarloose	2016	26 GeV	Tight likelihood ID required, and variable loose isolation required
HLT_e60_lhmedium_nod0	2016	60 GeV	Medium ID likelihood required
HLT_e124_lhloose_nod0	2016	140 GeV	Loose ID likelihood required

Table 13.2.: Single electron triggers used during the 2015 & 2016 data period taking.

medium variable cone criteria, where for a cone of size $\Delta R = \min\{0.3, 10 \text{ GeV}/p_T \text{ [GeV]}\}$, the ratio of the scalar summed track p_T to the muon p_T must be less than 0.16. Table 13.3 summarises the single muon triggers used by the 2-lepton channel.

Trigger Name	Period	Threshold (GeV)	Description
HLT_mu20_iloose_L1MU15	2015	20 GeV	Seeded using L1MU15 level 1 trigger with a threshold of 15 GeV, and requiring loose isolation requirements.
HLT_mu40	2015 & 2016	40 GeV	No isolation requirements.
HLT_mu50	2015 & 2016	50 GeV	No isolation requirements.
HLT_mu24_iloose	2016	24 GeV	Variable and Fixed cone Loose isolation requirements
HLT_mu24_ivarmedium	2016	24 GeV	Variable cone medium isolation requirements
HLT_mu26_ivarmedium	2016	26 GeV	Variable cone medium isolation requirements

Table 13.3.: Single muon triggers used during the 2015 & 2016 data period taking.

13.4. Trigger Matching

For all lepton triggers the offline reconstructed lepton and online reconstructed Level 1/HLT object that fired the trigger are checked and matched. Specifically, a $\Delta R(i, j)$ matching is performed between the offline reconstructed electron/muon (i), and the online electron/muon (j) that fired the relevant Level 1 $\rightarrow$ HLT trigger chain. If the offline

reconstructed lepton in the 1-/2-lepton analyses does not match the online trigger firing object then the event is vetoed.

13.5. Common 0-/1-/2-Lepton Event Selection

13.5.1. Resolved Regime

For the resolved regime it is required that each event must have *at least* 2 small-R signal+forward jets (N_{jet}), and two or more signal jets ($N_{\text{jet}}^{\text{sig}} \geq 2$). The leading jet $p_T > 45$ GeV, and the sub-leading jets must exceed $p_T > 20$ GeV. There is no requirement on the number of forward jets.

The events are categorised as either 0/1/2/3+ b-tagged for the AZh analysis, or 0/1/2 b-tagged for the HVT analysis, by using the MV2c10 70% working point outlined in section 11.5, to b-tag the small-R jets within the event. The *All Signal Jets* tagging+selection strategy is used to select the three leading jets, and allocate the event to a b-tag category. The definition of this strategy is as follows:

1. **0 b-tagged jets in event ($N_b^{\text{Evt}} = 0$):** Allocated as 0-tag, with the highest jet $p_T > 45$ GeV and all sub-leading jets $p_T > 20$ GeV.
2. **1 b-tagged jet in event ($N_b^{\text{Evt}} = 1$):** Regardless of b-tagging, the highest p_T jet within event must have $p_T^{\text{lead}} > 45$ GeV, this is labelled as the *lead signal jet*. The *second-leading signal jet* is allocated as either the second highest p_T jet within the event if the lead signal jet is b-tagged, or as the highest p_T b-tagged jet if the lead signal jet is not b-tagged. This second-leading jet must have $p_T^{2nd} > 20$ GeV, and all remaining jets $p_T > 20$ GeV.
3. **2 b-tagged jets in event ($N_b^{\text{Evt}} = 2$):** Two signal jets within the event must be b-tagged, where the highest p_T jet of the pair, must have $p_T > 45$ GeV and the second jet must have $p_T > 20$ GeV. These jets do not need to be the highest and second highest jet within the event. All remaining jets must have $p_T > 20$ GeV.
4. **3+ b-tagged jets in event ($N_b^{\text{Evt}} \geq 3$):** Same as *2 b-tagged jets* category, except the 3rd jet is either a signal or forward jet with $p_T > 20$ GeV and b-tagged.

An alternative tagging strategy was considered, referred to as the *Leading Signal Jet* strategy, this scheme requires the same criteria as the *All Signal Jets* strategy, except for the 1-/2-/3+ tag categories. In the 1-/2-/3+ tag category the lead signal jet must be b-tagged, have $p_T > 45$ GeV, and be the highest p_T jet within the event. If this is not the case, then

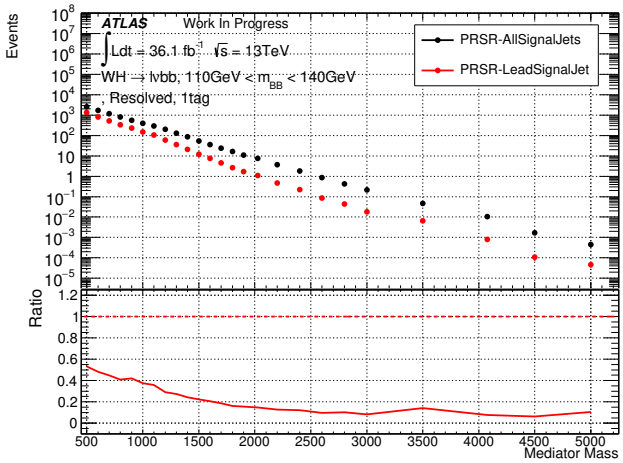

(a) 1-tag Resolved SR signal acceptance.

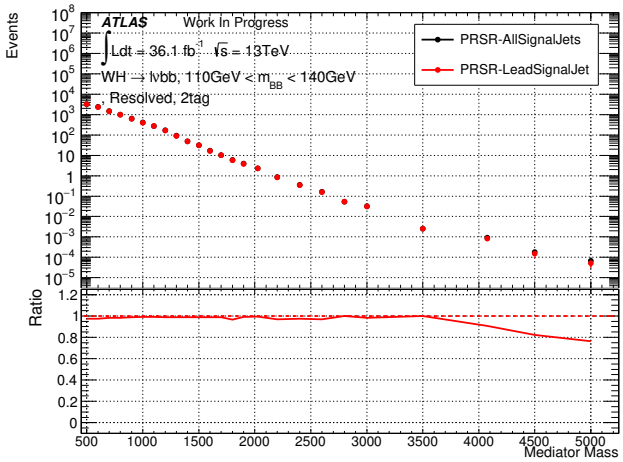

(b) 2-tag Resolved SR signal acceptance.

Figure 13.2.: Signal event yield for LeadingSignalJet and AllSignalJet tagging schemes as a function of the HVT signal mass (see Section 10.2.1) within the 1-tag (a) and 2-tag (b) SR. Signal acceptance is defined as the event yield within a 95% window centered on the mode of the $m_{V'}$ mass distribution.

the event is vetoed. Figure 13.2 shows the 1-lepton HVT signal event yield for the 1-tag resolved SR and 2-tag resolved SR categories, when defining a 95% window centered on the peak of the $m_{V'}$ HVT signal distribution. Figure 13.3 shows the variation of the predicted sensitivity of the analysis to the HVT signal by using the sensitivity measure given by equation 12.3 for the 1+2-tag m_h SR window.

In conclusion, the aforementioned figures show that the sensitivity of the analysis benefits from use of the *All Signal Jets* strategy in the 700 GeV $< m_{V'} <$ 2200 GeV mass range, albeit a small 5% sensitivity gain at best. Rather, the largest benefit of the *All Signal*

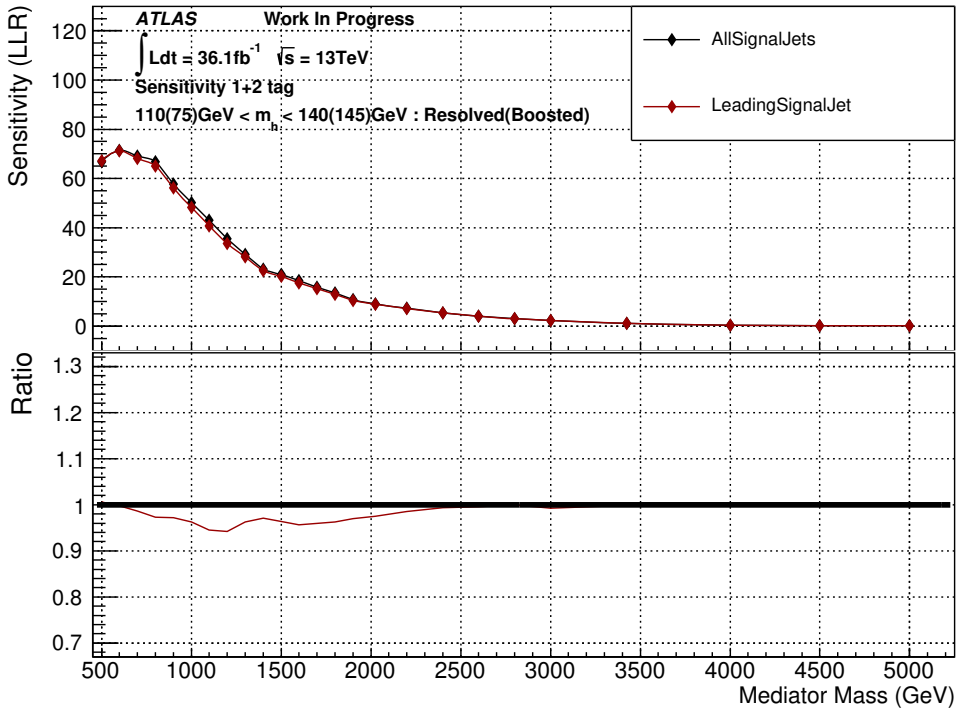

Figure 13.3.: LLR sensitivity comparison of the All Signal Jets and Leading Signal Jets b-tagging strategies. Sensitivity measure corresponds to LLR, and is constrained to the m_h signal regions of the analysis.

Jets tagging strategy is the larger signal and background acceptance rate when compared to the *Leading Signal Jet* scheme. By having a larger signal and background acceptance the associated statistical error on each sample is smaller. This aids in deriving MC theory uncertainties, and helps suppress the statistical error from limiting the analysis exclusion or discovery significance.

The invariant mass of the two leading small-R jets (m_h) is constrained to the 50–200 GeV regime. Adopted from the 2-lepton analysis, due to an observed disagreement between the data and MC simulations in the extreme edges of the mass distributions, $m_h < 50$ GeV and $m_h > 200$ GeV, the motivation for propagating these tighter side band cuts to the 0-/1-lepton channels is as follows:

- The low ($m_h < 110$ GeV) and high ($m_h > 140$ GeV) m_h sidebands are used within the 1-lepton channel as CRs for the $W+bb$, $W+bl$, $W+bc$, and $t\bar{t}$ processes. Extrapolating constraints on these backgrounds to the signal regions is only valid if the regions are kinematically similar.

- The sidebands around the signal regions are used as validation regions for the 0-/2-lepton channels. Having validation regions too distant from the SR throws into question the validity of extrapolating the SR fit results to the distant side band regions.
- The end goal is to set limits on the W' and Z' HVT mediators. As such the combined 0+1-lepton and 1+2-lepton fits are used to derive these limits. Therefore to prevent a mismatch in the CR definitions, the same definitions were used.

13.5.2. Boosted Regime

The boosted regime is defined as an event that has at least 1 large-R jet with $p_T^J > 250$ GeV, and must be within the fiducial detector volume of $|\eta| < 2.0$. Furthermore, the large-R jet must have at least one ghost associated track-jet in order to be considered a viable boosted event.

The reason for requiring at least 1 or more ghost associated track-jets to the large-R jet is best shown by Figure 13.4, which shows the signal and background acceptances for the boosted only analysis divided into the 1- and 2+ ghost associated track-jet categories for 1-tag events. The signal acceptance is defined as the event yield within an asymmetric window around the peak of the signal m_{Vh} distribution, which contains 95% of the signal events, whilst the background acceptance is the corresponding event yield of the summed SM background processes within the same window.

It can be seen from Figure 13.4 that for light mediator masses (0.5 TeV $< m_{V'} <$ 2.0 TeV) the signal is primarily composed of 2+ ghost associated track-jets, meaning that the acceptance gained by loosening the cut to one or more track-jets is at best an $\approx 5\%$ increase in the event yield. The corresponding increase in the background yield is $\approx$ 2–5%. However, for masses larger than 2.0 TeV, the 1+ track-jet inclusive category is approximately equal parts 1 track-jet only and 2+ track-jet events. By adding the 1 track-jet and 2+ track-jet categories, the signal yield doubles in the high mediator mass range.

The impact of this signal acceptance gain can be quantified by the sensitivity of the analysis to the presence of the signal using the LLR definition given by equation 12.3. Figure 13.5 shows the LLR sensitivity measure as a function of the mediator mass for the 2+ track-jet (Boosted Only 2+ Trk) and 1+ track-jet (Boosted Only 1+ Trk) categories, when using the Boosted only reconstruction scheme. From this figure it can be seen that for $m_{V'} > 2.5$ TeV the 2+ track-jet boosted scheme becomes increasingly less sensitive to the HVT signal, due to the merging of the b-quarks from the Higgs decay into a single track-jet.

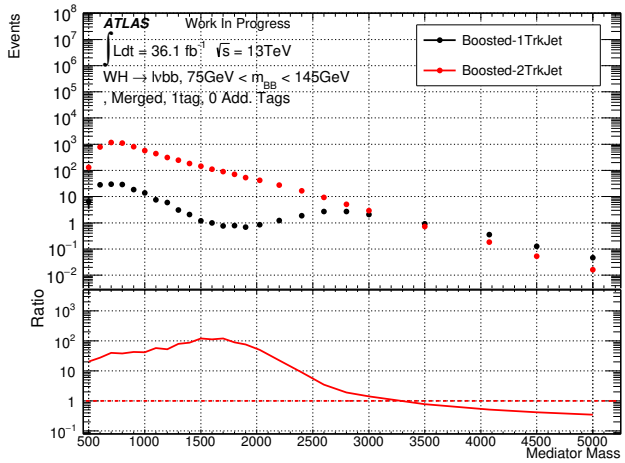

(a) 1-tag Boosted SR signal event yield.

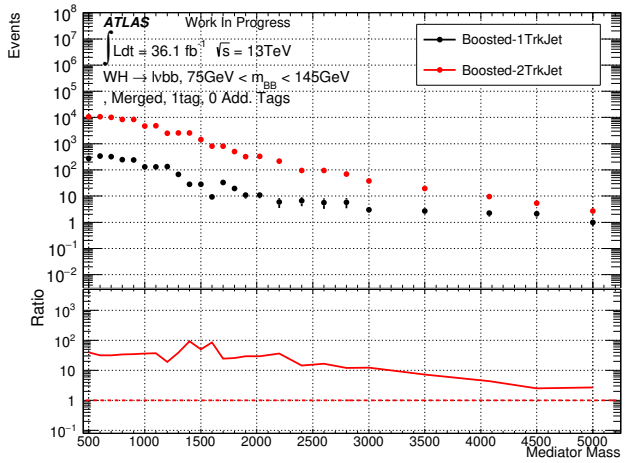

(b) 1-tag Boosted SR background event yield.

Figure 13.4.: Signal (a) and SM background (b) event yield for each of the 24 HVT signal mass points for the 1- and ≤ 2 ghost associated track-jet scenarios. Signal/Background event yield is defined as the event yield within an asymmetric 95% window centered on the $m_{V'}$ mass distribution of the MC predicted signal.

The invariant mass of the reconstructed Higgs candidate is also restricted to the range 50 GeV $< m_h <$ 200 GeV. The upper, 145 GeV $< m_h <$ 200 GeV, side band restrictions are applied following the same logic as previously explained for the resolved regime.

The lower $m_h <$ 50 GeV region is excluded because it was noticed that the large-R jets of mass $m_J <$ 50 GeV predominantly contain a single ghost-associated track-jet, whilst large-R jets within the signal region are at best a 50/50 split of single and double ghost associated track-jets (see Figure 13.4). Therefore the region is excluded from the analysis,

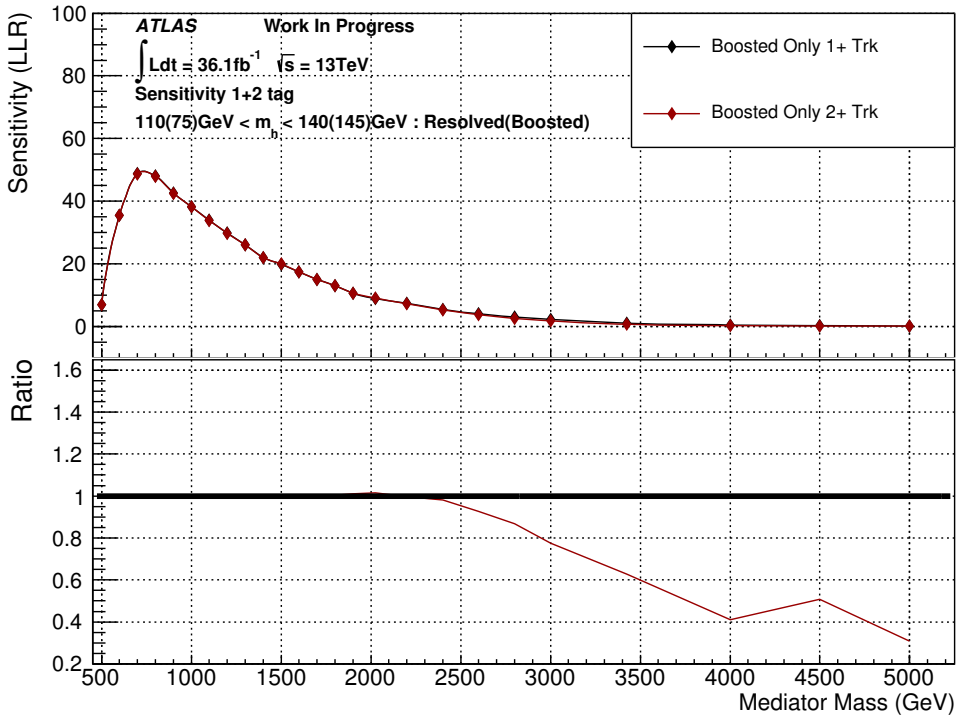

Figure 13.5.: LLR sensitivity comparison of the boosted only analysis when requiring either 1+ track-jet events (black) or 2+ track-jet events (red). Sensitivity measure corresponds to LLR, and is constrained to the m_h signal regions of the analysis, and formed using only the 1+2-tag categories.

because the kinematic and topological composition of the low mass region and SR are no longer equivalent. Details of this disagreement can be found in the following sub-section.

HVT Boosted 1-Lepton m_h Restriction

It was observed that low mass large-R jets are typically the result of a large-R jet with a single ghost-associated track-jet. Figure 13.6 shows the m_h spectrum decomposed into the 1- and 2+ ghost-associated track-jet categories for 1-tag boosted events with 0 additional b-tagged track-jets unassociated to the large-R jet. It is immediately obvious that the large-R jets in the SR and high mass sideband, $m_h \geq 75$ GeV, are predominantly comprised of two or more ghost-associated track-jets, whilst the low mass regime ($m_h < 40$ GeV) is primarily comprised of the 1-track-jet category.

This means that the SR and high mass side bands topologically look very different to the low mass side bands, specifically for large-R jet masses of $m_h < 40$ GeV. It is therefore questionable if the fit results from the SR can be extrapolated to the low mass

side bands in order to test the performance of the fit, due to this fundamentally different topological structure. It is therefore necessary to restrict the low large-R jet mass side bands to the range 50 GeV $< m_h <$ 75 GeV, whilst the high mass side bands are restricted to 145 GeV $< m_h <$ 200 GeV in order to mimic the resolved regime fiducial phase space.

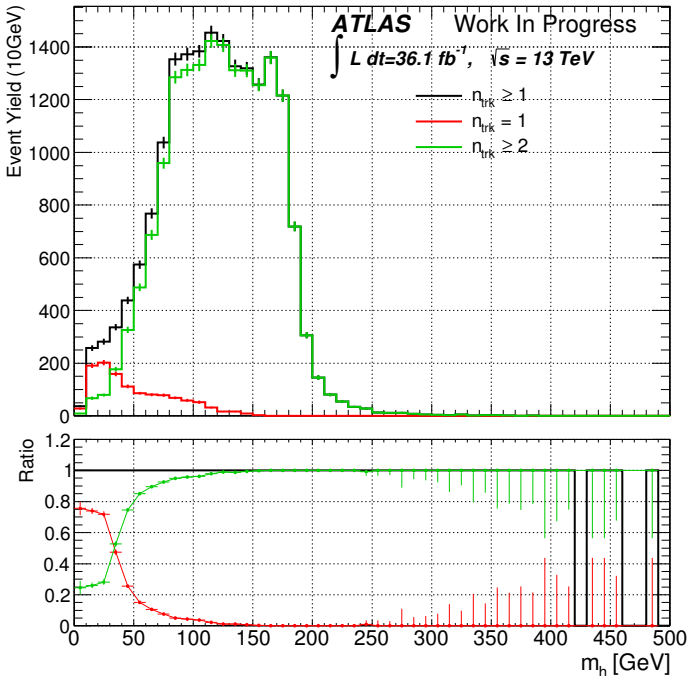

(a) $t\bar{t}$

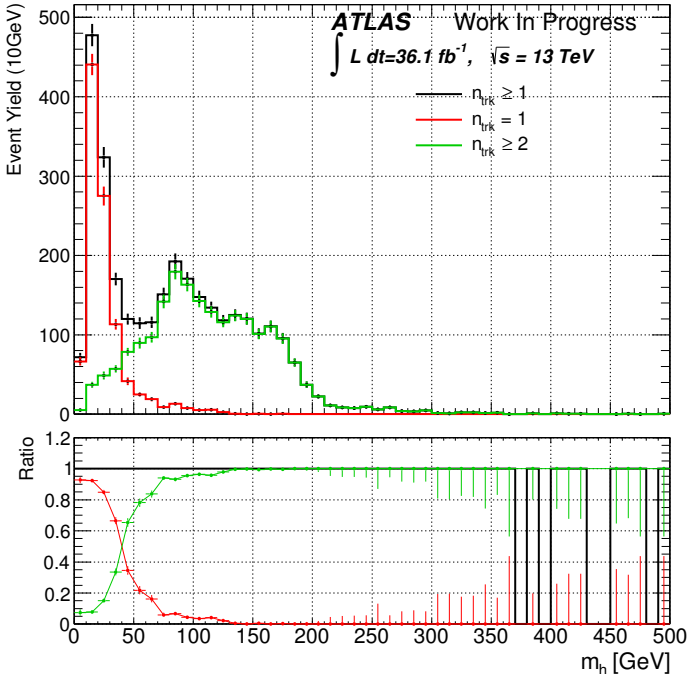

(b) Single Top (s-,t-, Wt-channel)

Figure 13.6.: 1-lepton large-R jet mass distribution for the boosted 1-tag category requiring all events to have 0 additional b-tagged track-jets unassociated to the large-R jet, decomposed into the 1- and 2+ ghost-associated track-jet categories for the $t\bar{t}$, and single top backgrounds. Black corresponds to the $n_{\text{trk}} \geq 1$ category, whilst the red and green correspond to the $n_{\text{trk}} = 1$ and $n_{\text{trk}} \geq 2$ categories.

Chapter 14.

0-Lepton & 2-Lepton Event Selection

The following chapter details the event selection used to define the resolved and boosted fiducial phase space of the analysis for the 0-lepton (Section 14.1), and 2-lepton (Section 14.2) channels. These sections will make reference to previously defined terms pertaining to reconstructed objects given in Chapter 11, or to methods of reconstructing part of the event as given by Chapter 12.

14.1. 0-Lepton

The 0-lepton channel is defined as events that do not contain any `VHloose` electrons or muons, and the presence of τ-leptons results in an event veto. To suppress non-collisional background (beam-induced, cosmic, detector noise), p_T^{miss} must be larger than 30 GeV for 0-/1-tag categorised events.

To suppress the contamination of QCD multijet background, caused by mismeasurements of the jets within the event (which is propagated to the MET determination), a series of cuts are implemented:

- $\Delta\Phi(\boldsymbol{E}_T^{\text{miss}}, \boldsymbol{p}_T^{\text{miss}}) < 90^\circ$
- $\Delta\Phi(\boldsymbol{E}_T^{\text{miss}}, \boldsymbol{p}_T^{h}) > 120^\circ$, where $\boldsymbol{p}_T^{h}$ represents the reconstructed Higgs boson transverse momentum vector.
- $\min\{\Delta\Phi(\boldsymbol{E}_T^{\text{miss}}, \text{pre-sel jets})\} > 20^\circ(30^\circ)$ for $N_{\text{jet}} = [2, 3, (4+)]$, i.e. the minimum azimuthal difference between the missing transverse energy vector and the jets satisfying Table 11.1, must exceed $20(30)^\circ$.

In addition to the QCD multijet rejection cuts, a τ-lepton veto is applied when producing limits for the HVT/AZh Z' mediator (not applied when combining with the 1-lepton channel for a limit setting on the HVT W' mediator), in order to reduce the SM W/Z+Jet and $t\bar{t}$

Selection	0-Lepton Resolved	0-Lepton Boosted
Trigger	MET trigger	
0 lepton	veto `VHloose` electrons and muons	
	veto medium taus	
E_T^{miss}	> 150	> 200
p_T^{miss}	> 30 GeV (not in 2-/3+ tag resolved)	
$\sum p_T$	> 120 (2 jets) or 150 GeV (at least 3 jets)	-
Jets	≥ 2 signal jets	≥ 1 fat jet
		≥ 1 track-jet associated to leading fat jet
Leading jet p_T	> 45 GeV	large-R jet '$p_T > 250$ GeV
m_h	50 GeV $< m_h <$ 200 GeV	
$\min\{\lvert\Delta\phi(\boldsymbol{E}_T^{\text{miss}}, \boldsymbol{p}_T^{\text{jet}})\rvert\}$	$> 20^\circ$ or $> 30^\circ$ (at least 4 jets)	
$\lvert\Delta\phi(\boldsymbol{E}_T^{\text{miss}}, \boldsymbol{p}_T^{h})\rvert$	$> 120^\circ$	
$\lvert\Delta\phi(\boldsymbol{p}^{\text{jet1}}, \boldsymbol{p}^{\text{jet2}})\rvert$	$< 140^\circ$	-
$\lvert\Delta\phi(\boldsymbol{E}_T^{\text{miss}}, \boldsymbol{p}_T^{\text{miss}})\rvert$	$< 90^\circ$	

Table 14.1.: Summary of the event selection in the 0-lepton Resolved and Boosted regime.

backgrounds. Visible components of the τ-lepton decay are reconstructed using the *Tau Particle Flow* methodology outlined in Ref [135]. Events that contain a τ candidate satisfying the `Medium` quality definition, $p_T > 20$ GeV, $|\eta| < 2.5$ (excluding $1.37 < |\eta| < 1.52$), and are constructed from 1 or 3 tracks, are rejected.

The full set of 0-lepton event selections for both the resolved and boosted regime are summarised by Table 14.1, however Section 14.1.1 provides details of the resolved event selections, whilst Section 14.1.2 details the boosted regime event selections.

14.1.1. Resolved Regime

The E_T^{miss} is required to be larger than 150 GeV as a result of the HLT_xe70 offline trigger, which is 85% efficient for $p_T \approx 150$ GeV, but this also helps reduce QCD multijet contamination.

Furthermore, the scalar sum of transverse momentum for the 2 leading jets in the $N_{\text{jet}} = 2$ category, or the 2 leading jets plus the third leading signal/forward jet in the $N_{\text{jet}} = 3$ category is required to be greater than 120 GeV or 150 GeV, respectively. This cut is designed to remove a poorly modelled phase space region resulting from the non-trivial dependence of the MET trigger efficiencies on the number of jets.

To further suppress the contamination of QCD multijet background a constraint on the azimuthal separation of the two small-R jets forming the Higgs candidate is imposed: $\Delta\Phi(\boldsymbol{p}^{\text{jet1}}, \boldsymbol{p}^{\text{jet2}}) < 140^{\circ}$, where $\boldsymbol{p}^{\text{jet1(2)}}$ corresponds to the 3-vector of the reconstructed small-R jets forming the Higgs candidate. Table 14.1 summarises the resolved 0-lepton channel event selection.

14.1.2. Boosted Regime

To reduce QCD multijet background further the event must contain a significant proportion of missing transverse energy. Therefore the constraint on E_T^{miss} is tightened to $E_T^{\text{miss}} > 200$ GeV. The cuts given above are summarised in Table 14.1

14.2. 2-Lepton

The 2-lepton channel is defined as events that contain 2 leptons of the same flavour (ee or $\mu\mu$), where for di-muon events, an additional opposite charge requirement is made. This opposite charge requirement is not applied to the electron channel due to the high rate of charge mis-identification. The exact lepton definition used depends on whether the event is classified as either a resolved or boosted event. Therefore this explanation is left to Sections 14.2.1 and 14.2.2, respectively.

The invariant mass of the di-lepton system must be consistent with the mass of the Z-boson. However, due to the large mediator masses predicted by the 2HDM and HVT models, m_A and $m_{V'}$ respectively, boosted di-lepton systems are a common occurrence. As the Z-boson system becomes increasingly boosted the mass resolution of the reconstructed Z-boson or m_{ll} distribution deteriorates (difficulty in measuring the curvature of increasingly straighter muon tracks etc), therefore, a di-lepton invariant mass (m_{ll}) cut dependent on the invariant mass of the $Z + h$ system (m_{Zh}) is used, which widens as m_{Zh} increases. Referred to as $m_{ll}(m_{Zh})$, the analytic form found to give optimal analysis sensitivity for the AZh and HVT analyses is:

$$87 \text{ GeV} - 0.030 \cdot m_{Zh}[\text{GeV}] < m_{ll}[\text{GeV}] < 97 \text{ GeV} + 0.013 \cdot m_{Zh}[\text{GeV}] \tag{14.1}$$

To further suppress $t\bar{t}$ background, the missing transverse energy significance, defined as the ratio of the missing transverse energy in the event to the scalar sum of all final state momenta (jets+leptons), must be small, specifically $E_T^{\text{miss}}/\sigma_{E_T^{\text{miss}}} < 1.15 + 0.008 \cdot m_{Zh}/1$ GeV. This capitalises on the relatively large E_T^{miss} component of $t\bar{t}$ processes originating from the neutrinos of the W-boson decays.

Finally an optimised cut for signal sensitivity is also applied on the Z-candidates transverse momentum, p_T^Z. This cut scales with the invariant mass of the $Z + h$ system, m_{Zh}, in order to capitalise on the strong correlation of the two variables in the case of the signal, however the weaker correlation in the case of the Z+jets and $t\bar{t}$ backgrounds. See the 1-lepton section for an explanation of the methodology behind the $p_T^V(m_{Vh})$ cut. In the 2-lepton case the optimised analytic form of the cut is given by:

$$p_T^Z > 20 \text{ GeV} + 9\sqrt{\text{GeV}} \cdot \sqrt{\frac{m_{Vh}}{1 \text{ GeV}} - 320} \tag{14.2}$$

Given that the invariant mass of the $Z + h$ system (m_{Zh}) is used as the final fit discriminant, the resolution of the m_{Zh} distribution for muon events within the SR (110 GeV $< m_h <$ 140 GeV) is improved by scaling the four-momentum vectors of the muons by the factor 91 GeV/$m_{\mu\mu}$, in order to bring the invariant mass of the di-muon system onto the pole mass of the Z-boson.

Selection	2 lepton Resolved	2 lepton Boosted
Trigger	OR of lowest un-prescaled single lepton triggers	
2 lepton	1 `VHloose`+1 `ZHsignal`	2 `ZHsignal`
	same flavour (ee or $\mu\mu$) oppositely charged leptons for $\mu\mu$ events in resolved regime	
m_{ll}	$\max\{40 \text{ GeV}, -0.03 \cdot m(Zh) + 87 \text{ GeV}\} < m(\ell\ell)$ [GeV] $< 0.013 \cdot m(Zh) + 97$ GeV	
$E_T^{\text{miss}}/\sqrt{H_T}$	$< 0.008 \cdot m(Zh)/\sqrt{\text{GeV}} + 1.15\sqrt{\text{GeV}}$	
Jets	≥ 2 signal jets	≥ 1 fat jet ≥ 1 track-jet associated to leading fat jet
m_h	50 GeV $< m_h <$ 200 GeV	
Leading jet p_T	$p_T > 45$ GeV	large-R jet $p_T > 250$ GeV
$p_T(Z)$	$m_{VH} > 320$ GeV: $p_T(Z) > 20 \text{ GeV} + 9\sqrt{\text{GeV}} \cdot \sqrt{m(Zh)[\text{GeV}] - 320 \text{ GeV}}$	

Table 14.2.: Summary of the event selection in the 2-lepton Resolved and Boosted regime.

14.2.1. Resolved Regime

The 2-lepton channel is defined as events that contain 2 `VHloose` leptons of the same flavour, i.e. ee or $\mu\mu$, and at least one of those must satisfy the `ZHsignal` lepton definition. If additional `VHloose` leptons are present then the event is vetoed. Table 14.2 summarise the resolved 2-lepton event selections.

14.2.2. Boosted Regime

The 2-lepton channel is defined as events that contain two `VHloose` leptons of the same flavour, i.e. ee or $\mu\mu$, and both of those must satisfy the `ZHsignal` lepton definition. If additional `VHloose` leptons are present then the event is vetoed. The tighter requirements on the lepton definition is required to curb the background acceptance of fake leptons. The boosted regime is typically sensitive to HVT/AZh mediator masses of 1 TeV or larger, where boosted Z-boson topologies from the hypothesised signal have a higher p_T than the SM background processes like $t\bar{t}$ and Z+Jets. Therefore, requiring that both leptons satisfy the `ZHsignal` lepton definitions only incurs an additional constraint of $p_T^l > 27$ GeV. The loss of signal acceptance is small compared to the extra rejection power of the SM background, resulting in a favourable sensitivity gain. The above event selections are summarised in Table 14.2.

Chapter 15.

1-Lepton Event Selection

The following chapter details the event selection used by the 1-lepton channel within the HVT analysis for both the resolved and boosted regimes. This chapter will refer to previous sections pertaining to reconstructed objects or reconstruction methods, Chapter 11 and Chapter 12 respectively. As the lead 1-lepton analyst, the following chapter is predominantly the work of author of this thesis.

The 1-lepton channel is defined by the requirement that each event must contain only one `WHsignal` lepton, which can be either an electron or muon. The full event selection for the resolved and boosted regimes can be found in Table 15.1. However some explanation of each of the cuts is summarised within the Resolved Regime and Boosted Regime sections given below, see Sections 15.1 and 15.2 respectively.

15.1. Resolved Regime

Several cuts designed to reject $t\bar{t}$ events are implemented in order to reduce this dominant background process. The jet multiplicity requirements are tightened by requiring that $2 \leq n_{\text{jet}}^{\text{sig}} < 4$. Studies regarding this change can be found in Section 15.1.1. The number of b-tagged small-R jets for an event with a pool of three or more jets, as selected by the *All Signal Jets* selection scheme, must be two or smaller, otherwise the event is vetoed.

QCD multijet contamination as a result of jets faking leptons or non-prompt leptons from hadronic decays typically occupy the low E_T^{miss} regions of phase space, due to the mis-measurement and calibration of the fake leptons. Therefore, to reduce the MET contamination, the 1-lepton channel requires that for electrons $E_T^{e,\text{miss}} > 80$ GeV, whilst for muons $E_T^{\mu,\text{miss}} > 40$ GeV.

Selection	1-lepton Resolved	1-lepton Boosted
Trigger	electron trigger and E_T^{miss} trigger	
1 lepton	exactly 1 `WHloose` electron/muon which should also pass the `WHsignal` criteria	
E_T^{miss}	$>$ 80 GeV in electron events $>$ 40 GeV in muon events	$>$100 GeV
p_T^W	$p_T^W > \frac{(-3.26\times10^5)}{m_{Vh}[\text{GeV}]} + 709.60$	$p_T^W > 394 \cdot \ln(m_{Vh}[\text{GeV}]) - 2350$
	lower cap of $p_T(W) > 150$ GeV	
m_T^W	$m_T^W < 300$GeV	
m_h	50 GeV $< m_h <$ 200 GeV	
Jets	2 or 3 signal jets $\geq$ 0 forward jets	$\geq$ 1 fat jet $\geq$ 1 track-jet associated to leading fat jet
Leading jet p_T	$>$ 45 GeV	large-R jet $p_T >$ 250 GeV
Sub-leading jet p_T	$>$ 20 GeV	-
b-tagging	Veto events with 3 or more b-jets	-

Table 15.1.: Summary of the event selection in the 1-lepton Resolved and Boosted regimes.

The transverse momenta of the reconstructed W-boson and Higgs candidate are highly correlated with the reconstructed $V+h$ system ($m_{Vh} \approx m_{V'}$). For the SM backgrounds, like SM V+jets and $t\bar{t}$ processes, this correlation between $m_{Vh}^{(T)}$ and $p_T^{V/h}$ is substantially weaker. This principle can be used to reject the dominant $t\bar{t}$, single top, and V+Jets SM backgrounds, by using a scaling p_T^W cut as a function of the reconstructed invariant mass of the $V+h$ system (m_{Vh}). The analytic form of this equation is given by:

$$p_T^W > \max[150 \text{ GeV},\ 709.60 \text{ GeV} - 3.26 \cdot 10^5 \text{ GeV}^2/m_{Vh}] \tag{15.1}$$

See Section 15.3.1 for details on the derivation and investigation of the $p_T^W(m_{Vh})$ dynamic cut. The same technique used to optimise the $p_T^W(m_{Vh})$ dynamic cut was also used to determine the optimal m_h signal window, which for the resolved analysis was determined to be 110 GeV $< m_h <$ 140 GeV; these studies are summarised in Section 15.3.2. The resolved 1-lepton event selection is summarised in Table 15.1.

15.1.1. HVT Resolved 1-Lepton $n_{\text{jet}}^{\text{sig}}$ Rejection Studies

A characteristic of the SM $t\bar{t}$ process is high jet multiplicity events, especially for the 1-lepton resolved regime where one top quark decays leptonically $t \to b + W(\to l\nu)$, and the

Jet Category (n_{jet})	**1-tag [# yield]**	**1-tag $\frac{N^x_{\text{jet}}}{N^{2+}_{\text{jet}}}$ [%]**	**2-tag [# yield]**	**2-tag $\frac{N^x_{\text{jet}}}{N^{2+}_{\text{jet}}}$ [%]**
2+	83127.9	N/A	35527.7	N/A
2	5477.2	6.6%	484.3	1.4%
3	15617.6	18.8%	3194.46	9.0%
4	21771.5	26.2%	7575.0	21.3%
5+	40261.6	48.4%	24273.9	68.3%

Table 15.2.: Relative contribution of SM background processes to 2+ jet category for the 1-/2-tag 110 GeV $< m_h <$ 140 GeV SRs, with the absolute event yield predictions for each category, when normalised to a integrated luminosity of 36.1 fb^{-1}.

other decays hadronically $t \to b + W(\to q\bar{q})$. It is therefore very common for a semi-leptonic $t\bar{t}$ process to yield four or more high p_T central jets.

This is found to be the case within the resolved regime of the PRSR scheme, as summarised by Table 15.2. This table shows the total predicted background event yield for the 2+ small-R jet (n^{2+}_{jet}) category as well as the $n^{2,3,4,5+}_{\text{jet}}$ jet exclusive categorises normalised to an integrated luminosity of 36.1 fb^{-1}. The table also summarises the relative percentage contribution of each jet exclusive category to the total n^{2+}_{jet} category, i.e. $\% = n^x_{\text{jet}}/n^{2+}_{\text{jet}}$ for $x = [2, 3, 4, 5+]$. From this table it is apparent that $\sim 75\%$ and $\sim 90\%$ of the background comes from the 4+ jet category, for the 1- and 2-tag categories, respectively.

Therefore a $n^{\text{sig}}_{\text{jet}} < 4$ cut is placed, where the resulting sensitivity improvement of the analysis to the HVT signal is shown by Figure 15.1. This figure shows the LLR before and after the cut (see equation 12.3), for the 24 signal points within the m_h SR for the combined 1+2 tag categories. The signals are normalised to the MC predicted cross-sections, and scaled to a luminosity of 36.1 fb^{-1}.

An $\sim 30\%$ improvement for the lowest mass point ($m_{V'} = 500$ GeV) is observed, which slowly degrade until no improvement is seen at a mass point of $m_{V'} \approx 2000$ GeV. This turn off is the result of the slowly degrading influence of the resolved regime for masses above 1 TeV, as shown by Figure 12.3, therefore any sensitivity gain within the resolved regime has little impact on the overall analysis when the resolved regime is sub-dominant.

15.1.2. Data/MC modelling

Prior to the restriction imposed by the $n^{\text{sig}}_{\text{jet}} < 4$ cut, a mismodelling in the m_{Vh} fit discriminant was observed in the 140 GeV $< m_h <$ 200 GeV CR. This mismodelling is

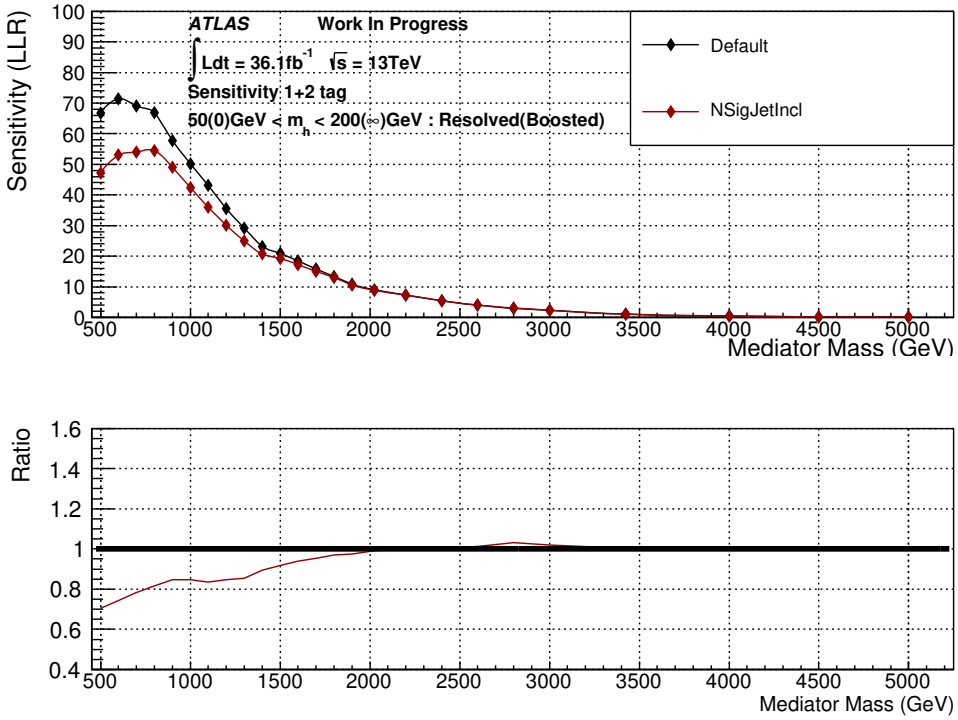

Figure 15.1.: LLR sensitivity comparison of the PRSR scheme with and without a cut on the number of signal small-R jets within the resolved regime. The signal and background MC are normalised to an integrated luminosity of 36.1 fb^{-1}, and all signal samples are normalised to the signal cross-section obtained from the MC generators, whilst the backgrounds are normalised to the NNLO fixed order calculations.

shown by figure 15.2a, and is attributed to the $t\bar{t}$ process produced by the POWHEG-BOX v2+PYTHIA 6 generator.

In applying the $n_{\text{jet}}^{\text{sig}} < 4$ cut, the Data/MC agreement quantified by the $\text{Stat}_{\text{shape-only}}$ χ^2/n_{dof} [1] displayed on each plot, shows a non-negligible improvement; $\chi^2_n = 3.86$ prior, and $\chi^2_n = 2.23$ after. It should be noted that some of this improvement in the Data/MC agreement will be the result of increased statistical error on the data and MC. Specifically, the increased statistical error suppresses the large residual terms contributing to the χ^2 value. Nevertheless, given the improved analysis sensitivity, and no clear sign of a degradation in the Data/MC agreement, the application of the $n_{\text{jet}}^{\text{sig}}$ cut was adopted by the analysis.

For completeness the data/MC agreement plots prior and post application of the $n_{\text{jet}}^{\text{sig}} < 4$ cut are shown by figure 15.3 for the 50 GeV $< m_h <$ 110 GeV low mass side band for the

[1] The $\text{Stat}_{\text{shape-only}}$ definition of the χ^2/n_{dof} metric, is the same as the typical metric $\chi^2/n_{\text{dof}} = \sum_i^{bins}(d_i - MC_i)^2/\sqrt{\sigma_d^2 + \sigma_{MC}^2}$, with the exception that the MC is normalised to the data yield prior to the calculation.

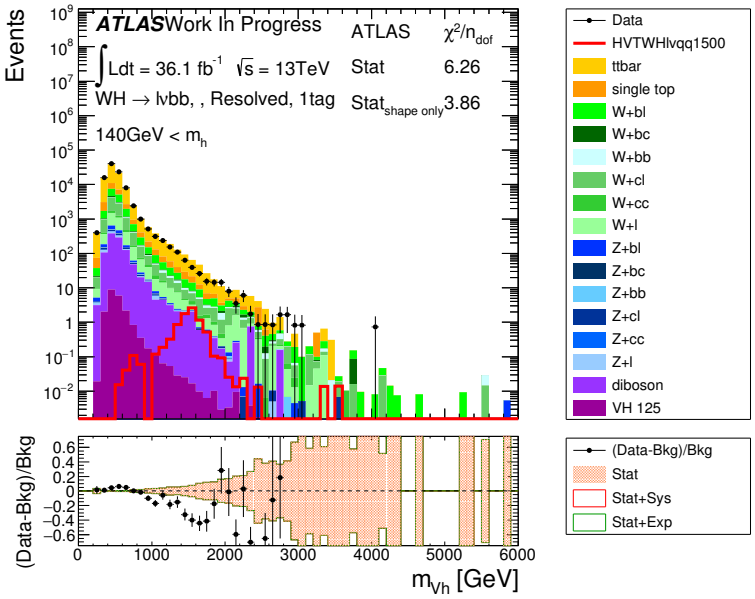

(a) $n_{\text{jet}}^{\text{sig}} \geq 2$ constrained

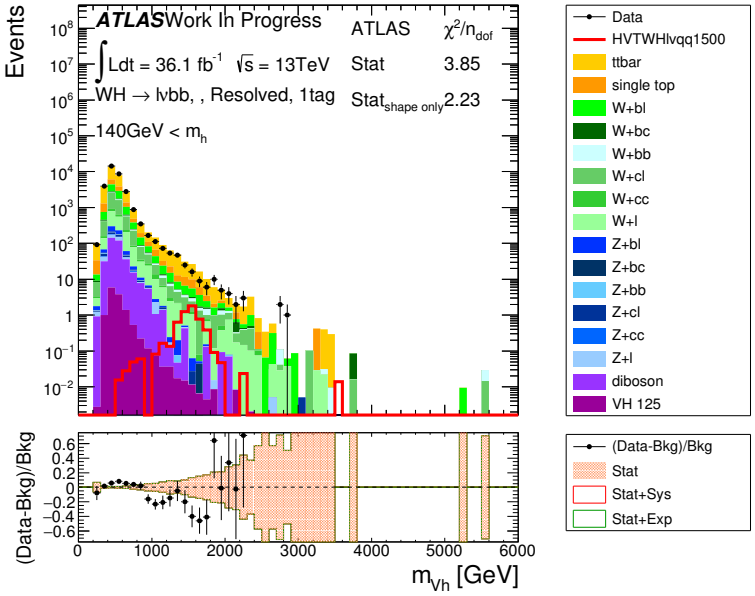

(b) $2 \leq n_{\text{jet}}^{\text{sig}} < 4$ constrained

Figure 15.2.: Pre-fit plots of the m_{Vh} data/MC agreement normalised to the data integrated luminosity of 36.1 fb^{-1} for the 1-tag resolved 140 GeV $< m_h <$ 200 GeV side band region. (a) corresponds to the m_{Vh} distribution prior to the additional $n_{\text{jet}}^{\text{sig}} < 4$ cut, whilst (b) is after applying the cut.

1-/2-tag regions, and the 2-tag region for the 140 GeV $< m_H <$ 200 GeV high mass region.

No statistically significant of the MC from the data is observed for any of the remaining resolved control regions, either prior or post application of the $n_{\text{jet}}^{\text{sig}} < 4$ cut.

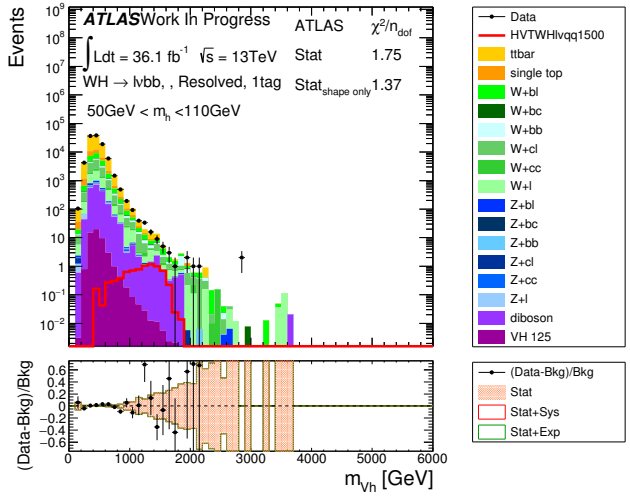

(a) 1-tag low m_h $n_{\text{jet}}^{\text{sig}} \geq 2$ constrained

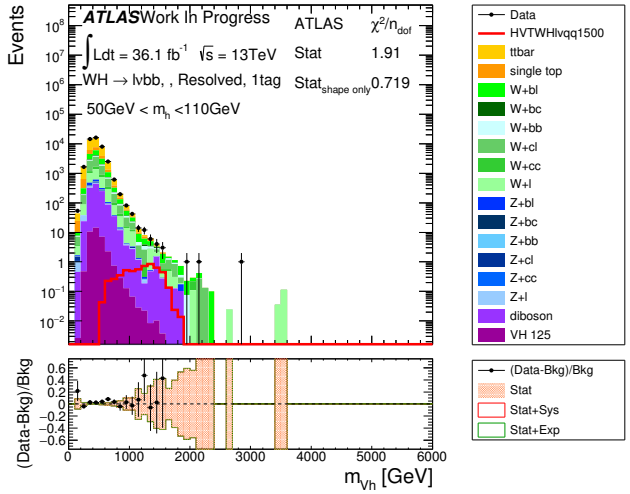

(b) 1-tag low m_h $2 \leq n_{\text{jet}}^{\text{sig}} < 4$ constrained

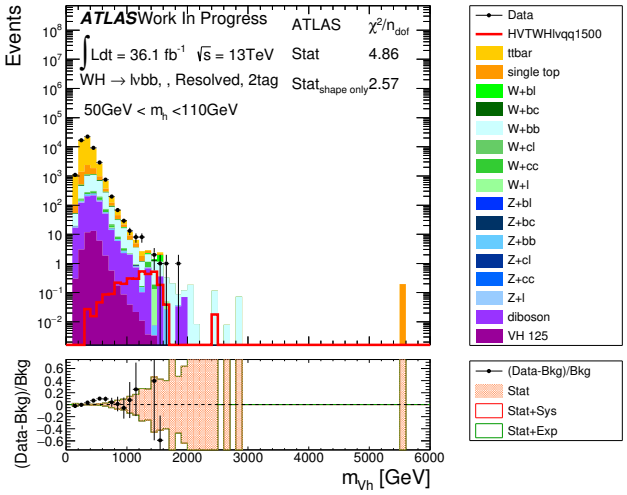

(c) 2-tag low m_h $n_{\text{jet}}^{\text{sig}} \geq 2$ constrained

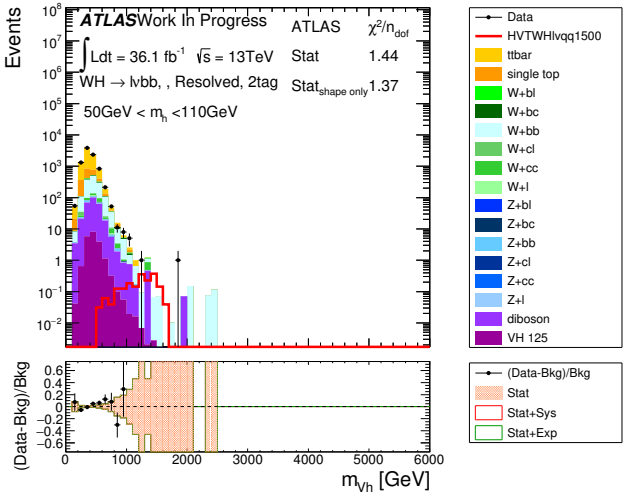

(d) 2-tag low m_h $2 \leq n_{\text{jet}}^{\text{sig}} < 4$ constrained

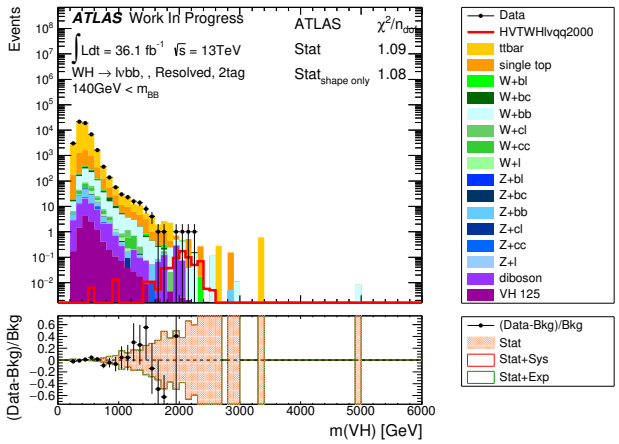

(e) 2-tag high m_h $n_{\text{jet}}^{\text{sig}} \geq 2$ constrained

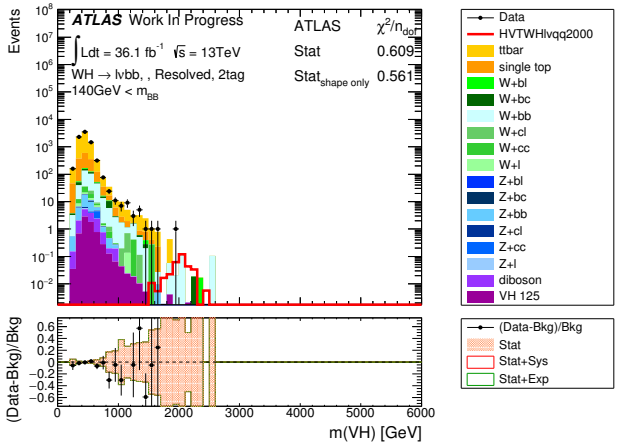

(f) 2-tag high m_h $2 \leq n_{\text{jet}}^{\text{sig}} < 4$ constrained

Figure 15.3.: Pre-fit plots of the m_{Vh} data/MC agreement normalised to the data integrated luminosity of 36.1 fb^{-1} for the 1-tag 50 GeV $< m_h <$ 110 GeV side band region prior (a) and post (b), 2-tag 50 GeV $< m_h <$ 110 GeV side band region prior (c) and post (d), and 2-tag 140 GeV $< m_h <$ 200 GeV side band region prior (e) and post (f) application of the $n_{\text{jet}}^{\text{sig}} < 4$ cut.

15.2. Boosted Regime

QCD multijet contamination is suppressed by the inherent $p_T^J > 250$ GeV constraint on the large-R jet, however to further suppress QCD multijet the event must contain significant missing transverse energy, $E_T^{\text{miss}} > 200$ GeV.

Like the resolved regime, the $t\bar{t}$ and V+Jet background is suppressed by using a dynamic $p_T^W(m_{Vh})$ cut:

$$p_T^W = \max[150 \text{ GeV}, 394 \text{ GeV} \times \ln(m_{Vh}[\text{GeV}]) - 2350 \text{ GeV}]. \tag{15.2}$$

Details on the derivation and methodology can be found in Section 15.3.1. The event selection is summarised in Table 15.1.

15.3. HVT Resolved & Boosted m_{Vh} Dependent Cuts

As highlighted in Chapter 4 and Section 8.2, the invariant mass of the V' mediators is a free parameter which is only limited to $m_{V'} \geq 500$ GeV due to electroweak precision measurements. The analysis therefore searches for the presence of a new resonance consistent with the aforementioned model within the 500 GeV $\leq m_{V'} \leq$ 5000 GeV range. Consequently, for each simulated mass point, the m_{Vh} signal distribution sits on top of a varying background composition. As such the event selection that maximises the sensitivity of the analysis to the predicted signal, must be a function of the invariant mass of the underlying mediator. For the purpose of brevity, only the 1-lepton HVT optimisation results are shown.

Deriving these dynamic $m_{Vh}^{(T)}$ dependent cuts is done by generating a 2-dimensional map of the background and signal MC, where one of these dimensions is m_{Vh} (primary axis). The remaining dimension (secondary axis) can be any remaining event observable, for example $\mathcal{O} = p_T^V/m_h$ etc ..., that has the power to discriminate the electroweak backgrounds from the signal. Cuts are then iteratively placed on the secondary axis of the 2D map. At each iteration the events that pass this cut configuration are projected onto the m_{Vh} axis in order to form a 1-dimensional m_{Vh} distribution. With a signal and background (combined electroweak sources) 1D m_{Vh} distribution, the sensitivity of the analysis to the predicted HVT signal is quantified by the sensitivity measure given by equation 12.3 in Chapter 12.

The LLR value is recorded for the cut configuration, and then the process continues for the next iteration; this process is referred to as a LLR scan. The optimal cut is defined as the configuration or iteration of the scan that maximises the analysis sensitivity, i.e. the largest LLR value. With an optimal cut for each simulated mediator mass point (24 in

total), the optimised $(O)(m_{Vh})$ cut is obtained by fitting a scalar function (polynomial or linear combination of $\ln(x), x^{n/2}, ...$) to the mass points.

The resolved and boosted regimes are considered independently during the optimisation process in order to maximise the statistics within each of the analysis regions. The analysis regions considered during the optimisation include the 1-tag and 2-tag m_h (Higgs mass) signal region. The 0-tag region is excluded due to its rejection from the overall analysis fit model.

All event selection cuts are kept the same as outlined in Table 15.1, except the cuts on the observables being tested. For example, during the $p_T^V(m_{Vh})$ cut optimisation all event selections remain unchanged, except the p_T^V cut which is turned off. This is applied to both the resolved and boosted analysis regimes.

15.3.1. HVT 1-Lepton $p_T^W(m_{Vh})$ dynamic cut

The invariant mass of the $V + h$ system, m_{Vh}, is highly correlated with the transverse momentum of the W-boson and reconstructed Higgs candidate, meaning that high mass HVT mediators give rise to high transverse momentum W/Z and Higgs bosons. Whilst for the W+Jets and $t\bar{t}$ backgrounds, the comparatively low mass of the W-boson or $t\bar{t}$ system, means that the reconstructed decay products of these background processes should give rise to lower p_T objects, and the correlation between the invariant mass of the system and the p_T^V is substantially weaker. This is shown by Figure 15.4, where the 2-dimensional relationship between m_{Vh} & p_T^V can be seen for the total electroweak (EW) background and combined signal samples, for both the resolved and boosted analysis schemes.

From this figure it can also be seen that the correlation between m_{Vh} & p_T^V for the backgrounds, is smaller than that of the signal. These two distinct differences drive the signal and background distributions apart; a feature that can be utilised in the analysis. Considering the expected and observed behaviour of signal and background, a p_T^V cut that scales with the invariant mass of the system is therefore a logical choice. All event selection cuts are kept the same for both the resolved and boosted reconstruction schemes. Note should be made of the Resolved regime, where the flat $p_T^V = 150$ GeV is kept unchanged due to its impact on the MJ estimate.

The LLR scan is performed independently on each of the 24 HVT mass points, where the p_T^V cut is iteratively increased from a starting value of 150 GeV for the resolved or 0 GeV for the merged analysis, in 50 GeV increments. An example of the LLR scan for the 1000 GeV & 3000 GeV HVT mass points, is given by Figure 15.5a & Figure 15.5b, for the

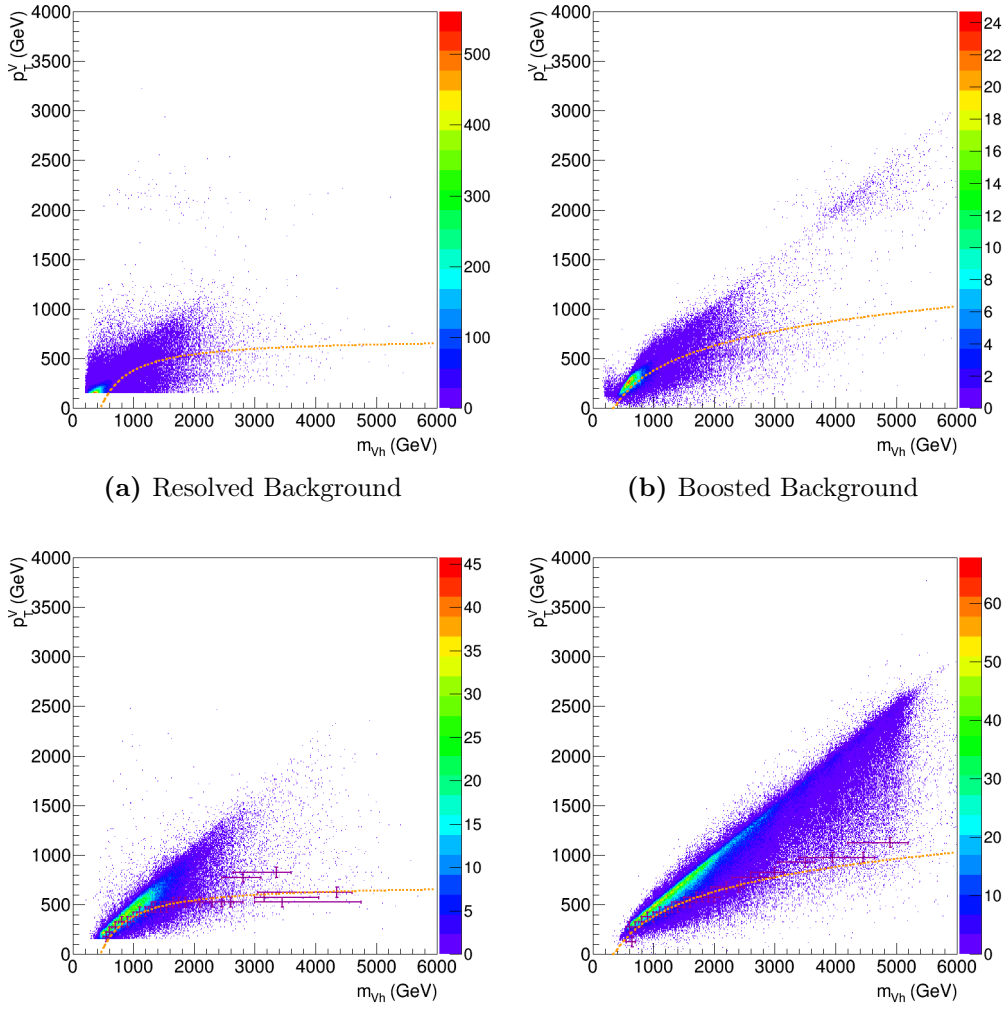

(a) Resolved Background **(b)** Boosted Background

(c) Resolved Signal **(d)** Boosted Signal

Figure 15.4.: Relationship between m_{Vh} & p_T^V in the 1-lepton channel. The top row shows the inclusive electroweak background distributions for the 1+2 tag categories in the mass signal window defined as 110 GeV $< m_h <$ 140 GeV & 75 GeV $< m_h <$ 145 GeV for the resolved and boosted analysis regimes. The bottom row shows the sum of all 24 signal mass points ranging from 500 GeV to 5000 GeV. The magenta crosses correspond to the optimised p_T^V cut values for each of the 24 signal mass points within the resolved and boosted analysis reconstruction schemes. The orange lines correspond to fitted scalar functions used to smooth the $p_T^V(m_{Vh})$ trend.

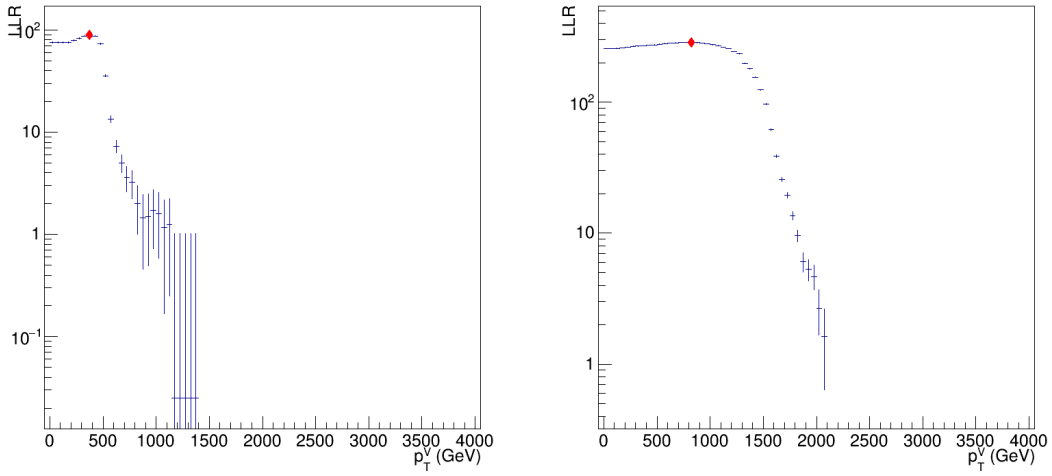

(a) Resolved Scheme $m_{V'} = 1$ TeV **(b)** Boosted Scheme $m_{V'} = 3$ TeV

Figure 15.5.: LLR scan of the p_T^V cut for the resolved and boosted reconstruction schemes using a mediator mass of $m_{V'} = 1$ TeV and $m_{V'} = 3$ TeV, respectively. The optimal LLR value is highlighted in red.

resolved and boosted reconstruction schemes. The p_T^V cut value that maximises the LLR value is shown as a red diamond on the figures.

Completing this scan for all 24 HVT signal samples yields a set of 24 points in the m_{Vh}–p_T^V plane. These are placed on the 2D maps shown by Figure 15.4 as magenta crosses, with an x-axis bin center determined by the mode of the m_{Vh} distribution prior to the p_T^V cut optimisation, an asymmetric x-axis error defined as the difference in the mode from the lower and upper 68% m_{Vh} mass window, a y-axis bin center given by the LLR maximised p_T^V cut, and a y-axis error defined as ±50 GeV (increment size).

A scalar function of the form, $y = b/x + a$ and $y = b\ln(x) + a$, are then fitted to the 24 signal mass points for the resolved and boosted regimes, respectively, where $\{a, b\}$ are the parameters of the function and y/x represent p_T^V/m_{Vh}. The final fit results are shown in Figure 15.4, as orange dotted lines. The fit results can be found in Table 15.3.

Analysis Scheme	**Functional Form**	χ^2/N_{dof}
Resolved	$p_T^W = -3.26(\pm0.44) \times 10^5/m_{Vh}[\text{GeV}] + 709.60(\pm33.44)$ & $p_T^V > 150$ GeV	0.99
Boosted	$p_T^W > 394(\pm31) \cdot \ln(m_{Vh}[\text{GeV}]) - 2350(\pm233)$	0.82

Table 15.3.: Table summarising the optimised $p_T^W(m_{Vh})$ cut for the resolved and boosted reconstruction scheme, and the quality of the fit.

The optimised cuts are then integrated into the *Priority Resolved Signal Region* (PRSR) analysis scheme logic. The new cuts are applied irrespective of the mass region definitions (low, SR or high m_h) and b-tag categories, i.e. the cuts are applied identically in all mass bands and tag regions. This was done to simplify the modelling systematics outlined in Section 18.3. Figure 15.6 shows the sensitivity gain expected in the 1+2-tag mass SR, for the combined Resolved+Boosted analysis regimes. Note that the event selection used for this test is the same as that outlined in table 12.1, except the $p_T^V > 150$ GeV cut in the boosted regime is not applied, and the $2 \leq n_{\text{jet}}^{\text{sig}} < 4$ is loosened to $n_{\text{jet}}^{\text{sig}} \geq 2$.

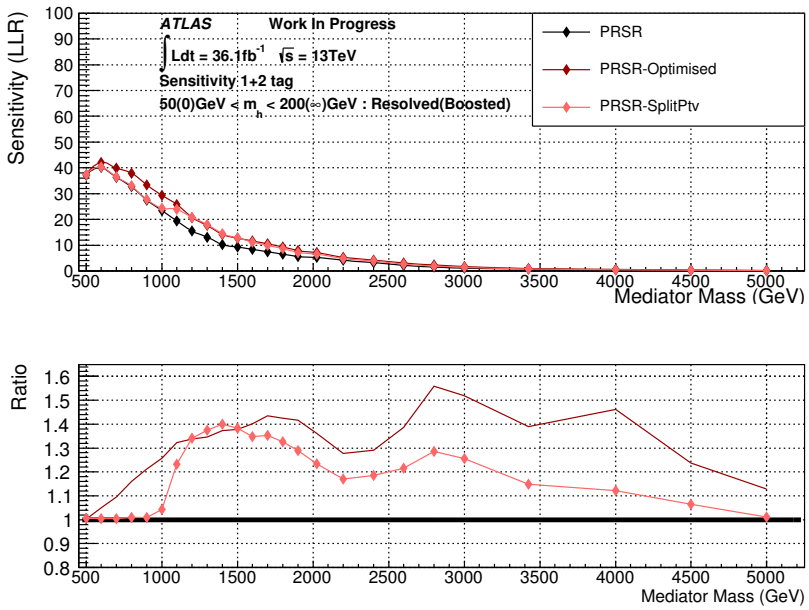

Figure 15.6.: LLR sensitivity comparisons for the 1+2-tag m_h SRs using the PRSR scheme, the new LLR optimised mass dependent p_T^V cuts (Optimised), and the PRSR analysis where the resolved and boosted m_{Vh} histograms are divided in two using a $p_T^V = 500$ GeV cut (SplitPtv). All signal mass samples are normalised to their corresponding MC cross-section predictions.

15.3.2. HVT 1-Lepton $m_h(m_{Vh})$ Scaling Cut

The reconstructed Higgs candidate, whether it be constructed from the two small-R jets or a single large-R jet, is a powerful background/signal discriminant due to the peaked behaviour of the signal around the Higgs mass, $m_h \approx 125$ GeV. Unfortunately, due to the rapidly increasing jet energy scale and resolution uncertainties for low p_T jets (see Ref [110]), it was observed that the invariant mass resolution of the reconstructed Higgs candidate degrades for lower $m_{V'}$ masses.

This effect is shown by sub-figure 15.7a, which shows the m_{Vh} (x-axis) and m_h (y-axis) 2D map for the combined 24 HVT signal samples under the Resolved reconstruction scheme. From this figure, it is observed that for lower m_{Vh} values the m_h distribution widens asymmetrically towards smaller m_h values. Given the wide range of HVT mediator masses predicted by the theory, a 2-dimensional LLR scan is performed in order to identify the optimal m_h signal window cut as a function of the invariant mass of the $V + h$ system.

The magenta and blue crosses in sub-figure 15.7a represent the optimised lower and upper m_h cuts determined from a 2-dimensional LLR scan. The same methodology as above is used, however one alteration is made. Starting with a lower cut at $m_h = 5$ GeV a second ("upper") cut initialised at $m_h = 495$ GeV is placed; this pair of cuts is referred to as a window cut. The background and signal events within this window are projected onto the x-axis to give a 1-dimensional m_{Vh} distribution. The same procedure is then used to record the analysis sensitivity given the aforementioned window cut. Once complete, the upper cut is decreased by a 5 GeV interval and the process repeats until the upper and lower cuts are 5 GeV apart. At this stage the lower cut is then incremented by 5 GeV, and the whole process repeats. This is referred to as a 2D LLR scan.

An example of this scan is shown by Figure 15.8, where the x-axis and y-axis represent the lower and upper m_h cut, respectively. The z-axis shows the ΔLLR value for the pair of (x, y) m_h cuts. The (x, y) co-ordinates that maximise the LLR correspond to the optimal m_h SR window for the Higgs candidate. This is repeated for all 24 mass points, giving rise to the aforementioned data points on sub-figure 15.7a. The central x-axis position is obtained by determining the mode of the m_{Vh} distribution prior to the cut optimisation, and the x-axis errors correspond to difference between the mode and the lower/upper 68% window edges of the m_{Vh} distribution. The optimised (x, y) m_h values yield the lower (magenta) and upper (blue) y-axis central values, and the y-axis errors are set to ± 5 GeV, i.e. the scan intervals.

In analysing sub-figure 15.7a, it is apparent that the optimal lower boundary is approximately $m_h \approx 110$ GeV for all mediator mass points, i.e. independent of the reconstructed m_{Vh}. However, the upper boundary is dependent on the mediator mass, where the optimal upper boundary starts at $m_h = 140$ GeV and widens to $m_h = 200$ GeV. Considering though that the resolved regime of the PRSR analysis quickly becomes sub-dominant for $m_{V'} > 1.2$ TeV (Figure 12.3), the benefit of increasing the upper boundary of the SR window for the resolved part of the analysis to the overall sensitivity is highly suppressed. Therefore, the SR window in the resolved part of the analysis is defined according to the cut, 110 GeV $< m_h <$ 140 GeV.

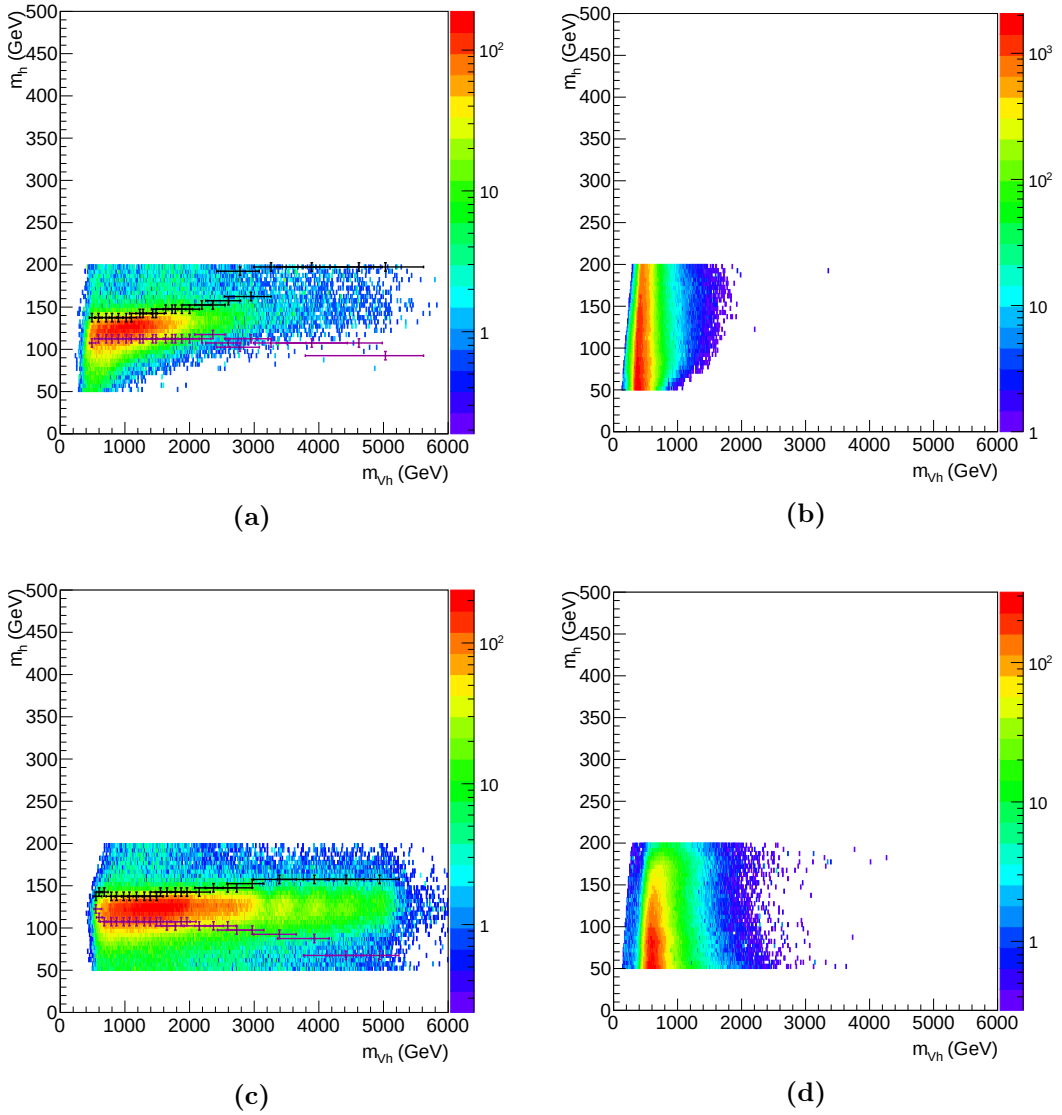

Figure 15.7.: 2D map showing the behaviour of the invariant mass distribution of the Higgs candidate for the Resolved (a+b) and Boosted (c+d) reconstruction schemes, using the HVT signal samples (a+c) and the combined electroweak background samples (b+d), as a function of m_{Vh}.

For the Boosted regime (Figure 15.7c), the optimal m_h signal region progressively widens as a function of m_{Vh}. Given the insignificant contribution of the Boosted reconstruction scheme in the PRSR combination scheme for mediator masses of $m_{V'} < 1.0$ TeV, the optimised cuts below this point can be considered irrelevant. A variable m_h SR window is the optimal solution for mediator masses in the $m_{V'} > 1$ TeV range, however given the rapid fall of the SM backgrounds for $m_{Vh} > 0.8 - 1.0$ TeV, the optimised boundaries in the high m_{Vh} regimes become increasingly susceptible to statistical fluctuations. Therefore, to

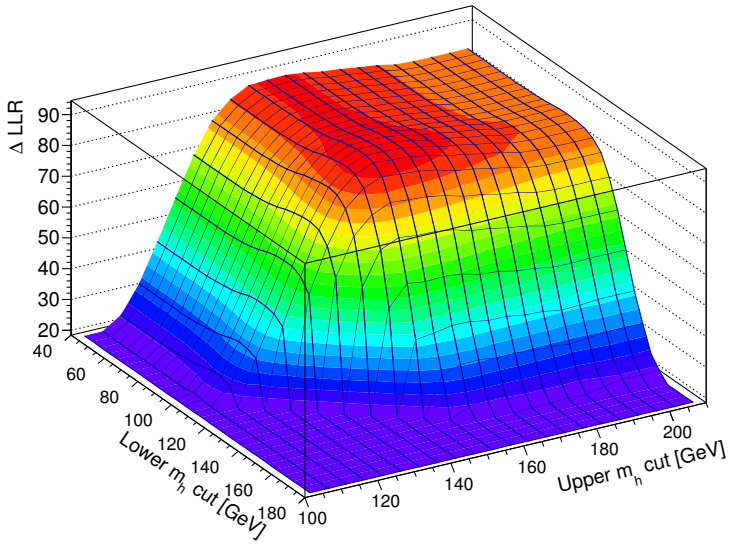

Figure 15.8.: 2D LLR scan of m_h cut for the Resolved reconstruction scheme in the 1-lepton channel. The x- and y-axis represent the lower and upper m_h cut, whilst the z-axis shows the ΔLLR sensitivity measure.

reduce the complexity of the analysis a fixed m_h SR is defined as 75 GeV $< m_h <$ 145 GeV for the boosted regime. Furthermore, the 2-lepton channel favoured this wider m_h window, therefore to optimise the overall sensitivity of the analysis to the HVT V' mediator, the aforementioned window was selected.

Chapter 16.

1-Lepton Multijet Estimate

Within the 1-lepton analysis, the QCD multijet process is highly suppressed by requiring a high-p_T good quality lepton that is well isolated, large E_T^{miss} in the event, and requiring that the hadronic side of the event contains either 1 or more b-tagged jets. Nevertheless, a small fraction of multijet events containing two real b-quarks from gluon splitting, or mistagged light-jets (1 in $\sim$ 381 [129]), can give the b-tagged jet signatures needed by the analysis. Furthermore, in the electron channel non-prompt leptons from weak decays of hadrons from inside the jet, and jets faking electrons, are two possible methods in which the signal electron can be generated. In the case of the muon channel, non-prompt muons originating from weak decays of b-hadrons predominantly give rise to the single lepton needed for the event to pass the selection.

The following chapter will summarise the multijet template method used to estimate the event yield contribution and obtain a m_{Vh} spectrum for the multijet background.

16.1. Template Method

Leptons within multijet events typically fail the isolation requirements imposed by the `WHsignal` requirement (see Section 11.2), because the leptons originate from the weak decays of hadrons, and so are located inside of a jet. The *Template Method* exploits this characteristic by defining two regions: an isolated region which meets the requirements of the nominal event selection given by Chapter 15, and a non-isolated region enriched in multijet background.

In the case of the electron channel, $E_T^{\text{cone}}/p_T < 0.06$ and $p_T^{\text{var-cone}}/p_T < 0.06$ define the isolated region, whilst the non-isolated region is defined by inverting the calorimeter isolation requirement, i.e. $E_T^{\text{cone}}/p_T > 0.06$. Due to track isolation requirements on the single electron triggers outlined in Section 13.2, inverting the track isolation on the signal lepton definition

	criterion	isolated region	non-isolated region
Electrons	ID	`TightLH`	`TightLH`
	track isolation	$p_T^{\text{var-cone}}/p_T < 0.06$	$p_T^{\text{var-cone}}/p_T < 0.06$
	calorimeter isolation	$E_T^{\text{cone}}/p_T < 0.06$	$E_T^{\text{cone}}/p_T > 0.06$
Muons	ID	`Tight`	`Tight`
	track isolation	$p_T^{\text{var-cone}}/p_T < 0.06$	$0.06 < p_T^{\text{var-cone}}/p_T < 0.15$

Table 16.1.: Identification and isolation requirements for the signal lepton in the isolated and non-isolated regions of the 1-lepton channel. See Section 11.2 for details.

would require additional trigger efficiency uncertainties due to a trigger bias induced by the track isolation inversion. Therefore, to prevent this bias and additional trigger efficiency uncertainties, only the calorimeter isolation is inverted. Whilst this choice induces a bias in the neutral-to-charged hadron fraction, appropriate systematics are implemented to control the effects of the bias, and given the small nature of the multijet template to each fit region in the Resolved regime, the overall impact of the bias is suppressed.

For the muon channel, only the track-based isolation requirement is used to define the isolation of the object. For the isolated region $p_T^{\text{var-cone}}/p_T < 0.06$, whilst for the non-isolated region $p_T^{\text{var-cone}}/p_T > 0.06$. Table 16.1 summarises the electron and muon identification and isolation requirements that make up the two aforementioned regions.

In both the electron and muon channels, as well as the isolated and non-isolated regions, the identification requirements on the leptons remain unchanged, including all other cuts outlined in Chapter 15.

Events are then categorised further according to four criteria:

- Resolved and Boosted regimes are considered separately, due to different event selections
- Electron and muon channels separated due to the different production mechanisms
- Number of b-tagged small-R or track-jets, since the multijet content is suppressed with increasing number of tags
- Split into the m_h SRs and CRs

For each category in the non-isolated region a data template ($m_{Vh}, p_T^{jet}, p_T^{l}, ...$ spectrum) is obtained in addition to an Electroweak (EWK) background template composed of all SM background processes. The difference between the data and EWK templates,

$h_{\text{QCD}}(\mathcal{O}) = h_{\text{data}}(\mathcal{O}) - h_{\text{EW}}(\mathcal{O})$, is expected to be the multijet backgrounds, where $h_k(\mathcal{O})$ represents the data/EWK/QCD binned spectrum for an observable $\mathcal{O}$.

In order to account for a discrepancy in normalisation between the data and EWK background in the non-isolated region, prior to extracting the QCD multijet template, a Poisson Likelihood fit[1] considering only statistical errors, between the data and EWK MC E_T^{miss} templates for $E_T^{\text{miss}} > 200$ GeV is performed[2]. The resulting fit yields a unique electron and muon EWK scale factor for the fitted region.

An example of this procedure is shown by Figure 16.1a for the resolved 1-tag muon channel in the 50 GeV $< m_h <$ 200 GeV region, where the pre-fit EWK background is shown in purple, and the post-fit scaled EWK background is shown as a blue shaded histogram. The EWK background is scaled by a factor of 1.42 to transform the purple to the blue.

These unique multiplicative scale factors are derived for each fit region and for the muon and electron channels separately. For each kinematic variable plotted ($m_{Vh}, p_T^{jet}, ...$), the EWK template in the non-isolated region is scaled by the appropriate region and lepton flavour scale factor. The difference between the data and EWK templates as a function of the respective kinematic variable is then the QCD multijet template.

An example is shown by Figure 16.1b, which shows for the same non-isolated 1-tag resolved 50 GeV $< m_h <$ 200 GeV region the E_T^{miss} distribution post scaling. The discrepancy between the data and EWK MC backgrounds is the direct result of the QCD multijet process, and so the QCD multijet template can be estimated by this difference. This is shown in the lower panel of Figure 16.1b.

Following this, the extracted QCD multijet template from the non-isolated region is then imported to the isolated region. Unfortunately the normalisation of the multijet template must be corrected prior to being fed to the Binned Profile Likelihood fit used in the hypothesis testing stage of the analysis. As such a final Binned Poisson Likelihood fit is performed, using the imported QCD multijet template and the EWK template in the isolated region for variable $\mathcal{O}$, to the data template in the corresponding region.

Figure 16.1c shows the muon m_{Vh} distributions post fit, for the isolated 1-tag resolved 50 GeV $< m_h <$ 200 GeV region. The blue template represents the combined EWK background, whilst the pink represents the QCD multijet template. For the final Binned Profile Likelihood fit used in the hypothesis testing (see Section 9), the QCD multijet

[1] The ROOT `TFractionFitter` package was used to perform the Poisson Likelihood fit between data and EWK MC templates.

[2] $E_T^{\text{miss}} > 200$ GeV was chosen because the expected QCD multijet contribution is negligible. Systematics relating to this choice of fit region are considered within the analysis, see section 18.

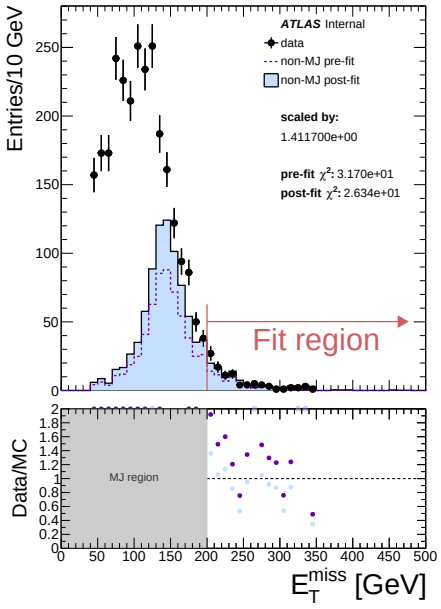

(a) E_T^{miss} fit between data and EWK MC templates in the 1-tag resolved 50 GeV $< m_h <$ 200 GeV region for the muon channel.

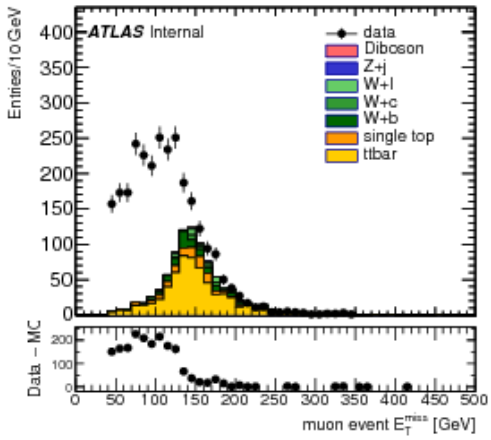

(b) E_T^{miss} distribution for muons in the non-isolated region for events with one b-tagged jet and 50 GeV $< m_h <$ 200 GeV. The scale factor from the E_T^{miss} fit for the EWK background has been applied.

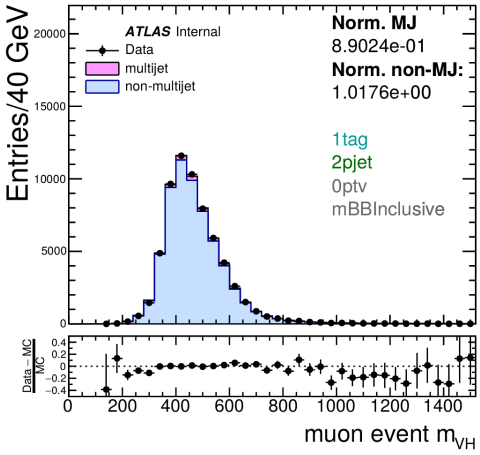

(c) m_{Vh} distribution in the isolated region for muons events with one b-tagged jet and 50 GeV $< m_h <$ 200 GeV, where the QCD multijet template imported from the non-isolated regime (pink), and EWK template from the isolated region has been fitted to data.

Figure 16.1.: Diagrammatic breakdown of the 1-lepton multijet Template Method.

templates for the electron and muon channels are combined for each region. A QCD template is generated in this fashion for each fit region summarised in Table 17.1.

To account for systematic uncertainties relating to the methodology of the QCD multijet derivation, trigger biases, electroweak background modelling, and Poisson Likelihood fit, nuisance parameters are assigned to both shape and normalisation variations of the multijet m_{Vh} template. These systematics are described in more detail in Section 18.2.

Chapter 17.

Fit Model

Within the fiducial region of phase space defined by the event selection of the analysis, and reconstructed objects, the data, SM MC, data-driven multijet estimate, and signal MC are used to test the background only hypothesis (H_0) via a Binned Profile Likelihood Fit using the m_{Vh}^{T} variable for the 0-lepton channel, and the m_{Vh} variable for the 1-/2-lepton channels. Fits are performed individually for the 0-/1-/2-lepton channels in addition to combined 0+2-lepton fits for the HVT Z' and AZh signal, 0+1-lepton for the HVT W' signal interpretations, and a 0+1+2-lepton combined fit sensitive to the $V' = W' + Z'$ HVT signal.

However, in order to run this hypothesis testing, two key components are needed. The first is the *fit model*, which refers to the signal and control regions that are used by the Binned Profile Likelihood fit. The second is the collection of $m_{Vh}^{(T)}$ distributions that represent the HVT/AZh signal, SM backgrounds, and the data, which are referred to as *fit templates* from here on in. These two components are detailed below, in addition to binning procedures used to bin the fit templates, and how the systematic templates are manipulated during the fit process.

17.1. Fit Regions

In the following analysis four criteria are used to define a series of kinematically bounded regions referred to as *fit regions*. These regions are orthogonal to one another, meaning that events within each region are unique and not duplicated in the other regions. These four criteria are:

1. Number of Loose Leptons: The number of `VHLoose` leptons (see definition in Chapter 11) defines the 0-/1-/2-lepton categorisation of the event, where each category is completely unique, i.e. no overlapping of events.

Channel	Kinematic Region	Resolved	Boosted
0-LEPTON	Signal Region (m_h)	{1,2}-tag	{1,2}-tag×{0 add.}-tag
	Control Region (m_h)	Validation Region	Validation Region
1-LEPTON	Signal Region (m_h)	{1,2}-tag	{1,2}-tag×{0 add.}-tag
	Control Region (m_h)	{1,2}-tag	Validation Region
2-LEPTON	Signal Region (m_h)	{1,2}-tag	{1,2}-tag×{0 add.}-tag
	Control Region (m_h)	Validation Region	Validation Region
	Top $e\mu$ CR (110 GeV $< m_h <$ 140 GeV)	{1+2}-tag	Validation Region

Table 17.1.: Summary of HVT 0-/1-/2-lepton channel fit regions included within the Binned Profile Likelihood fit performed on the m_{Vh}^{T} and m_{Vh} distributions.

2. Higgs Candidate Mass (m_h): The invariant mass of the two small-R jet system in the resolved regime, or the invariant mass of the large-R jet in the boosted regime.

3. Number of b-tagged Jets: The n-tag category is defined by the number of b-tagged small-R jets for the resolved regime, or the number of tagged track-jets ghost associated to the large-R jet in the boosted regime. The boosted analysis also has an additional b-tagging identifier, depicted by the notation *n add. tag*, corresponding to the number of additional b-tagged track-jets unassociated to the large-R jet.

4. Lepton Flavour Composition (2-lepton): The 2-lepton channel is unique in that it can have either a same dilepton flavour event (ee or $\mu\mu$) or an opposite dilepton flavour event ($e\mu$).

The signal region (SR) is defined as the 110 GeV $< m_h <$ 140 GeV window for the 0-/1-lepton channels, and 100 GeV $< m_h <$ 145 GeV window for the 2-lepton channel. The sidebands around this mass window are then used to define the low mass, 50 GeV $< m_h <$ 110(100) GeV for the 0-/1-lepton (2-lepton) channels, and high mass, 140(145) GeV $< m_h <$ 200 GeV for the 0-/1-lepton (2-lepton) channels, control regions.

Due to the different production modes and the underlying physical differences between the HVT and 2HDM model, the fit regions passed to the Binned Profile Likelihood fit vary between the two interpretations. The fit regions for the HVT analysis are summarised by Table 17.1, whilst the AZh fit model is summarised by Table 17.2. Figure 17.1 diagrammatically summarises these regions as well.

Channel	Kinematic Region	Resolved	Boosted
0-LEPTON	Signal Region (m_h)	{1,2,3+}-tag	{1,2}-tag × {0 add.,1+ add.}-tag
	Control Region (m_h)	Validation Region	Validation Region
2-LEPTON	Signal Region (m_h)	{1,2,3+}-tag	{1,2}-tag×{0 add.}-tag, {1+2}-tag×{1+ add.}-tag
	Control Region (m_h)	Validation Region	Validation Region
	Top $e\mu$ CR (100 GeV $< m_h <$ 145 GeV)	{1+2, 3+}-tag	Validation Region

Table 17.2.: Summary of AZh 0-/2-lepton channel fit regions included within the Binned Profile Likelihood fit performed on the m_{Vh}^T and m_{Vh} distributions.

17.2. Fit Templates

For each region a series of fit templates are provided, originating from either MC or data. The possible templates that will be seen throughout this analysis are as follows:

- $\boldsymbol{t\bar{t}}$: Top-quark pair production.
- $\boldsymbol{V}$**+Jets** : SM vector boson production in association with jets. The selected jets, as per the Resolved/Boosted criteria, are truth tagged by a ΔR matching of the final state hadrons. The truth flavour labelled V+Jets event is then collected into 3 template categories:
  - V+HF = $Vbb + Vbc + Vcc$
  - V+hl = Vbl + Vcl
  - Vl = Vll
- **Single Top** : Top-quark production sub-divided into s-/t-channel and Wt associated production mechanisms, where these templates are merged into a single top template.
- **Diboson** : Diboson production for the WW, WZ, and ZZ processes.
- **SM Higgs (**$\boldsymbol{Vh}$**)** : Associated production of SM vector boson with Higgs boson as predicted by the SM.
- $\boldsymbol{t\bar{t}H}$: Top-quark pair production in association with SM Higgs.
- $\boldsymbol{t\bar{t}V}$: Top-quark pair production in association with SM vector boson.
- **Data:** Data points to which the hypothesis testing is performed.

- **Multijet 1-lepton Template** : Data-driven template estimate for the multijet in the 1-lepton channel only.

The truth labelling of the V+Jets process is obtained by ΔR matching final state hadrons from within the event record of the MC to the small-R jets in the resolved regime or ghost associated track-jets in the boosted regime. The label of the jet is assigned based on the flavour of the leading p_T hadron associated to the selected jets. If the leading hadron at the truth-level is a b-hadron then the jet is labelled b, if the leading hadron is a c-hadron then the jet is assigned as a c label, otherwise the jet is labelled a *light*-jet (l).

It should be noted, that due to the > 1 track-jet requirement in the boosted regime, an event categorised as a boosted event may only have a single truth flavour label for the V+Jets process. In this situation, the leading and sub-leading ΔR matched hadrons to the jet are used. This yields two truth labels for a single jet.

17.3. Binning

To maximise the performance of the hypothesis testing procedure, the binning of the $m_{Vh}^{(T)}$ fit discriminant is optimised to encapsulate the resonant peak of the signal within a single bin (or as close as possible). This maximises the localised excess within a given bin, thereby increasing the significance of an excess if one does exist. However, due to the different mass ranges of interest to the 2HDM and HVT signal, different binning strategies are used for two interpretations of the data within the Binned Profile Likelihood fit.

17.3.1. HVT

For all lepton channels and analysis regions the $m_{Vh}^{(T)}$ distributions are initially binned using 10 GeV bin widths. These distributions are rebinned using a series of iterative algorithms to form distributions with variable bin widths. Various algorithms are used, however the underlying procedure iteratively merges bins from right to left in $m_{Vh}^{(T)}$ based on an array of criteria.

Table 17.3 summarises the bin widths used in the 0-lepton channel for various m_{Vh}^{T} intervals. Before a bin of the pre-defined width is formed, the bin must have a statistical error of less than 75%.

m_{Vh}^{T}	**Bin width (Δh)**
0-1000 GeV	100 GeV
1000-1200 GeV	200 GeV
1200-1500 GeV	300 GeV
1500-2200 GeV	700 GeV
2200+ GeV	1000 GeV

Table 17.3.: Summary of the m_{Vh}^{T} binning used in the 0-lepton channel.

In the 1-lepton channel the bin widths are defined by the resolution of the invariant mass of the $V + h$ system, $\sigma_{m_{Vh}}$, which is a function of m_{Vh}:

$$\Delta h = \sigma_{m_{Vh}}(m_{Vh}) = 40 + \left(\frac{115}{2300}\right).(m_{Vh} - 500) \tag{17.1}$$

In addition to this, for the signal (control) regions the bin must have least 0.05 (50) background events and an error on the MC/data-driven background that is smaller than 15 (70)%, before the bin is formed.

In the case of the 2-lepton channel, the m_{Vh} binning strategy given by equation 17.1 is used for both the resolved and boosted SRs. In the case of the boosted signal region twice the bin width is used. For the control regions, the bins are iteratively merged to a width of 250 GeV checking that the event yield prediction from the background exceeds 0.05. If this condition is not met then the bin is extended beyond the 250 GeV width until this condition is met.

17.3.2. *AZh*

A variable binning strategy is used in all channels and analysis regions for the AZh interpretation, starting from a $m_{Vh}^{(T)}$ distribution with 10 GeV bin widths. Table 17.4 summarises the number of bins used by each region of the fit, constrained to the $m_{Vh}^{(T)}$ range of 200–2200 GeV. In the case of the 0-lepton channel, the m_{Vh}^{T} bins are equidistant with a total number of bins given by the aforementioned table, however during the merging process the bins are required to have a statistical error $< 20\%$. In the 2-lepton channel, a variable bin width defined by resolution of the 2HDM signal is used as a function of m_{Vh}, but each bin must have a statistical error $< 20\%$.

Region	Number of bins	
	2 lepton	0 lepton
Resolved SR		
1 tag	28	14
2 tag	51	14
3+ tag	9	8
Merged SR		
1 tag, 0 add. tag	16	9
2 tag, 0 add. tag	6	8
1 tag, 1+ add. tag	-	8
2 tag, 1+ add. tag	-	4
1+2 tag, 1+ add. tag	10	-
Top-$e\mu$ region		
1+2 tag	7	-
3+ tag	4	-

Table 17.4.: Number of bins in the 200–2200 GeV $m_{Vh}^{(T)}$ range for the AZh binned profile likelihood fit.

17.4. Treatment of Systematics

17.4.1. Smoothing

Shape systematics are propagated to the fit discriminant as either variations on the event weights, or by re-selecting events after altering the underlying kinematic properties of the event. Flavour tagging systematics are an example of the former, whilst the JES uncertainties alter the underlying jet kinematics. In situations when the statistical population in each $m_{Vh}^{(T)}$ bin is small, the systematic is highly prone to statistical fluctuations.

To prevent these fluctuations from having any bearing on the fit, two *smoothing* algorithms are used. The first algorithm identifies all stationary points ($dh/dm_{Vh}^{(T)} = 0$, where h represents the histogram) in the systematic-over-nominal ratio, and merges bins between these stationary points, starting with those closest in distance in the x-axis ($m_{Vh}^{(T)}$). The output from this algorithm is a ratio of the systematic variation to the nominal $m_{Vh}^{(T)}$ distribution with a single stationary point. The second algorithm takes this rebinned histogram and merges bins from right to left in $m_{Vh}^{(T)}$ till the statistical error is 5% or less.

17.4.2. Averaging and Symmetrising Systematic Shapes

Typically most $m_{Vh}^{(T)}$ shape systematics come with a $\pm 1\sigma$ variation around the nominal prediction, for example the Jet Energy Scale uncertainties. These are referred to as *2-sided asymmetric* uncertainties, because each up/down variation induces a shape change that is inverse of its partner, but not necessarily equal in magnitude. However, as in the case of the MadGraph5+Pythia8 vs Sherpa 2.2.1 MC systematics for the V+Jet background, some shape systematics are *one-sided*; either a $+1\sigma$ or -1σ variation, but not both. For a physically meaningful interpretation of the nuisance parameter pulls for these type of systematic variations, the one-sided systematics are symmetrised around the nominal prediction generating a *2-sided symmetric* uncertainty.

In some cases, the $+1\sigma$ and -1σ variations of a systematic variation yield approximately the same shape distortion effect on the nominal $m_{Vh}^{(T)}$ shape. This yields a degeneracy in the minimisation process of the profile likelihood fit, because both the positive and negative scan directions of the nuisance parameter θ_k during the minimisation process, yield approximately the same signed change in the likelihood function (both directions increase or decrease the likelihood function). To prevent this minimisation issue, the $+1\sigma$ and -1σ variations are averaged after being smoothed (as outlined in Section 17.4.1), and then symmetrised around the nominal prediction, thereby generating a 2-sided symmetric uncertainty.

17.4.3. Pruning

Systematics that have a negligible impact on the analysis are removed, or *pruned*, from the analysis according to the procedure below:

- Neglect normalisation uncertainty if the variation is $< 0.5\%$
- Neglect shape uncertainties if fewer than two bins deviate from the nominal by more than 1%, after normalising the nominal and systematic templates to the same area. If it is an asymmetric uncertainty, then both sides must pass this condition.

This pruning procedure is applied to the templates that pass the *smoothing*, and *averaging and symmetrisation* steps outlined in Sections 17.4.1 and 17.4.2. This is done for each fit region in the analysis.

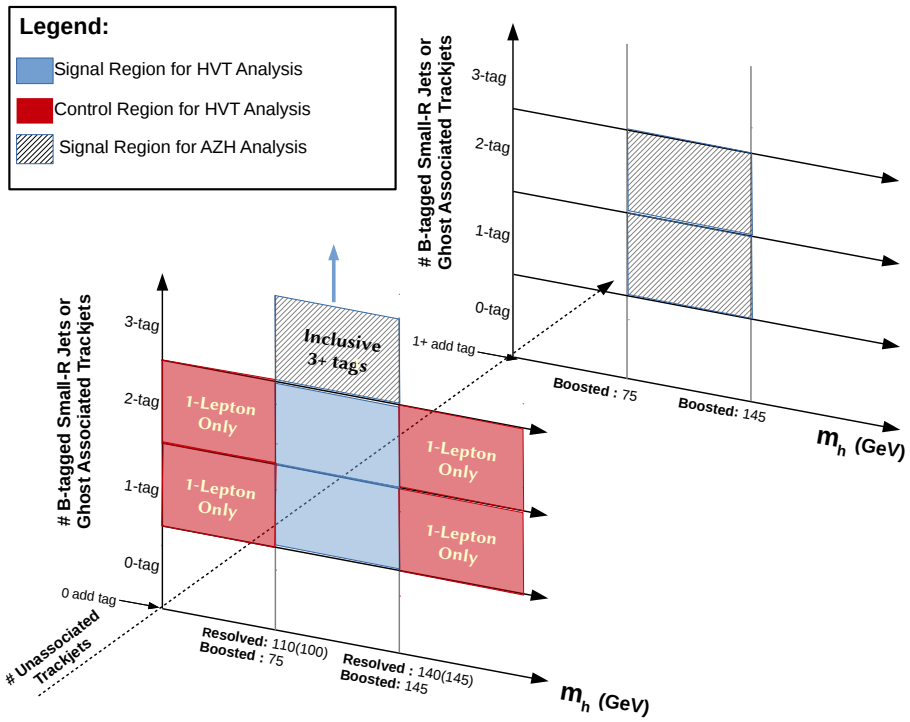

(a)

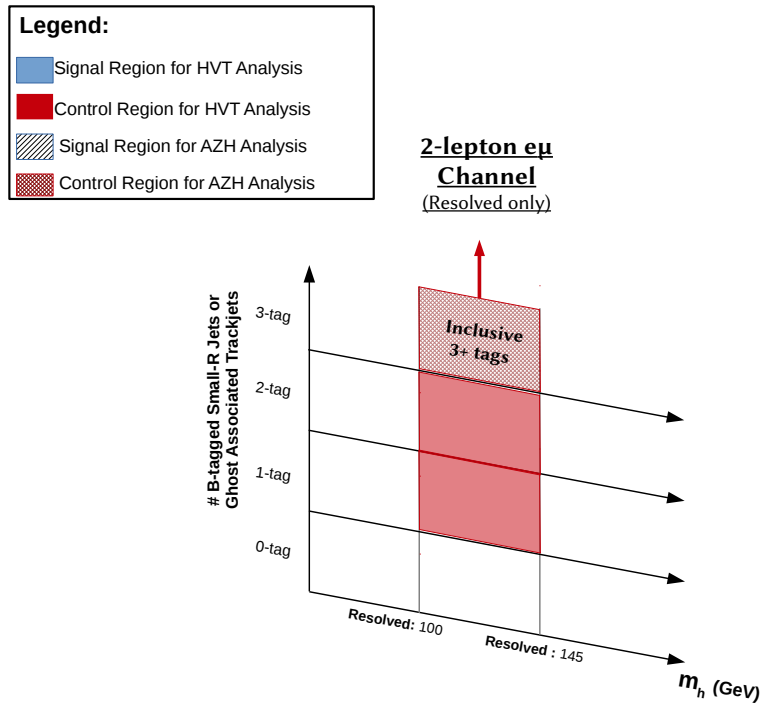

(b)

Figure 17.1.: Analysis fit regions for the PRSR recycling scheme used by the 0-/1-/2-lepton AZh and HVT analyses. SRs common to the AZh and HVT analysis are shown in solid blue, whilst hatched blue are unique to the AZh analysis. CRs are labelled red, where again hatched red regions are unique CRs to the AZh analysis. For the 2-lepton channel, an $e\mu$ region with a 100 GeV $< m_h <$ 145 GeV mass cut is used as a CR.

Chapter 18.

Systematics & Corrections

The following section details the sources of systematic uncertainty taken into account. These systematic uncertainties can be sub-divided into three primary categories: experimental, multijet estimation, and background/signal MC systematics.

The experimental uncertainties correspond to the sources of systematic error originating from the apparatus used to collect the data, i.e. the ATLAS detector and the LHC. As such the systematic errors are concerned with encompassing our uncertainty relating to the object reconstruction (jets, electron, muons, MET, etc), triggering, b-tagging, luminosity, and pile-up estimation/rejection. These uncertainties are summarised within Section 18.1.

Due to the MC/data-driven methodology used to derive the multijet templates for the 1-lepton channel, the systematic uncertainties related to this fit template are correlated with the experimental uncertainties above, the modelling uncertainties below, but also include a systematic source of error on the methodology used to derive the template shape and normalisation. These uncertainties are summarised in Section 18.2.

The last sub-section explains the methodology used to derive the theoretical uncertainties on the dominant SM background processes and the HVT/AZh signal. These uncertainties stem from the choice of Monte Carlo generator, and the underlying phenomenological choices made in order to model the physical process. These are explained in Section 18.3.

18.1. Experimental Uncertainties

The experimental uncertainties are sub-divided into seven major classifications:

- **Event:** Systematics relating to the luminosity and pile-up re-weighting on the event level.
- **Electrons:** Trigger and reconstruction related uncertainties.

- **Muons:** Reconstruction, trigger, and track-to-vertex uncertainties.
- **Small-R Jets:** Reconstruction (energy scale/resolution), pile-up correction/rejection, and flavour-tagging related uncertainties.
- **Large-R Jets:** Reconstruction uncertainties, specifically related to the energy scale/resolution and mass resolution.
- **Track Jets:** Flavour tagging related uncertainties.
- **MET:** Trigger efficiencies, soft-term, and MET energy scale uncertainties.

The systematics encompassed by each classification, and a short description of each systematic are given by Table 18.1. A brief description of the dominant experimental uncertainties is given below.

The largest experimental uncertainties found to impact the parameter of interest, μ, within the following analysis were the calibration and resolution of the small/large-R jet energy, calibration and resolution of the large-R jet mass, and the flavour-tagging systematics.

In the case of the small-R jets, uncertainties pertaining to the Jet Energy Scale (JES) arise from in-situ analyses (Z+Jets, γ+Jets, and multijet balance), η inter-calibration (modelling, statistics,...), single-hadron behaviour in high-p_T jets, pile-up corrections (dependent on $\langle\mu\rangle$ & number of primary vertices), and ATLAS fast simulation calibration. Additional uncertainties concerning the flavour composition (light-quark vs gluon jet composition) [136], flavour response (response of detector to light-quark and gluon jets), punch-through, and b-jet response are also incorporated [110, 137–140]. These uncertainties are propagated to the E_T^{miss} calculation.

The systematic uncertainties related to the large-R jet energy and mass scale/resolution are obtained by comparing the ratio of the calorimeter-based to track-based measurements in di-jet data and simulation [113, 114, 141].

The flavour-tagging efficiency and its corresponding systematic uncertainties are evaluated for b-jets, c-jets, and light-jets using $t\bar{t}$, $W + c$, and di-jet events, respectively. Uncertainties related to either the b-/c-jet tagging efficiency or light-jet misidentification stem from MC modelling of $t\bar{t}$, single top Wt associated production, and W+Jets processes, in addition to experimental uncertainties like pile-up, jet energy scale, electron and muon reconstruction/identification/isolation efficiencies, etc. These uncertainties are implemented as event-weight systematics within the analysis [129, 142–144].

The uncertainty in the 2015+2016 integrated luminosity is derived, following a methodology similar to that detailed in Ref. [145], from a preliminary calibration of the luminosity scale using x–y beam-separation scans performed in May 2016. This is implemented as a constrained normalisation NP with a prior of 3.2%, which acts on all data and MC templates across all analysis fit regions simultaneously.

Systematic uncertainty	Short description	Reference
Event		
Luminosity	Uncertainty on total integrated luminosity	Ref. [145, 146]
PRW_DATASF	pile-up re-weighting uncertainty	Ref. [147]
Electrons		
EL_EFF_Trigger_TOTAL_1NPCOR_PLUS_UNCOR	trigger efficiency uncertainty	-
EL_EFF_Reco_TOTAL_1NPCOR_PLUS_UNCOR	reconstruction efficiency uncertainty	-
EL_EFF_ID_TOTAL_1NPCOR_PLUS_UNCOR	ID efficiency uncertainty	-
EL_EFF_Iso_TOTAL_1NPCOR_PLUS_UNCOR	isolation efficiency uncertainty	-
EG_SCALE_ALL	energy scale uncertainty	Ref. [148, 149]
EG_RESOLUTION_ALL	energy resolution uncertainty	Ref. [148, 149]
Muons		
MUON_EFF_TrigStatUncertainty MUON_EFF_TrigSystUncertainty	trigger efficiency uncertainty	-
MUON_EFF_STAT MUON_EFF_SYS	reconstruction and ID efficiency uncertainty for muons with $p_T > 15$ GeV	Ref. [116]
MUON_EFF_STAT_LOWPT MUON_EFF_SYST_LOWPT	reconstruction and ID efficiency uncertainty for muons with $p_T < 15$ GeV	Ref. [116]
MUON_ISO_STAT	isolation efficiency uncertainty	Ref. [116]

MUON_ISO_SYS		
MUON_TTVA_STAT	track-to-vertex association efficiency uncertainty	Ref. [150]
MUON_TTVA_SYS		
MUONS_SCALE	energy scale uncertainty	Ref. [116]
MUONS_ID	energy resolution uncertainty from inner detector	Ref. [116]
MUONS_MS	energy resolution uncertainty from muon system	Ref. [116]
Small-R Jets		
JET	energy scale uncertainty split into 21 components	Ref. [137–139]
JET_JER_SINGLE_NP	energy resolution uncertainty	Ref. [110]
JvtEfficiency	JVT efficiency uncertainty	-
FT_EFF_Eigen_B		
FT_EFF_Eigen_C	b-tagging efficiency uncertainties ("BTAG_MEDIUM"): 3 components for b-jets, 4 for c-jets and 5 for light-jets	Ref. [129, 142–144]
FT_EFF_Eigen_L		
FT_EFF_Eigen_extrapolation	b-tagging efficiency uncertainty on the extrapolation to high-p_T jets	Ref. [129, 142–144]
FT_EFF_Eigen_extrapolation_from_charm	b-tagging efficiency uncertainty on tau jets	Ref. [129, 142–144]
Large-R Jets		
SysJET_Comb_Baseline_Kin		Ref. [113, 114, 141]
SysJET_Comb_Modelling_Kin	energy scale uncertainties (p_T and mass scales are fully correlated)	
SysJET_Comb_TotalStat_Kin		
SysJET_Comb_Tracking_Kin		

FATJET_JER	energy resolution uncertainty	-
FATJET_JMR	mass resolution uncertainty	-
Track Jets		
FT_EFF_Eigen_B FT_EFF_Eigen_C FT_EFF_Eigen_L	b-tagging efficiency uncertainties ("BTAG_MEDIUM"): 3 components for b-jets, 4 for c-jets and 5 for light-jets	Ref. [129, 142–144]
FT_EFF_Eigen_extrapolation	b-tagging efficiency uncertainty on the extrapolation to high-p_T jets	Ref. [129, 142–144]
FT_EFF_Eigen_extrapolation_from_charm	b-tagging efficiency uncertainty on tau jets	Ref. [129, 142–144]
MET		
METTrigStat METTrigTop/Z	trigger efficiency uncertainty	-
MET_SoftTrk_ResoPara	track-based soft term related longitudinal resolution uncertainty	Ref. [128]
MET_SoftTrk_ResoPerp	track-based soft term related transverse resolution uncertainty	Ref. [128]
MET_SoftTrk_Scale	track-based soft term related longitudinal scale uncertainty	Ref. [128]
MET_JetTrk_Scale	track MET scale uncertainty due to tracks in jets	Ref. [128]

Table 18.1.: Summary of the names and meanings of the experimental systematic uncertainties.

18.2. Multijet Estimate Systematics

Systematic uncertainties on the data-driven QCD multijet templates derived via the template method (see Chapter 16) are divided into a normalisation and shape component.

As outlined in Chapter 16, a Poisson Likelihood fit in E_T^{miss} is performed in the isolated region using the combined EWK background and the QCD multijet template extracted from the non-isolated region. This step is designed to correct the normalisation of each multijet template prior to being fed to the hypothesis testing stage of the analysis. This likelihood fit however has an associated error, therefore by varying the template fit result within its associated error by $\pm 1\sigma$, an uncertainty on the multijet normalisation can be obtained.

It should be noted however, that the 1-tag resolved muon channel is the only region in which the MJ normalisation is non-negligible, and so the only region where the normalisation error is small enough that the above methodology yields a reliable variance. In this region the method demonstrated that the relative contribution of the multijet process to the 1-tag resolved muon channel inclusive in m_h was $2.7\% \pm 1.0\%$. This corresponds to an uncertainty of $\approx 37\%$. However, since this fit does not consider any systematic variations of the EWK background, a conservative error of $\pm 50\%$ is applied to the multijet process. This is assigned to the fit as a constrained nuisance parameter θ_{QCD} with an associated prior of $\sigma_{\text{QCD}} = 50\%$, acting on the multijet cross-section across all fit regions in the analysis simultaneously.

In the case of the shape systematics three variations are considered, these are summarised below.

18.2.1. Trigger Bias In Non-Isolated Region

The template method used the lowest unprescaled trigger for each data period, therefore a correction is applied to account for any inefficiency inherent to the lowest unprescaled electron triggers. The correction is derived by performing a fit to the ratio of the highest p_T^e threshold trigger to the lowest p_T^e threshold trigger for $p_T^e > 150$ GeV. This function is used to re-weight the events as a function of p_T^e in order to correct the distribution for any trigger bias. The systematic is taken as the difference between the corrected and uncorrected m_{Vh} distribution.

18.2.2. Relative EWK Background Scaling

The EWK backgrounds are considered as a single entity throughout the multijet template method. However, it is known from similar analyses, older iterations of the HVT analysis, and preliminary fit tests of this HVT analysis that the dominant $t\bar{t}$ and W+HF backgrounds are scaled by approximately 0.9 and 1.6, respectively. These scale factors are applied to the EWK background during the multijet derivation steps. The variation induced in the multijet template is then considered a 1σ variation. This is symmetrised within the fit.

18.2.3. EWK $E_T^{\text{miss}} > 200$ GeV Normalisation Correction Uncertainty

The uncertainty relating to the $E_T^{\text{miss}} > 200$ GeV template fit of the EWK backgrounds in the non-isolated region, is measured by varying the fit ranges. This varies the scale factor applied to the EWK background in the non-isolated region. It was observed that by varying the fit ranges in E_T^{miss} from $>$ 160–300 GeV, and performing the non-isolated template fit using the m_T^W distribution in the $m_T^W > 70 - 90$ GeV tails, the largest difference in the scale factors was $\pm 20\%$.

Therefore, after fitting the EWK template fit to data using the $E_T^{\text{miss}} > 200$ GeV fit range in the non-isolated region, the derived EWK scale factor is varied by $\pm 20\%$. The resulting scaled EWK backgrounds are propagated throughout the template method, and the resulting multijet template under this variation defines a $\pm 1\sigma$ systematic variation.

18.3. Modelling Uncertainties

Uncertainties in the m_{Vh} and m_{Vh}^T distributions are assigned to the dominant SM backgrounds, $t\bar{t}$ and V+Jets for the 0-/1-/2-lepton channels and single top for the 1-lepton channel, by comparing the nominal MC samples described in Chapter 10, to a number of alternative MC generators. These comparisons are made for each fit region detailed in Chapter 17, with the exception that the b-tag categories are summed. The event selection described in Chapters 13-15 is applied prior to deriving the systematics.

The uncertainty on each process is divided into two components: shape and normalisation/acceptance effect. These are discussed below.

Shape Systematic The shape systematic corresponds to an event-by-event re-weighting function derived by fitting a scalar function dependent on $m_{Vh}^{(T)}$ to the normalised ratio of the alternative MC configuration, referred to as the *variation sample*, over the nominal

sample, this is defined as $R(m_{Vh}^{(T)}) = h_i^{\text{var}}/h_i^{\text{nom}}$. Here h_i^{nom} corresponds to the i^{th} $m_{Vh}^{(T)}$ bin of the nominal MC sample, and similarly for the variation sample.

It should be noted that all histograms ($h_i^{\text{nom/var}}$) prior to the comparisons are iteratively binned from right to left requiring the bin error to be less than 5(10)% (MadGraph5_aMC@NLO+Pythia8 comparisons of the W/Z+HF background suffered from poor statistics, therefore the requirement was loosened). In some cases the background yield within a given fit region is too small for a reasonable shape estimate to be derived, in such a scenario no shape systematic exists, and only a normalisation/acceptance uncertainty exists (see next section).

A scalar function is fit to the ratio $R(m_{Vh}^{(T)})$, due to the finite statistics of the nominal and variation MC samples. To be precise, the true $m_{Vh}^{(T)}$ distribution is defined by a combination of the SM Lagrangian and empirical hadronisation/MPI/UE models, $\tilde{h}_i^{\text{nom/var}}$, however it is sampled to some finite statistical precision via the MC approach. This yields the sampled distributions previously defined ($h_i^{\text{nom/var}}$), meaning that the ratio $R(m_{Vh}^{(T)})$ suffers from statistical fluctuations. Consequently, the ratio is smoothed by fitting a series of functional forms constructed of terms $\zeta = \ln(m_{Vh}^{(T)}), m_{Vh}^{(T)}, (m_{Vh}^{(T)})^{-1}, (m_{Vh}^{(T)})^{1/2}$ raised to the n^{th} power according to $f^n(m_{Vh}^{(T)}) = \sum_a^{n=[1,2]} c_a \zeta^a$ (c_a is a scalar coefficient).

Since the true distribution of $R(m_{Vh}^{(T)})$ is not known *a priori*, a wide array of functional forms are fit to the ratio. The functional form used as the shape systematic within the analysis is then chosen by forming a *precedence* table that ranks the quality of the fit. This table is constructed as follows:

S.1 Any functional form that yields a fit result of $\chi^2/n_{\text{dof}} < 0.5$ is ranked in descending order with the function closest to $\chi^2/n_{\text{dof}} = 0$ at the top (every bin in the distribution must have an error of $< 10\%$).

S.2 All $n = 1$ functional forms are appended to the list, ordered according to how close the χ^2/n_{dof} is to 1.

S.3 All $n = 2$ functions are then interwoven with the $n = 1$ fits in the list by placing any $n = 2$ fit above a given $N = 1$ fit entry in the list, if the χ^2/n_{dof} is closer to unity by 10% or more.

The $\chi^2/n_{\text{dof}} = 1$ best fit criteria is chosen because under the hypothesis that a fit function, $f^n(m_{Vh}^{(T)})$, does represent the true distribution from which $R(m_{Vh}^{(T)})$ has been sampled, the χ^2 fit values should follow a χ^2 distribution ($f(\chi^2, n_{\text{dof}})$). This distribution has a mean of $\langle f(\chi^2, n_{\text{dof}})\rangle = n_{\text{dof}}$, therefore the expected fit result is $\chi^2/n_{\text{dof}} = 1$, if the hypothesised true form of the ratio is correct. A full explanation of this rationale,

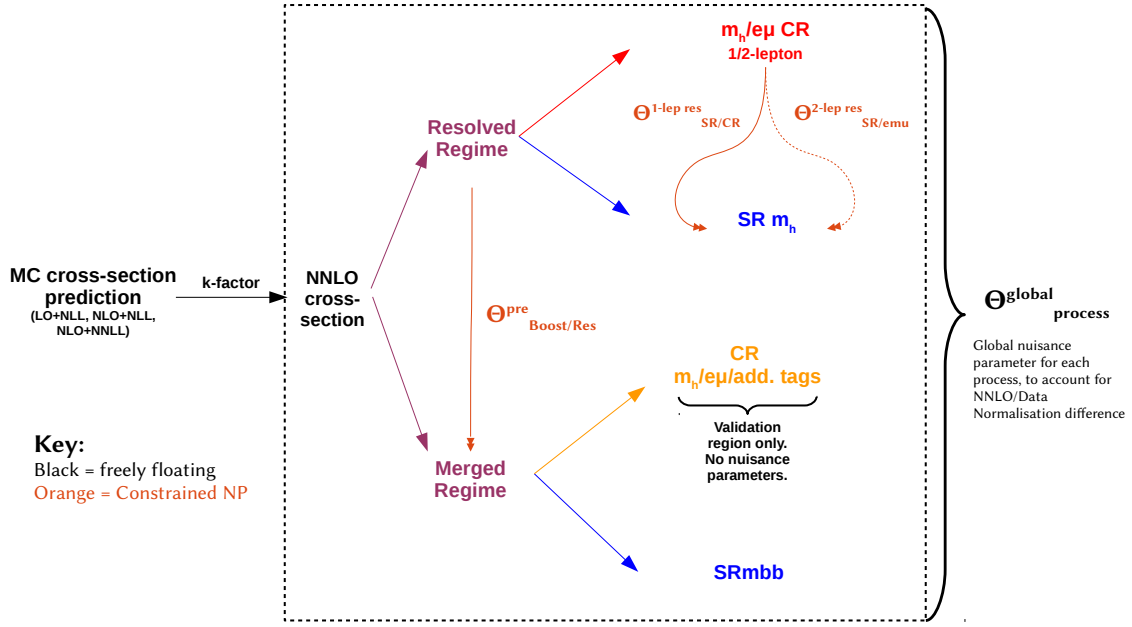

Figure 18.1.: Illustration of the acceptance variation nuisance parameters, designed to allow the relative normalisation of any two coupled regions to vary within the assigned prior.

alternative smoothing procedures, and a discussion of how the χ^2 fit value can be used to rank the quality of a fit, can be found in Appendices A–B

It should be noted that the χ^2 minimisation process attempts to obtain a χ^2 that is as close to 0 as possible in each fit instance. Since the errors on each bin in the ratio $R(m_{Vh}^{(T)})$ are constrained to be less than 5(10)%, the fear of obtaining a $\chi^2/n_{\text{dof}} \to 0$ fit result, due to an overestimation of the bin variance, is highly suppressed. Therefore, it is possible that a fitted function yields a χ^2/n_{dof} closer to 0 than to unity, and because the order of the fit functions is limited to $n = [1, 2]$, there are insufficient degrees of freedom in the functional form to capture random statistical fluctuations. This is why Step **S.1** in the above procedure exists; upon inspection some fits closer to 0 were better than those closer 1, these however are rare occurances.

Acceptance & Normalisation Priors The event yield prediction for a given process within a single fit region, as outlined in Section 17, is obtained from the MC generator. Therefore, this event yield is model dependent, and so an associated theoretical uncertainty was derived. This uncertainty is evaluated by using the same MC-to-MC comparisons to

measure variations in the event yield. Two types of uncertainty exist: a normalisation and an acceptance uncertainty.

Figure 18.1 diagrammatically summarises the normalisation degrees of freedom between the various fit regions of the HVT and AZh analysis, when assessing MC uncertainties. The MC predicted event yield, whether it be the nominal or variation sample, is normalised to a process specific fixed order NNLO cross-section prediction prior to the application of the event selection, as depicted by the *k-factor* labelled black arrow in Figure 18.1. The events are then distributed to the various fit regions according to the event selection and fit model given by Chapters 13-15 and Chapter 17, respectively. The Black/Blue/Red single arrow headed lines depict how the total number of events at the pre-event selection stage are divided amongst the various fit regions.

A global nuisance parameter denoted as $\Theta^{\text{global}}_{\text{process}}$ (see figure), is assigned to each physical process ($t\bar{t}$, single top, etc). This nuisance parameter is either freely floating, or constrained using a prior. This nuisance parameter acts upon all templates of the process in all fit regions in a correlated manner, and is designed to account for any disagreement between the fixed order NNLO cross-section and the data.

In the case of the constrained global nuisance parameter, the prior is derived by comparing the event yield predictions, inclusive of all fit regions, from the nominal and alternative MC samples. The prior is then calculated via the formula:

$$\sigma_{w^{\text{global}}_{\text{accept}}} = \sqrt{\sum_{i}^{M} \left(\frac{|N_P^{\text{var}^i} - N_P^{\text{nom}}|}{N_P^{\text{nom}}} \right)^2}, \tag{18.1}$$

where $\sum_i^M$ corresponds to the sum over the M MC-to-MC 2-point comparisons (e.g. 4 for $t\bar{t}$), $N_P^{\text{nom}} = \sum_q^{\text{regions}} n_{P;q}$ corresponds to the event yield inclusive of all fit regions q, and the superscripts 'nom' and 'var' denote the nominal and alternative MC samples. Subscript P denotes the process ($t\bar{t}$, V+Jets, ...). This type of nuisance parameter is known as a *normalisation* nuisance parameter, and the prior is referred to as a *normalisation prior*.

The distribution of the fixed order NNLO normalised event yield amongst the various fit regions is also dependent on the MC generator. To account for this uncertainty, nuisance parameters designed to allow the relative normalisation of two coupled regions, denoted as $R = A/B$, to change, are introduced to the fit. These are depicted by the orange double headed arrows in Figure 18.1, where the direction of the arrows denotes the region on which the nuisance parameter is applied. For example the $\Theta^{\text{res}}_{\text{SR/CR}}$ allows the relative ratio of the event yield between the resolved m_h SR and m_h CR to change, by altering the event yield of the m_h SR.

The coupled regions are as follows:

- $\boldsymbol{R = \frac{m_h^{\text{resolved}}\,\textbf{SR}}{m_h^{\text{resolved}}\,\textbf{CR}}}$: Relative ratio of Resolved m_h SR to Resolved m_h CR for the 1-lepton analysis. The 0-/2-lepton analyses do not use the Resolved m_h CRs.
- $\boldsymbol{R = \frac{\textbf{0-lepton}}{\textbf{1-lepton}}}$: Relative ratio of 0-lepton event yield prediction inclusive of all 0-lepton fit regions, to the 1-lepton event yield prediction inclusive of all fit regions. All fit regions internal to the individual lepton channels are considered correlated.
- $\boldsymbol{R = \frac{\textbf{0-lepton}}{\textbf{2-lepton}}}$: Relative ratio of 0-lepton event yield prediction inclusive of all 0-lepton fit regions, to the 2-lepton event yield prediction inclusive of all fit regions. All fit regions internal to the individual lepton channels are considered correlated.
- $\boldsymbol{R = \frac{\textbf{Resolved}}{\textbf{Boosted}}}$: Relative ratio of the resolved event yield prediction to the boosted event yield prediction. All regions within the resolved or boosted regime are considered 100% correlated.
- $\boldsymbol{R = \frac{m_h^{\text{resolved}}\,\textbf{SR}(ee,\mu\mu)}{m_h^{\text{resolved}}\,\textbf{SR}(e\mu)}}$: The event yield ratio between the same flavour $(ee, \mu\mu)$ 2-lepton m_h SR and opposite flavour $(e\mu)$ m_h SR fit regions. Used only by the 2-lepton analysis for extrapolation uncertainty between the SR and $t\bar{t}$ background enriched CR.

Each nuisance parameter is constrained using a prior uncertainty ($\sigma_{w_{\text{accept}}}$) derived from the MC-to-MC comparisons, where a $\theta_{k,R} = \pm 1$ pull corresponds to a $1 \pm 1\sigma_{w_{\text{accept}}}$ scale factor on the physical process in the numerator region. The prior uncertainty is derived using the formula:

$$\sigma_{w_{\text{accept}}} = \sqrt{\sum_{i}^{M} \left(\frac{\left| \frac{n_A^{\text{var},i}}{n_B^{\text{var},i}} - \frac{n_A^{\text{nom}}}{n_B^{\text{nom}}} \right|}{\frac{n_A^{\text{nom}}}{n_B^{\text{nom}}}} \right)^2}, \tag{18.2}$$

where n corresponds to the total event yield for a given fit region denoted by the subscripts A or B, and M represents the total number of MC comparisons made for each physical process (see sub-sections 18.3.1 and 18.3.2). The superscripts *nom* & var, i denote the nominal MC and i^{th} variation samples. When multiple MC-to-MC comparisons are made ($M \geq 2$), the quadrature sum of the individual priors is taken. Physically this is interpreted as the percentage difference between the expected A/B (where A, B represent the phase space regions of the analysis) acceptance ratio observed using the nominal sample, and the variation sample.

In summary there exist two types of priors, those that are associated to a nuisance parameter that control the ratio of two regions (*acceptance priors*), and those that are associated to the normalisation of an entire physical process (*normalisation priors*). The

multiplicative scale factor extracted from the fitted nuisance parameter pull value is referred to as an *acceptance/normalisation factor*, from here on.

18.3.1. V+Jets

The nominal V+Jets prediction, as outlined by Chapter 10, uses the ME+PS generator Sherpa 2.2.1 interfaced with the NNPDF 3.0 NNLO PDF set. This default configuration provides a prediction for vector boson plus jets production at NLO accuracy at the ME level for up to two extra partons, and LO accuracy for three and four extra partons. The merging of additional parton multiplicities arising from the internal Sherpa 2.2.1 PS, is regulated by the MEPS@NLO merging technique [86].

The alternative samples used to assess the modelling uncertainties are:

- **MadGraph5_aMC@NLO+Pythia 8.186:** An alternative ME generator, MadGraph5_aMC@NLO using the NNPDF3.0(2.3)[1] NLO(LO) PDF set, is interfaced with an alternative PS generator, Pythia 8.186 using the A14 tune, offering a LO+LL accurate prediction for vector boson production in association with jets for up to four extra partons from the ME and 4+ partons from Pythia 8 at LL accuracy [151].
- **Sherpa 2.2.1 scale variations:** Configured in the same manner as the nominal V+Jets sample, the renormalisation μ_R and factorisation μ_F scales are varied up/down by a factor of 2 [151].
- **Sherpa 2.2.1 PDF variations:** Configured in the same manner as the nominal V+Jets sample, 100 NNPDF3.0 NNLO replicas and the central values of two alternative PDFs, MMHT2014NNLO 68%CL and CT14NNLO are available [151].
- **Sherpa 2.2.1 α_s(PDF) variations:** Configured in the same manner as the nominal V+Jets sample, the α_s value used by the nominal NNPDF3.0 NNLO PDF is varied up and down according to a variation of the μ_R scale by a factor of 2 [151].

These alternative samples define two sets of available comparisons. The first comparison with MadGraph5_aMC@NLO+Pythia 8 convolves the ME and PS model variation into a single, one sided uncertainty. In essence it considers the hard scatter, parton shower, hadronisation, UE and MPI model variances simultaneously. The systematic shape difference (re-weighting function) is symmetrised around the nominal and applied as a 2-sided symmetric uncertainty in the binned profile likelihood fit.

[1] For $Z \to \nu\nu$ & $Z \to \tau\tau$, NNPDF2.3 is used.

Four further comparisons between the nominal and SHERPA 2.2.1 renormalisation scale, factorisation scale, PDF, and α_s PDF variations are also performed. In the case of the renormalisation and factorisation scale variations, the $\times 0.5$ and $\times 2$ variations straddle the nominal V+Jets prediction, therefore a two sided asymmetric systematic is used for each. The intrinsic α_s variations of the nominal NNPDF3.0 NNLO PDF set also form a two-sided asymmetric shape systematic.

For the PDF variations, an envelope comprised of the error arising from the 100 NNPDF replicas, and the two alternative PDF sets (CT14 NNLO & MMHT2015NNLO 68%CL) is formed to give rise to a two-sided asymmetric uncertainty. This envelope is derived by forming a composite spectrum made up of the three comparisons, where for each m_{Vh} or m_{Vh}^{T} bin the largest deviation of the three alternative spectrums from the nominal is used to construct the composite spectrum shape. This is done separately for the positive and negative directions relative to the nominal, in order to construct a two-sided asymmetric uncertainty. However, due to the small size of the PDF variations ($\sim$ 1–2% shape deviation on the m_{Vh} spectrum and event yield variation across all fit regions) relative to the scale variations, and the loss of shape information resulting from the envelope construction method, the PDF uncertainty is dropped from the analysis.

In short, the renormalisation, factorisation, and α_s PDF variations are controlled by three uncorrelated nuisance parameters from within the fit.

V+Jets NNLO Cross-Section

For the $W \to l\nu$+jets process the total SHERPA 2.2.1 and MADGRAPH5_aMC@NLO+PYTHIA 8 cross-section, averaged for all three lepton flavours, as predicted by the generator (20.07 nb and 16.71 nb) is scaled to the NNLO cross-section 20.08 nb.

For $Z \to ll$+jets the NNLO prediction is calculated using a dilepton invariant mass range of 66 GeV $< m_{ll} <$ 116 GeV, whilst SHERPA 2.2.1 and MADGRAPH5_aMC@NLO+PYTHIA 8 used a mass range of 40 GeV $< m_{ll}$. This mismatch in the phase space requires an extrapolation factor in order to map the generator prediction into the NNLO prediction regime. This extrapolation factor takes the form:

$$f = \frac{N_{\text{events}}(40 \text{ GeV} < m_{ll})}{N_{\text{events}}(66 \text{ GeV} < m_{ll} < 116 \text{ GeV})} \tag{18.3}$$

For SHERPA 2.2.1 the phase space extrapolation factor is $f = 1.105$, whilst for MADGRAPH5_aMC@NLO+PYTHIA 8 $f = 1.104$. Averaging over all three lepton flavours,

the total SHERPA 2.2.1 (MADGRAPH5_aMC@NLO+PYTHIA 8) generator cross-section, 2.160 nb (1.706 nb) is scaled to the NNLO cross-section 1.906 nb.

For $Z/\gamma* \to \nu\nu$+jets the total generator cross-section for SHERPA 2.2.1 is 11.69 nb and for MADGRAPH5_aMC@NLO+PYTHIA 8 is 9.259 nb. Since no NNLO prediction exists for $Z \to \nu\nu$, the $Z \to ll$ NNLO cross-section excluding $Z/\gamma*$ interferences, and imposing no dilepton invariant mass cuts, is corrected by the ratio of the branching fractions for $Z \to \nu\nu$ and $Z \to ll$ (using the PDG recommendation from Ref. [11]). This yields the $Z \to \nu\nu$ NNLO cross-section prediction of 11.37 nb, which the generator cross-sections for SHERPA 2.2.1 and MADGRAPH5_aMC@NLO+PYTHIA 8 are then scaled to.

Sherpa 2.2.1 Vs MADGRAPH5_aMC@NLO+PYTHIA 8 V+Jets Shape Systematics

Following the methodology outlined in Section 18.3, an m_{Vh} shape systematic for the V+Jets process is derived for each of the fit regions given by Tables 17.1 and 17.2. Furthermore, a shape systematic is derived for each of the three V+Jets truth flavour categories that enter into the fit, as outlined in Section 17.2, inclusive of the b-tagging categories, i.e. the b-tagging categories are summed together. Therefore a fit systematic is derived for each sub-process, in each of the defined kinematic regions of the fit.

An example of the 2-point MC-to-MC comparisons is given for the Z+hl processes in the 2-lepton channel for the resolved m_h SR, as shown by Figure 18.2. Each re-weighting function by definition corresponds to a 1-sided shape systematic, which is then symmetrised in to a 2-sided systematic according to Section 17.4.2.

Sherpa 2.2.1 Scale, PDF & α_s PDF V+Jets Shape Systematics

In addition to the MADGRAPH5_aMC@NLO+PYTHIA 8 to SHERPA 2.2.1 comparisons, internal variations of the SHERPA 2.2.1 MC configuration are also considered. The recommended methodology for implementing the scale, α_s PDF, and PDF variations as a shape uncertainty on some observable O, is to construct for each of these three sub-sets of uncertainty a corresponding asymmetric envelope around the nominal. These will be referred to as *component* envelopes from here on in.

Each envelope is constructed by forming a up/down spectrum that straddles the nominal prediction. This is done by taking the single largest deviation of all variations for a given $m_{Vh}^{(T)}$ bin. The component envelopes are then combined into a single asymmetric envelope

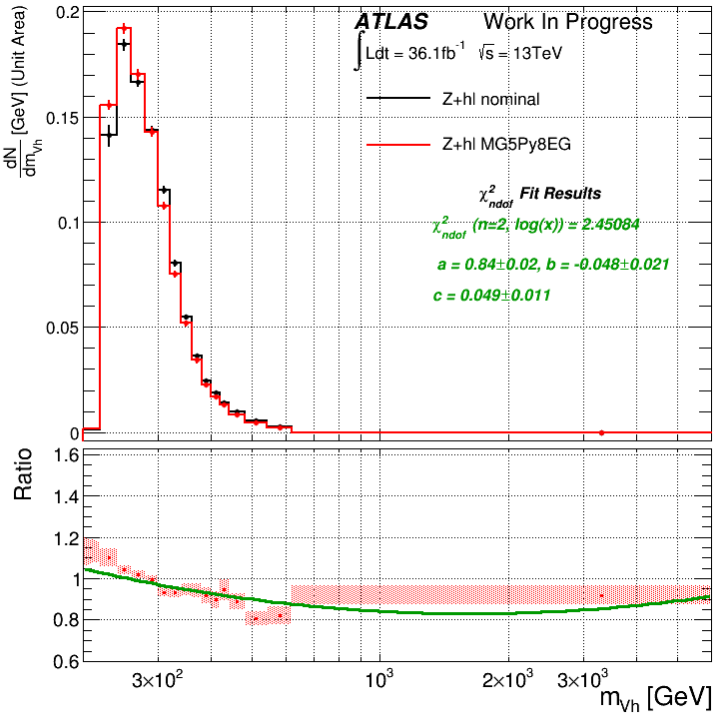

Figure 18.2.: The 2-lepton m_{Vh} unit normalised differential cross-section comparisons for the Z+hl sub-process in the resolved m_h SR window for SHERPA vs MADGRAPH5_aMC@NLO+PYTHIA 8. All comparisons are inclusive of the b-tag categories.

constructed by summing the squared difference between the nominal and the three envelope spectrum predictions.

Unfortunately, this methodology is not applicable when passing the systematics to a binned profile likelihood. This is because the component envelopes by construction are formed from multiple variations, meaning that the correlated bin-by-bin shape deviations induced by the individual scale, PDF, and α_s PDF variations are lost when forming an envelope.

This loss of information when forming the envelopes is shown by Figure 18.3 and Table 18.2, which together show the scale and PDF component envelopes (see figure) and the the percentage contribution of each individual variation to the two sides of the scale component envelope (see table). Figure 18.3a shows the envelopes when keeping the individual variations normalised to the MC generator cross-section, whilst Figure 18.3b unit normalises all variations prior to forming the envelope. As can be seen, the scale component

Individual Variation	+(−)ve Scale Envelope Edge (σ normalised)	+(−)ve Scale Envelope Edge (unit normalised)
W+HF $0.5 \times \mu_R$	36.8(0)%	21.1(5.3)%
W+HF $0.5 \times \mu_F$	0(0)%	5.3(0)%
W+HF $0.5 \times \mu_{F+R}$	63.2(0)%	47.4(26.3)%
W+HF $2 \times \mu_R$	0(26.3)%	5.3(5.3)%
W+HF $2 \times \mu_F$	0(0)%	0(0)%
W+HF $2 \times \mu_{F+R}$	0(73.7)%	21.1(63.2)%

Table 18.2.: Percentage breakdown of each of the scale envelope edges given by Figure 18.3.

envelope is a combination of many individual scale variations. This percentage breakdown also differs when comparing the pre/post unit normalised plots.

Therefore, passing these scale/PDF envelopes to the binned profile likelihood fit according to the methodology outlined in Section 9.1.1, would mean that the nominal $m_{Vh}^{(T)}$ template could be distorted to resemble a non-physical shape (one that does not represent a single physical/phenomenological parameter variation).

In summary, given that the envelope method does not retain the shape information of the individual variations, it was concluded that this method is invalid for a Binned Profile Likelihood fit. Therefore the renormalisation, factorisation, and α_s PDF variations are provided to the binned profile likelihood fit as a set of three nuisance parameters. It should be noted that the SHERPA 2.2.1 variations are not statistically independent, but rather they are the same event with an altered event weight to reflect the underlying variation. This means that the error on the ratio can not be calculated via standard error propagation without assessing the correlation of the events. Therefore the systematics are passed to the fit as binned systematic variations.

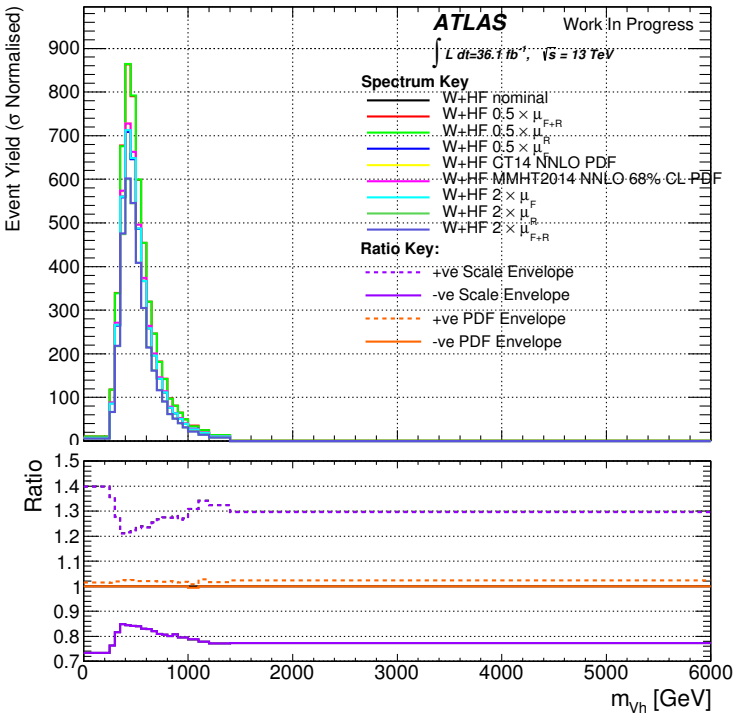

(a)

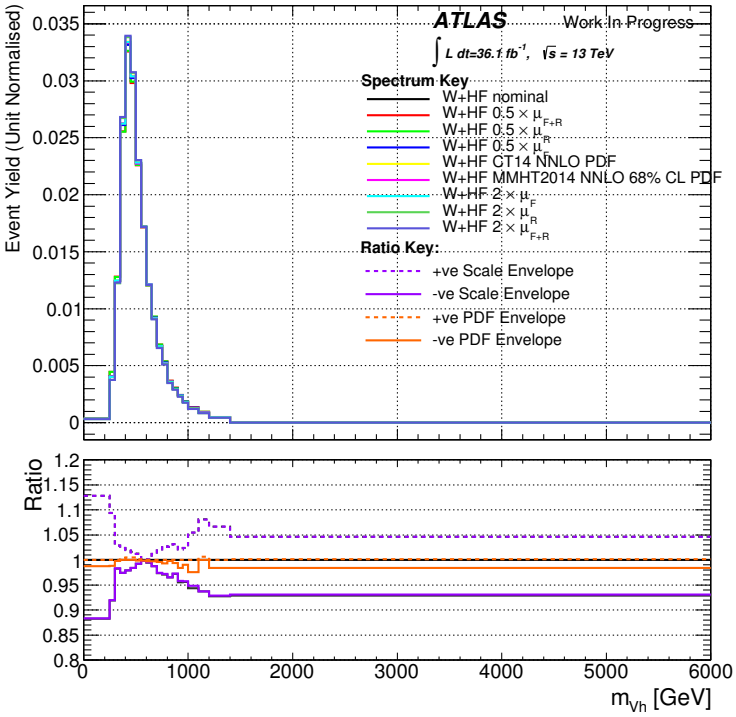

(b)

Figure 18.3.: MC-to-MC comparisons of the SHERPA 2.2.1 event weight variations for the W+HF category in the low+high m_h sidebands for the 1-lepton channel. (a) shows the comparisons prior to unit normalisation of all templates, (b) shows the same comparisons post unit normalisation.

In the case of the renormalisation scale variations the up(down), $0.5(2) \times \mu_R$, variations are considered as a 2-sided asymmetric uncertainty. An example is given by Figure 18.4a, for the W+HF sub-process in the 1-lepton boosted m_h SR. The lower pane shows the ratio of the variations to the nominal prediction, and so represents the binned re-weighting that will be applied to the nominal prediction as a $\pm 1\sigma$ systematic

The factorisation scale (μ_F) variations are grouped together to form a single asymmetric uncertainty, whereby the up(down) ($\times 0.5/ \times 2$) variations form a 2-sided asymmetric uncertainty. An example is given by Figure 18.4b, for the W+HF sub-process in the 1-lepton boosted m_h SR. Again the lower pane shows the ratios, and so corresponds to the binned re-weighting function that is applied to the nominal prediction as a $\pm 1\sigma$ uncertainty.

The NNPDF3.0 NNLO α_s variations are also grouped together to define a single 2-sided asymmetric uncertainty. The two α_s variations used by the PDF define the upper/lower systematic bands of the asymmetric uncertainty. An example of the comparison can be found in Figure 18.4c, for the W+HF sub-process in the 1-lepton boosted m_h SR.

Table 18.3 summarises the aforementioned grouping scheme for the Sherpa 2.2.1 systematics, where the nuisance parameter name within the fit, the grouped systematics, and a short description of the purpose, are given by the first, second, and third columns.

Sherpa 2.2.1 PDF Uncertainty

With regards to the PDF variations, an adaptation of the methodology outlined in Ref. [152] for *Beyond the Standard Model Searches* (see Section 6.1 *"Delivery and guidelines"*) was used. In this method, the central values of the alternative MMHT2014NNLO 68%CL and CT14 NLO PDF sets, and the NNPDF3.0 NNLO PDF error, are grouped together under a single nuisance parameter. The error arising from the CT14 NNLO and MMHT2014 68%CL PDF sets should be used, and added in quadrature to the NNPDF3.0 NNLO error, however due to technical limitations this was not possible.

Given that the alternative PDFs do not represent an up/down variation, and in this analysis the $\pm 1\sigma$ uncertainty obtained from the 100 NNPDF3.0 replicas is not guaranteed to straddle the nominal prediction, the envelope procedure was adopted to assess the size of the systematic arising from the PDF [2].

[2] Whilst this approach is susceptible to the same issue outlined previously, it was found that the alternative PDFs and NNPDF3.0 NNLO error impart little to no variation in the $m_{Vh}^{(T)}$ distributions, therefore the PDF errors were never derived because the envelope method demonstrated that the largest effect that systematic could impart was a 1-2% shape variation. Therefore the individual variations must be even smaller by definition, and so negligible.

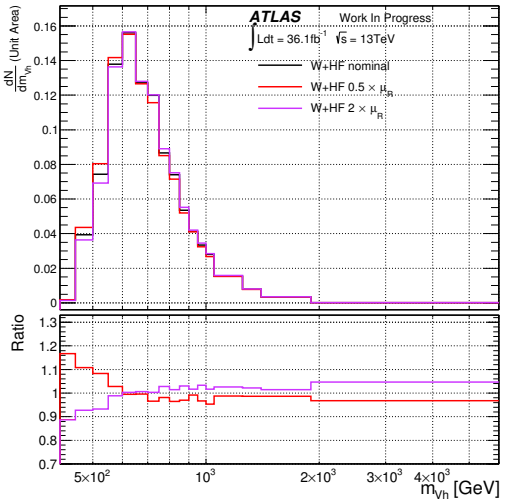

(a) Renormalisation Scale

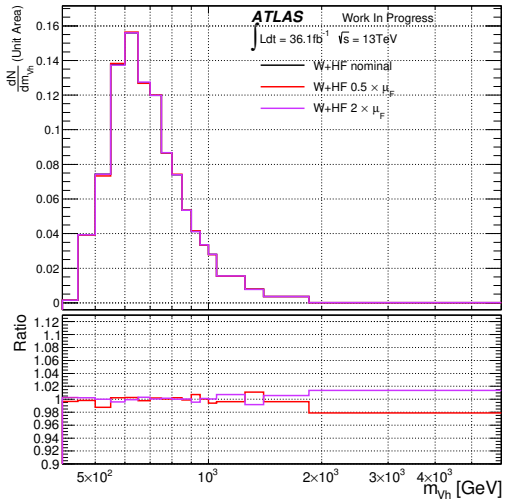

(b) Factorisation Scale

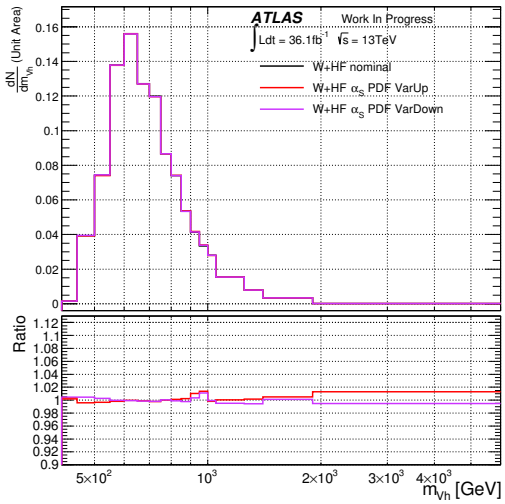

(c) α_s PDF

Figure 18.4.: W+HF Renormalisation (a), Factorisation (b), and α_s (c) PDF scale comparisons for the 1-lepton channel, inclusive of the b-tag categories for the boosted m_h SR regions. The $0.5 \times \mu^{\text{PDF}}_{R/F/\alpha_s}$ variation (red) and $2 \times \mu^{\text{PDF}}_{R/F/\alpha_s}$ variation (green) form the upper and lower bound of the systematic.

An example of this is given by Figure 18.5, which shows the alternative PDF component envelope (CT14 & MMHT2015 68%CL) for the W+l process in the b-tag inclusive 0-lepton resolved m_h signal region. As can be seen, the deviation imparted to the m_{Vh} distribution is at most 2%.

The $\pm 1\sigma$ error on the nominal NNPDF3.0 NNLO PDF set is extracted on a bin-by-bin basis in the observable O (e.g. $O = m_{Vh}$ within the fit). Specifically, the 100 replicas

Nuisance Parameter Name	Grouped Systematics	Nature of NP
MODEL_V(HF/hl/l)Jets _SherpaRenorm	$0.5 \times \mu_R$ & $2 \times \mu_R$	Encompasses the uncertainty arising from the Renormalisation scale
MODEL_V(HF/hl/l)Jets _SherpaFac	$0.5 \times \mu_F$ & $2 \times \mu_F$	Encompasses the uncertainty arising from the Factorisation scale
MODEL_V(HF/hl/l)Jets _SherpaAlphaPDF	$\alpha_s(0.5 \times \mu_R)$ & $\alpha_s(2 \times \mu_R)$	Encompasses uncertainty due to variations in α_s used by PDF

Table 18.3.: Summary of the nuisance parameters assigned to the grouped SHERPA 2.2.1 MC parameter variations.

provide 100 predictions of the event yield for a given bin, meaning that the replicas form an ensemble of $N = 100$ randomly sampled values. As such the associated error of this random sampling can be extracted by calculating the standard deviation of the sample:

$$\sigma_{\text{sample}}(j) = \sqrt{\frac{1}{N}\sum_{i=1}^{N}(x_i(j) - \mu(j))^2}, \tag{18.4}$$

where σ_{sample} is the sample standard deviation, N corresponds to the sample size (100 in this case), $x_i(j)$ corresponds to the event yield of the i^{th} NNPDF3.0 NNLO variation for the j^{th} bin, and $\mu(j) = \frac{1}{N}\sum_{i=1}^{N} x_i(j)$ represents the sample mean of the same bin. The $\pm 1\sigma$ deviation of the NNPDF3.0 NNLO prediction for the corresponding bin is therefore $x_0 \pm \sigma_{\text{sample}}$, where x_0 represents the nominal value.

Figure 18.6, shows the nominal (black) and PDF component envelope (orange) constructed when using the central values of the alternative CT14 NNLO and MMHT2014 68%CL PDF sets, and the $\pm 1\sigma$ NNPDF3.0 NNLO error. As can be seen, the envelope uncertainty is substantially larger and experiences significant fluctuations. Looking at the event yield distribution of the 100 replicas for each m_{Vh} bin, it was found that due to the low sample size ($\vec{X} = [x_1, x_2, ..., x_{100}]$), and the tendency of the SHERPA 2.2.1 generator in creating events with extremely large event weights (several orders of magnitude higher than the statistical mean), the event yield prediction for a given m_{Vh} bin can suffer from a high variance due to this low sample size.

An example of this event yield variation for a single m_{Vh} bin in the 0-lepton W+l m_h CR spectrum is shown by Figure 18.7. As can be seen, a small subset of the sample experiences highly discrepant event yield predictions that bias/distort the sample standard

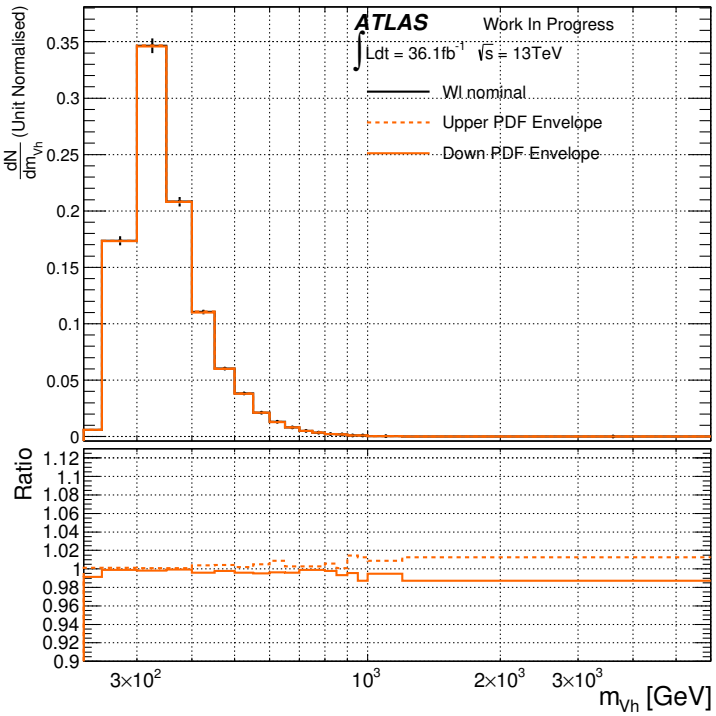

Figure 18.5.: W+ll MMHT2014NNLO 68%CL & CT14 NNLO PDF variation envelope for the 0-lepton channel, inclusive in b-Tags for the m_h SR region. The up variation (dotted orange) and down (solid orange) correspond to the asymmetric up/down systematic bounds.

deviation. To overcome this problem, the event yield distributions are fitted with a Gaussian function, where outliers are excluded by fitting to the 95% window centered on the event yield distribution mode. The standard deviation of the corresponding fit is then used as the $\pm 1\sigma$ error on the nominal NNPDF3.0 NNLO central value. This Gaussian fit is shown on the plots as a solid red line.

Figure 18.8, shows the revised component PDF envelope when the Gaussian fit standard deviation is used instead of the sample standard deviation. As can be seen, the Gaussian fit results in a less variable standard deviation estimate of the sample. Consequently the fluctuations in the component envelope are no longer present. With this in mind, the Gaussian fit procedure is used from here on in when assessing the NNPDF3.0 NNLO PDF error.

Following this investigation, the central values of the alternative CT14 NNLO and MMHT2014NNLO 68%CL PDFs, and the 1σ error of the 100 NNPDF3.0 NNLO error sets would be combined into a single PDF envelope uncertainty propagated to the fit controlled

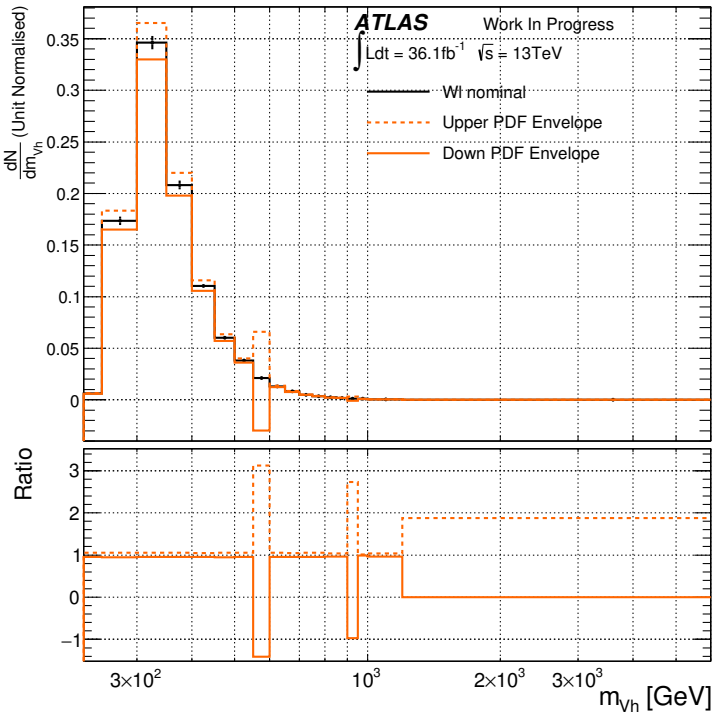

Figure 18.6.: W+ll PDF envelope for the combination of the MMHT2014NNLO 68%CL & CT14 NNLO PDF alternative PDFs, and the NNPDF3.0 NNLO $\pm 1\sigma$ ensemble error variations, where the $\pm 1\sigma$ NNPDF3.0 NNLO PDF error in each bin is the sample standard deviation.

via a single nuisance parameter, similar to those presented by Table 18.3. However, due to the small impact of the PDF uncertainties on the $m_{Vh}^{(T)}$ distribution (on the order of 1–2%), with only a couple of bins in the tail of the fit discriminant bordering on 4% (other fit regions), and the small normalisation offset that they induce (<1%, the PDF envelopes in Figure 18.3 are a good indication of this), the decision was taken to drop the uncertainty altogether in order to reduce the complexity of the analysis.

V+Jets Acceptance Priors

Following the methodology outlined in Section 18.3, the acceptance priors for the Z/W+HF, Z/W+hl, and Z/W+l processes are derived using equation 18.2. Tables 18.5–18.7 summarises these priors for both the Z-boson and W-boson processes across all lepton channels.

As stated earlier the MadGraph5_aMC@NLO+Pythia 8 to Sherpa 2.2.1 comparison is considered independent of the Sherpa 2.2.1 internal comparisons. Consequently, when

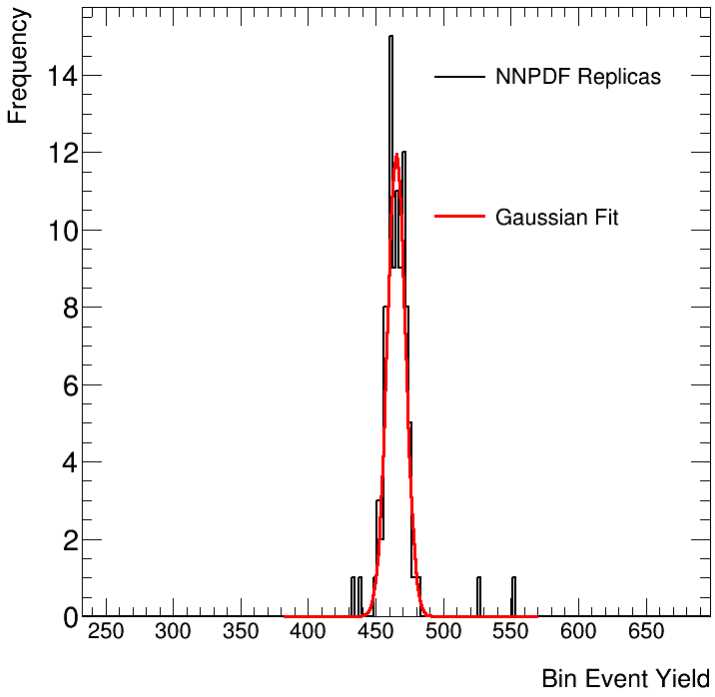

Figure 18.7.: Event yield distribution for a single m_{Vh} bin using the W+ll b-tag inclusive m_h signal region in the 0-lepton channel. The black histogram contains 100 entries (100 NNPDF3.0 NNLO replicas), whilst the red line corresponds to the fitted Gaussian. The Gaussian fit is performed to the central 95% core centered on the mode of the distribution.

deriving the acceptance and normalisation priors two estimates are generated, one for each collection. The former will be referred to as the MG5Py8 prior, and the latter will be referred to as the internal SHERPA 2.2.1 prior.

For the MG5Py8 prior only one variation sample exists by construction, therefore $M = 1$ for equation 18.2.

For the internal SHERPA 2.2.1 prior, eight comparisons exist: $0.5(2) \times \mu_R$, $0.5(2) \times \mu_F$, $0.5(2) \times \mu_R \otimes 0.5(2) \times \mu_F$, and up(down) α_s PDF. The scale and α_s PDF variations are fed independently into equation 18.2, yielding eight estimates of the prior. The maximum estimate of the six scale variations is added in quadrature with the largest α_s PDF prior estimate.

In summary, two acceptance priors are generated, one from the MG5Py8 comparison, and one from the internal SHERPA 2.2.1 variations. The largest prior is then taken as an assessment of the modelling uncertainty.

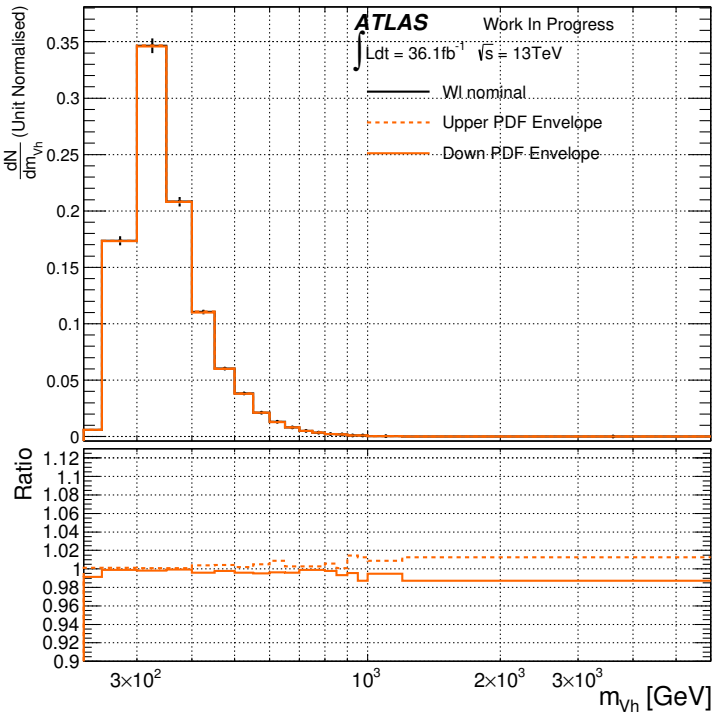

Figure 18.8.: W+ll PDF envelope for the combination of the MMHT2014NNLO 68%CL & CT14 NNLO PDF alternative PDFs, and the NNPDF3.0 NNLO $\pm 1\sigma$ ensemble error variations. The $\pm 1\sigma$ NNPDF3.0 NNLO PDF error in each bin is the standard deviation extracted from a Gaussian fit.

One caveat exists however; typically the MadGraph5_aMC@NLO+Pythia 8 comparisons yield the largest acceptance priors. Unfortunately, the statistical population of the MadGraph5_aMC@NLO+Pythia 8 sample is an order of magnitude smaller than that of the Sherpa 2.2.1 setup. Consequently, the $n^{\text{var},i}$ variable in equation 18.2 suffers from a higher statistical error when calculating the MG5Py8 prior, meaning that in some circumstances the comparison yields a prior within an extremely large associated error. In these situations the susceptibility of the prior to statistical noise makes the estimate useless, therefore even if this prior is the largest, the smaller prior from the internal Sherpa 2.2.1 comparisons is chosen. These cases are highlighted in red in Tables 18.6–18.7.

V+Jets Normalisation Priors

The V+Jets global normalisation priors are calculated using equation 18.1, where again two estimates of the prior, MG5Py8 and Sherpa 2.2.1, are considered independent.

In the case of the SHERPA 2.2.1 internal variations the methodology varies based on the lepton channel.

0-/2-lepton channel: The six scale and two α_s PDF variations listed earlier, are used in conjunction with equation 18.1 to calculate eight estimates of the prior. The largest of the six scale priors is added in quadrature with the largest of the two α_s PDF priors. Of the MG5Py8 and internal SHERPA 2.2.1 priors, the largest prior is adopted.

1-lepton channel: For the boosted part of the 1-lepton analysis the same methodology as that used by the 0-/2-lepton channels is used. However, the 1-lepton resolved analysis is restricted to the 2+3 signal jet exclusive bin (see Chapter 15 for the $n_{\text{jet}}^{\text{sig}}$ cut). As such, the *Stewart-Tackmann* method [153] is used to assess the normalisation uncertainty on the exclusive 2+3 signal jet bin, arising from the choice of the renormalisation or factorisation scale. This method replaces the six scale variations in the resolved regime with a single asymmetric (±ve) error on the predicted normalisation.

The motivation for this approach stems from the fact that scale variations of jet exclusive perturbative calculations underestimate the associated uncertainty, due to cancellations between the perturbative corrections that lead to large k-factors and those that induce logarithmic sensitivity to the neighbouring jet bins [153]. Simply assessing the difference in the cross-section via the alternative scale variations of the SHERPA 2.2.1 configuration, leads to a potentially underestimated uncertainty.

The calculation of uncertainties via this methodology relies on the assumption that the N-jet exclusive cross-section (σ_N) can be constructed from the difference between the $\geq N$ jet bin cross-section, and the $\geq N+1$ jet bin cross-section, i.e. $\sigma_N^{\text{excl}} = \sigma_{\geq N} - \sigma_{\geq N+1}$. From this the uncertainty in the corresponding N-jet exclusive bin (Δ_N) is defined as $\Delta_N^{2,\text{excl}} = \Delta_{\geq N}^2 + \Delta_{\geq N+1}^2$, where $\Delta_{\geq N/N+1}$ corresponds to the cross-section error on the $\geq N/N+1$ jet bin cross-section.

For the resolved regime of the analysis the N-jet bin is defined as $N = (2+3)$ small-R signal jets. Using the methodology outlined in Ref. [153], the error formula for the 2+3 exclusive jet bin is therefore:

$$\Delta_{2+3}^2 = \Delta_{2+}^2 + \Delta_{4+}^2, \tag{18.5}$$

where Δ_{2+} and Δ_{4+} denote the ≥ 2 and ≥ 4 jet inclusive error. The fractional error is therefore given by $\Delta_{2+3}/\sigma_{2+3}$. To determine this cross-section uncertainty, the variation of the event yield prediction is used (inclusive of all resolved analysis regions), meaning that

Process	Scale Comparisons (Up/Down %)	Stewart-Tackmann (Up/Down %)
W+HF	16/-12 %	47/-32 %
W+hl	15/-11 %	32/-22 %
W+ll	14/-11 %	26/-19 %
Z+HF	18/-13 %	60/-39 %
Z+hl	13/-9 %	34/-23 %
Z+ll	12/-10 %	27/-20 %

Table 18.4.: Comparison of the normalisation priors derived from the maximum of the six scale variations against the Stewart-Tackmann derived normalisation priors using the same underlying scale variations. The Up/Down refers to the asymmetric error derived by both methods on the nominal predicted normalisation of the V+Jets process.

the error assigned to a generic N-jet bin is given by:

$$\Delta_N = \max_i^{k^{\pm}} \{h^{\text{evts},N}_{\text{nominal}} - h^{\text{evts},N}_{\text{var}^i}\}, \tag{18.6}$$

where $h^{\text{evts},N}_{\text{nominal}}$ is the event yield predicted by the nominal Sherpa 2.2.1 configuration, $h^{\text{evts},N}_{\text{var}^i}$ is the event yield prediction of the i^{th} variation, and N denotes the N^{th}-jet bin. The six underlying scale variations predict either an upwards or downwards variation on the predicted normalisation, therefore the positive and negative normalisation variations are separated, and each group is calculated separately to yield a positive and negative *'Stewart-Tackmann'* error. $k^{\pm}$ denotes this separation of the six underlying scale variations. The maximum of the $k^{\pm}$ scale comparisons against the nominal is then taken as the assigned error to the N^{th}-jet bin.

With this defined, the fractional error for the V+HF, V+hl and V+l normalisation can be calculated according to equation 18.5, yielding two up/down variations on the aforementioned processes.

Table 18.4, shows the normalisation priors as calculated by the raw scale comparison methodology given by equation 18.1, where the largest of the six scale variations (sub-divided into the ±ve variations) is used, and the Stewart-Tackmann errors defined above. Analysing Table 18.4, it is immediately apparent that the normalisation uncertainty estimated via the Stewart-Tackmann method results in a substantially larger normalisation error (as is expected), typically on the order of 2–3 times that of the raw scale comparison methodology.

From the fit perspective the asymmetric errors on the normalisation can not be assigned as a prior to the normalisation nuisance parameters (a Gaussian has a symmetric width).

Therefore the largest of the two asymmetric Stewart-Tackmann errors is chosen as the uncertainty; for example, for the W+ll process the 26% error is selected as the Stewart-Tackmann estimate of the error. The largest is chosen for conservative reasons, and given that profile likelihoods constrain the backgrounds, over-estimating the error is preferable.

Since the normalisation prior fed to the fit corresponds to the error on both the resolved and boosted normalisation, $\Delta_{\text{Resolved}} + \Delta_{\text{Boosted}}$ (because the nuisance parameter controls the global resolved+boosted normalisation), the Stewart-Tackmann errors following the above procedure are combined with the boosted regime error estimates stated above, by averaging the estimated prior uncertainties. These values are summarised in Table 18.6.

Summary: Tables 18.5–18.7, summarises the V+Jet acceptance and normalisation priors for 0-/1-/2-lepton channels. It should be noted that for the 1-lepton components, the normalisation uncertainties are represented as σ_k, where k denotes the type of of prior (MG5Py8, Stewart-Tackmann, or Sherpa), and the superscripts *res/boost* denote the resolved or boosted analysis regimes. The bold highlighted values in the 1-lepton normalisation section correspond to the chosen prior uncertainties.

Nuisance Parameter	Description	Samples/Categories	Value	Effect
		0-lepton		
norm_Zbb	$Z+hf$ normalisation	$Z+hf$, all 1-/2-tag & kinematic regions	25%	normalisation
norm_Zclbl	$Z+hl$ normalisation	$Z+hl$, all 1-/2-tag & kinematic regions	20%	normalisation
norm_Zl	$Z+l$ normalisation	$Z+l$, all 1-/2-tag & kinematic regions	19%	normalisation
norm_Zjets_3ptag	$Z+hf$+Zcl+Zbl normalisation	$Z+hf$, Zcl and Zbl, all 3+ tag regions	Floating & decorrelated from 1-/2-tag regions	normalisation
norm_Wbb	$W+hf$ normalisation	$W+hf$, all 1-/2-tag & kinematic regions	26%	normalisation
norm_Wclbl	$W+hl$ normalisation	$W+hl$, all 1-/2-tag & kinematic regions	23%	normalisation
norm_Wl	$W+l$ normalisation	$W+l$, all 1-/2-tag & kinematic regions	20%	normalisation
norm_Wjets_3ptag	$W+hf$+Wcl+Wbl normalisation	$W+hf$, Wcl and Wbl, all 3+ tag regions	Floating & decorrelated from 1-/2-tag regions	normalisation
Zbb_ResMergedRatio	boosted / resolved ratio	$Z+hf$, resolved & boosted regions	14%	acceptance
Zclbl_ResMergedRatio	boosted / resolved ratio	$Zclbl$, boosted regions	19%	acceptance
Zl_ResMergedRatio	boosted / resolved ratio	Zl, boosted regions	17%	acceptance
Zbb_mbbCatRatio	SR / CR ratio	$Z+hf$,m_h sideband and SR window	6% (1%) resolved (boosted)	acceptance
Zclbl_mbbCatRatio	SR / CR ratio	$Zclbl$, m_h sideband and SR window	2% (14%) resolved (boosted)	acceptance
Zl_mbbCatRatio	SR / CR ratio	Zl, m_h sideband and SR window	3% (5%) resolved (boosted)	acceptance
Wbb_ResMergedRatio	boosted / resolved ratio	$W+hf$, boosted regions	43%	acceptance
Wclbl_ResMergedRatio	boosted / resolved ratio	$Wclbl$, boosted regions	35%	acceptance
Wl_ResMergedRatio	boosted / resolved ratio	Wl, boosted regions	20%	acceptance
Wbb_mbbCatRatio	SR / CR ratio	$W+hf$,m_h sideband and SR window	6% (15%) resolved (boosted)	acceptance
Wclbl_mbbCatRatio	SR / CR ratio	$Wclbl$, m_h sideband and SR window	5% (2%) resolved (boosted)	acceptance
Wl_mbbCatRatio	SR / CR ratio	Wl, m_h sideband and SR window	2% (3%) resolved (boosted)	acceptance

Table 18.5.: Summary of Z+jet and W+jet nuisance parameter priors for the 0-lepton channel. The first column quotes the name of the nuisance parameter, the second quotes the source of the uncertainty, third states the categories and samples on which it is applied, the fourth column states the value of the prior uncertainty (if applicable), and the fifth column summarises the effect of the systematic uncertainty.

Nuisance Parameter	Description	Samples/Categories	Value	Effect
		1-lepton		
norm_Zbb	$Z+hf$ normalisation	$Z+hf$, all 1-/2-tag & kinematic regions	$\sigma_{ST/Sherpa} = \mathbf{46}/20\%$ ($\sigma^{res}_{ST} = 60\%$, $\sigma^{boost}_{Sherpa} = 32\%$)	normalisation
norm_Zclbl	$Z+hl$ normalisation	$Z+hl$, all 1-/2-tag & kinematic regions	$\sigma_{ST/MG5Py8} = 33/\mathbf{61}\%$ ($\sigma^{res}_{ST} = 34\%$, $\sigma^{boost}_{Sherpa} = 32\%$)	normalisation
norm_Zl	$Z+l$ normalisation	$Z+l$, all 1-/2-tag & kinematic regions	$\sigma_{ST/MG5Py8} = 30/\mathbf{46}\%$ ($\sigma^{res}_{ST} = 27\%$, $\sigma^{boost}_{Sherpa} = 32\%$)	normalisation
norm_Wbb	$W+hf$ normalisation	$W+hf$, all 1-/2-tag & kinematic regions	$\sigma_{ST/MG5Py8} = \mathbf{39}/19\%$ ($\sigma^{res}_{ST} = 47\%$, $\sigma^{boost}_{Sherpa} = 31\%$)	normalisation
norm_Wclbl	$W+hl$ normalisation	$W+hl$, all 1-/2-tag & kinematic regions	$\sigma_{ST/MG5Py8} = \mathbf{33}/17\%$ ($\sigma^{res}_{ST} = 32\%$, $\sigma^{boost}_{Sherpa} = 33\%$)	normalisation
norm_Wl	$W+l$ normalisation	$W+l$, all 1-/2-tag & kinematic regions	$\sigma_{ST/MG5Py8} = \mathbf{30}/16\%$ ($\sigma^{res}_{ST} = 26\%$, $\sigma^{boost}_{Sherpa} = 32\%$)	normalisation
Zbb_ResMergedRatio	boosted / resolved ratio	$Z+hf$, boosted regions	12%	acceptance
Zclbl_ResMergedRatio	boosted / resolved ratio	$Zclbl$, boosted regions	27%	acceptance
Zl_ResMergedRatio	boosted / resolved ratio	Zl, boosted regions	62%	acceptance
Zbb_mbbCatRatio	SR / CR ratio	$Z+hf$,m_h sideband and SR window	1% (1%) resolved (boosted)	acceptance
Zclbl_mbbCatRatio	SR / CR ratio	$Zclbl$, m_h sideband and SR window	22% (5%) resolved (boosted)	acceptance
Zl_mbbCatRatio	SR / CR ratio	Zl, m_h sideband and SR window	10% (6%) resolved (boosted)	acceptance
Wbb_ResMergedRatio	boosted / resolved ratio	$W+hf$, boosted regions	28%	acceptance
Wclbl_ResMergedRatio	boosted / resolved ratio	$Wclbl$, boosted regions	15%	acceptance
Wl_ResMergedRatio	boosted / resolved ratio	Wl, boosted regions	16%	acceptance
Wbb_mbbCatRatio	SR / CR ratio	$W+hf$,m_h sideband and SR window	2% (6%) resolved (boosted)	acceptance
Wclbl_mbbCatRatio	SR / CR ratio	$Wclbl$, m_h sideband and SR window	1% (1%) resolved (boosted)	acceptance
Wl_mbbCatRatio	SR / CR ratio	Wl, m_h sideband and SR window	7% (3%) resolved (boosted)	acceptance

Table 18.6.: Summary of Z+jet and W+jet nuisance parameter priors for the 1-lepton channel. The first column quotes the name of the nuisance parameter, the second quotes the source of the uncertainty, third states the categories and samples on which it is applied, the fourth column states the value of the prior uncertainty (if applicable), and the fifth column summarises the effect of the systematic uncertainty.

Nuisance Parameter	Description	Samples/Categories	Value	Effect
		2-lepton		
norm_Zbb	$Z+hf$ normalisation	$Z+hf$, all 1-/2-tag & kinematic regions	31%	normalisation
norm_Zclbl	$Z+hl$ normalisation	$Z+hl$, all 1-/2-tag & kinematic regions	11%	normalisation
norm_Zl	$Z+l$ normalisation	$Z+l$, all 1-/2-tag & kinematic regions	12%	normalisation
norm_Zjets_3ptag	$Z+hf$+Zcl+Zbl normalisation	$Z+hf$, Zcl and Zbl, all 3+ tag regions	Floating & decorrelated from 1-/2-tag regions	normalisation
norm_Wbb	$W+hf$ normalisation	$W+hf$, all 1-/2-tag & kinematic regions	34%	normalisation
norm_Wclbl	$W+hl$ normalisation	$W+hl$, all 1-/2-tag & kinematic regions	28%	normalisation
norm_Wl	$W+l$ normalisation	$W+l$, all 1-/2-tag & kinematic regions	29%	normalisation
norm_Wjets_3ptag	$W+hf$+Wcl+Wbl normalisation	$W+hf$, Wcl and Wbl, all 3+ tag regions	Floating & decorrelated from 1-/2-tag regions	normalisation
Zbb_ResMergedRatio	boosted / resolved ratio	$Z+hf$, boosted regions	19%	acceptance
Zclbl_ResMergedRatio	boosted / resolved ratio	$Zclbl$, boosted regions	28%	acceptance
Zl_ResMergedRatio	boosted / resolved ratio	Zl, boosted regions	23%	acceptance
Zbb_mbbCatRatio	SR / CR ratio	$Z+hf$,m_h sideband and SR window	3% (8%) resolved (boosted)	acceptance
Zclbl_mbbCatRatio	SR / CR ratio	$Zclbl$, m_h sideband and SR window	3% (8%) resolved (boosted)	acceptance
Zl_mbbCatRatio	SR / CR ratio	Zl, m_h sideband and SR window	6% (5%) resolved (boosted)	acceptance
Wbb_ResMergedRatio	boosted / resolved ratio	$W+hf$, boosted regions	5%	acceptance
Wclbl_ResMergedRatio	boosted / resolved ratio	$Wclbl$, boosted regions	11%	acceptance
Wl_ResMergedRatio	boosted / resolved ratio	Wl, boosted regions	13%	acceptance
Wbb_mbbCatRatio	SR / CR ratio	$W+hf$,m_h sideband and SR window	2% (19%) resolved (boosted)	acceptance
Wclbl_mbbCatRatio	SR / CR ratio	$Wclbl$, m_h sideband and SR window	5% (1%) resolved (boosted)	acceptance
Wl_mbbCatRatio	SR / CR ratio	Wl, m_h sideband and SR window	1.2% (1%) resolved (boosted)	acceptance

Table 18.7.: Summary of Z+jet and W+jet nuisance parameter priors for the 2-lepton channel. The first column quotes the name of the nuisance parameter, the second quotes the source of the uncertainty, third states the categories and samples on which it is applied, the fourth column states the value of the prior uncertainty (if applicable), and the fifth column summarises the effect of the systematic uncertainty.

18.3.2. Top-quark Production – $t\bar{t}$ & Single Top

As outlined in Chapter 10, the nominal $t\bar{t}$ and single top quark prediction uses the NLO Matrix Element (ME) generator Powheg-Box v2 with the CT10 NLO PDF set, interfaced with Pythia 6.428 using the PERUGIA2012 tune. Four alternative MC $t\bar{t}$ samples are used to assess three aspects of the MC modelling, whilst five alternative single top MC samples are used to assess four aspects of the MC modelling. Table 18.8 summarises the differences between the nominal sample and each variation. The alternative samples considered are:

- **Powheg-Box v2+Herwig++ :** The ME Powheg-Box v2 generator uses the same setup as that used for the nominal Powheg-Box v2+Pythia 6 configuration, but the parton shower (PS) generator is swapped out for Herwig++ version 2.7.1 using the UE-EE-5 tune and CTEQ6L1 PDF set. The purpose therefore of this comparison is to test the parton shower, hadronisation, underlying event (UE) and Multiple Parton Interaction (MPI) models whilst maintaining the same hard scattering model given by Powheg-Box v2.

- **MadGraph5_aMC@NLO+Herwig++ :** The ME generator is swapped out for MadGraph5_aMC@NLO using the CT10 PDF set, interfaced with Herwig++ using the CTEQ6L1-UE-EE-5 tune and CTEQ6L1 PDF set. This sample is compared to the previous Powheg-Box v2+Herwig++ sample. This fixes the PS generator component, but alters the hard scattering generator, making this variation sensitive to the hard scatter model.

- **Powheg-Box v2+Pythia 6 RadHi/RadLo :** Using the same setup as that used for the nominal Powheg-Box v2+Pythia 6 sample, the RadHi and RadLo samples correspond to either the enhancement (Hi) or reduction (Lo) of initial/final state radiation (IFSR). The two samples are compared to the nominal sample setup, and so are sensitive to variations of IFSR models.

  - RadHi: The renormalisation (μ_R) and factorisation scale (μ_F) scales are decreased by a factor of 0.5, the Powheg-Box v2 hdamp parameter is doubled ($2 \times m_{\text{top}}$), and the high radiation PERUGIA2012 tune is used.

  - RadLo: The renormalisation (μ_R) and factorisation scale (μ_F) scales are increased by a factor of 2, the Powheg-Box v2 hdamp parameter is kept at m_{top}, and the low radiation PERUGIA2012 tune is used.

- **Powheg-Box v2+Pythia 6 Diagram Subtraction :** For the production of a single top quark in association with a W-boson (Wt) the interference with the $t\bar{t}$ production process at NLO in QCD is removed by subtracting the cross-section

Sample	Configuration	Systematic impact	Process
POWHEG-BOX v2+Herwig++	UE-EE-5 PS tune CT10 PDF set for ME & CTEQ6L1 PDF set for PS hdamp $=m_t$	Parton Shower model	$t\bar{t}$ & single top
MADGRAPH5_aMC@NLO+Herwig++	UE-EE-5 PS tune CT10 PDF set for ME & CTEQ6L1 PDF set for PS	Matrix Element model	$t\bar{t}$ & single top
POWHEG-BOX v2+PYTHIA 6	RadHi : $0.5 \times \mu_R$, $0.5 \times \mu_F$, hdamp $= 2 \times m_t$ & high radiation PERUGIA2012 tune RadLo : $2 \times \mu_R$, $2 \times \mu_F$, hdamp $= m_t$ & RadLo: low radiation PERUGIA2012 tune	IFSR variations	$t\bar{t}$ & single top
POWHEG-BOX v2+PYTHIA 6	Same setup as nominal Wt production, except the diagram subtraction scheme is used to remove $t\bar{t}$ double resonance	$Wt + t\bar{t}$ interference	single top (Wt channel only)

Table 18.8.: Summary of $t\bar{t}$ sample variations for assessing model dependent systematic effects.

associated with the $t\bar{t}$ double resonance amplitude terms, rather than subtracting the same terms from the amplitude prior to the calculation (Diagram Removal). As such the same POWHEG-BOX v2+PYTHIA 6 setup is used, however the nominal Diagram Removal scheme is replaced with the Diagram Subtraction scheme [154].

$t\bar{t}$ NNLO Cross-Section

The $t\bar{t}$ cross section for pp collisions at a center of mass energy of $\sqrt{s}$ = 13 TeV is $\sigma_{t\bar{t}}$ = $831.76^{+40.2}_{-45.6}$ pb for a top quark mass of 172.5 GeV. It has been calculated at next-to-next-to leading order (NNLO) in pQCD including resummation of next-to-next-to-leading logarithmic (NNLL) soft gluon terms with top++2.0 [155–161]. The PDF and α_s uncertainties were calculated using the PDF4LHC prescription [162] with the MSTW2008 68% CL NNLO [51, 163], CT10 NNLO [91, 164] and NNPDF2.3 5f FFN [165] PDF sets, added in quadrature to the scale uncertainty.

The uncertainty of the total NNLO+NNLL cross-section is ±35.06 pb from the PDF, and +19.77(−29.20)pb from QCD scale variations (renormalisation & factorisation). For completeness the cross-section variation with the top-quark mass is +23.18(−22.45) pb, however this is not included in the above total uncertainty.

Single Top NNLO Cross-Section

The t-channel single-top cross section for pp collisions at a center of mass energy of $\sqrt{s} = 13$ TeV is $\sigma_t = 136.02^{5.40}_{-4.57}$ pb for the top quark and $\sigma_{\bar{t}} = 80.95^{+4.10}_{-4.61}$ pb for the anti-top quark. For the s-channel the top quark production cross-section is $\sigma_t = 6.35^{+0.25}_{-0.22}$ pb, and the anti-top production cross-section is $\sigma_{\bar{t}} = 4.42^{+0.10}_{-0.10}$ pb, for the same pp collision center of mass energy of $\sqrt{13}$ TeV. The production cross-section for the Wt associated production is calculated to be $\sigma_{Wt} = 71.7^{+1.80}_{-1.80}$ pb, inclusive of top and anti-top quarks, for pp collisions at a center of mass energy of $\sqrt{s} = 13$ TeV.

All calculations are done using a top quark mass of 172.5 GeV, calculated at next-to-leading order (NLO) in QCD with Hathor v2.1 [166, 167]. PDF and α_s uncertainties are calculated using the PDF4LHC prescription [162] with the MSTW2008 68% CL NLO [51, 163], CT10 NLO [91, 164] and NNPDF2.3 [165] PDF sets, added in quadrature to the scale uncertainty. For completeness the cross-section variation resulting from the top quark mass dependence is: ±1.11 pb for the top quark and +0.71(−0.70) pb for the anti-top quark in the t-channel, +0.14(−0.13) pb for the top quark and ±0.09 pb for the anti-top quark in the s-channel, and +3.46(−4.31) pb for the top and anti-top quark in the Wt production mode.

$t\bar{t}$ Shape Systematics

Following the methodology outlined in Section 18.3 a shape systematic is obtained for each of the fit regions outlined in Tables 17.1 & 17.2, inclusively of the b-tag category. MC-to-MC comparisons are made between the nominal Powheg-Box v2+Pythia 6 MC configuration and the four alternative MC configurations given by Table 18.8, where an example is given by Figure 18.9, which shows the boosted 1-lepton channel signal regions.

The best fitting smoothing function for each of the comparisons, and thus the re-weighting function used within the analysis, are shown in the ratio pane of each plot. The nominal MC setup is given as black, which in all but one case will correspond to the Powheg-Box v2+Pythia 6 configuration (sub-figures 18.9a, 18.9b, 18.9c), whilst the variation/alternative sample corresponds to the red curve.

The exception is the comparison of the POWHEG-BOX v2+Herwig++ and MADGRAPH5_aMC@NLO+Herwig++ generator configurations, which is sensitive to the matrix element component of the prediction. The former is considered the nominal and the later is considered the variation. Switching the nominal $t\bar{t}$ configuration to POWHEG-BOX v2+Herwig++ is necessary because MADGRAPH5_aMC@NLO+PYTHIA 8 sample was unavailable. Therefore to factorise out the uncertainty arising from the matrix element calculation, the parton shower generator must remain unchanged. An example is given by sub-figure 18.9d.

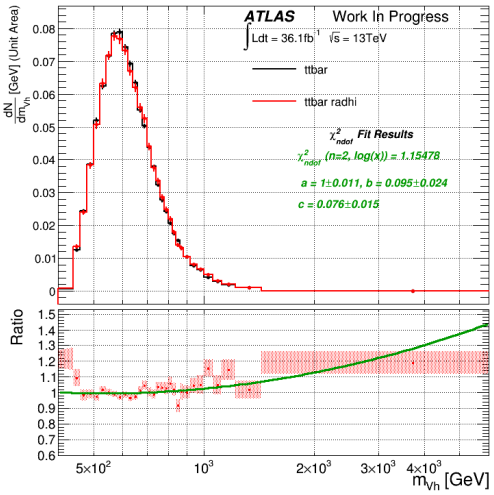

(a) RadHi

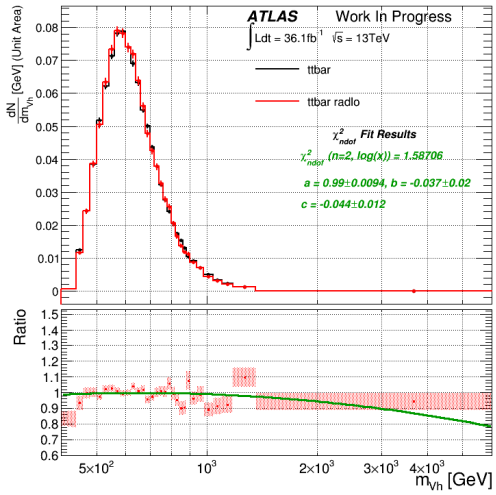

(b) RadLo

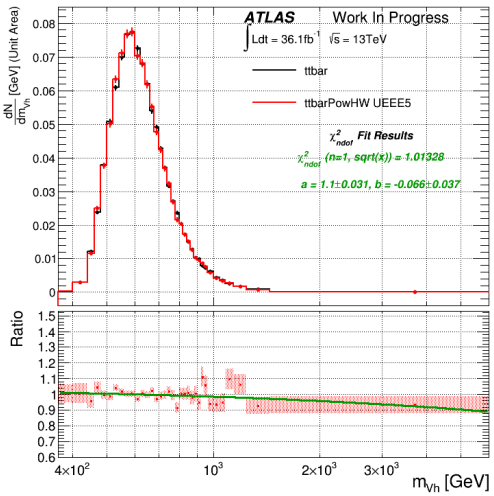

(c) PS

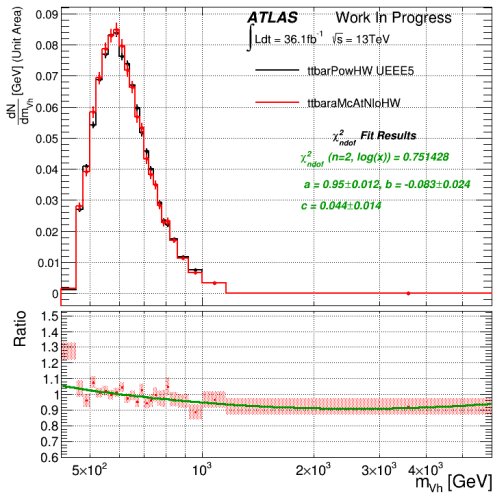

(d) PS

Figure 18.9.: The 1-lepton m_{Vh} unit normalised comparisons for $t\bar{t}$ in the boosted 0+ additional b-tagged track-jet m_h SR for Powheg-Box v2+Pythia 6 vs RadHi (top left), vs RadLo (top right), vs Powheg-Box v2+Herwig++ (bottom left), and Powheg-Box v2+Herwig++ vs MadGraph5_aMC@NLO+Herwig++ (bottom right). All comparisons inclusive of b-tags, and the solid green lines correspond to the smoothing function.

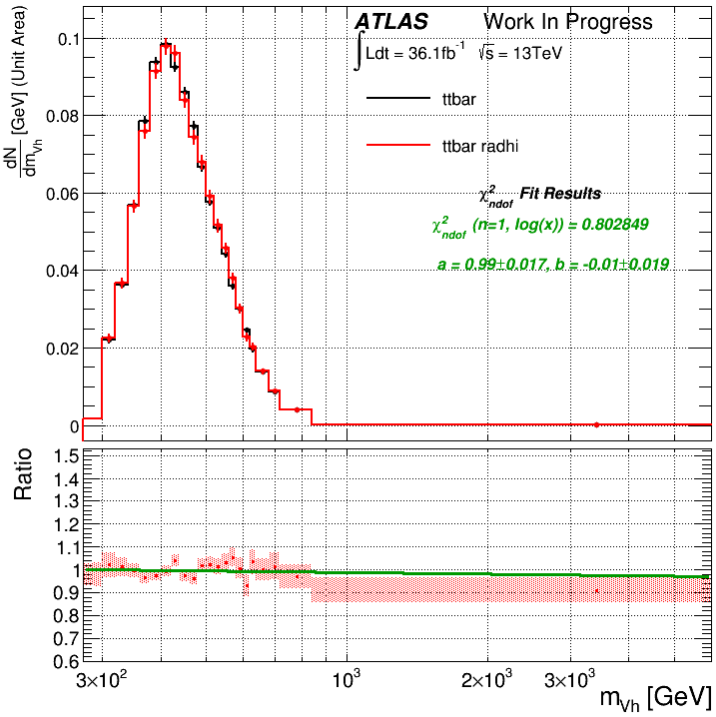

(a) RadHi

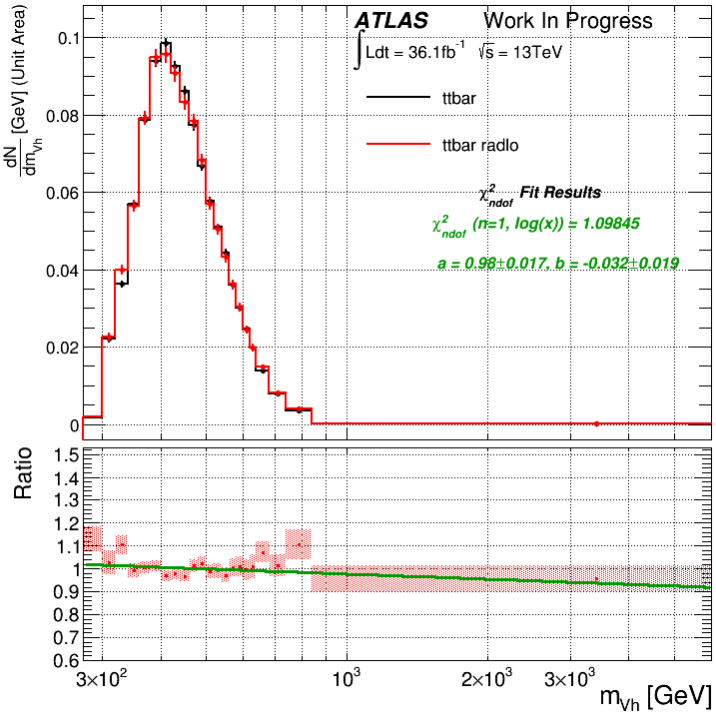

(b) RadLo

Figure 18.10.: The 1-lepton m_{Vh} unit normalised comparisons for $t\bar{t}$ in the resolved m_h SR for POWHEG-BOX V2+PYTHIA 6 vs RadHi (top), vs RadLo (bottom). All comparisons are inclusive of b-tags, and the solid green lines correspond to the smoothing function.

In the case of the ME and PS systematics, the two re-weighting functions are reflected around $y = 1$ in order to symmetrise the variations to form a 2-sided systematic. In the case of the RadHi and RadLo comparisons, the two variations are considered a pair because they each represent a variation on the amount of additional initial/final-state radiation. However, it was found that in some regions of the analysis the two variations demonstrate the same single sided behaviour. An example of this is shown by Figures 18.10a and 18.10b, which show the RadHi and RadLo comparisons for the resolved 1-lepton m_h SR; the RadHi and RadLo ratios have the same negative trend as a function of m_{Vh}. In these cases the result is symmetrised according to the procedure outlined in Section 17.4.2. Otherwise, as in the boosted regions, e.g. sub-figures 18.9a and 18.9a, the two variations are used to form a 2-sided asymmetric uncertainty.

The special treatment of the RadHi and RadLo systematics is necessary to prevent convergence issues in the Binned Profile Likelihood fit. The above scheme is adopted because symmetrising the individual comparisons and allocating them to the fit as two separate nuisance parameters is invalid (poorly motivated from a physical perspective), because the RadHi and RadLo systematics represent the up/down variation of the same source of uncertainty (variations on IFSR). Specifically, the two variations should induce a shape and normalisation distortion that results in two alternative spectrums that straddle the nominal prediction. For example Figure 18.11 shows the small-R jet multiplicity for the 2-lepton m_h SR, where this behaviour can be seen. This is expected because the jet multiplicity of an event is sensitive to additional radiation (radiated partons can be reconstructed as a separate jet), however for m_{Vh} this behaviour is not guaranteed for such a complex variable.

Single Top Shape Systematics

The SM single top prediction is divided into three sub-processes, s- and t-channel, and Wt associated production. The contribution of each sub-process to each of the fit regions outlined in Section 17.1, relative to the total single top expected event yield is given below by Table 18.9. From this table it can be seen that the s-channel is sub-dominant across all fit regions in the 1-lepton channel, typically forming 1% of the overall single top background (4% at most).

As such the alternative MC configurations summarised by Table 18.8, apply only to the t-channel and Wt sub-processes, since the s-channel contribution is negligible. Therefore, comparisons of the total single top process are between the nominal configuration $\text{stop}_{\text{nom}} = s_{\text{nom}} + t_{\text{nom}} + Wt_{\text{nom}}$ and the variation configuration $\text{stop}_{\text{var}} = s_{\text{nom}} + t_{\text{var}} + Wt_{\text{var}}$.

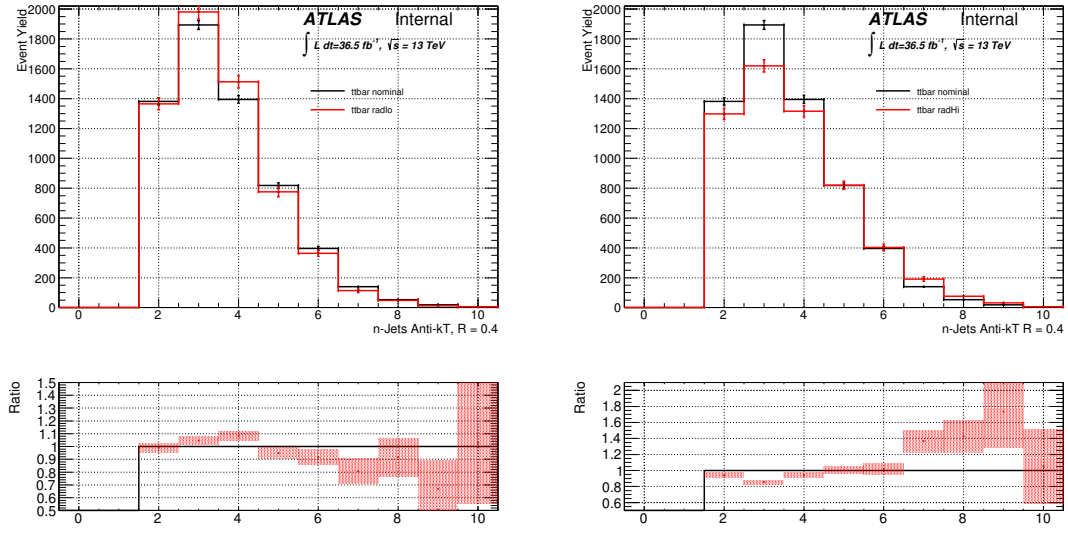

(a) RadLo **(b)** RadHi

Figure 18.11.: $t\bar{t}$ MC-to-MC comparisons of anti-k_T $R = 0.4$ jet multiplicity for the 0+ b-tag resolved m_h SR for the 2-lepton channel. (a) shows the RadLo variation, and (b) shows the RadHi variation.

Sub-Process	**Resolved**			
	SR		CR	
s-channel	50.3 (1.3%)	28.6 (3.9%)	17.7 (0.2%)	10.5 (0.5%)
t-channel	729.5 (19.4%)	412.4 (56.4%)	2691.9 (31.7%)	1322.0 (63.5%)
Wt	2986.2 (79.3%)	290.6 (39.7%)	5787.3 (68.1%)	747.6 (35.9%)
Total	3766.0	731.6	8496.9	2080.1
	Boosted			
	SR (0 add. tag)		CR(0 add. tag)	
s-channel	13.0 (1.2%)	1.08 (1%)	10.1 (1.3%)	0.33 (0.5%)
t-channel	76.0 (7.2%)	7.7 (7.1%)	71.5 (9.4%)	2.34 (3.6%)
Wt	966.5 (91.6%)	99.4 (91.9%)	679.1 (89.3%)	62.2 (95.9%)
Total	1055.5	108.2	760.7	64.87

Table 18.9.: Single top sub-process breakdown for the various fit regions used within the 1-lepton HVT analysis.

A shape systematic is derived for each of the fit regions outlined in Table 17.1, inclusively of the b-tag category assigned. The nominal Powheg-Box v2+Pythia 6 stop MC configuration is compared to the RadHi, RadLo, and Powheg-Box v2+Herwig++ MC

configurations given by Table 18.8, whilst Powheg-Box v2+Herwig++ is compared to MadGraph5_aMCNLO+Herwig++. The 5$^{\text{th}}$ comparison, corresponding to the comparison of the Diagram Removal (DR) and Diagram Subtraction (DS) scheme for Wt associated production, by definition only exists for the Wt process.

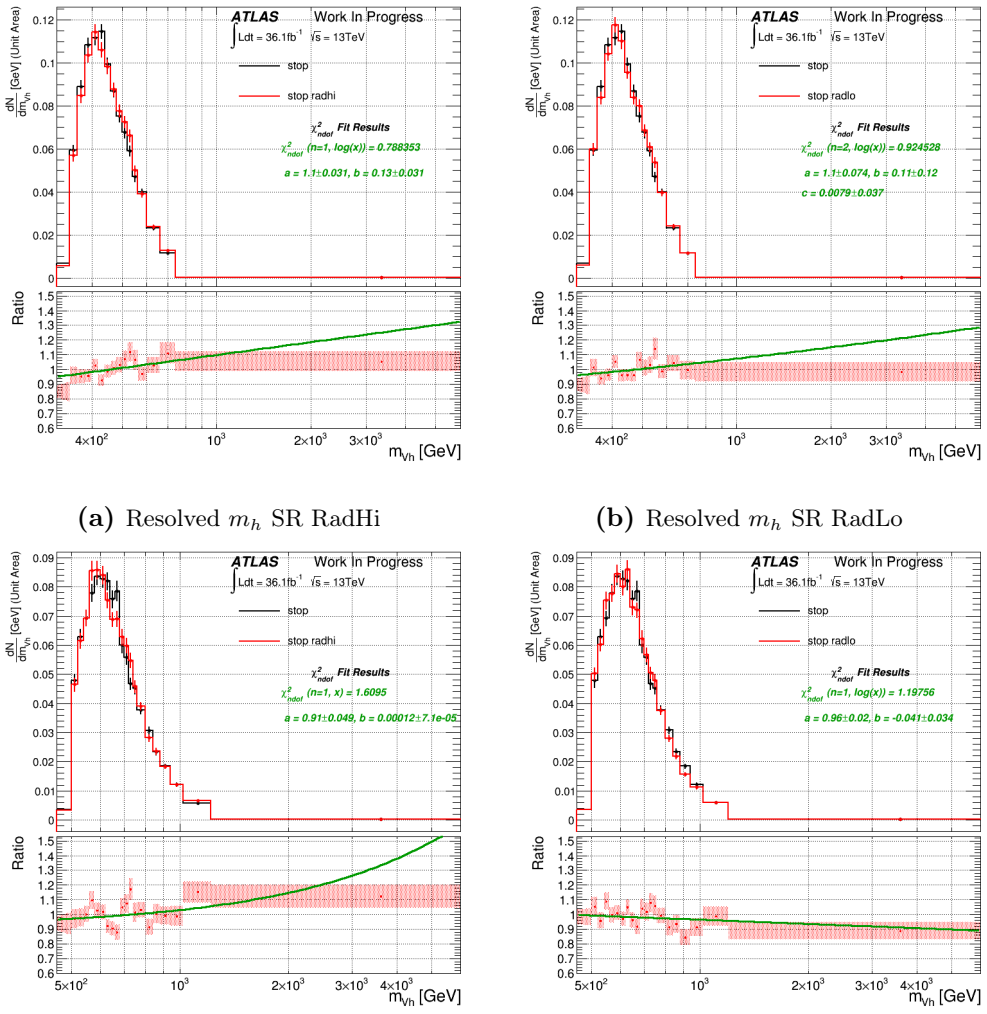

(a) Resolved m_h SR RadHi

(b) Resolved m_h SR RadLo

(c) Boosted m_h SR RadHi

(d) Boosted m_h SR RadLo

Figure 18.12.: The 1-lepton m_{Vh} unit normalised comparisons for single top (Wt+s+t channel processes) in the resolved (top) and boosted (bottom) m_h SRs for Powheg-Box v2+Pythia 6 vs RadHi (left), and vs RadLo (right). All comparisons are inclusive of b-tags, and the solid green lines correspond to the smoothing function. In the case of the Powheg-Box v2+Herwig++ vs MadGraph5_aMC@NLO+Herwig++ comparison, insufficient statistics means no shape systematic is derived.

Like the $t\bar{t}$ systematics, the ME and PS re-weighting functions are given to the fit as a symmetrised 2-sided systematic, whilst the RadHi and RadLo comparisons are either

averaged and symmetrised when they demonstrate the same single sided behaviour, as in the case of sub-figures 18.12a and 18.12b, or formed into a 2-sided asymmetric uncertainty when the pair straddle the nominal predictions like those shown in sub-figures 18.12c and 18.12d.

In the case of the DR-vs-DS comparisons, the predicted m_{Vh} spectrums from the two MC configurations differed greatly. Figure 18.13 shows this comparison using a uniform binning of 100 GeV (Wt sub-process) for all 1-lepton fit regions (resolved and boosted m_h SRs/CRs).

In analysing this figure it is apparent that the DS scheme predicts a quickly falling m_{Vh} spectrum, meaning that the Wt final states are substantially softer (lower momentum) than those predicted by the DR scheme. The uncertainty on the m_{Vh} spectrum from this source of modelling uncertainty ranges from $+5\%$ to -100% for the resolved m_h SR or $+20\%$ to -100% for the boosted m_h SR. The magnitude of the uncertainty is consistent across all regions of the 1-lepton fit model.

Furthermore, looking at the boosted regime, the DS scheme (red) spectrum vanishes for $m_{Vh} > 1.5$ TeV, however the DR scheme (black) still has a substantial tail. The smoothing function is derived by fitting to the ratio, meaning that the 0 TeV $< m_{Vh} <$ 1.5 TeV range drives the functional form of the uncertainty. This uncertainty must then be extrapolated to the $m_{Vh} > 1.5$ TeV tail within the fit, which brings with it some large degree of uncertainty.

It is a well known problem [154, 168] that Wt and $t\bar{t}$ are not fundamentally separable processes. This is because at NLO in QCD the Wt sub-process receives corrections from doubly resonant $t\bar{t}$ production; one of the top-quarks in the pair decays according to $t \to Wb$ giving rise to the process $\alpha\beta \to Wt + b$. Where α/β represent incident partons. One can denote the amplitude of Wt production at NLO as:

$$\mathcal{A}_{Wt}^{\text{NLO}} = \mathcal{A}_1 + \mathcal{A}_2 \tag{18.7}$$

$$\to |\mathcal{A}_{Wt}^{\text{NLO}}|^2 = |\mathcal{A}_1|^2 + 2\text{Re}[\mathcal{A}_1\mathcal{A}_2^\dagger] + |\mathcal{A}_2|^2, \tag{18.8}$$

where $\mathcal{A}_1$ represents the diagrams with a single top quark, either virtual or real, whilst $\mathcal{A}_2$ corresponds to the doubly resonant $t\bar{t}$ diagrams where there are two intermediate top-quark pairs. Taking the squared amplitude (second line), introduces a Wt and $t\bar{t}$ interference term.

The DR scheme overcomes this problem by removing the $t\bar{t}$ resonant diagrams directly from the amplitude prior to the calculation, i.e. reducing the matrix element down to $|\mathcal{A}_1|^2$. However in the case of the DS scheme, the resonant $t\bar{t}$ diagrams are removed at the cross-section level by introducing a locally dependent cross-section estimate that cancels

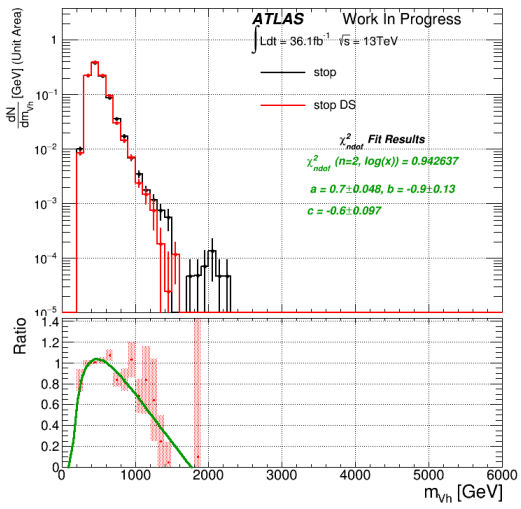

(a) Resolved m_h SR

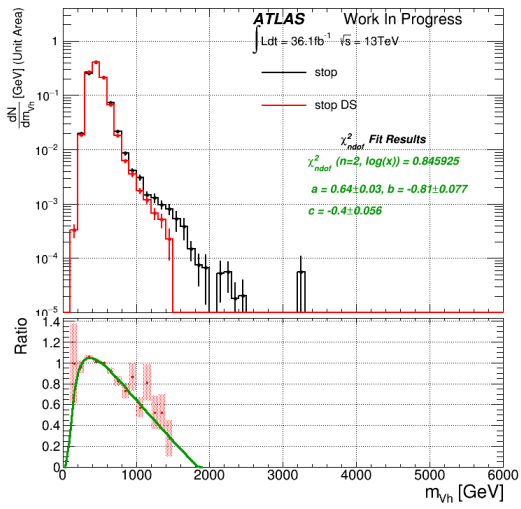

(b) Resolved m_h CR

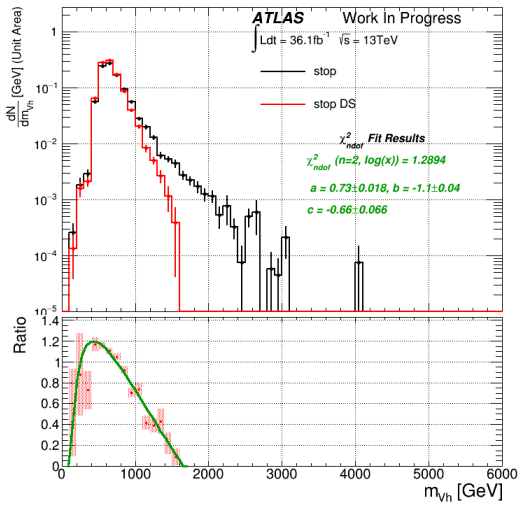

(c) Boosted m_h SR

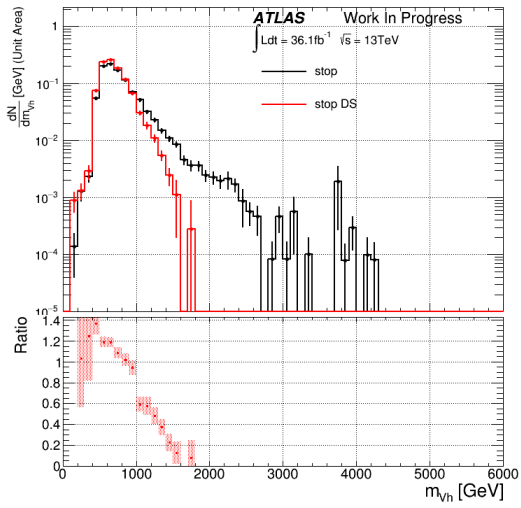

(d) Boosted m_h CR

Figure 18.13.: 2-point MC-to-MC comparisons of the DR (nominal = black) and DS (variation = red) schemes for the resolved and boosted m_h SRs and CRs in the 1-lepton channel. It should be noted that no functional form was capable of capturing the shape of the ratio for the Boosted m_h CR, due to the step at $m_{Vh} = 1$ TeV, therefore none are shown.

the $|\mathcal{A}_2|^2$ term after integrating over the fiducial phase space. Consequently, the DS scheme leaves behind the interference terms, and therefore the DR and DS schemes agree reasonably well only when the interference terms are negligible, which can be the case if the event selection isolates and enriches only one of these processes.

However, given that the event selection outlined in Chapters 13-15 is inclusive of both the Wt and $t\bar{t}$ process, it is therefore questionable as to whether the DS-vs-DR MC comparison is meaningful when in a fiducial phase space region where the interference terms are non-negligible. Bearing in mind the extrapolation concerns above as well, it was decided to drop the DS-vs-DR systematic from the analysis.

$t\bar{t}$ Acceptance & Normalisation Priors

Using equations 18.1 and 18.2, the normalisation and acceptance priors for the $t\bar{t}$ process are derived using the same MC-to-MC comparisons outlined in Section 18.3.2. The four MC-to-MC comparisons (ME, PS, and Radiation sensitive comparisons) yield three estimates of the normalisation and acceptance prior; the average of the two RadHi and RadLo priors is taken, thereby reducing the total number of priors by 1.

Table 18.10 summarises the derived priors for each channel, where the *normalisation* priors take the string format *norm_ttbar_L* and labelled *normalisation* under the effect column, however the global $t\bar{t}$ normalisation is controlled by a freely floating nuisance parameter, therefore these priors are never used within the analysis and are only shown for completeness. The *acceptance* priors take the string format *'ttbar_'*, and are labelled *acceptance* in the effect column.

Single Top Acceptance & Normalisation Priors

Using equation 18.1 and 18.2, the normalisation and acceptance priors are calculated. Like the $t\bar{t}$ priors, the four common sets of MC-to-MC comparisons (ME, PS and Radiation sensitive comparisons) yield three estimates of the normalisation/acceptance prior. Unique to the single top process, the additional DR-vs-DS comparison introduces an additional comparison, yielding a total of four estimates of the priors. Two sets of calculations are presented, with (w/) and without (w/o) the DS-vs-DR comparisons, which can be found in Table 18.11, however the priors used within the fit are those calculated when excluding the DS-vs-DR comparison.

The DS-vs-DR comparison is shown to illustrate the large effect that this comparison has on the ratio of the boosted to resolved event yield. The event yield predicted by the DS scheme for the resolved(boosted) regime is approximately 3.07(33.6)% smaller than the DR scheme. This drives the large Boosted/Resolved acceptance prior, which can be seen in the aforementioned table to be 36% when including the DS scheme, and 24% when excluding the DS scheme from the calculation.

Nuisance Parameter	Description	Samples/Categories	Value	Effect
		0-lepton		
norm_ttbar_L0	$t\bar{t}$ normalisation	All kinematic regions and 1-/2-tag regions	13%	normalisation
ttbar_ResMergedRatio_L0	boosted / resolved ratio	$t\bar{t}$, boosted regions	15%	acceptance
ttbar_mbbCatRatio_L0	SR / CR ratio	$t\bar{t}$, m_h sideband and SR window	6% (11%) resolved (boosted)	acceptance
		1-lepton		
norm_ttbar_L1	$t\bar{t}$ normalisation	All kinematic regions and 1-/2-tag regions	24%	normalisation
ttbar_ResMergedRatio_L1	boosted / resolved ratio	$t\bar{t}$, boosted regions	26%	acceptance
ttbar_mbbCatRatio_L1	SR / CR ratio	$t\bar{t}$, m_h sideband and SR window	7% (5%) resolved (boosted)	acceptance
ttbar_L0_Ratio_L1	Ratio of 0-lepton/1-lepton inclusive of all fit regions	All $t\bar{t}$ regions for each channel	28%	acceptance
		2-lepton		
norm_ttbar_L2	$t\bar{t}$ normalisation	All kinematic regions and 1-/2-tag regions	23%	normalisation
ttbar_ResMergedRatio_L2	boosted / resolved ratio	$t\bar{t}$, boosted regions	46%	acceptance
ttbar_mbbCatRatio_L2	SR / CR ratio	$t\bar{t}$, m_h sideband and SR window	3.4% (22%) resolved (boosted)	acceptance
ttbar_L0_Ratio_L2	Ratio of 0-lepton/2-lepton inclusive of all fit regions	All $t\bar{t}$ regions for each channel	26%	acceptance

Table 18.10.: Summary of $t\bar{t}$ specific nuisance parameter priors for the 0-/1-/2-lepton channels, derived using the comparisons outlined in section 18.3.2. The first column quotes the name of the nuisance parameter, the second column the source of the uncertainty, the third summarises the fit regions it effects, the fourth column gives the prior (if applicable), and the fifth column the effect of the systematic uncertainty.

Nuisance Parameter	Description	Samples/Categories	Value	Effect
StopNorm	Single Top (s-/t-/Wt inclusive) normalisation	All kinematic regions and 1-/2-tag regions	19% (21% with DS)	normalisation
stop_ResMergedRatio_L1	boosted / resolved ratio	Single Top, boosted regions	24% (36% with DS)	acceptance
stop_mbbCatRatio_L1	SR / CR ratio	Single Top,m_h sideband and SR window	resolved : 7(7)%, boosted 5(9)% w/o(w/) DS	acceptance

Table 18.11.: Summary of the single top nuisance parameter priors for the 1-lepton channel derived using the event yield predictions from the nominal setup and the alternative MC generator comparisons, fed into equation 18.2. The first column quotes the name of the nuisance parameter, the second column the source of the uncertainty, the third summarises the fit regions it effects, the fourth column gives the prior (if applicable), and the fifth column the effect of the systematic uncertainty. The priors with (w/) and without (w/o) the Diagram Subtraction scheme comparisons are provided for completeness.

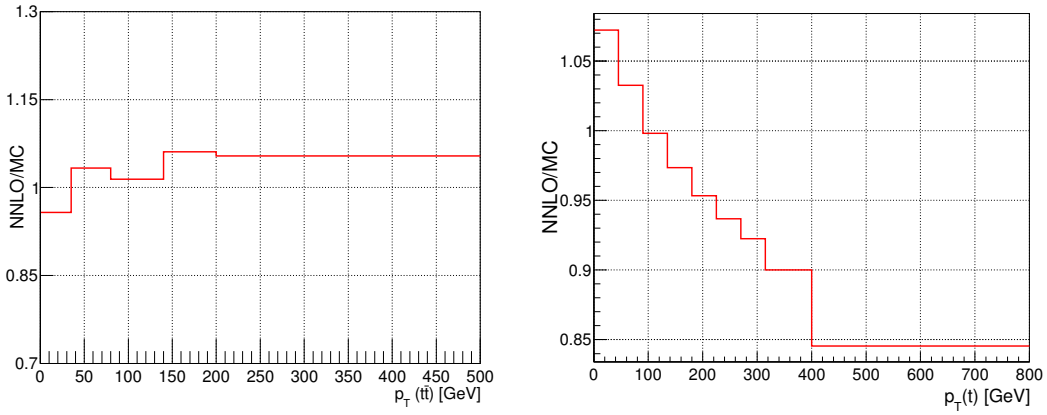

(a) **(b)**

Figure 18.14.: The $p_T(t\bar{t})$ and $p_T(t)$ ((anti-)top quark) re-weighting distributions as used within the 0-/1-/2-lepton analysis.

18.3.3. $t\bar{t}$ NNLO Re-weighting

It was highlighted in Section 15.1.1 that a mismodelling in the m_{Vh} distribution was observed for the 1-lepton $m_h > 140$ GeV region; this region is dominated by $t\bar{t}$ background and so the likely candidate for causing the problem. It was found upon further investigation that the p_T^V and m_h distribution also suffered from a substantial data/MC disagreement. Figure 18.16a and Figure 18.16b illustrate this point, by showing the discrepant data/MC predictions within an enriched $t\bar{t}$ region. From these figures it can be seen that the combined experimental, modelling, and statistical sources of uncertainty fail to envelop the data/MC disagreement, meaning that the data/MC agreement falls outside of the total $\pm 1\sigma$ error band placed on the MC. This observation was corroborated by the SM $Vhbb$ measurement given by Ref. [169], which shares a very similar fiducial phase space.

In order to help correct this discrepancy, the simulated $t\bar{t}$ process using Powheg-Box v2+Pythia 6 is re-weighted to match the differential cross-section calculated at NNLO given by Ref. [170]. This is achieved by re-weighting the (anti-)top quark and $t\bar{t}$ p_T distributions to match the NNLO spectrum, where the $p_T(t\bar{t})$ re-weighting is applied first, and the $p_T(t)$ re-weighting second. In the latter case the re-weighting function for the (anti-)top quark p_T distribution is obtained by taking the ratio between the $p_T(t\bar{t})$ corrected MC prediction and fixed order NNLO prediction. Figure 18.14 shows the $p_T(t\bar{t})$ and $p_T(t)$ re-weighting functions as used within the analysis.

To cover the uncertainty attributed to this correction, the difference between the uncorrected $t\bar{t}$ and NNLO corrected $t\bar{t}$ prediction is symmetrised and used as a systematic

shape difference. This systematic by construction incorporates both a normalisation and shape component, therefore the normalisation component is removed at the fit stage by normalising the systematic to the same area as the nominal prediction.

Figure 18.15 shows an example of the effect of the $t\bar{t}$ NNLO re-weighting on the m_{Vh} and p_T^V distributions, referred to as NNLORW from here on in, for the most problematic region within the 1-lepton analysis. For the resolved 1-tag 140 GeV $< m_h <$ 200 GeV CR region, both the m_{Vh} and p_T^V spectrums show a substantial data/MC disagreement with a $\chi^2/n_{\text{dof}} = 3.92$ and $\chi^2/n_{\text{dof}} = 5.87$, respectively, when normalising MC and data to the same area (shape only). However, when the NNLORW correction is applied the shape discrepancy is slightly improved in the case of the m_{Vh} distribution, $\chi^2/n_{\text{dof}} = 2.98$, whilst in the case of the p_T^V spectrum, the Data/MC agreement demonstrates a substantial improvement in the shape only agreement, $\chi^2/n_{\text{dof}} = 2.19$.

18.4. Data/MC agreement

The previous sections of this chapter outlined the systematic sources of uncertainty that impact either the shape or normalisation of the $m_{Vh}^{(T)}$ fit templates. With these defined, the level of compatibility between the data and SM only hypothesis, where the latter corresponds to the combined MC/data-driven $m_{Vh}^{(T)}$ templates representing SM only processes, can now be evaluated. As touched on in Sections 15.1.1 and 18.3.3, the only statistically significant disagreement between the data and expected SM only hypothesis (calculated using MC and data-driven methods), was the data/MC issues found within the 1-lepton 140 GeV $< m_h <$ 200 GeV sideband CR of the resolved analysis, which is largely attributed to a mismodelling of the $t\bar{t}$ SM process.

18.4.1. Pre-fit Data/MC

The underlying issue is illustrated by Figure 18.16a, which shows the m_{Vh} data/MC spectrum for the aforementioned region, with the full statistical and systematic sources of uncertainty shown in the ratio pane. The event selection in this case is loosened by requiring $n_{\text{jet}}^{\text{sig}} \geq 2$, which results in a larger $t\bar{t}$ contribution, in order to show the full extent of the mismodelling. The full statistical and systematic error on the data/MC agreement is given by the red band, whilst the green shows just the experimental sources of uncertainty added in quadrature to the statistical error. Note that in this plot the $t\bar{t}$ NNLO re-weighting has not been applied.

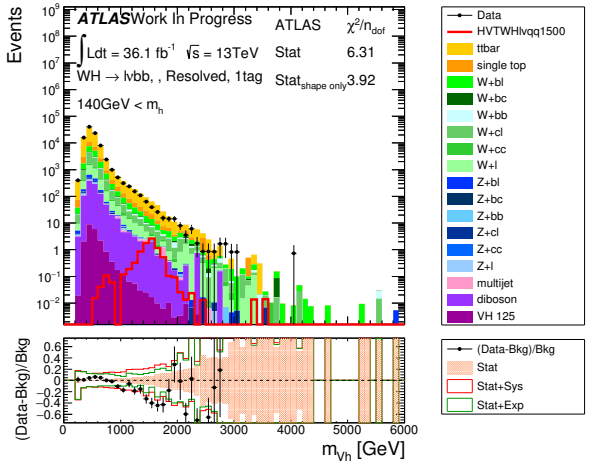

(a) NNLORW off

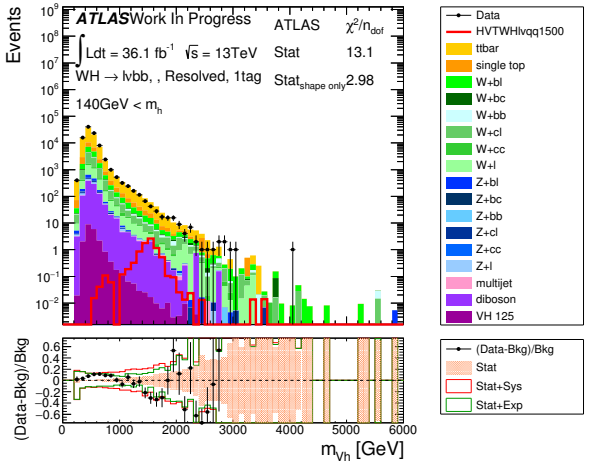

(b) NNLORW on

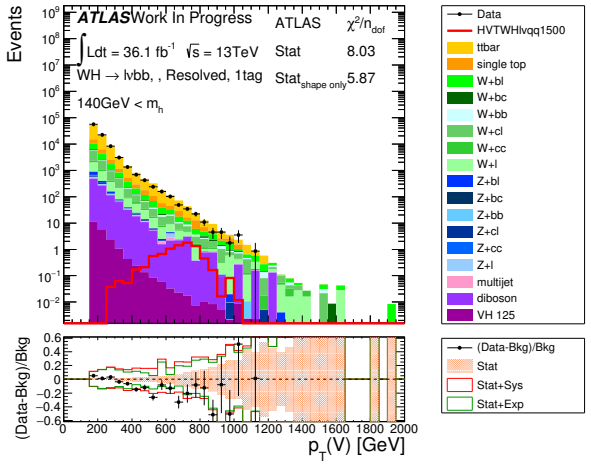

(c) NNLORW off

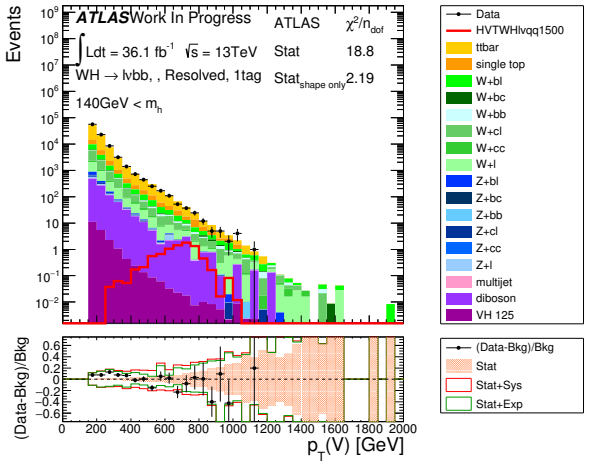

(d) NNLORW on

Figure 18.15.: Pref-fit m_{Vh} and p_T^V Data/MC plot for the 1-lepton HVT analysis in the resolved 1-tag 140 GeV $< m_h <$ 200 GeV region, when the $t\bar{t}$ NNLORW is not applied as a correction (a+c) and when it is used a correction (b+d). The event selection is loosened slightly to $n_{jet}^{\text{sig}} \geq 2$ for an enriched $t\bar{t}$ contribution.

As is shown, the differential event yield as a function of m_{Vh} for the data progressively underestimates the expected event yield calculated using the SM only (null) hypothesis. This is shown as a slope in the data when looking at the ratio pane, which extends beyond the -1σ statistical+systematic error band in the 1400 GeV $< m_{Vh} <$ 1800 GeV range. This is mimicked in the p_T^V distribution as well, which is shown by sub-figure 18.16b.

Restoring the nominal event selection, the $2 \leq n_{\text{jet}}^{\text{sig}} \leq 3$ cut, sub-figure 18.16c shows the data/MC agreement when the $t\bar{t}$ NNLO re-weighting is turned off (no systematic or correction). In this situation it can be seen that the data/MC agree only when all sources of uncertainty, statistical and systematic (red error band), are considered. However when considering only the statistical and experimental uncertainties (green band), several data bins extend beyond the $\pm 1\sigma$ error band, and so are considered significant deviations.

Fortunately when applying the NNLORW to the $t\bar{t}$ process, as shown by sub-figure 18.16e, and using the corresponding systematic for this correction the data/MC disagreement is improved. This is illustrated best by analysing the figures sequentially from 18.16a→18.16c→18.16e, where it becomes apparent that the shape discrepancy between the data and MC is reduced by applying the tighter cuts and applying the NNLORW as a correction. This is best demonstrated by the χ^2/n_{dof} values after normalising the data and MC to the same integrated area ($\text{Stat}_{\text{shape only}}$), where a reduction from $3.92 \rightarrow 1.73$ [3] can be observed.

This mismodelling was observed in other variables such as p_T^V, where an example of the mismodelling is shown by the right column of Figure 18.16. The same format as that for the m_{Vh} applies. The remaining regions of the analysis demonstrated no significant disagreements initially, nor any substantial issues when applying the additional cuts and the $t\bar{t}$ NNLORW.

[3] Please note that the drop in χ^2 value for 18.16a→18.16c is likely to include a contribution from the increase in the MC and data statistical error, when re-applying the $n_{\text{jet}}^{\text{sig}} < 4$ cut. However it is known that this does not account for the entire gain

(a) Loosened Evt Selection (NNLORW off)

(b) Loosened Evt Selection (NNLORW off)

(c) Default Evt Selection (NNLORW off)

(d) Default Evt Selection (NNLORW off)

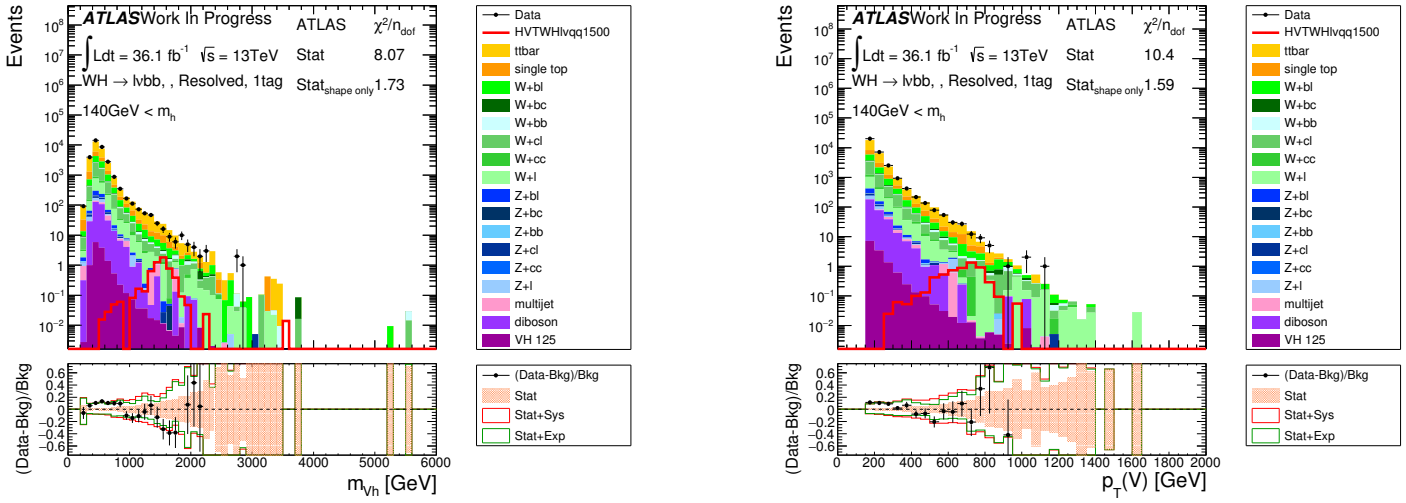

(e) Default Evt Selection - NNLORW Syst+Corr

(f) Default Evt Selection - NNLORW Syst+Corr

Figure 18.16.: Data/MC agreement pre-fit plots for the 1-lepton HVT analysis, in the 140 GeV $< m_h <$ 200 GeV resolved sidebands. The left column shows m_{Vh}, and the right column shows p_T^V. The top row corresponds to a loosened event selection on the $n_{\text{jet}}^{\text{sig}}$ variable with no $t\bar{t}$ NNLO re-weighting. The middle row shows the data/MC for the nominal event selection with no $t\bar{t}$ NNLO re-weighting. The bottom row shows the data/MC for the nominal event selection, but includes the $t\bar{t}$ NNLO re-weighting as a correction and systematic.

18.4.2. Post-fit Data/MC & Fit Model Construction

The binned profile likelihood methodology outlined in Chapter 9 is by definition dependent on the fit regions that enter into the procedure. Furthermore, within the frequentist statistical paradigm, the significance of the hypothesised signal (BSM physics) is dependent on the ability to model the SM only (null) hypothesis. Therefore, to prevent the previously demonstrated modelling issues in the 1-lepton 1-tag resolved 140 GeV $< m_h <$ 200 GeV region from either inducing a false discovery or concealing new physics, various fit models were tested to ensure that the data and SM only hypothesis agree to within $\pm 1\sigma$ of the total statistical and systematic error band, once the background uncertainties have been constrained through the use of the CR auxiliary measurements.

The simplest fit model that can be constructed is one that includes only the signal regions, which within the HVT analysis (1-lepton channel only contributes to the HVT interpretation) includes the 1-tag and 2-tag m_h SRs for the resolved and boosted regimes; this is referred to as *fit model A*. This fit model can then be extended to include the resolved 1-tag and 2-tag m_h sideband regions, followed by the addition of the boosted 1-tag and 2-tag m_h sideband regions, where these serve as control regions used in the profiling of the SM background processes. These models are referred to as *fit model B* and *fit model C*, respectively. Table 18.12 summarises the analysis regions used within the three fit models tested.

Each fit model is tested by comparing the exclusion capability of each model under an unconditional $\mu = 1$ fit using the Asimov dataset. In addition to this an unconditional fit to the data is performed, in order to test the data and SM only hypothesis, called data/MC agreement for short, within the control regions of the analysis. During these tests the data/MC post-fit plots within the SR, and μ value remain blinded in order to prevent any discovery bias from being introduced.

Figure 18.17 shows the previously problematic 1-tag resolved m_h control region under the unconditional μ fit for the three aforementioned fit models. As can be seen, little

Fit Model	**Resolved Regions**		**Boosted Regions**		
...	m_h SR	m_h CR	m_h SR 0 add. tag	m_h CR 0 add. tag	m_h SR 1 add. tag
A	✓	...	✓	...	...
B	✓	✓	✓	...	...
C	✓	✓	✓	✓	✓

Table 18.12.: Summary of analysis regions included within 1-lepton fit model tests.

difference in the Data/MC agreement can be observed when comparing fit models B and C. In the case of fit model A, the Data/MC ratio falls outside of the statistical and systematic error bands (depicted as black hatched markings in the ratio pane) for the 1-tag resolved m_h control region.

This discrepancy was found to be primarily caused by the small contribution of the W+hl process within the resolved SRs, when compared to the other dominant background processes such as $t\bar{t}$ and single top. Specifically, the 1-tag resolved m_h control region not only has ≈ 3 times more events than the m_h signal region, but as shown by Figure 18.21a and Figure 18.21c, the relative contribution of the W+cl and W+bl sub-processes to the total event yield is 50% larger in the control region. Consequently, the larger event population and relative contribution of the $W + b/c$l sub-processes within the m_h CRs results in a reduced statistical uncertainty on the m_{Vh} templates, but also increases the sensitivity of the likelihood maximisation procedure to the presence of the $W + b/c$l sub-processes.

Therefore, under fit model A the statistical procedure had less information to constrain the W+hl background shape and normalisation; the freely floating W+hl normalisation parameter under an unconditional data fit yielded a value of $\theta^{\mathrm{A}}_{W+\mathrm{hl}} = 0.72 \pm 0.22$ for fit model A, whilst for fit model B(C) $\theta^{\mathrm{B(C)}}_{W+\mathrm{hl}} = 1.12(1.18) \pm 0.16(0.15)$. Therefore, on this basis fit model A is excluded as a viable fit model, due to the inability of the fit to obtain good agreement between the data and SM backgrounds.

Figures 18.18-18.19, show the boosted 1-tag and 2-tag categories for the 1+ add. tag region within the m_h signal window. These are the only other regions that demonstrated a dependency on their inclusion in the fit in order to meet the $\pm 1\sigma$ Data/MC compliance post-fit. As can be seen, fit models A and B, which exclude this region in the fit, suffer from a degraded Data/MC agreement when compared to fit model C. Naturally this leads to the conclusion that fit model C is realistically the only fit model that yields the necessary $\pm 1\sigma$ data/MC compliance across all phase space regions possible within the analysis.

Furthermore, in assessing the sensitivity performance of each fit model using the Asimov dataset, the expected exclusion limits show that the fully inclusive model, fit model C, offers the best limit setting capabilities. These expected exclusion limits are shown by Figure 18.20, where fit model A/B/C are shown as red/green/bue dotted curves, and the ratio pane shows the ratio of fit model A/B/C to fit model C. The superior exclusion capability of fit model C is an expected outcome due to the presence of a small amount of signal within the resolved and boosted analysis CRs, therefore by iteratively adding the resolved and then boosted CRs to the fit model (fit model A→B→C), the sensitivity of the analysis to the signal will grow accordingly. However, the benefits over fit model B are marginal given the extra complexity it adds in the form of additional nuisance parameters, like m_{Vh}

shape systematics, normalisation nuisance parameters, and additional extrapolation factors needed to account for event migrations between the larger pool of fit regions within the analysis.

Therefore, in considering the increased complexity of fit model C in terms of nuisance parameters, noting that the event yield within the boosted 1-/2-tag 1+ add. tag regions is an order of magnitude smaller than the other CRs, and realising that the 1+ add. tag boosted categories are topologically very different from the 0 add. tag SR/CRs of the boosted regime, the need for $\pm 1\sigma$ data/MC agreement within the 1+ add. tag regions is void, since this region does not serve as a strong validation region. Therefore, fit model B was adopted as outlined in Section 17.1.

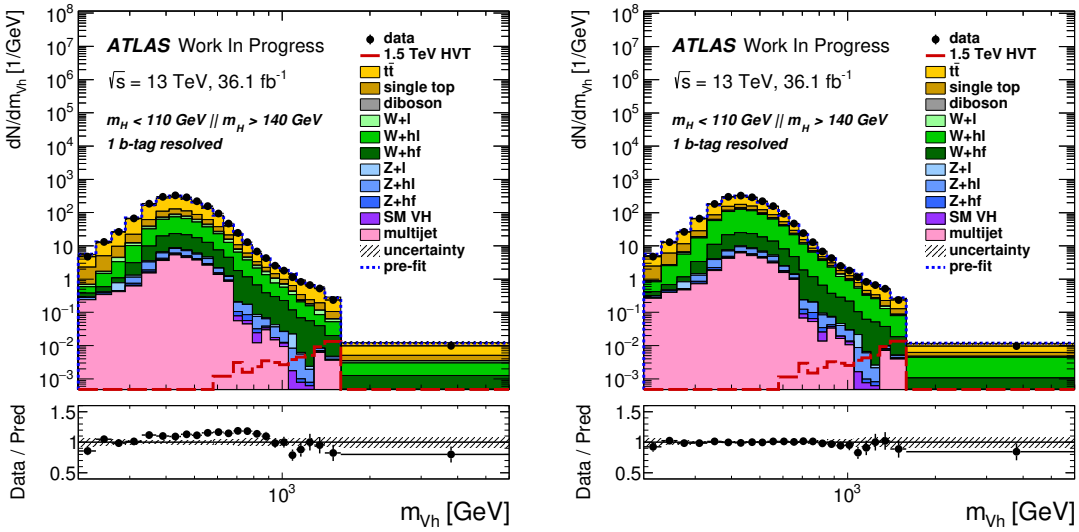

Fit Model A

Fit Model B

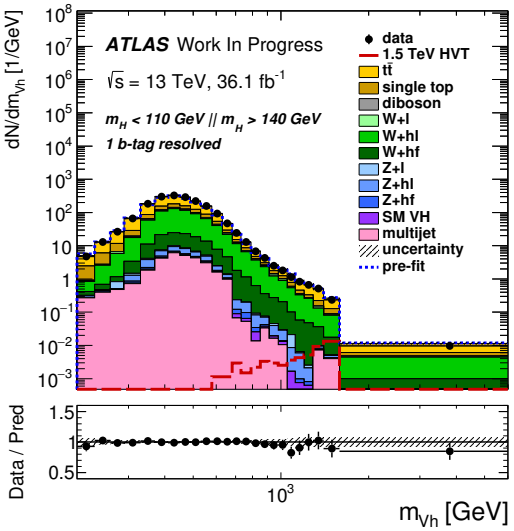

Fit Model C

Figure 18.17.: 1-lepton HVT post-fit Data/MC plots for the 1-tag resolved m_h control region, using an unconditional fit to data, under the three fit models A, B, and C.

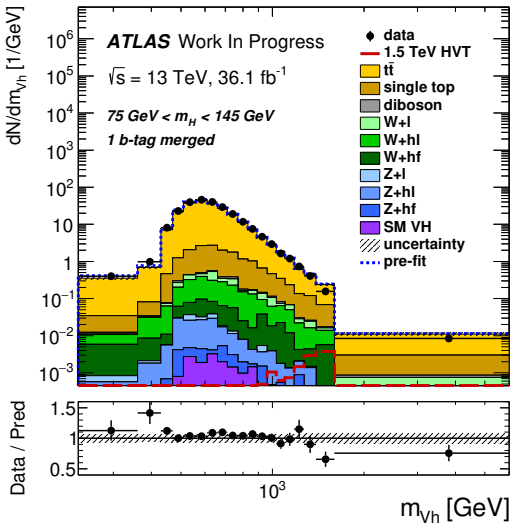

Fit Model A

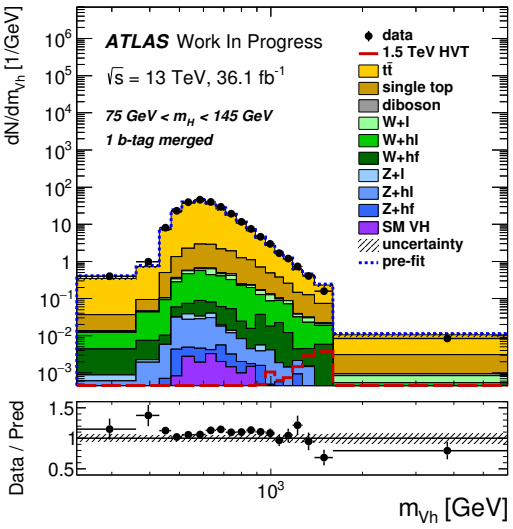

Fit Model B

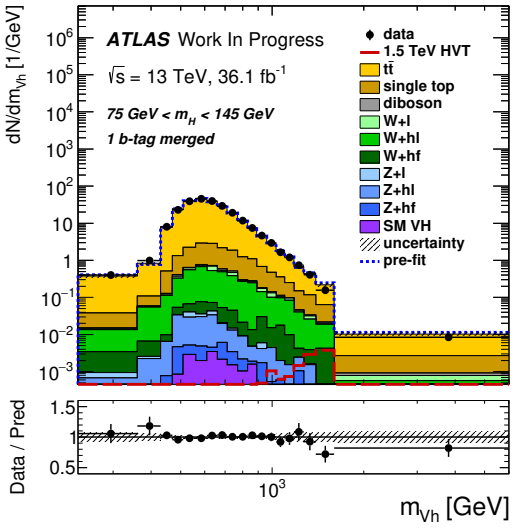

Fit Model C

Figure 18.18.: 1-lepton HVT post-fit Data/MC plots for the 1-tag boosted m_h signal region with 1+ additional b-tagged track-jets, using an unconditional fit to data, under the three fit models A, B, and C.

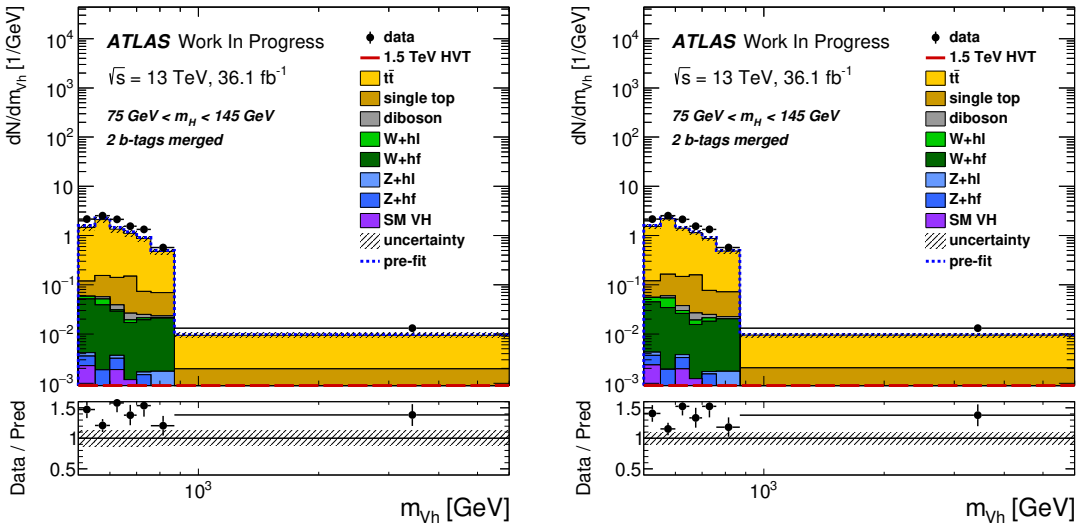

Fit Model A

Fit Model B

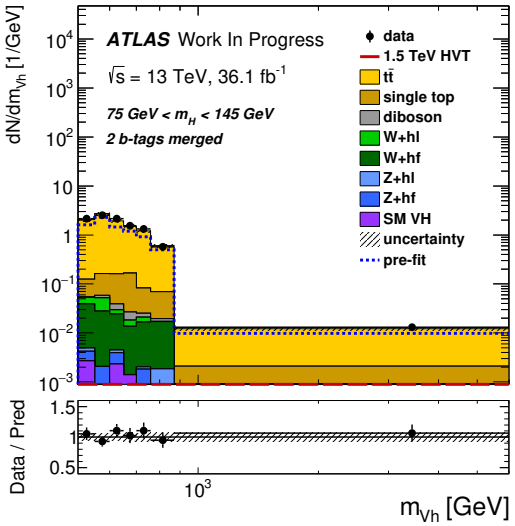

Fit Model C

Figure 18.19.: 1-lepton HVT post-fit Data/MC plots for the 2-tag boosted m_h signal region with 1+ additional b-tagged track-jets, using an unconditional fit to data, under the three fit models A, B, and C.

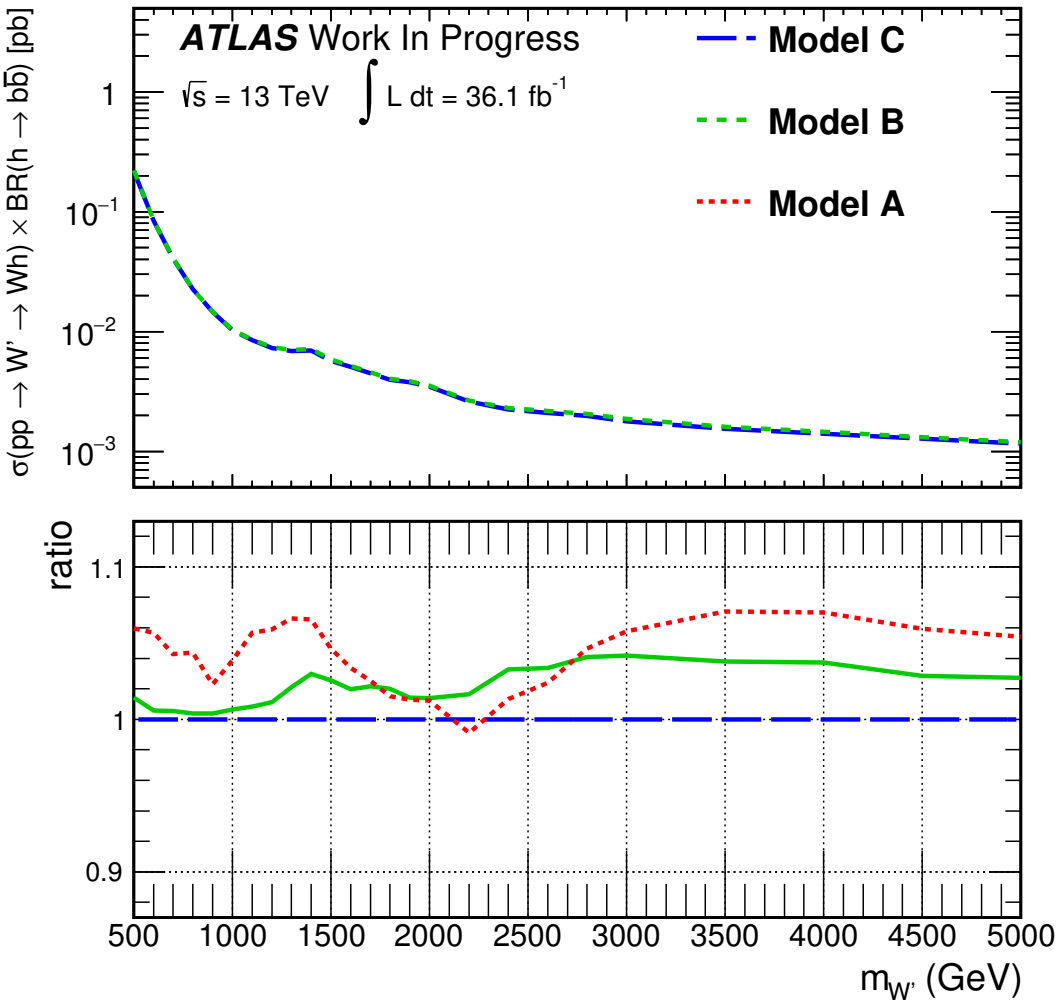

Figure 18.20.: Comparison of the expected limits for fit models A, B, and C, using the Asimov dataset with injected signal

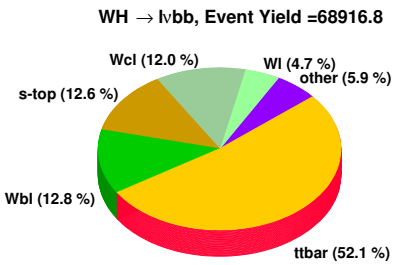

(a) 1-tag Resolved CR

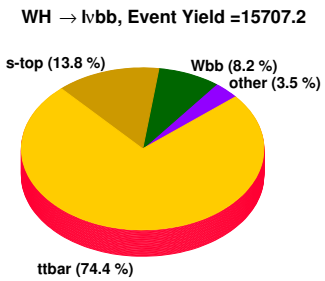

(b) 2-tag Resolved CR

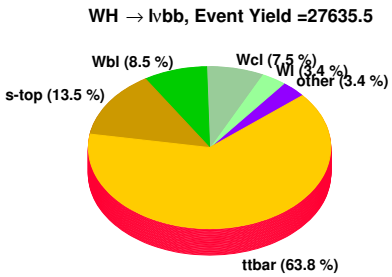

(c) 1-tag Resolved SR

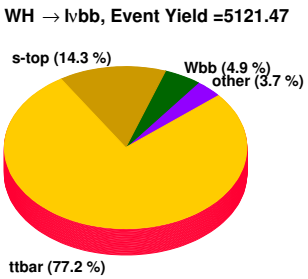

(d) 2-tag Resolved SR

Figure 18.21.: 1-lepton PRSR SM background composition for the resolved regime divided into the m_h SRs and CRs, in addition to the 1-/2-tag categories.

18.5. Summary of Normalisation and Shape Systematic Nuisance Parameters

Following the methodology outlined in Chapter 9, the systematics given above are included in the fit using the nuisance parameter scheme. All experimental systematic uncertainties listed in Table 18.1 are included in the fit using the constrained nuisance parameter prescription. The modelling systematic uncertainties described in Section 18.3, are implemented using two types of nuisance parameters: shape only nuisance parameters use a prior of width 1, whilst normalisation nuisance parameters set their priors to the values quoted in Tables and 18.5–18.7, 18.10, and 18.11.

The exact priors assigned to these nuisance parameters are summarised in Tables 18.13–18.17. Besides the names of the nuisance parameters (corresponding to the names used in pull plots etc.) a short description of the nuisance parameter is given, on which samples/regions each nuisance parameter is applied, whether the nuisance parameter is a systematic affecting the shape, normalisation, or acceptance, and the value of the prior if applicable.

Nuisance Parameter	Description	Samples/Categories	Value		Effect
			0-/2-lepton	1-lepton	
norm_Zbb	Zhf normalisation	Zhf, all 1- / 2-tag regions	Float	31%	normalisation
norm_Zclbl	Zcl+Zbl normalisation	Z+hl, all 1- / 2-tag regions	Float	20%	normalisation
norm_Zjets_3ptag	Zhf+Zcl+Zbl normalisation	Zhf, Zcl and Zbl, all 3+-tag regions	Float	N/A	normalisation
ZlNorm	Zl normalisation	Zl, all 1-/2-tag regions	19%		normalisation
Zbb_ResMergedRatio	boosted / resolved ratio	Zhf, boosted regions	19%		acceptance
Zclbl_ResMergedRatio	boosted / resolved ratio	Z+hl, boosted regions	28%		acceptance
Zl_ResMergedRatio	boosted / resolved ratio	Zl, boosted regions	23%		acceptance
Zbb_LepRatio	0-lepton / 2-lepton ratio	Zhf, 0-lepton regions	15%	N/A	acceptance
Zclbl_LepRatio	0-lepton / 2-lepton ratio	$Zclbl$, 0-lepton regions	12%	N/A	acceptance
Zl_LepRatio	0-lepton / 2-lepton ratio	Zl, 0-lepton regions	8%	N/A	acceptance
Zbb_mbbCatRatio	SR / CR ratio	Zhf,m_h sideband	6% (8%) resolved (boosted)		acceptance
Zclbl_mbbCatRatio	SR / CR ratio	Z+hl, m_h sideband	4% (14%) resolved (boosted)		acceptance
Zl_mbbCatRatio	SR / CR ratio	Zl, m_h sideband	6% (5%) resolved (boosted)		acceptance
VjetsMadGraph_Zhf/Zclbl/Zl	m_{Vh} shape (Sherpa vs. MadGrpah)	Zhf/Z+hl/Zl, all regions, decorr. for 3+ tag	Applicable	N/A	shape-only
VjetsShRenorm_Zhf/Zclbl/Zl	m_{Vh} shape (Sherpa renorm. scale)	Zhf/Z+hl/Zl, all regions, decorr. for 3+ tag	Applicable	N/A	shape-only
VjetsShFac_Zhf/Zclbl/Zl	m_{Vh} shape (Sherpa fact. scale)	Zhf/Z+hl/Zl, all regions, decorr. for 3+ tag	Applicable	N/A	shape-only
VjetsShAlphaPDF_Zhf/Zclbl/Zl	m_{Vh} shape (Sherpa α_s PDF scale)	Zhf/Z+hl/Zl, all regions, decorr. for 3+ tag	Applicable	N/A	shape-only
Total	10 (9) with priors, 3 (0) floating, 24 (0) shape-only for the 0-/2-lepton (1-lepton) channels				

Table 18.13.: Summary of the Z+jets systematic uncertainties that are decorrelated between the different flavour components. For details on the evaluation of these systematics see Section 18.3.

Nuisance Parameter	Description	Samples/Categories	Value		Effect
			0-/2-lepton	1-lepton	
WbbNorm	Whf normalisation	Whf, all regions	26%	Float	normalisation
WblclNorm	Wcl normalisation	W+hl, all regions	23%	Float	normalisation
WlNorm	Wl normalisation	Wl, all regions	20%	30%	normalisation
Wbb_ResMergedRatio	boosted / resolved ratio	Whf, boosted regions	43%	28%	acceptance
Wblcl_ResMergedRatio	boosted / resolved ratio	W+hl, boosted regions	35%	15%	acceptance
Wl_ResMergedRatio	boosted / resolved ratio	Wl, boosted regions	20%	16%	acceptance
Wbb_LepRatio	0-lepton / 1-lepton ratio	Zhf, 0-lepton regions	26%	N/A	acceptance
Wclbl_LepRatio	0-lepton / 1-lepton ratio	$Wclbl$, 0-lepton regions	22%	N/A	acceptance
Wl_LepRatio	0-lepton / 1-lepton ratio	Wl, 0-lepton regions	19%	N/A	acceptance
Wbb_mbbCatRatio	SR / CR ratio	Whf, m_h sideband	6% (15%)	2% (6%) resolved (boosted)	acceptance
Wclbl_mbbCatRatio	SR / CR ratio	W+hl,m_h sideband	5% (2%)	1% (1%) resolved (boosted)	acceptance
Wl_mbbCatRatio	SR / CR ratio	Wl, m_h sideband	2% (3%)	7% (3%) resolved (boosted)	acceptance
VjetsMadGraph_Whf/Wclbl/Wl	m_{Vh} shape (Sherpa vs. MadGraph)	Zhf/W+hl/Wl, all regions, decorr. for 3+ tag	0-lepton Only	Applicable	shape-only
VjetsShRenorm_Whf/Wclbl/Wl	m_{Vh} shape (Sherpa renorm. scale)	Zhf/W+hl/Wl, all regions, decorr. for 3+ tag	0-lepton Only	Applicable	shape-only
VjetsShFac_Whf/Wclbl/Wl	m_{Vh} shape (Sherpa fact. scale)	Zhf/W+hl/Wl, all regions, decorr. for 3+ tag	0-lepton Only	Applicable	shape-only
VjetsShAlphaPDF_Whf/Wclbl/Wl	m_{Vh} shape (Sherpa α_s PDF scale)	Zhf/W+hl/Wl, all regions, decorr. for 3+ tag	0-lepton Only	Applicable	shape-only
Total	12/7/9 with priors, 0/0/2 floating, 12/0/12 shape-only for the 0-/2-/1-lepton channels				

Table 18.14.: Summary of the W+jets systematic uncertainties that are decorrelated between the different flavour components. For details on the evaluation of these systematics see Section 18.3.

Nuisance Parameter	Description	Categories	Value			Effect
			0-lepton	1-lepton	2-lepton	
norm_ttbar_L0	$t\bar{t}$ normalisation	0-lepton, all regions	Float	N/A	N/A	normalisation
norm_ttbar_L1	$t\bar{t}$ normalisation	1-lepton, all regions	N/A	Float	N/A	normalisation
norm_ttbar_L2	$t\bar{t}$ normalisation	2-lepton, all 1- / 2-tag regions	N/A	N/A	Float	normalisation
norm_ttbar_3pTag_L2	$t\bar{t}$ normalisation	2-lepton, all 3+-tag regions	N/A	N/A	Float	normalisation
ttbar_ResMergedRatio_L0	boosted / resolved ratio	All resolved and boosted regions, 0L	15%	N/A	N/A	acceptance
ttbar_ResMergedRatio_L1	boosted / resolved ratio	All resolved and boosted regions, 1L	N/A	26%	N/A	acceptance
ttbar_ResMergedRatio_L2	boosted / resolved ratio	All resolved and boosted regions, 2L	N/A	N/A	46%	acceptance
ttbar_mbbCatRatio_L0	m_h SR / m_h CR ratio	m_h signal and sideband regions, 0L	6% (11%) resolved (boosted)	N/A	N/A	acceptance
ttbar_mbbCatRatio_L1	m_h SR / m_h CR ratio	m_h signal and sideband regions, 1L	N/A	7% (5%) resolved (boosted)	N/A	acceptance
ttbar_mbbCatRatio_L2	m_h SR / m_h CR ratio	m_h signal and sideband regions, 2L	N/A	N/A	3.4% (22%) resolved (boosted)	acceptance
ttbar_topemuRatio_L2	top $ee + \mu\mu$ m_h SR / top $e\mu$ m_h SR, 2L	$ee + \mu\mu$ and $e\mu$ m_h SR window regions	N/A	N/A	2.4%; decorr. for 3+ tag	acceptance
NNLORW_L0/L1/L2	Impact of re-weighting $t\bar{t}$ & top p_T to NNLO	all regions	Applicable			shape + normalisation
TTbar_Herwig_L0/L1/L2	m_{Vh} shape (parton shower)	all 0-/1-/2-lepton regions; decorr. for 3+ tag in 2-lepton	Applicable			shape-only
TTbar_aMCAtNlo_L0//L1/L2	m_{Vh} shape (ME)	all 0-/1-/2-lepton regions; decorr. for 3+ tag in 2-lepton	Applicable			shape-only
TTbar_rad_L0/L1/L2	m_{Vh} shape (ISR/FSR)	all 0-/1-/2-lepton regions; decorr. for 3+ tag in 2-lepton	Applicable			shape-only
Total	2/2/3 with priors, 1/1/2 floating, 1/1/1 shape + normalisation, 3 shape-only for the 0-/1-/2-lepton channels					

Table 18.15.: Summary of the $t\bar{t}$ systematic uncertainties decorrelated between 0-/1-/2-lepton channels. For details on the evaluation of these systematics see Section 18.3.

Nuisance Parameter	Description	Categories	Value			Effect
			0-lepton	1-lepton	2-lepton	
StopNorm	single-top normalisation	s-/t- and Wt-channel, all regions	19%			normalisation
Stop_ResMergedRatio	boosted / resolved ratio	s-/t- and Wt-channel, boosted regions	24%			normalisation
Stop_mbbCatRatio	SR / CR ratio	Resolved m_h sideband for s-/t- and Wt-channel	7% (5%) resolved (boosted)			normalisation
Stop_Herwig_L1	m_{Vh} shape (parton shower)	all 1-lepton regions	N/A	Applicable	N/A	shape-only
Stop_aMCAtNlo_L1	m_{Vh} shape (ME)	all 1-lepton regions	N/A	Applicable	N/A	shape-only
Stop_rad_L1	m_{Vh} shape (ISR/FSR)	all 1-lepton regions	N/A	Applicable	N/A	shape-only
Total	3/3/3 with priors, 0/0/0 floating, 0/3/0 shape-only for the 0-/1-/2-lepton channels					

Table 18.16.: Summary of the single top systematic uncertainties decorrelated between 0-, 1-, and 2-lepton channels. For details on the evaluation of these systematics see Section 18.3.

Nuisance Parameter	Description	Categories	Value	Effect
		$t\bar{t}$+V/h		
ttVNorm	$t\bar{t}$+V normalisation	all regions	50%	normalisation
ttHNorm	$t\bar{t}$+h normalisation	all regions	50%	normalisation
		Diboson		
VVNorm	diboson normalisation	WW, WZ, ZZ, all regions	11%	normalisation
		AZh Signal		
AZhTheory	normalisation variation	all regions	2-8% (depending on mass point)	normalisation
HVT PDF	normalisation variation	all regions	1%	normalisation
HVT ISR/FSR	normalisation variation	all regions	3%	normalisation
		SM Vh		
HiggsNorm	normalisation variation	all regions	50%	normalisation
Total	8 with priors			

Table 18.17.: Summary of the systematic uncertainties for single-top, $t\bar{t}+V/h$, diboson, AZh signals and SM Vh processes.

Chapter 19.

Results

For the AZh and HVT analysis no significant excess is observed. As such, limits on the $\sigma_{\mathrm{HVT}/AZh}\,(m_{V'/A}) \times BR(h \to b\bar{b}/c\bar{c})$ are set using a 95% confidence level via the aforementioned $\mathrm{CL_s}$ method. This chapter will summarise the exclusion limits derived from the hypothesis testing. Additional information in the form of data/MC plots after applying the fit results, nuisance parameter pulls, and the nuisance parameter ranking plots are also provided.

Only the 1-lepton fit and V' fits are shown in full detail, Sections 19.2.1 and 19.2.2, due to the significant contributions from the author to the 1-lepton channel, and thus by extension, to the final V' result. It is expected that if an isotriplet extension to the SM exists then both the W' and Z' will manifest as predicted. Therefore the W' and Z' limits are shown in conjunction with the V' limits, however additional material related to these fits (nuisance parameter plots and post-fit plots) are omitted for clarity.

19.1. Presentation of Results

The results of the hypothesis testing detailed in Chapter 9, can be presented in a number of different ways. As such the following section will outline the methods used to present the results, specifically the post fit plots (Section 19.1.1), nuisance parameter pull values (Section 19.1.2), and the nuisance parameter rankings (Section 19.1.3).

19.1.1. Post Fit Plots

A first impression of the fit result is summarised in what is referred to as a *post-fit* plot. These plots take the input histograms to the fit, referred to as *pre-fit* plots, and apply the results of the fit to the MC and data-driven templates, in addition to the bin edges defined

by the strategy outlined in Section 17.3. In short, the normalisation and shape of the MC and data-driven templates are modified according to the maximised likelihood estimates of the nuisance parameters, $\hat{\vec{\theta}}$.

For the HVT analysis, the pre-fit and post-fit plots can be found in Section 19.2.1 for the 1-lepton fit, and Section 19.2.2 for the V' combined fit. For each figure, the plots in the left column correspond to the pre-fit plots, and those in the right column correspond to the post-fit plots.

19.1.2. Nuisance Parameter Pull Plots

The maximum likelihood estimated values for each of the constrained nuisance parameters, $\hat{\theta}_k$, used within the fit, are quoted using the *pull* value prescription. The pull value is defined as:

$$\text{pull} = \frac{\hat{\theta}_k - \theta_k^0}{\sigma_{\hat{\theta}_k}}, \tag{19.1}$$

where θ_k^0 is the initial value (0 or 1) of the k^{th} nuisance parameter, $\hat{\theta}_k$ represents the maximum likelihood estimate, and $\sigma_{\hat{\theta}_k}$ is the post-fit uncertainty on the nuisance parameters. By default the starting value of each shape and acceptance nuisance parameter is $\theta_k^0 = 0$, whilst for normalisation nuisance parameters $\theta_k^0 = 1$.

The post-fit uncertainty ($\sigma_{\hat{\theta}_k}$) assigned to each nuisance parameter is extracted from the diagonal elements of the covariance matrix of all nuisance parameters, $\mathbf{cov}(i,j)$. This is estimated from the inverse of the *Hessian* matrix, $\mathbf{H}_{ij}$, which represents the second derivative of the natural log of the maximum likelihood function: [73]

$$\mathbf{cov}(i,j) = \mathbf{H}_{i,j}^{-1} = \left[\frac{-\partial^2 \ln(L(\hat{\mu}, \hat{\vec{\theta}}))}{\partial\theta_i \partial\theta_j}\right]^{-1} \tag{19.2}$$

The floating nuisance parameters are the exception to this rule since they do not have an assigned prior uncertainty. Furthermore, since their initial central values are set to 1, these nuisance parameters are not shown as pull values, but instead shown below in tables representing background normalisation scale factors.

19.1.3. Nuisance Parameter Rankings

The impact of each nuisance parameter on the parameter of interest μ, is evaluated by performing scans of the likelihood function. Fixing one parameter θ_k, all other parameters are floated to maximise the likelihood, $\mathcal{L}(\theta_i) = \mathcal{L}(\hat{\mu}, \hat{\hat{\theta}}_1, ..., \theta_i, ..., \hat{\hat{\theta}}_N)$. This is repeated for all θ_k, therefore producing a scan of the nuisance parameter.

The difference between the maximised likelihood value $\mathcal{L}(\hat{\mu}, \hat{\theta}_1, ..., \hat{\theta}_N)$, and the $N-1$ dimensional scan of the likelihood function is then expressed via the negative logarithm:

$$\Delta\mathcal{L}(\theta_i) = -\Big(\ln(\mathcal{L}(\theta_i)) - \ln(\mathcal{L}(\hat{\mu}, \hat{\vec{\theta}})) \Big), \tag{19.3}$$

where $\Delta\mathcal{L}(\theta_i) = 0$ represents the global minimum. The scan is stopped when the log of the likelihood function decreases by half relative to the global maximum, i.e. $\Delta\mathcal{L}(\theta_i) = +1/2$ [171]. This equates to $\pm 1\sigma$ uncertainty interval for a given nuisance parameter.

At the extremes of the $\pm 1\sigma$ nuisance parameter interval, the variation in the $\hat{\mu}$ parameter is measured. This variation, $\Delta\hat{\mu}$, represents the corresponding uncertainty imparted by the nuisance parameter on the sensitivity of the analysis. This procedure is repeated for all nuisance parameters, and the results are ranked in descending order of $\Delta\hat{\mu}$. These nuisance parameter ranking plots can be found in Section 19.2.1 for the 1-lepton only fit.

19.2. HVT Results

19.2.1. 1-Lepton:

Local *p*-values & 95% Confidence Limits

Figure 19.1 shows for the 1-lepton only fit model the expected (dashed blue) and observed (solid black) local p-values, for the 24 simulated HVT signals ranging in mediator mass from 500 GeV to 5000 GeV. The smallest p-value is $p_{\text{min}} = 0.028$ at a mediator mass of $m_{W'} = 3$ TeV, which corresponds to a conditional probability significance of $\text{Z}_0 = 1.911$, therefore no excess compatible with a HVT W' candidate of any mass between 500 GeV to 5000 GeV was observed.

As a result of no statistically significant HVT signal observation, an upper limit on the signal cross-section, $\sigma^{\text{HVT}}_{W'}$, is extracted using the CL_s technique outlined in Chapter 9, which is shown by sub-figure 19.1b. For the latter, the observed limit (black) and expected limit (blue) are shown, along with the 68% (green) and 95% (yellow) confidence bands

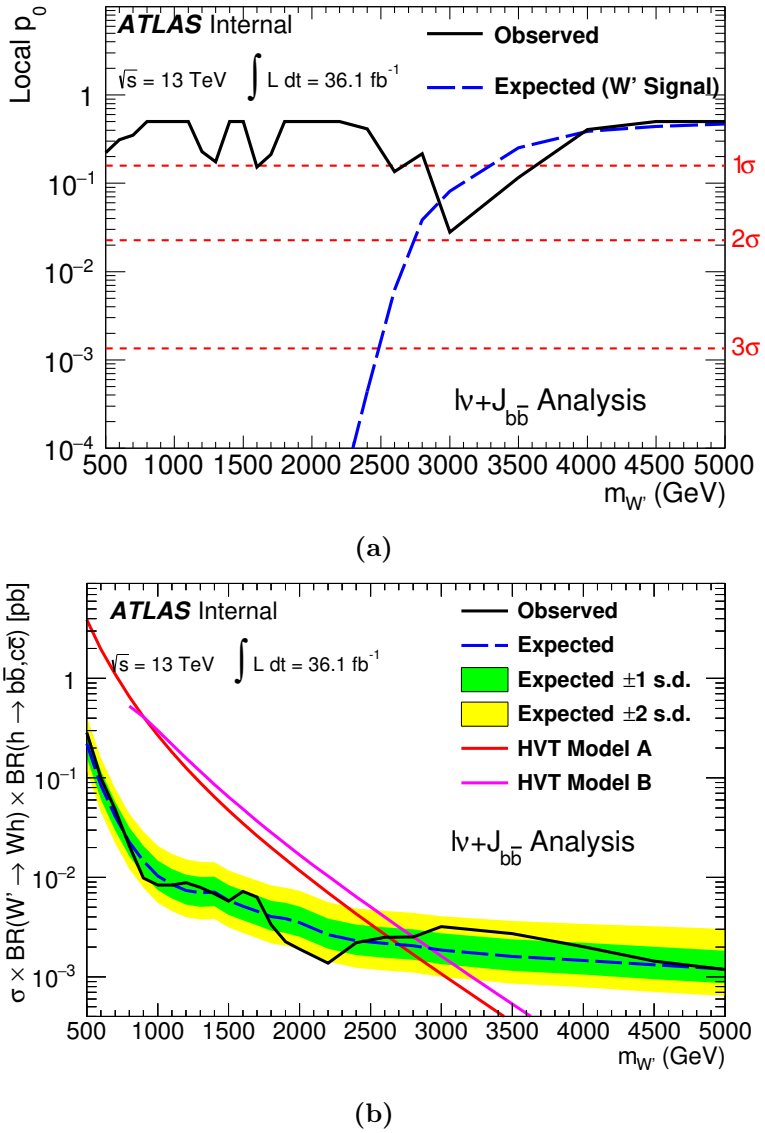

Figure 19.1.: 1-lepton HVT local p-values and 95% CL_s for the 24 mediator mass points from 500 GeV to 5000 GeV.

on the expected exclusion curve. Two benchmark models are shown, these are the HVT Model A and Model B, corresponding to the fermiophilic and fermiophobic coupling of the iso-triplet extension (see Chapter 4).

Pre- and Post-Fit plots

Figure 19.2 shows the pre-fit and post-fit plots for the four resolved regions included within the 1-lepton fit using a single W' HVT signal sample of mass $m_{W'} = 1.5$ TeV (red line).

Typically it was found that at the pre-fit level, the data/MC agreement for the 1- and 2-tag m_h SR agreed well when considering only the $\pm 1\sigma$ statistical uncertainty. However, in the case of the 1- and 2-tag m_h CRs the data/MC demonstrates some disagreement when considering only the $\pm 1\sigma$ statistical uncertainty, but when the combined statistical and systematic sources of uncertainty are considered (red band) the data/MC agrees to within $\pm 1\sigma$. After adjusting the background and signal pre-fit distributions using the maximised likelihood nuisance parameter values, the data and SM only hypothesis post-fit m_{Vh} distributions agree based on the $\pm 1\sigma$ statistical plus systematic uncertainty band (black hatched area). Therefore within the resolved regime of the 1-lepton analysis no statistically significant deviation between the data and SM only hypothesis is observed in the m_{Vh} distributions, which complies with the conclusions extracted from the local p-value plots shown in the previous sub-section; no HVT signal is observed.

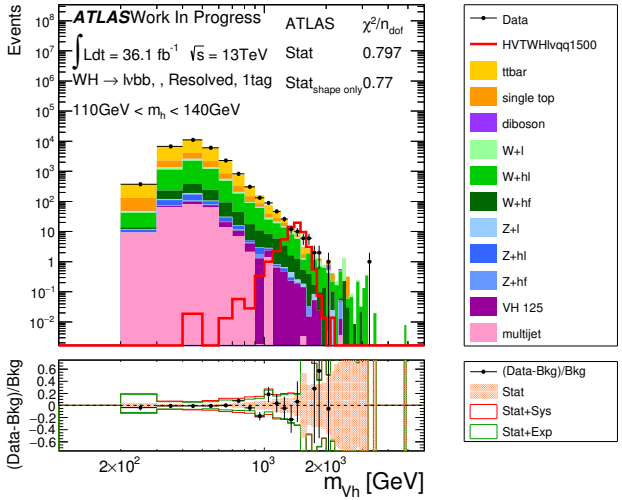
ATLAS Work In Progress
ATLAS χ²/n_dof
∫Ldt = 36.1 fb⁻¹ √s = 13TeV Stat 0.797
WH → lνbb, , Resolved, 1tag Stat_shape only 0.77
110GeV < m_h < 140GeV
Events
(Data-Bkg)/Bkg
m_Vh [GeV]
Data
HVTWHlvqq1500
ttbar
single top
diboson
W+l
W+hl
W+hf
Z+l
Z+hl
Z+hf
VH 125
multijet
(Data-Bkg)/Bkg
Stat
Stat+Sys
Stat+Exp

(a)

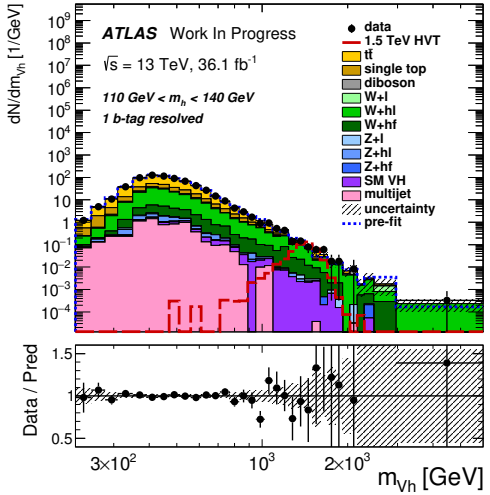
ATLAS Work In Progress
√s = 13 TeV, 36.1 fb⁻¹
110 GeV < m_h < 140 GeV
1 b-tag resolved
dN/dm_Vh [1/GeV]
Data / Pred
m_Vh [GeV]
data
1.5 TeV HVT
tt̄
single top
diboson
W+l
W+hl
W+hf
Z+l
Z+hl
Z+hf
SM VH
multijet
uncertainty
pre-fit

(b)

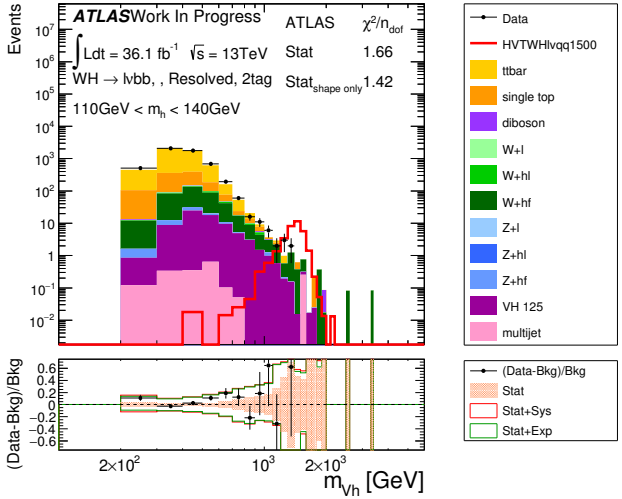
ATLAS Work In Progress
ATLAS χ²/n_dof
∫Ldt = 36.1 fb⁻¹ √s = 13TeV Stat 1.66
WH → lνbb, , Resolved, 2tag Stat_shape only 1.42
110GeV < m_h < 140GeV
Events
(Data-Bkg)/Bkg
m_Vh [GeV]
Data
HVTWHlvqq1500
ttbar
single top
diboson
W+l
W+hl
W+hf
Z+l
Z+hl
Z+hf
VH 125
multijet
(Data-Bkg)/Bkg
Stat
Stat+Sys
Stat+Exp

(c)

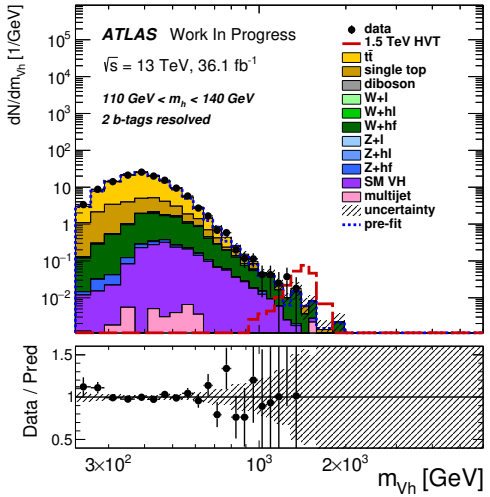
ATLAS Work In Progress
√s = 13 TeV, 36.1 fb⁻¹
110 GeV < m_h < 140 GeV
2 b-tags resolved
dN/dm_Vh [1/GeV]
Data / Pred
m_Vh [GeV]
data
1.5 TeV HVT
tt̄
single top
diboson
W+l
W+hl
W+hf
Z+l
Z+hl
Z+hf
SM VH
multijet
uncertainty
pre-fit

(d)

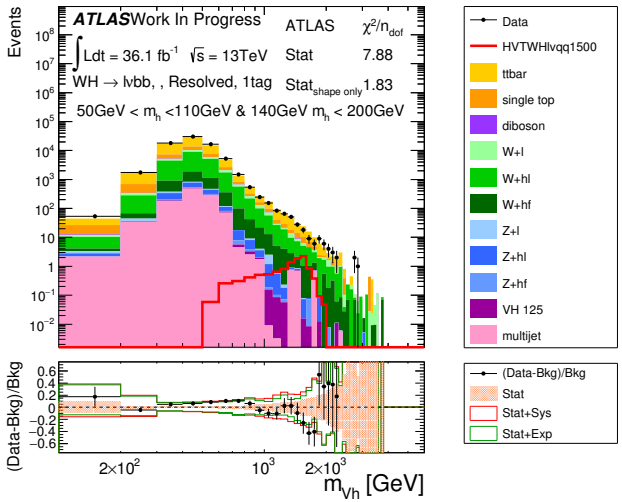

(e)

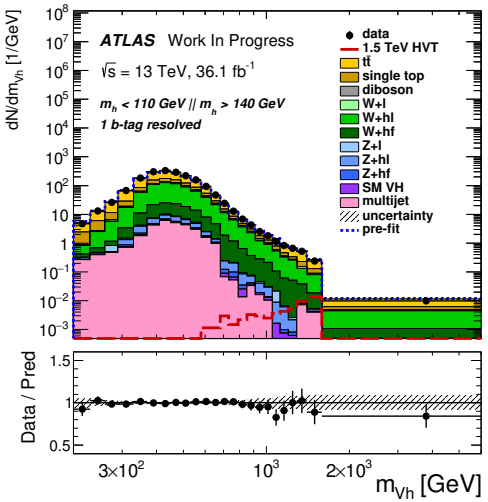

(f)

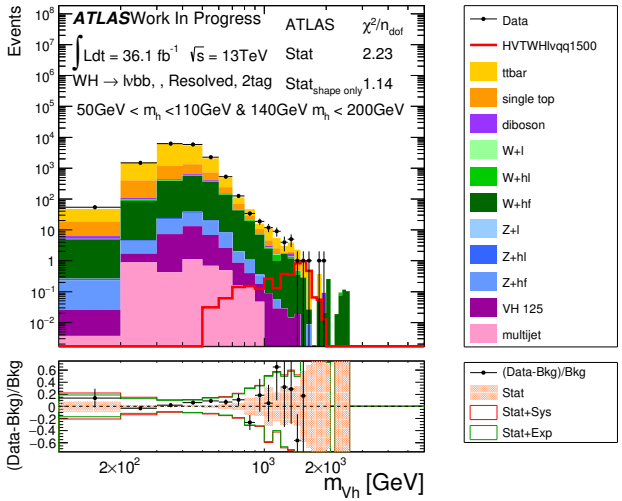

(g)

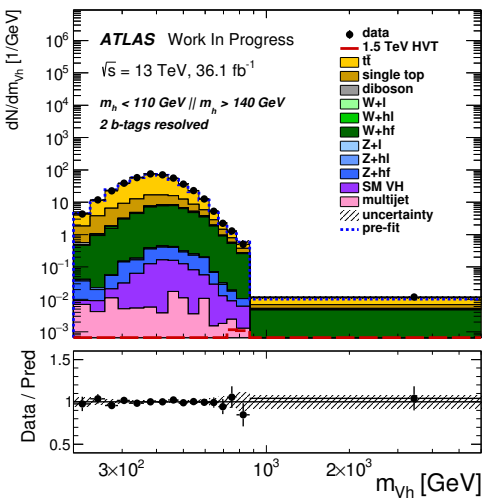

(h)

Figure 19.2.: Resolved 1-lepton pre-/post-fit plots for the 1-tag (top row) and 2-tag (bottom row) HVT fit regions using a W' HVT signal mass of $m_{W'} = 1.5$ TeV. The left column shows the pre-fit plots for all regions included within the fit, and the right column shows the corresponding post-fit plots. The black hatched markings in the lower pane of the post-fit plots correspond to the statistical and systematic error bands.

Figure 19.3 shows the pre-fit and post-fit plots for the two boosted regions included within the 1-lepton fit, 1-/2-tag m_h SR with 0 add. tags, where a single W' signal sample of mass $m_{W'} = 1.5$ TeV is overlaid as an example. For the 2-tag region, the data/MC agreement at the pre-fit level demonstrates large statistical fluctuations which is expected given the statistically limited data sample. However, within statistical uncertainty alone, no systematic data/MC deviation is observed. At the post-fit level, the data/MC agreement demonstrates a marked improvement, with all bins falling within the combined $\pm 1\sigma$ statistical and systematic uncertainty band.

However, in the 1-tag region the pre-fit MC estimation systematically overestimates the event yield within the 0 GeV $\leq m_{Vh} \leq$ 600 GeV regime, as shown by sub-figure 19.3a. This disagreement is statistically significant since the two do not agree within the $\pm 1\sigma$ statistical error band, however, once the systematic sources of uncertainty are considered the two agree well. In the $m_{Vh} >$ 600 GeV regime, the data/MC demonstrates nearly perfect agreement when considering just the $\pm 1\sigma$ statistical uncertainty, let alone the systematic uncertainties as well. Following the application of the maximum likelihood estimated nuisance parameter central values, the data/MC agreement across the entire m_{Vh} spectrum agrees within the $\pm 1\sigma$ statistical and systematic error band, meaning that the systematic deviation observed in the m_{Vh} regime was corrected using the systematic degrees of freedom within the fit.

In short, within the boosted regime of the 1-lepton analysis no statistically significant deviation between the data and SM only hypothesis is observed as shown by the m_{Vh} distributions at the post-fit level. This complies with the conclusions extracted from the local p-value plots shown in the previous sub-section, i.e. no HVT signal is observed.

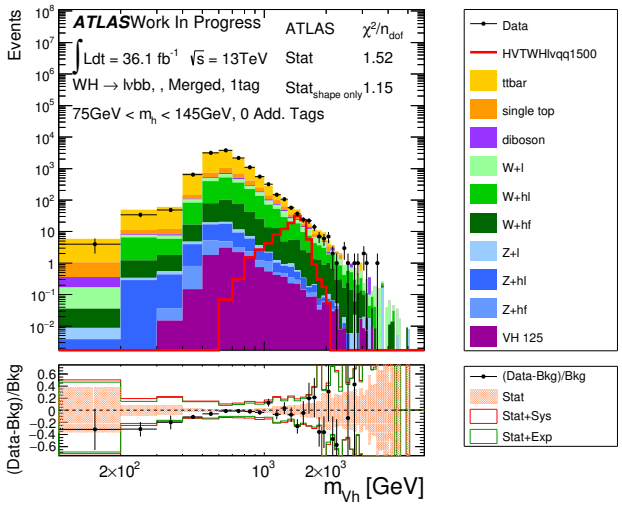

(a)

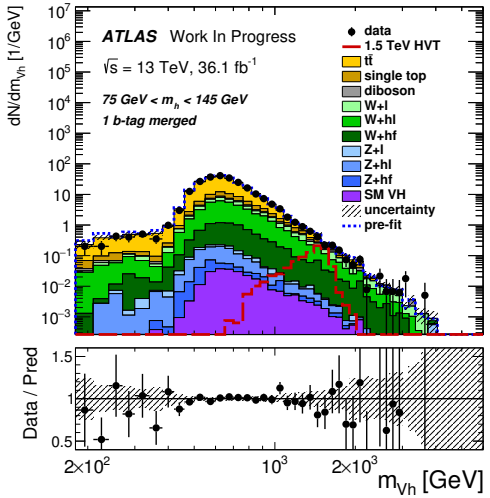

(b)

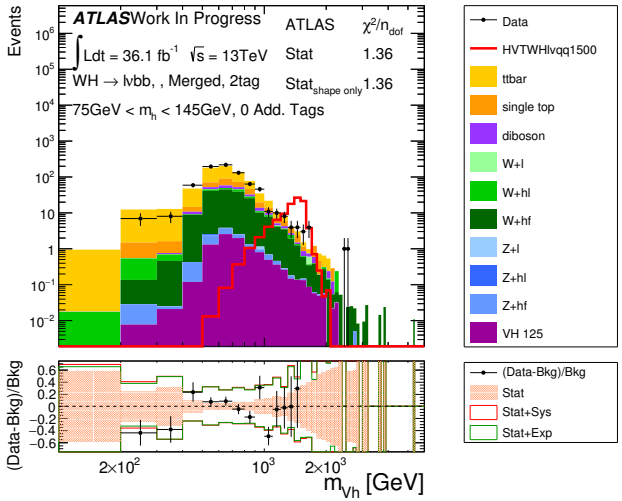

(c)

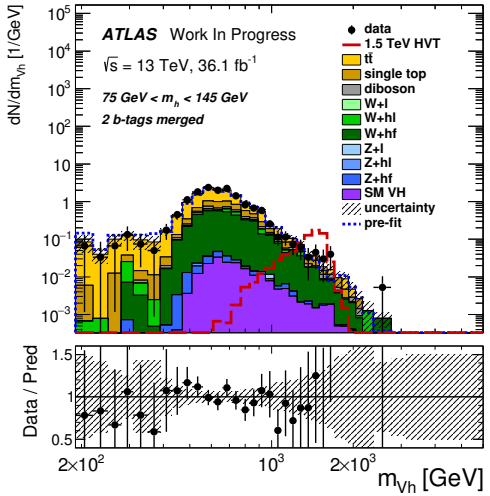

(d)

Figure 19.3.: Boosted 1-lepton pre-/post-fit plots for 1-tag (top row) and 2-tag (bottom row) HVT fit regions using a W' HVT signal mass of $m_{W'} = 1.5$ TeV. The left column shows the pre-fit plots for all regions included within the fit, and the right column shows the corresponding post-fit plots. The black hatched markings in the lower pane of the post-fit plots represent the statistical and systematic error bands.

Nuisance Parameter Pulls

Figure 19.4 shows the nuisance parameter pull plots for the b-tagging, and top-quark MC modelling uncertainties. Two results are quoted, the data SR+CR (black) and Asimov (red) fits where a signal mass of $m_{W'} = 1500$ GeV is used, and both fits are performed using an unconditional $\mu = 1$ fit (where initially the parameter of interest is set to 1). Meanwhile the unconstrained nuisance parameters, specifically the $t\bar{t}$, W+hl, and W+HF SM background normalisations, are summarised by Table 19.1.

From the b-tagging systematics (Figure 19.4a) it is shown that the leading charm-tagging (labelled `c-tag eff. 0` on the plots), is pulled to $\hat{\theta}^{\text{lead}}_{c\text{-tag}} = -0.96 \pm 0.59$. The cause of this pull and constrained nuisance parameter was found to be the large uncertainties attributed to the charm-tagging calibration method. Specifically, the charm-jet efficiency scale factors used by the b-tagging procedure within this analysis originated from a $W + c$ event calibration method (see Ref. [172][1]). An alternative calibration method using $t\bar{t}$ events yielded very different results for the charm-jet efficiency scale factors.

Figure 19.5 shows the charm-jet efficiency scale factors for the MV2c10 70% working point derived using either the $W + c$ (red) or $t\bar{t}$ (blue) methods. In the case of the $W + c$ method, the error on the scale factors includes the difference between the central values of the $W + c$ and $t\bar{t}$ methods added in quadrature. Therefore, considering that a -1σ pull on this systematic corresponds to an increase in the applied scale factors, the observed $\theta^{\text{lead}}_{c-\text{tag}} = -0.96$ pull corresponds to the analysis preferring the $t\bar{t}$ derived scale factors. This is made possible by the bloated errors assigned to the $W + c$ calibrated scale factors.

In the case of the top-quark modelling systematics, Figure 19.4b, it was observed that the $t\bar{t}$ NNLORW and MC matrix element modelling uncertainties (labelled as `ttbar Matrix Element`) are significantly pulled away from the prior assertion of 0, $\hat{\theta}_{\text{NNLORW}} = 0.85$ and $\hat{\theta}_{\text{ttbarME}} = -1.16$ respectively. Furthermore, the prior uncertainties are also significantly constrained in each case, $\sigma_{\hat{\theta}_{\text{NNLORW}}} = 0.55$ and $\sigma_{\hat{\theta}_{\text{aMCAtNLO}}} = 0.45$.

Given the dominance of the $t\bar{t}$ background to the 1-lepton analysis, both within the signal and the control regions, and noticing that the Asimov and SR+CR data fits both yield an equivalent post-fit uncertainty, the highly pulled and constrained nuisance parameters are attributed to a sensitivity of the analysis to the $t\bar{t}$ process. Furthermore, as outlined in Section 18.4, data/MC modelling issues were observed in $t\bar{t}$ enriched regions of the analysis. Attributing this data/MC disagreement to the $t\bar{t}$ process, observing large pulls on $t\bar{t}$ modelling systematics is expected; the fit is attempting to correct the data/MC agreement using the $t\bar{t}$ systematics.

However, a fundamental question is raised at this point regarding the applicability of 2-point MC-to-MC systematics; is the procedure of profiling 2-point MC-to-MC comparisons valid, and what does a non-integer pull value correspond to. A pull value of $\hat{\theta}_{\text{Shape/Norm/Accept}} = 0(1)\sigma$ corresponds to the fit determining that the nominal (alternative) MC template maximises the likelihood function. In essence nature is better modelled by the nominal (alternative) MC template.

[1] *ATLAS Internal* only - currently undergoing internal ATLAS review.

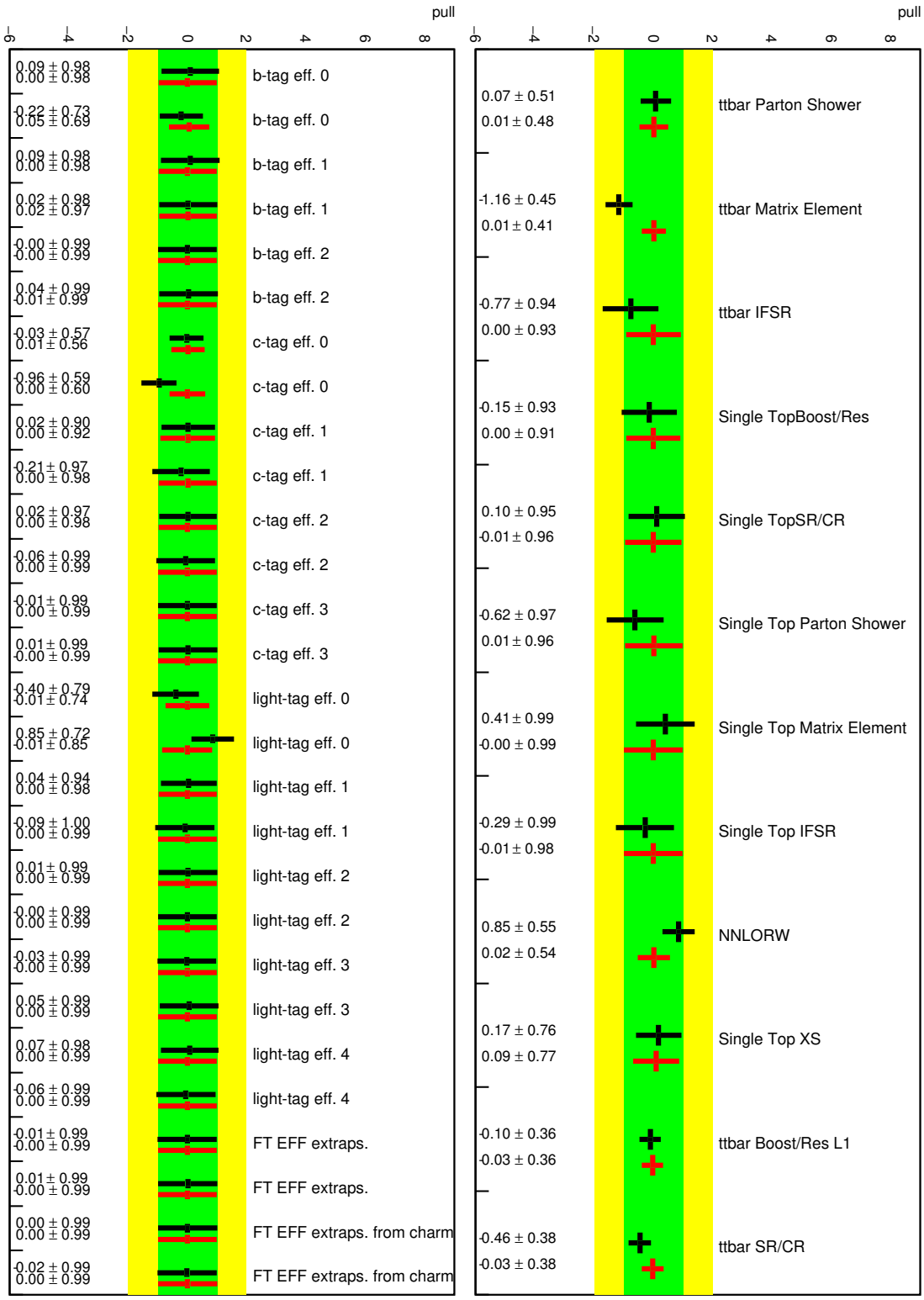

(a) **(b)**

Figure 19.4.: 1-lepton HVT pull values concerning the (a) b-tagging, and (b) top-quark systematics, for the unconditional Asimov fit (red) and unconditional SR+CR data fit (black). $\mu = 1$ (initially) and a signal mass of $m_{V'} = 1.5$ TeV is used. The green and yellow bands represent the pre-fit $\pm 1\sigma$ error.

Nuisance Parameter	SR+CR Data Fit	Asimov Fit
NORM_TTBAR	$\hat{\theta}_{t\bar{t}} = 0.95 \pm 0.06$	$\hat{\theta}_{t\bar{t}} = 1.01 \pm 0.06$
NORM_WHF	$\hat{\theta}_{W+\mathrm{HF}} = 1.24 \pm 0.22$	$\hat{\theta}_{W+\mathrm{HF}} = 0.99 \pm 0.20$
NORM_WHL	$\hat{\theta}_{W+\mathrm{hl}} = 1.12 \pm 0.16$	$\hat{\theta}_{W+\mathrm{hl}} = 0.98 \pm 0.17$

Table 19.1.: Summary of unconstrained nuisance parameters for the unconditional SR+CR data fit and Asimov fit. The parameter of interest is initialised to $\mu = 1$ at the start of the fit.

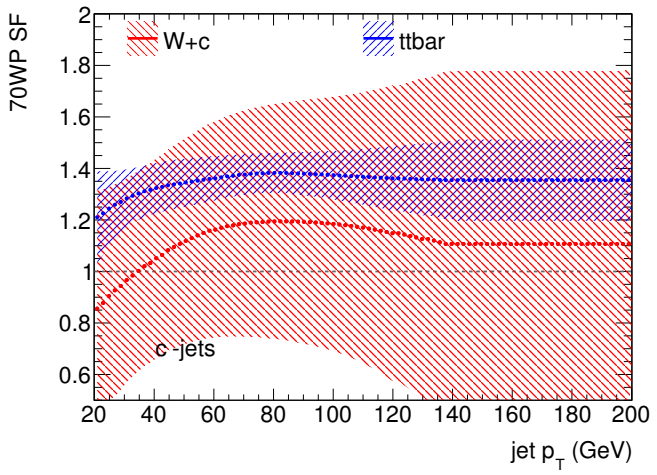

Figure 19.5.: Comparison of the charm-jet efficiency scale factors for the MV2c10 70% working point as a function of the anti-k_T $R = 0.4$ EM topologically clustered jet p_T. Solid lines represent the central values of the scale factors, whilst the shaded regions depict the uncertainties associated with the calibration method. Plot produced by Valerio Dao (Stony Brook University).

However, a non-integer value such as $\hat{\theta}_{\mathrm{Shape/Norm/Accept}} = 0.7 \pm 0.1$, means that the data is best modelled by taking 30% of the nominal MC template shape/normalisation and 70% of the alternative MC template shape/normalisation (assuming linear interpolation). Such an interpolation of the template shape, normalisation, or acceptance, is not well defined and physically meaningless.

The solution to this problem is to parameterise the response of the likelihood as a function of the physical/phenomenological parameter. For example, variations of phenomenological parameters like $\mu_{R/F}$ and `hdamp`, enter into the likelihood function directly, $\mathcal{L}(\mu, \vec{\theta}, \vec{\gamma})$ becomes $\mathcal{L}(\mu, \vec{\theta}', \vec{\gamma}, \mu_R, \mu_F, \texttt{hdamp}, ...)$, where $\vec{\theta}'$ is the same vector of nuisance parameters previously defined in Chapter 9, minus the MC parameters. This however, often requires a sampling of an N-dimensional model parameter space, where the N-dimensions of this hyper-cube represent a MC phenomenological/physical parameter, or modelling scheme choice (cluster vs string hadronisation). Generating a single point in this model parameter space (one MC prediction) is often time consuming, meaning that an exhaustive parameterisation

of the model parameter space is sometimes impractical. Therefore, the above methodology is necessary until an alternative methodology is presented.

Ranking Plots

In analysing the pre-fit distributions previously shown by Figures 19.2 and 19.3, it is apparent that the tails of the m_{Vh} distribution suffer from a higher statistical error. Consequently, heavier mediators sit on top of a smaller SM background which has a corresponding larger statistical error, meaning that the precision with which the parameter of interest μ is known, is limited more by the statistical error than the systematics assigned in the analysis.

This is demonstrated by Figure 19.6c, which shows as a function of the invariant mass of the mediator the relative contribution of the statistical and systematic sources of error as a percentage of the total uncertainty on μ, i.e. $\%_{\text{syst/stat}} = \Delta_{\mu}^{\text{syst/stat}}/\Delta_{\mu}^{\text{Total}}$. This is shown for the Asimov dataset using five mediator mass points, $m_{V'} = [0.5, 1, 1.5, 2, 5]$ TeV, where the black curve represents the combined systematic uncertainty, and the red the statistical.

In order to understand which systematics sources contribute the most, Figure 19.6a and Figure 19.6b, show the top 15 ranked nuisance parameters extracted from the Asimov dataset fit for two mass points, $m_{V'} = [0.5, 3]$ TeV; $m_{V'} = 0.5$ TeV is systematically limited, whilst $m_{V'} = 3$ TeV is limited via the statistical precision of the MC/data. In looking at Figure 19.6a, the $m_{V'} = 0.5$ TeV mass point, it can be seen that the most dominant sources of uncertainty pertain to the uncertainty on the collected data (`Luminosity`), the HVT signal uncertainties, the top-quark/W+Jets modelling, and flavour-tagging systematics.

This trend is still observed for the larger mediator mass point, $m_{V'} = 3$ TeV shown by Figure 19.6b, however the flavour-tagging, and W+Jets modelling uncertainties take precedence, whilst the signal uncertainties (`HVT Signal PDF/IFSR`), overall uncertainty on the collected data (`Luminosity`), and top-quark modelling systematics become less influential. The reduced impact of the $t\bar{t}$ modelling systematics is the direct result of the smaller contribution of the $t\bar{t}$ background to the tail of the m_{Vh}, therefore the impact of the associated systematics are suppressed.

The same evaluation can also be made using the observed data fit with which the exclusion limits are produced. Specifically, Figure 19.7, shows the nuisance parameter rankings for the $m_{W'} = [0.5, 1.5]$ TeV mass points [2] (Figures 19.7a and 19.7b), in addition to the percentage contribution of the systematic and statistical sources of error to the total error on μ, as a function of the mediator mass. The same conclusions are drawn from the observed data ranking plots as in the Asimov dataset case; within the expected systematically limited regime of the analysis ($m_{V'} < 1.2$ TeV) the $t\bar{t}$/W+Jets, and b-tagging systematics typically induce the largest uncertainty in the parameter of interest μ.

[2] Unfortunately, due to the limited data statistics in the tail of the m_{Vh} distribution, performing a N-dimensional scan as outlined by Section 19.1.3, is not possible, therefore a smaller m_{Vh} range is shown in this case.

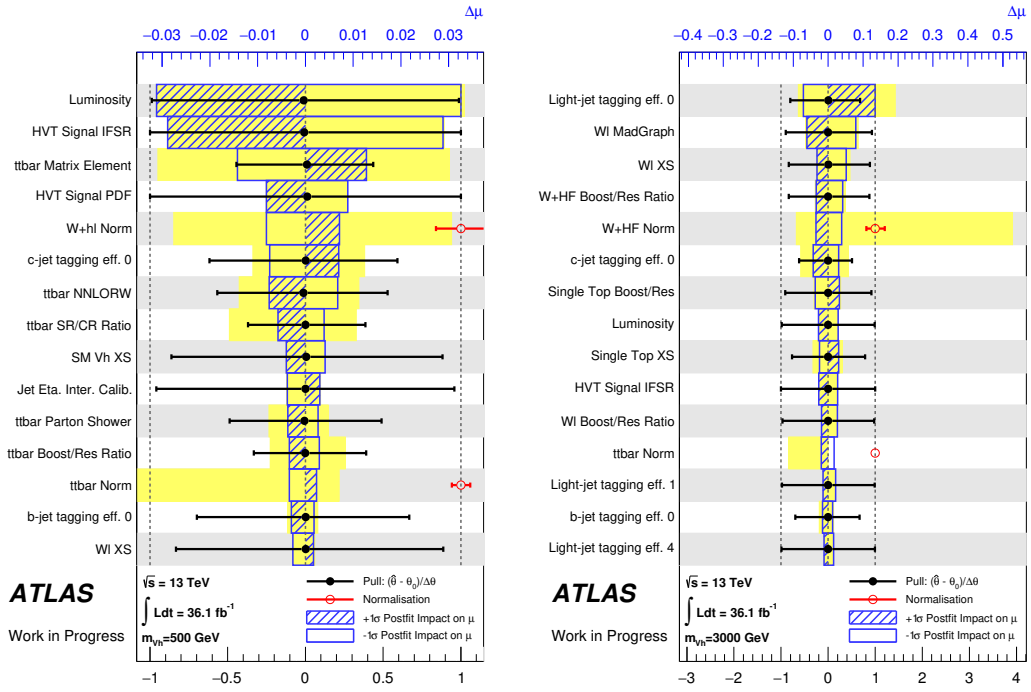

(a) **(b)**

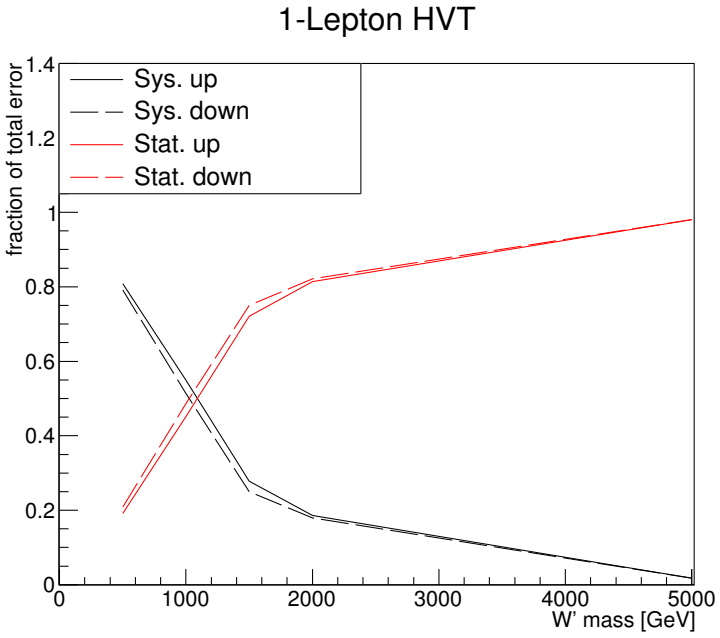

(c)

Figure 19.6.: 1-lepton HVT ranking plots for nuisance parameter impact on $\hat{\mu}$, using the fit to Asimov dataset, for a W' mass of $m_{W'} = 0.5$ TeV (a), and $m_{W'} = 3$ TeV (b) The central values of the nuisance parameters are depicted as black markers with an x-axis error representing the post-fit uncertainty (red markers for unconstrained NPs). The uncertainty imparted by this nuisance parameter on μ is represented by the blue box. The yellow shaded region represents the uncertainty imparted to μ, when the nuisance parameters central value and uncertainty pre-fit are used. Figure (c) corresponds to the relative contribution of the statistical and systematic uncertainties to the total uncertainty on the parameter of interest μ, for different masses of W'. Specifically, $m_{V'} = [0.5, 1, 1.5, 2, 5]$ TeV.

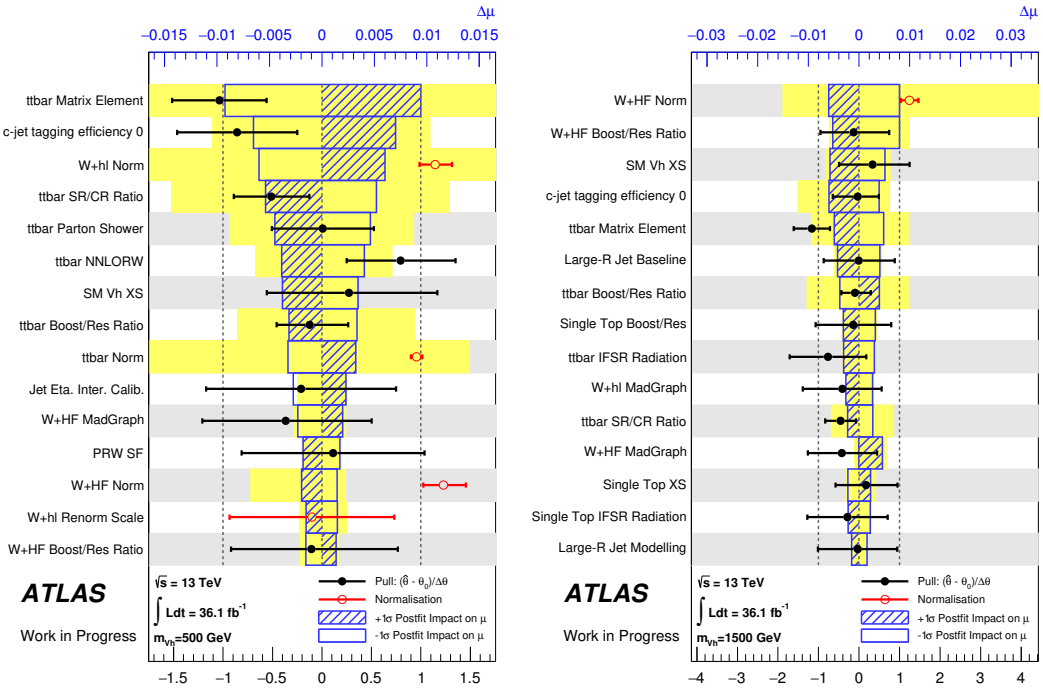

(a) (b)

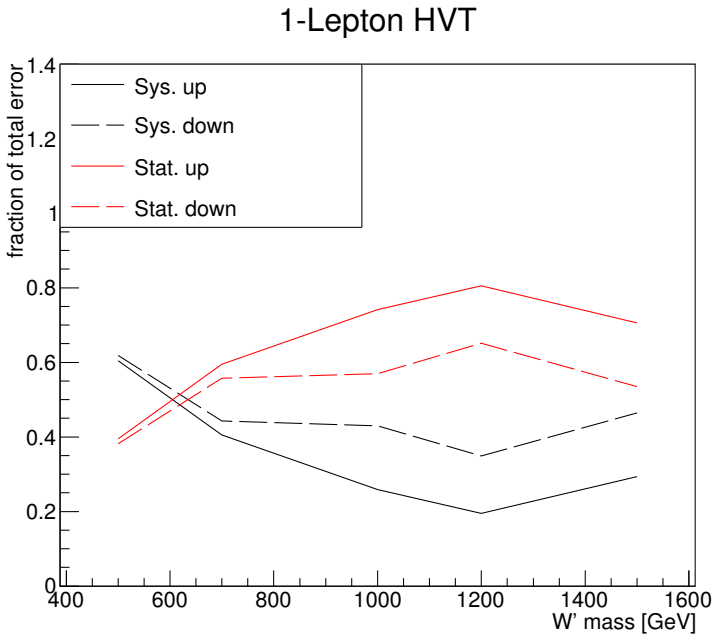

(c)

Figure 19.7.: 1-lepton HVT ranking plots for nuisance parameter impact on $\hat{\mu}$, using the fit to data, for a W' mass of $m_{W'} = 0.5$ TeV (a), and $m_{W'} = 1.5$ TeV (b). The central values of the nuisance parameters are depicted as black markers with an x-axis error representing the post-fit uncertainty (red markers for unconstrained NPs). The uncertainty imparted by this nuisance parameter on μ is represented by the blue box. The yellow shaded region represents the uncertainty imparted to μ, when the nuisance parameters pre-fit central value and uncertainty are used. Figure (c) corresponds to the relative contribution of the statistical and systematic uncertainties to the total uncertainty on the parameter of interest μ, for different masses of W'. Specifically, $m_{V'} = [0.5, 0.7, 1, 1.5, 2]$ TeV.

19.2.2. HVT W', Z', and V'Combinations

Given the limited detector acceptance and object reconstruction efficiencies, it is possible that the $W^{\pm} \to l^{\pm}\nu$ decay process could be reconstructed as a 0-lepton event. Similarly, the $Z \to l^{\pm}l^{\mp}$ could contribute to the 0-lepton channel as a result of leptons failing to be reconstructed or $Z \to \nu\nu$ decay processes could contribute to the 2-lepton channel as a result of two jets faking a lepton. Therefore, limits for the W' and Z' HVT mediators can be enhanced by combining the 0+1-lepton channels and 0+2-lepton channels respectively.

Furthermore, it is assumed that the full HVT prediction would manifest within the data, meaning that the W' and Z' heavy vector bosons would both be produced. Consequently, a combined $V' = W' + Z'$ fit can be performed. In this situation, the relative production rate of the $W' \to Wh$ and $Z' \to Zh$ are fixed to the HVT model predictions. The HVT V' fit is therefore performed by including all the signal models, $W \to l\nu$ and $Z \to \nu\nu/ll$, within each lepton channel and run using the 0+1+2-lepton channel.

Table 19.2 summarises the signal components considered in each channel, and which channels are combined. For the binned profile likelihood fit, the same setup as explained in the preceding sections is used with the exception of additional nuisance parameters that control the event yield ratio of various MC backgrounds templates between channels.

	0-lepton channel	**1-lepton channel**	**2-lepton channel**
Z' combination	Z' signal with τ-veto	-	Z' signal
W' combination	W' signal without τ-veto	W' signal	-
HVT combination	W' & Z' signals with τ-veto	W' & Z' signals	Z' signal

Table 19.2.: Summary of the channels and signals used in HVT/AZh combinations.

Post-Fit plots

Figures 19.8-19.13 show the $m_{Vh}^{(T)}$ pre-fit and post-fit plots, for the 0-lepton, 1-lepton, and 2-lepton fit regions, for the V' combined fit. For the 0-lepton and 2-lepton channels the pre-fit and post-fit plots are shown side by side. For the 1-lepton channel both the pre-fit and post-fit plots are shown, however the pre-fit plots are an exact duplicate of those given in Section 19.2.1. They are repeated for completeness and clarity.

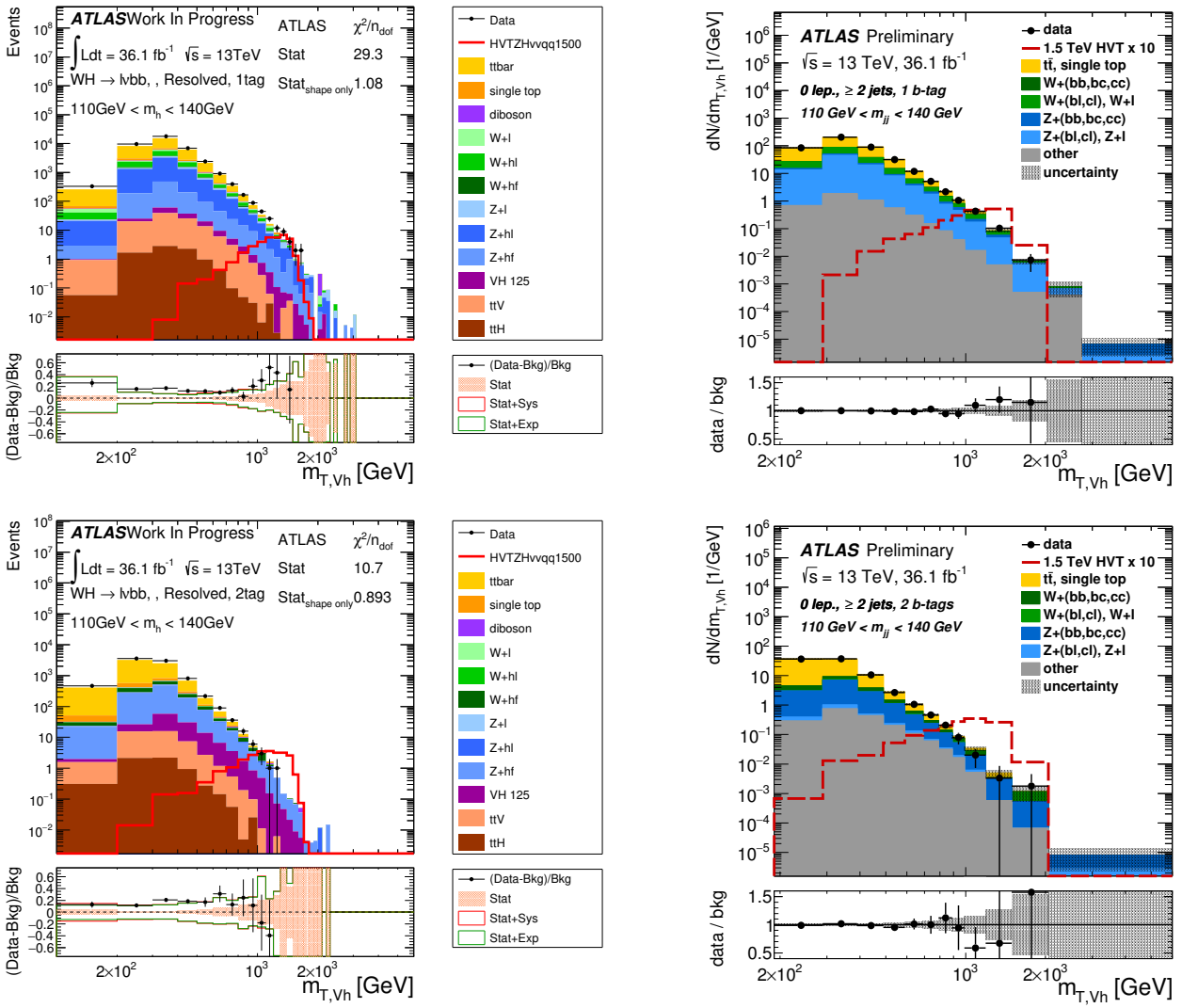

Figure 19.8.: Resolved 0-lepton pre-/post-fit plots extracted from the HVT V' combined fit. Left column shows the pre-fit plots for all regions included within the fit. Right column shows the corresponding post-fit plots, taken from Ref. [2].

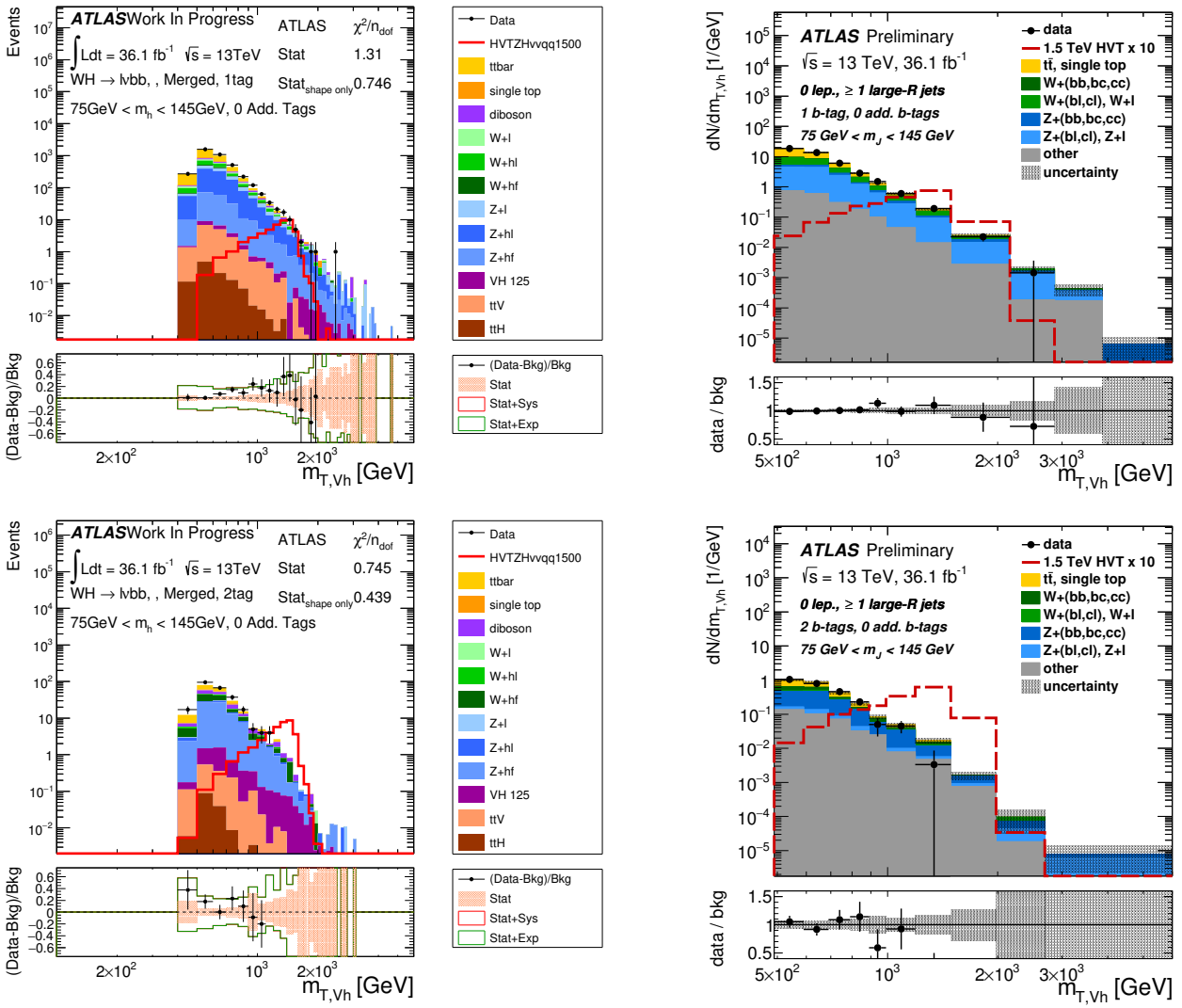

Figure 19.9.: Boosted 0-lepton pre-/post-fit plots extracted from the HVT V' combined fit. Left column shows the pre-fit plots for all regions included within the fit. Right column shows the corresponding post-fit plots, taken from Ref. [2].

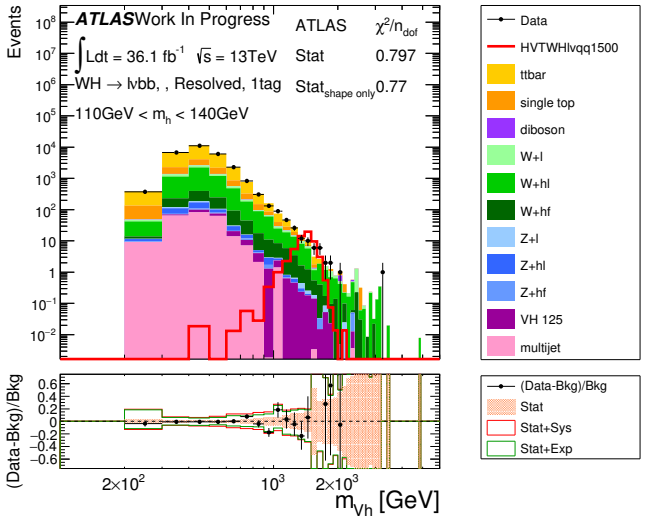
ATLAS Work In Progress
ATLAS
χ²/n_dof
∫Ldt = 36.1 fb⁻¹ √s = 13TeV
Stat 0.797
WH → lνbb, , Resolved, 1tag
Stat_shape only 0.77
110GeV < m_h < 140GeV
Events
(Data-Bkg)/Bkg
m_Vh [GeV]
Data
HVTWHlvqq1500
ttbar
single top
diboson
W+l
W+hl
W+hf
Z+l
Z+hl
Z+hf
VH 125
multijet
(Data-Bkg)/Bkg
Stat
Stat+Sys
Stat+Exp

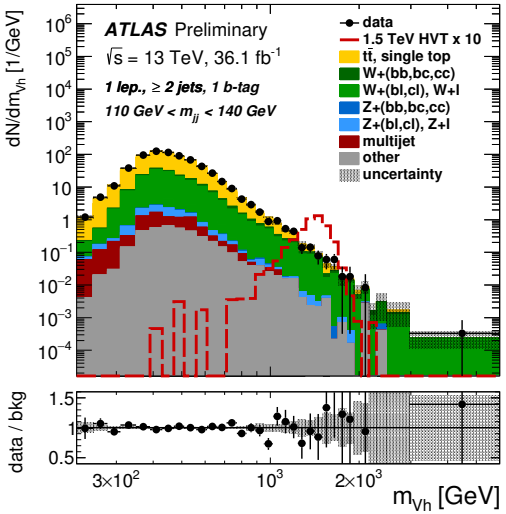
ATLAS Preliminary
√s = 13 TeV, 36.1 fb⁻¹
1 lep., ≥ 2 jets, 1 b-tag
110 GeV < m_jj < 140 GeV
dN/dm_Vh [1/GeV]
data / bkg
m_Vh [GeV]
data
1.5 TeV HVT x 10
tt̄, single top
W+(bb,bc,cc)
W+(bl,cl), W+l
Z+(bb,bc,cc)
Z+(bl,cl), Z+l
multijet
other
uncertainty

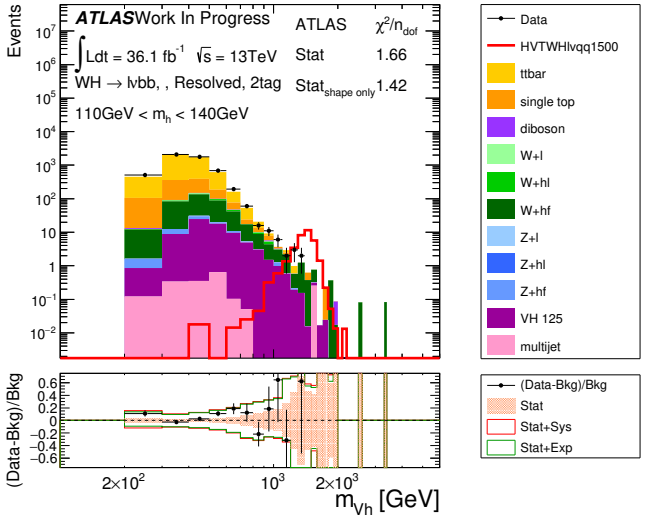
ATLAS Work In Progress
ATLAS
χ²/n_dof
∫Ldt = 36.1 fb⁻¹ √s = 13TeV
Stat 1.66
WH → lνbb, , Resolved, 2tag
Stat_shape only 1.42
110GeV < m_h < 140GeV
Events
(Data-Bkg)/Bkg
m_Vh [GeV]
Data
HVTWHlvqq1500
ttbar
single top
diboson
W+l
W+hl
W+hf
Z+l
Z+hl
Z+hf
VH 125
multijet
(Data-Bkg)/Bkg
Stat
Stat+Sys
Stat+Exp

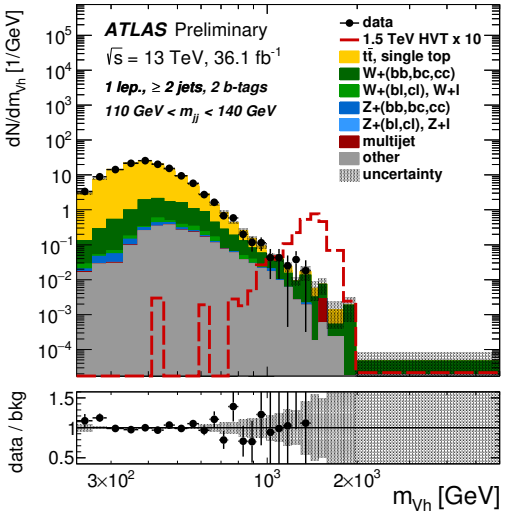
ATLAS Preliminary
√s = 13 TeV, 36.1 fb⁻¹
1 lep., ≥ 2 jets, 2 b-tags
110 GeV < m_jj < 140 GeV
dN/dm_Vh [1/GeV]
data / bkg
m_Vh [GeV]
data
1.5 TeV HVT x 10
tt̄, single top
W+(bb,bc,cc)
W+(bl,cl), W+l
Z+(bb,bc,cc)
Z+(bl,cl), Z+l
multijet
other
uncertainty

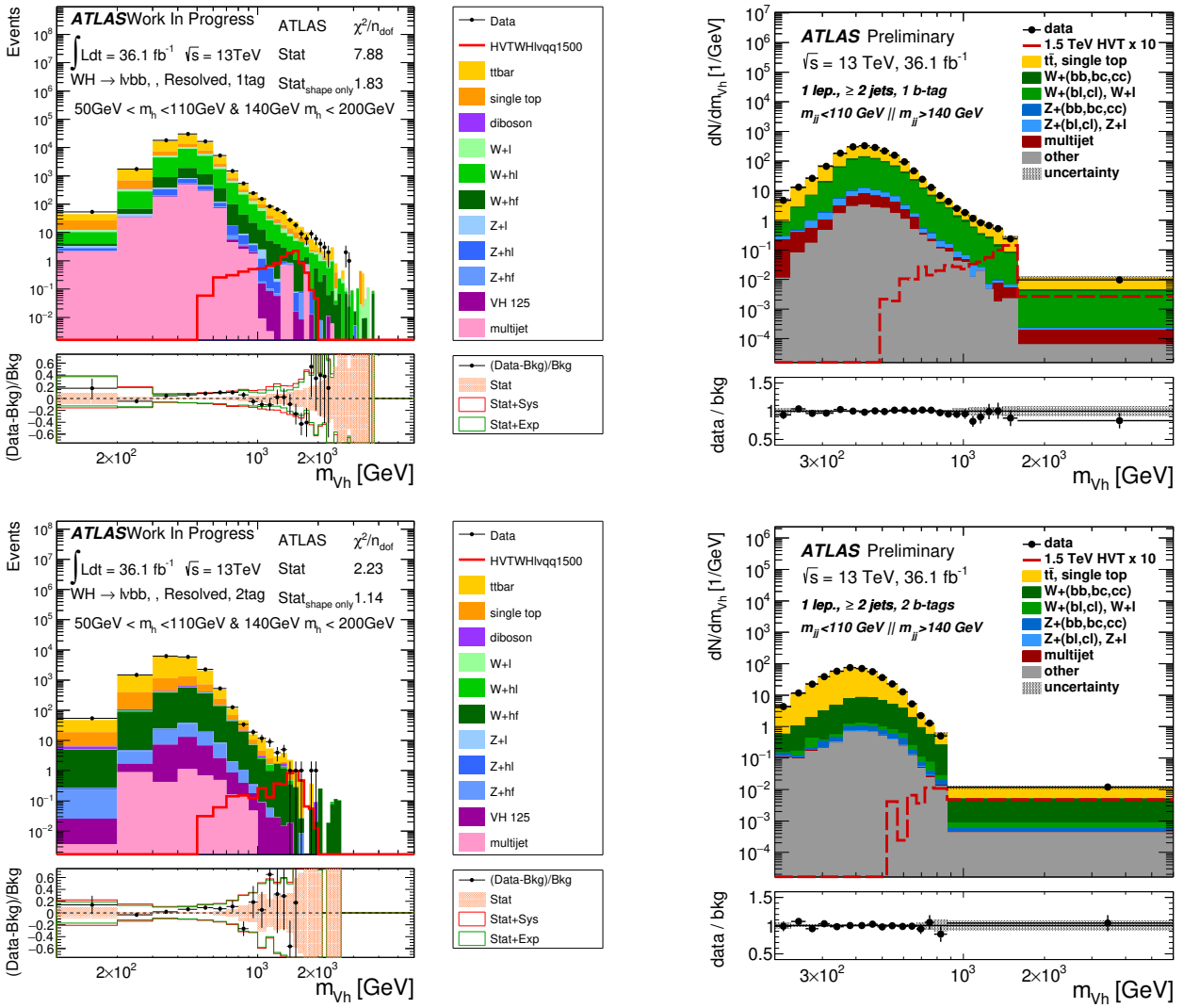

Figure 19.10.: Resolved 1-lepton pre-/post-fit plots extracted from the HVT V' combined fit. Left column shows the pre-fit plots for all regions included within the fit. Right column shows the corresponding post-fit plots, taken from Ref. [2].

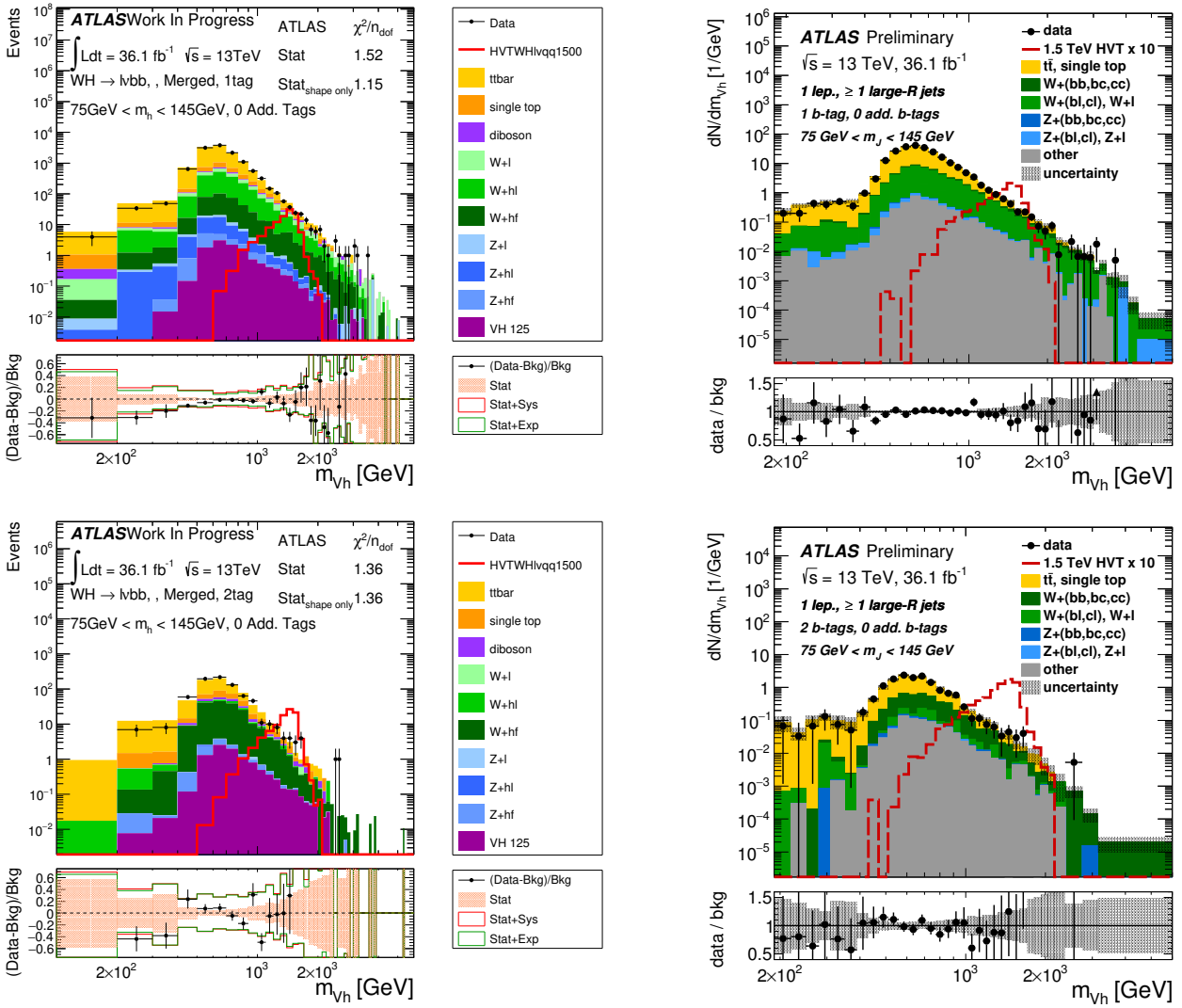

Figure 19.11.: Boosted 1-lepton pre-/post-fit plots extracted from the HVT V' combined fit. Left column shows the pre-fit plots for all regions included within the fit. Right column shows the corresponding post-fit plots, taken from Ref. [2].

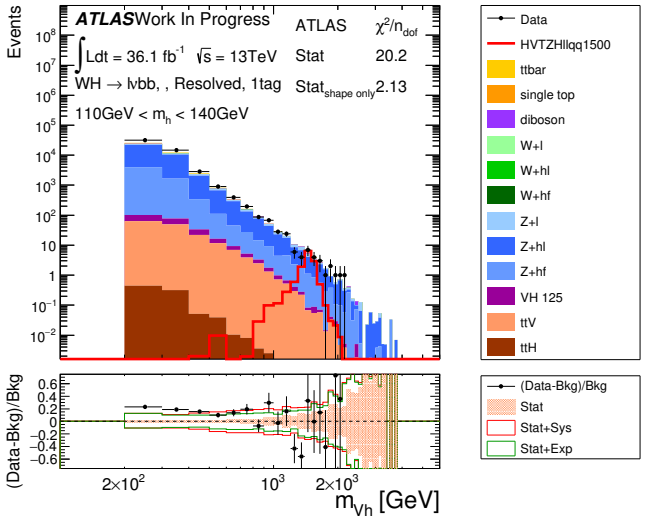
ATLAS Work In Progress
∫Ldt = 36.1 fb-1 √s = 13TeV
WH → lνbb, , Resolved, 1tag
110GeV < mh < 140GeV
ATLAS χ2/ndof
Stat 20.2
Statshape only 2.13
Events
(Data-Bkg)/Bkg
mVh [GeV]
Data
HVTZHllqq1500
ttbar
single top
diboson
W+l
W+hl
W+hf
Z+l
Z+hl
Z+hf
VH 125
ttV
ttH
(Data-Bkg)/Bkg
Stat
Stat+Sys
Stat+Exp

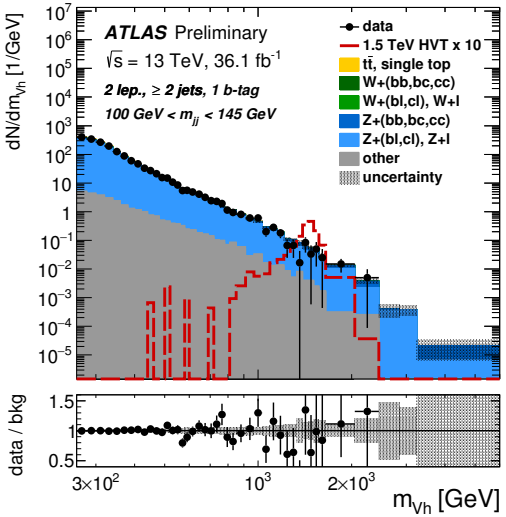
ATLAS Preliminary
√s = 13 TeV, 36.1 fb-1
2 lep., ≥ 2 jets, 1 b-tag
100 GeV < mjj < 145 GeV
dN/dmVh [1/GeV]
data / bkg
mVh [GeV]
data
1.5 TeV HVT x 10
tt̄, single top
W+(bb,bc,cc)
W+(bl,cl), W+l
Z+(bb,bc,cc)
Z+(bl,cl), Z+l
other
uncertainty

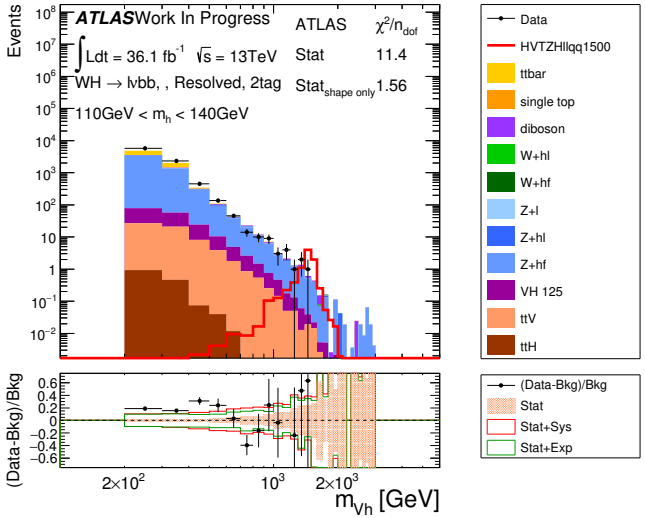
ATLAS Work In Progress
∫Ldt = 36.1 fb-1 √s = 13TeV
WH → lνbb, , Resolved, 2tag
110GeV < mh < 140GeV
ATLAS χ2/ndof
Stat 11.4
Statshape only 1.56
Events
(Data-Bkg)/Bkg
mVh [GeV]
Data
HVTZHllqq1500
ttbar
single top
diboson
W+hl
W+hf
Z+l
Z+hl
Z+hf
VH 125
ttV
ttH
(Data-Bkg)/Bkg
Stat
Stat+Sys
Stat+Exp

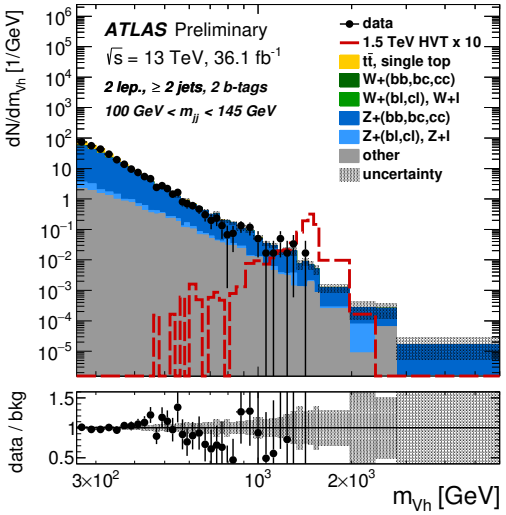
ATLAS Preliminary
√s = 13 TeV, 36.1 fb-1
2 lep., ≥ 2 jets, 2 b-tags
100 GeV < mjj < 145 GeV
dN/dmVh [1/GeV]
data / bkg
mVh [GeV]
data
1.5 TeV HVT x 10
tt̄, single top
W+(bb,bc,cc)
W+(bl,cl), W+l
Z+(bb,bc,cc)
Z+(bl,cl), Z+l
other
uncertainty

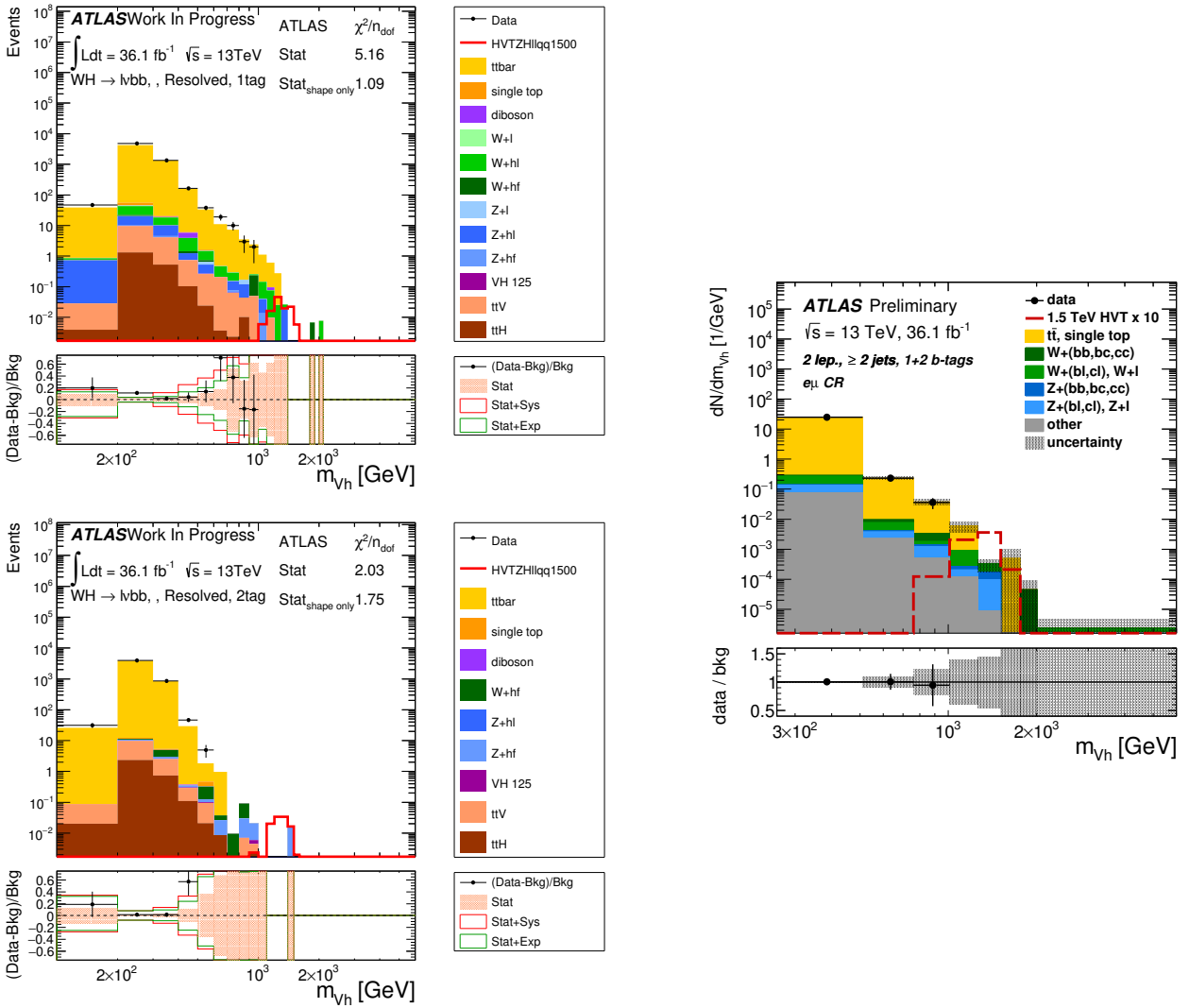

Figure 19.12.: Resolved 2-lepton pre-/post-fit plots extracted from the HVT V' combined fit. Left column shows the pre-fit plots for all regions included within the fit. Right column shows the corresponding post-fit plots, taken from Ref. [2]. The 1-tag and 2-tag top $e\mu$ control regions are an exception to this rule, where the pre-fit level get merged at the fit stage into the 1+2-tag category. As such the post-fit plot is shown in this merged state.

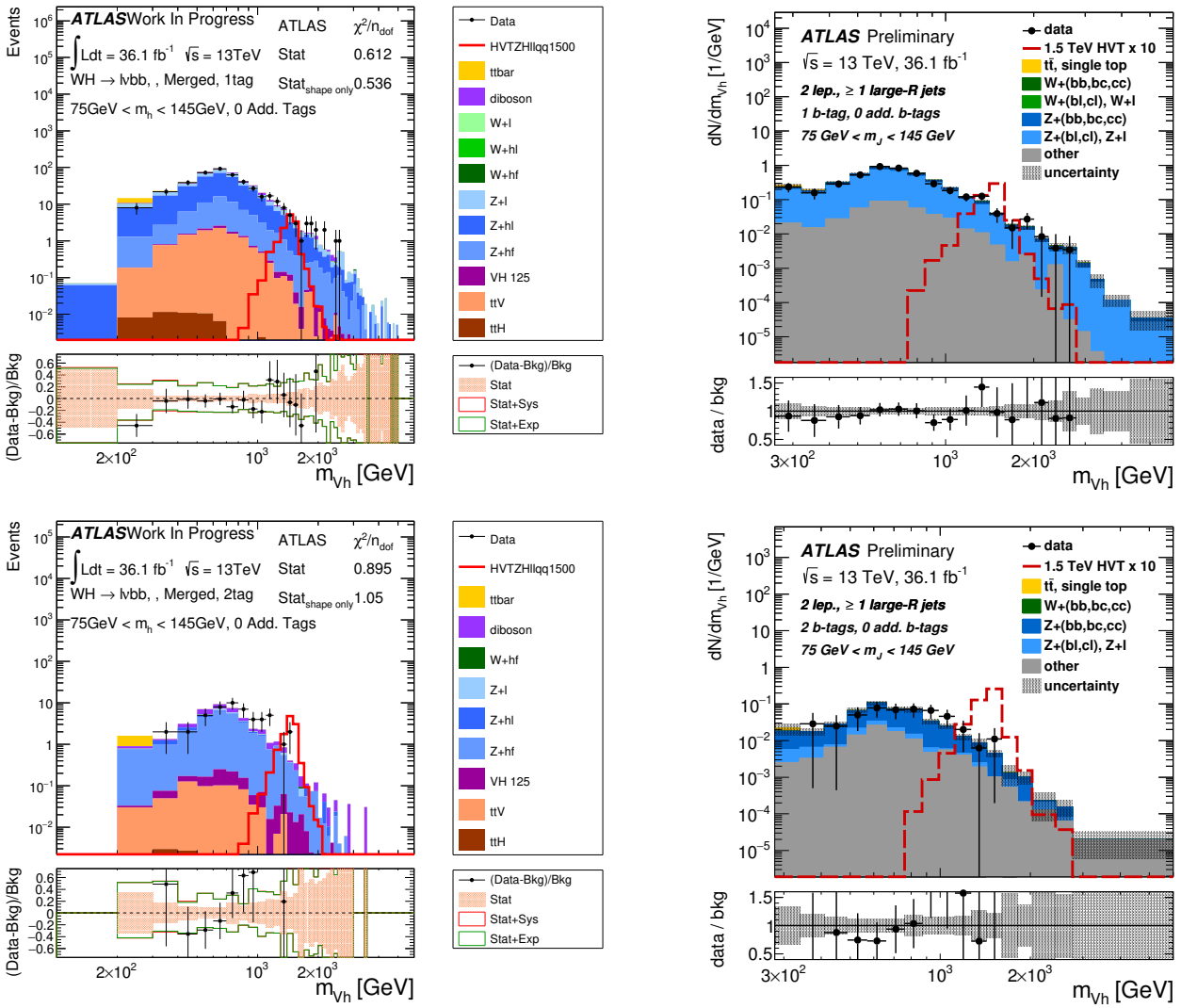

Figure 19.13.: Boosted 2-lepton pre-/post-fit plots extracted from the HVT V' combined fit. Left column shows the pre-fit plots for all regions included within the fit. Right column shows the corresponding post-fit plots, taken from Ref. [2].

Local *p*-values & 95% Confidence Limits

Figures 19.14b, 19.14d, and 19.14f show the 95% CL_s exclusion limits for the Z', W', and V' fits. The black curves represent the observed exclusion limit, dashed blue is the expected exclusion, and the green/yellow bands represent the $\pm 1/2\sigma$ (68%/95%) standard deviations on the expected exclusion limits. The upper limits are placed on $\sigma^{\text{HVT}}_{W'/Z'} \times BR(h \to b\bar{b}/c\bar{c})$ for the W'/Z' mediators and $(\sigma^{\text{HVT}}_{V'} \times BR(h \to b\bar{b}/c\bar{c}))/\sigma^{\text{HVT MC}}_{V'}$ for V'.

For the HVT benchmark models of A with $g_V = 1$ (fermiophilic), $m_{Z'} < 2650$ GeV, $m_{W'} < 2670$ GeV, and $m_{V'} < 2800$ GeV mediator masses are excluded with 95% confidence. For the benchmark model B with $g_V = 3$ (fermionphobic) the mediator masses of $m_{Z'} < 2830$ GeV, $m_{W'} < 2860$ GeV, and $m_{V'} < 2930$ GeV, are excluded to a 95% confidence level.

Model Interpretation

The limits placed on the production cross-section of a V' mediator under benchmark models A and B of the HVT paradigm, shown in the preceding sub-section, represent a 1-dimensional scan of the HVT model phase space. This is because, model A and B represent a single configuration of the iso-triplet $SU(2)_L$ coupling to the SM vector bosons, $g_V c_H$, and SM fermions, $c_F g^2/g_V$, but a variable mediator mass. However, as the production cross-section of the HVT V' mediator, $\sigma^{\text{HVT}}_{V'}$, is dependent on all three parameters of the simplified Lagrangian given by equation 4.2, it is physically more significant to place limits on the production cross-section as a function of the mediator mass, $m_{V'}$, and iso-triplet to SM vector boson ($g_V c_H$) and SM fermion ($c_F g^2/g_V$) couplings.

This is shown as exclusion contours in the HVT parameter space $\{g_V c_H, \frac{g^2}{g_V} c_F\}$, for sample mediator masses $m_{V'} = [1.2, 2.0, 3.0]$ TeV, by using the V' 95% CL_s exclusion curve shown by Figure 19.14f. Each mass contour is obtained by fixing the masses of the Z' and W' bosons (assumed degenerate) to the specified mass, and assuming c_F to be the same for quarks and leptons across all generations. The parameters $g_V c_{VVV}$, $g_V^2 c_{VVHH}$, and c_{VVW} that represent the couplings of the multiple heavy vector bosons are ignored due to the negligible impact of said parameters on the final result. A grid search of the 2-dimensional parameter space is then performed, calculating the cross-section at each sampled point. Cross-sections falling above the observed exclusion curve shown by Figure 19.14f are excluded with 95% confidence.

The benchmark models A and B are also presented on the figure, however since they correspond to a constant set of parameters, they are represented as single points in the parameter space. Benchmark model A is shown twice for two values of the generic coupling of the iso-triplet fields to the SM vector bosons or fermions, g_V, where $g_V = 1$ represents a stronger coupling of the iso-triplet $SU(2)_L$ sector to the SM when compared to $g_V = 3$, however the relative coupling to the SM vector bosons and fermions is identical in each case.

In conclusion, the aforementioned contour plot is the foundation of the Heavy Vector Triplet simplified model strategy, because the phenomenological Lagrangian detailed in

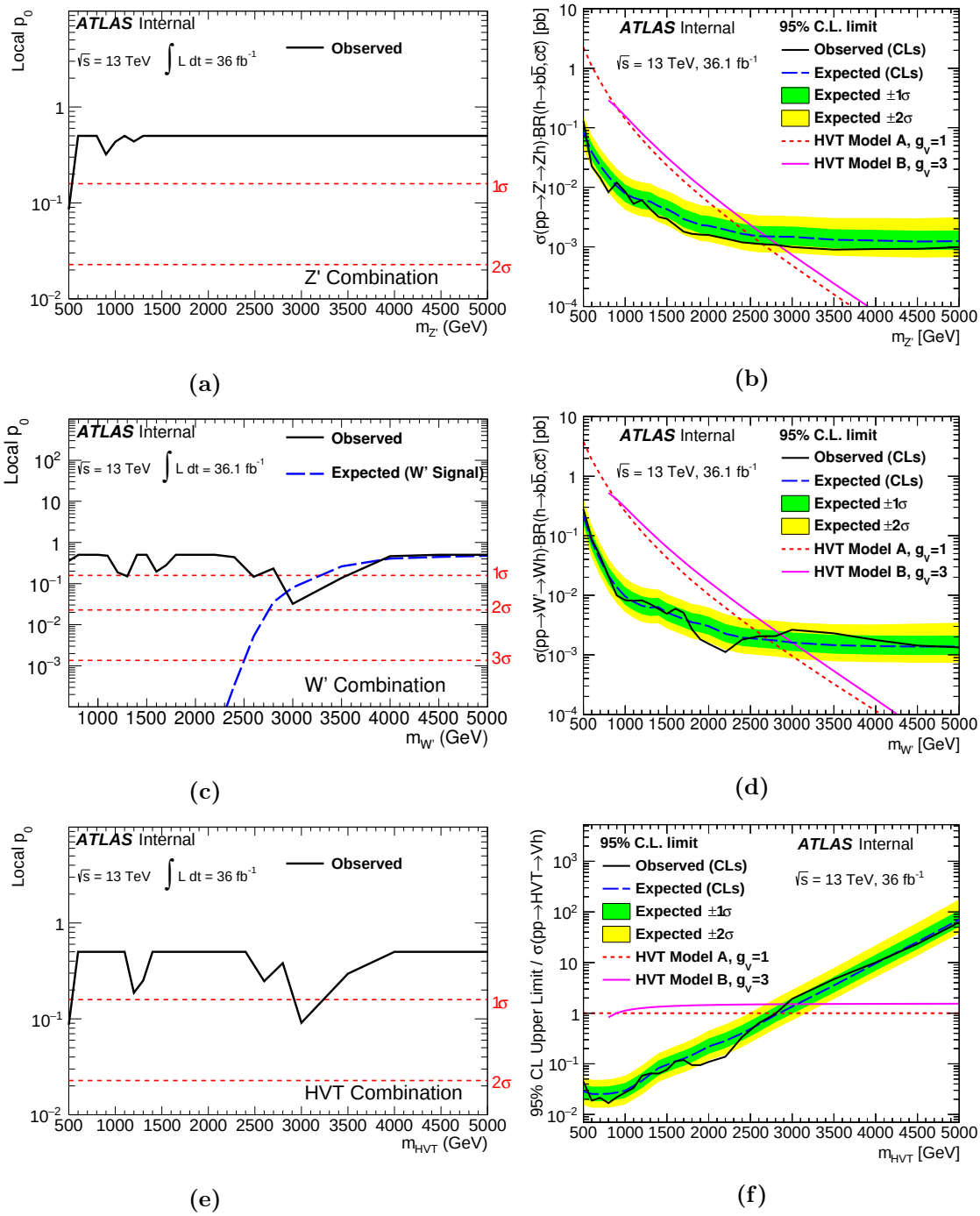

Figure 19.14.: Local p-values and 95% CL_s limits for the 24 mediator mass points from 500 GeV to 5000 GeV, for the Z' (a+b), W' (c+d), and V' (e+f) fits, taken from Ref. [2].

Chapter 4 encompasses a wide array of fundamental theories ranging from extra-dimensions to the Higgs being a composite particle. Therefore, as per the 'Bridge Method' outlined in Section 4.1, the HVT parameter contour plot is used to translate the limits placed on the

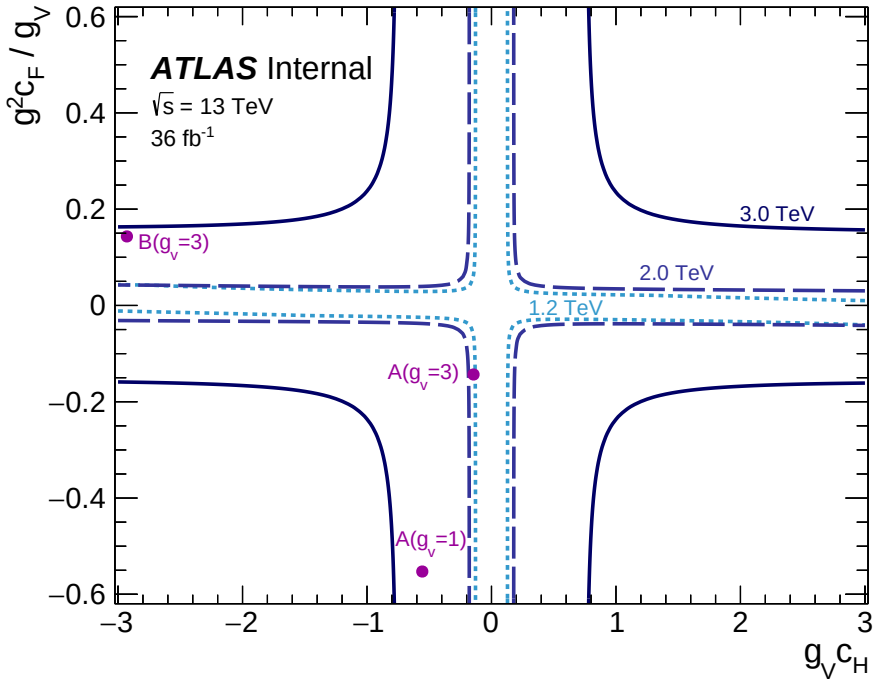

Figure 19.15.: Limits on the fermionic ($g^2 c_F / g_V$) and bosonic ($g_V c_H$) coupling parameters of the HVT model for selected heavy resonance masses of $m_{V'} = [1.2, 2.0, 3.0]$TeV. The points in parameter space corresponding to the HVT benchmark models are indicated as points, as such for a mediator mass of 3 TeV, no benchmark models are excluded. Plot taken from Ref. [2].

phenomenological parameters into the limits on the parameters of the underlying theoretical model, e.g. Composite Higgs Models [32]. It is these constraints on the fundamental theory that exclude new ideas about physics beyond the SM, and thereby redirect the effort of the theoretical community to alternative hypotheses.

19.3. *AZh* Results

Using the fit model outlined in Chapter 17 for the AZh analysis, a Binned Profile Likelihood fit is also performed using the AZh 2HDM MC samples summarised in Section 10.2.1. No significant excess is found to be compatible with the AZh model predictions, and so upper limits at the 95% confidence level are set on $\sigma_{bbA/ggA} \times BR(h \to b\bar{b})$ using the modified frequentist CL_s method (Ref. [77]), and profile-likelihood-ratio test statistic using the asymptotic approximation given by Ref. [73].

Figure 19.16 shows the gluon-gluon fusion initiated and b-quark associated production mode limits for the 0+2-lepton combined. It should be noted that in the search for the A boson with b-quark associated production, a mild excess of events is observed around 440 GeV. This is mainly driven by the dimuon channel in the resolved category with ≥ 3

b-tags. The local significance of this excess with respect to the background-only hypothesis is estimated to be 3.6σ, and the global significance, accounting for the look-elsewhere effect (Ref. [173]) is estimated to be 2.4σ.

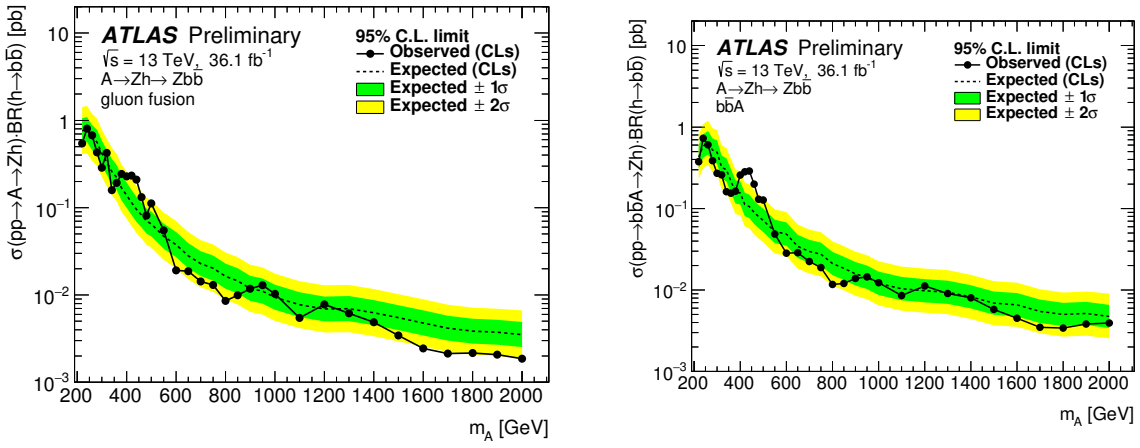

(a) ggA **(b)** bbA

Figure 19.16.: 95% CL_s limits on the $A \to Zh$ production cross-section times $h \to b\bar{b}$ branching fraction for mediator masses in the 220 GeV to 2000 GeV range. (a) shows the ggA production process limits, whilst (b) shows the bbA production limits [2].

19.4. Future Prospects - Total Predicted Run 2 Analysis Sensitivity

The 1-lepton HVT fit results shown above in Section 19.2.1, demonstrated that the systematic sources of uncertainty were the limiting factors for mediators masses in the 500 GeV $< m_{W'} <$ 700 GeV range, whilst the expected analysis sensitivity extracted using the Asimov dataset was systematically limited in the 500 GeV $< m_{W'} <$ 1000 GeV range. Looking to the future of the analysis, and noting that the expected integrated luminosity collected by ATLAS during the entire Run 2 schedule of 2015–2017 is estimated to be ~ 120 fb^{-1}, the main improvement to the analysis will come from the ~ 3.3 times larger dataset; the statistical precision of the data will increase by a factor of ~ 1.8.

However, for those mediators masses where the statistical precision of the data is already a sub-leading limitation, the statistical precision on the MC templates, the b-tagging systematics, and V+Jets/$t\bar{t}$ systematics will continue to limit the performance of the analysis. Furthermore, this systematically limited $m_{W'}$ regime will only continue to grow as more data is collected, especially as the statistical precision of the data approaches or even exceeds that of the MC templates.

This last point is demonstrated by Figure 19.17, which shows the fractional error on the integrated event yield of the data (black) and background MC (red) within a 95% window

around the peak of the m_{Vh} distribution as predicted by the simulated W' HVT signals outlined by Section 10.2.1. As shown by the figure, the statistical precision of the MC templates is either equivalent to the data in the low $m_{W'}$ regime (resolved regime) or only slighlty better (~ 1.5 times smaller in the boosted regime). However, for mediators above $m_{W'} > 1$ TeV, the statistical precision of the data rapidly degrades faster than that of the MC simulated background processes; the statistical precision of the data ~ 3.8 times worse than that of the background MC.

However, as shown by the data extrapolated to an integrated luminosity of 120 fb^{-1} (blue), the statistical precision of the data will exceed that of the current MC for mediators masses below $m_{W'} < 2$ TeV. Consequently, the statistical precision of the MC templates will by far be the most limiting factor for future iterations of the analysis.

That being said, as shown by Figure 19.6 and Figure 19.7, the signal, b-tagging and V+Jet/$t\bar{t}$ modelling uncertainties are the leading source of systematic uncertainty as predicted by the Asimov dataset, and confirmed by the observed results. Therefore, these will impose hard limits on the performance of any future iteration of the analysis. In order to assess the expected sensitivity of the analysis at an integrated luminosity of 120 fb^{-1}, an Asimov dataset is constructed using the same MC/data-driven templates as those above, scaled to an integrated luminosity of 120 fb^{-1} with the error reduced by the factor $\sqrt{120/36.1}$. This Asimov dataset is then used in an unconditional fit, configured in the same fashion as that used for the HVT 1-lepton results given in Section 19.2.1.

Figure 19.18 shows as a function of $m_{W'}$ the expected contribution of the statistical and systematic sources of uncertainty to the final result (Figure 19.18a) and the expected exclusion limits on the production cross-section (Figure 19.18b) at an integrated luminosity of 120 fb^{-1} and 36.1 fb^{-1}. From these plots it can be seen that the systematically limited region will grow from $m_{W'} < 1$ TeV to $m_{W'} < 1.4$ TeV. Furthermore, whilst the excluded region of phase space will increase for all mediator masses, the ratio of the 120 fb^{-1} normalised exclusion curve to the 36.1 fb^{-1} exclusion curve, shows a definitive negative trend, meaning that larger mediator masses will benefit more from the increase in the integrated luminosity. This is the direct result of the lower mediator masses being more systematically limited.

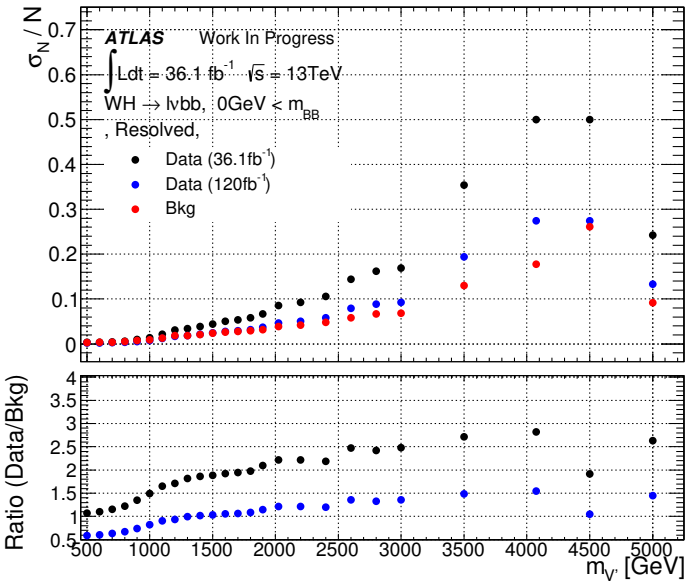

(a)

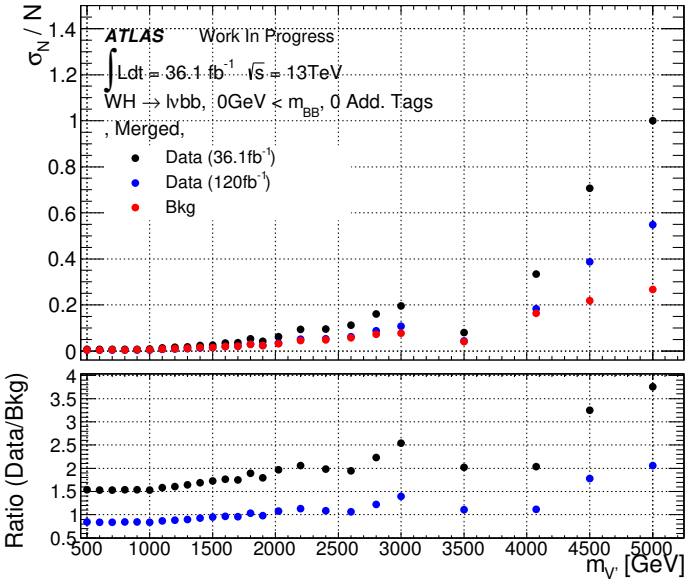

(b)

Figure 19.17.: The fractional error on the integrated data and background MC event yield within a 95% window around the m_{Vh} mass peaks of the 24 HVT MC simulated W' signals, for the resolved (a) and boosted (b) regimes of the analysis, inclusive of the 1+2-tag categories and m_h SR/CRs.

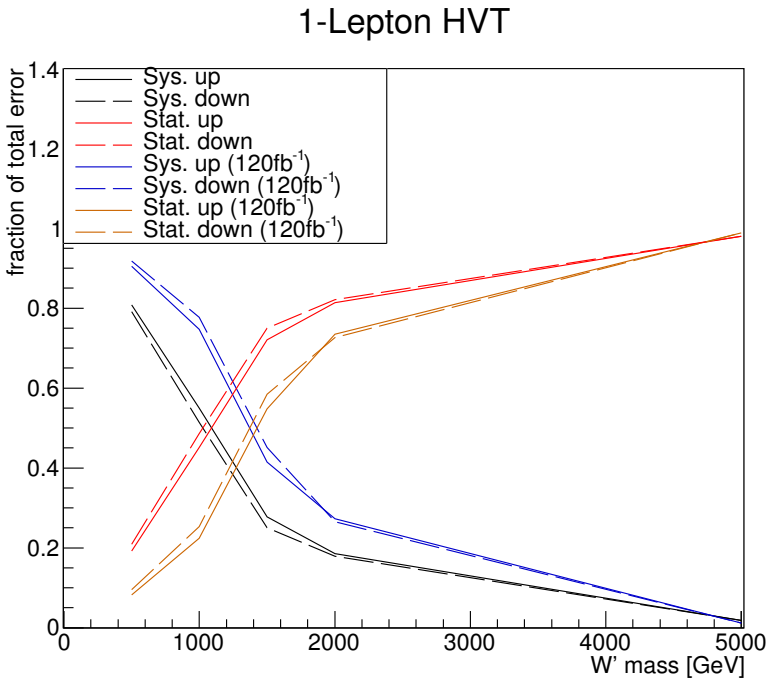

(a)

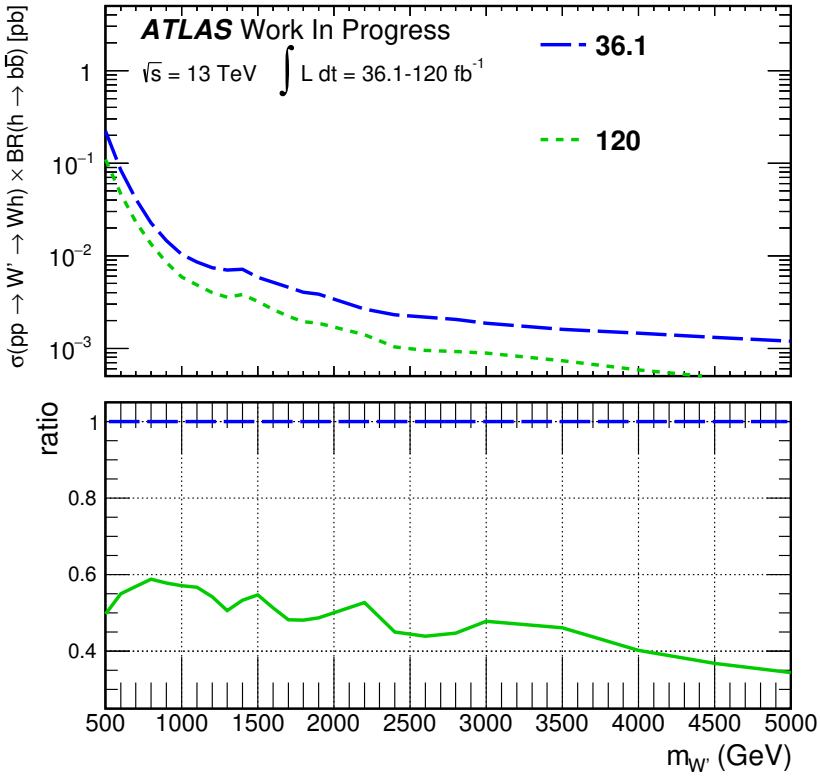

(b)

Figure 19.18.: (a): Contribution of the statistical and systematic sources of uncertainty on μ when using a conditional $\mu = 1$ Asimov fit for a luminosity of 36.1 fb^{-1} (red & black) and 120 fb^{-1} (orange & blue). (b): Asimov limits for a luminosity of 36.1 fb^{-1} (blue) and 120 fb^{-1} (green).

Chapter 20.

Conclusions

In this thesis a Beyond the Standard Model search for heavy vector boson resonances decaying to the final state signatures of $l^{\pm}l^{\mp}b\bar{b}$, $l^{\pm}\nu b\bar{b}$, and $\nu\nu b\bar{b}$, interpreted within the context of Heavy Vector Triplet, and 2 Higgs Doublet Models was presented. Using the 2015+2016 ATLAS proton-proton dataset totalling 36.1 fb^{-1}, excesses consistent with the aforementioned SM extensions were tested using a frequentist Binned Profile Likelihood fit and CL_s test statistic.

Analyses using a total integrated luminosity of 3.2 fb^{-1}, corresponding to the 2015 only ATLAS dataset, have set limits on the 2HDMs and HVT models prior to this analysis, see Ref. [70] and Ref. [55]. In the case of the HVT model, the 2015 analysis using a boosted substructure technique to reconstruct the $h \to b\bar{b}$ decay, observed no statistically significant excess, therefore upper limits on $\sigma_{W'/Z'/V'} \times BR(h \to b\bar{b}/c\bar{c}) \times BR(W/Z \to ll/l\nu/\nu\nu)$ for heavy W', Z', and V' (W'+Z') boson resonances were placed to a 95% CL_s confidence level; $m_{V'} < 1480(1490)$ GeV for two benchmark models labelled A and B, were excluded.

The analysis presented in this thesis was then a natural extension of its predecessor, where the 2015+2016 analysis presented in this thesis made several optimisations relating to the event reconstruction, and the fiducial phase space of the analysis, in order to increase the analysis sensitivity to the full HVT mass spectrum range. The most significant of these improvements was the *Priority Resolved Signal Region* combination scheme, which combines the small-R jet and trimmed large-R substructure techniques, followed by the implementation of a p_V^T cut that varies as function of the invariant mass of the $V + h$ system.

However, despite these analysis improvements and a 10× larger integrated luminosity, no statistically significant excess consistent with the HVT model was found, therefore upper limits on $\sigma_{W'/Z'/V'} \times BR(Z(W) \to ll/\nu\nu(l\nu)) \times BR(h \to b\bar{b})$ were set using the 95% CL_s technique for mediator masses in the 500 GeV to 5000 GeV range. The results showed that to a 95% confidence limit, Z' mediator masses of $m_{Z'} < 2650(2830)$ GeV were excluded under the hypothesis of benchmark model A/B. W' mediator masses of $m_{W'} < 2670(2860)$ GeV were excluded with 95% confidence for the same benchmark models. A combined $V' = W' + Z'$ fit, under the assumption that the W' and Z' mediator masses are degenerate ($m_{Z'} = m_{W'}$), excluded to a 95% confidence level mediator masses of $m_{V'} < 2800(2930)$ GeV.

For the 2HDM, no statistically significant excess is observed, and so upper limits on the $\sigma_{A\to Zh} \times BR(Z \to \nu\nu/ll) \times BR(h \to b\bar{b})$ were calculated to a 95% $\mathrm{CL_s}$ confidence level for mediator masses in the range of 220-2000 GeV. These limits are placed separately on the gluon-gluon fusion and b-quark associated production mechanisms, excluding $\sigma_{A\to Zh} \times BR(Z \to \nu\nu(ll)) \times BR(h \to b\bar{b})$ between 5.5×10^{-3} pb and 2.4×10^{-1} pb for $gg \to A$ production, and 3.4×10^{-3}–7.3×10^{-1} pb for bbA associated production.

In reviewing the analysis performance for future iterations, it was found that for $m_{V'} > 1.0$ TeV and $m_A > 400$–800 GeV, the HVT and 2HDM exclusion limits were statistically limited; sensitivity to a localised excess consistent with the HVT (2HDM) signal is limited by the data and MC bin errors in the $m_{Vh}^{(T)} > 1.0(0.4-0.8)$ TeV regime. This is the result of the rapidly falling tail of the $m_{Vh}^{(T)}$ distributions for SM background processes, which prove difficult to populate when using MC methods to simulate $m_{Vh}^{(T)}$ templates. However, for mediator masses in the $m_{V'} < 1.0$ TeV and $m_A < 400 - 800$ GeV regime, the results are systematically limited, where out of approximately 200 experimental/model based sources of systematic uncertainty, the signal (HVT or AZh), c/b-jet tagging systematics (experimental), and V+Jets/$t\bar{t}$ model based systematics were found to be the most dominant.

With the above analysis limitations in mind, and looking to the future, the next iterations of these analyses will enjoy the full Run 2 or 2015–2017 LHC data collection periods which is expected to yield an integrated luminosity of 120 fb^{-1}. As such, the HVT and 2HDM analyses will experience a reduction of the statistical error by a factor of ≈ 1.8. However, with systematically limited regions of the analysis all ready present, the discovery potential of future HVT and 2HDM signals using the $X \to Vh \to l^{\pm}l^{\mp}/l^{\pm}\nu/\nu\nu + b\bar{b}$ final state signature will slowly reach a hard limit imposed by the systematic sources of uncertainty unless otherwise addressed.

Appendix A.

Smoothing Procedure for Standard Model Modelling Uncertainties

Motivation for Smoothing and Smoothing Algorithms

The shape systematics applied to the V+Jets, $t\bar{t}$, and single top $m_{Vh}^{(T)}$ templates, are derived by comparing the nominal MC configuration outlined in Chapter 10, to alternative MC configurations detailed in Section 18.3.1 and Section 18.3.2. By forming the ratio $R(m_{Vh}^{(T)}) = h_i^{\text{var}}/h_i^{\text{nom}}$, where h_i^{nom} corresponds to the i^{th} $m_{Vh}^{(T)}$ bin of the nominal MC sample and similarly for the variation sample, each nominal MC event is re-weight by the multiplicative scale factor $R(m_{Vh}^{(T)})$, to yield the alternative MC $m_{Vh}^{(T)}$ template prediction.

However, due to the finite statistics of the nominal and variable MC samples, the true $m_{Vh}^{(T)}$ distribution, $\tilde{h}_i^{\text{nom/var}}$, is sampled to some finite statistical precision, yielding the sampled distributions previously defined ($h_i^{\text{nom/var}}$). Consequently, the sampled ratio $R(m_{Vh}^{(T)})$ suffers from statistical fluctuations, which can generate artifacts suchs as bumps or deficits. Therefore, when using the binned ratio to re-weight each event, non-physical features are often created in the $m_{Vh}^{(T)}$ templates during the profile likelihood fit process.

Furthermore, the template morphing procedure used in the binned profile likelihood procedure (see Chapter 9 for details) for shape systematics, linearly interpolates between the nominal $m_{Vh}^{(T)}$ template and the alternative MC template, where the former defines the 0σ value of the nuisance parameter and the latter defines the $\pm 1\sigma$ nuisance parameter value. This linear interpolation technique unfortunately amplifies statistical fluctuations, therefore the ratio $R(m_{Vh}^{(T)})$ is smoothed prior to its implementation into the fit. In this regard, three smoothing procedures were considered:

- **χ^2 Minimised Functional Form Smoothing:** The ratio $R(m_{Vh}^{(T)})$ has an unknown parent distribution $\tilde{R}(m_{Vh}^{(T)}$, from which it was sampled. Since the parent distribution is not known *a priori*, a wide variety of scalar fit functions, $f^n(m_{Vh}^{(T)})$, corresponding

to linear combinations of $\zeta = [x, \ln(x), 1/x, e^x, \sqrt{x}]$ raised to the n^{th} power, are constructed and fit to the ratio using a χ^2 minimisation process. First order ($n = 1$) and second order ($n = 2$) linear combinations are used, with the best fitting functional form defined as that which yields a reduced χ^2 fit result, χ^2/n_{dof} (where n_{dof} corresponds to the number of degrees of freedom), closest to unity.

The $\chi^2/n_{\text{dof}} = 1$ best fit definition, is chosen because under the assumption that a functional form $f^n(m_{Vh}^{(T)})$ does match the parent distribution of the ratio, $\tilde{R}(m_{Vh}^{(T)})$, the χ^2 fit value should follow a $f(\chi^2, n_{\text{dof}})$ distribution, where the mean of the distribution is given by the number of degree's of freedom, $\langle f(\chi^2) \rangle = n_{\text{dof}}$. This means that the expected fit result on average should correspond to a $\chi^2/n_{\text{dof}} = 1$. With this in mind, the procedure outlined in Section 18.3 is used to determine the best fitting functional form.

- **Kernel Smoothing:** For a given $m_{Vh}^{(T)}$ bin in the ratio $R(m_{Vh}^{(T)})$, referred to as y_i with x-axis coordinate x_i, the neighbouring bins to the left, y_{i-q}, and right, y_{i+r}, are weighted proportional to their distance from the bin y_i, using a weighting kernel of the form:

$$\mathcal{W}_{q(r)} = \frac{1}{\sigma^{\alpha}_{y_{q(r)}} \exp[\beta (dx_i)^{\epsilon}]}, \tag{A.1}$$

where σ_{y_i} is the statistical error on the bin $y_{q(r)}$, $\alpha = 0.5$ is the exponent that controls the impact of the bin error in the weight calculation, (dx_i) is the distance of the bin y_i from the neighbouring bin $y_{i \pm q(r)}$ in x-axis units, $\epsilon = 3.0$ is the exponent that controls the impact of the distance on the weight calculation, and $\beta = 1.0$ is a multiplicative factor. Using these weights, the smoothing procedure is as follows:

1. For the ratio $R(m_{Vh}^{(T)})$ with k bins, the sum of weights for the k bins in the ratio is computed, $\sum_{j=1}^{k} \mathcal{W}_j$. Following this the first bin, y_1, is selected, meaning that $i = 1$ is set.

2. For bin y_i, y_i', is computed by calculating the kernel weight for the first bin $y_{j=1}$, such that:

$$y_i' = y_1 \times \frac{\mathcal{W}_1}{\sum_j^k \mathcal{W}_j}, \tag{A.2}$$

3. Iterating j by one bin to the right, $j \to j+1 = 2$, the weighted value of y_i' expands to:

$$y_i' = y_1 \times \frac{\mathcal{W}_1}{\sum_j^k \mathcal{W}_j} + y_2 \times \frac{\mathcal{W}_2}{\sum_j^k \mathcal{W}_j}, \tag{A.3}$$

4. The above continues for all k bins in the ratio $R(m_{Vh}^{(T)})$, thereby iteratively forming the weighted average sum $y_i'^{\text{total}} = \sum_j^k y_j'$. The smoothed central y-value for the bin located at x_i is then set as $y_i'^{\text{total}}$. Note that the original ratio $R(m_{Vh}^{(T)})$ is left unchanged, as the remaining bins must be smoothed.

5. If $i \neq k$ incremented the bin i by one, e.g. $i \to i+1$, and revert back to step (2). If however $i = k$, then the procedure stops.

- **TSpline Smoothing:** Third order polynomials are used to interpolate between the points in the ratio $R(m_{Vh}^{(T)})$, which are marked as red dots in the ratio pane of Figure A.1 (shaded red regions depict the statistical error). The interpolated intervals are then combined to form a piecewise cubic curve that is doubly differentiable across the entire range. This is known as a *cubic spline interpolation*, and is implemented using the `TSpline3` ROOT package [174].

Smoothing Comparisons

An example of the three smoothing techniques is shown by Figure A.1, where in the ratio pane the solid green line represents the best fitting χ^2 minimised function (dotted lines represent the up/down error on the fit result), the purple represents the kernel smoothing approach, and the red is the cubic spline result. The cubic spline interpolation does little to smooth the distribution other than to interpolate between the data points which are shown as red dots in the ratio pane (the red shading is the statistical error). Therefore, the cubic spline smoothing is rejected as a smoothing possibility from here on in.

Meanwhile, the kernel and χ^2 minimised smoothing approaches often performed equally well across all fit regions and for all SM processes, as demonstrated by Figure A.1. However, as shown in the aforementioned example, the kernel smoothing approach often experienced issues at the far extremes of the distribution (left or right). Specifically, the kernel approach would not smooth the extreme edges of the ratio, but rather match the data points exactly. This often meant that artifacts, such as statistical fluctuations in the MC $m_{Vh}^{(T)}$ distributions, in the ratio would often be captured by the kernel smoothing approach; in the above example

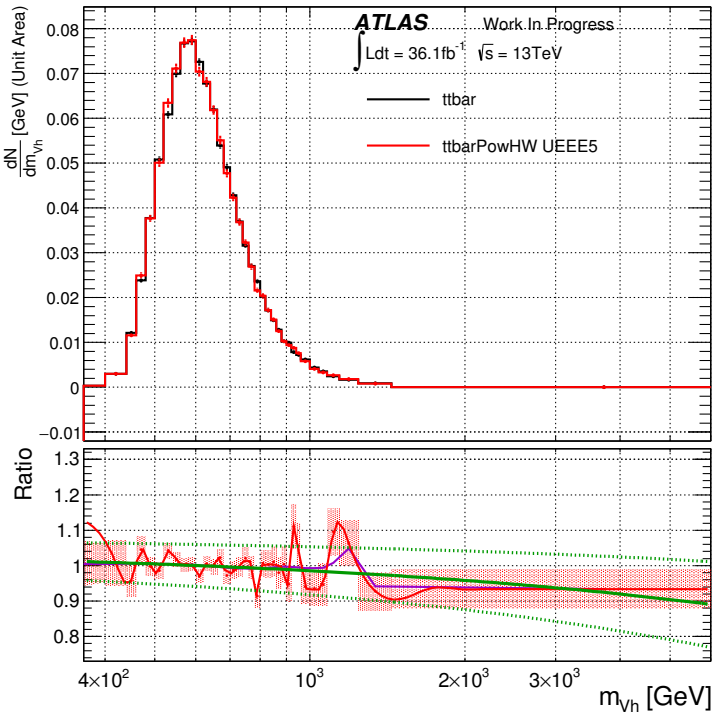

Figure A.1.: Example of the parton shower sensitive $t\bar{t}$ Monte Carlo modelling systematic shape difference in the 1-lepton boosted m_h signal region. The ratio pane shows the ratio $R(m_{Vh}^{(T)}) = h_i^{\text{var}}/h_i^{\text{nom}}$, for the i^{th} bin, along with the χ^2 minimised $y = -0.066(\pm 0.037)\sqrt{x} + 1.1(\pm 0.031)$ function in solid green ($\chi^2/m_{\text{dof}} = 1.013$), kernel smoothed ratio in purple, and cubic spline (TSpline) smoothed ratio in red. The dotted green represents the $\pm 1\sigma$ error on the χ^2 minimised fit function parameters obtained from the minimisation process.

a distinct spike in the kernel smoothed distribution is observed for $m_{Vh} = 1.25$ TeV, which is nothing more than a variation due to limited statistics in the tail.

Considering the above evidence, the χ^2 minimised functional form approach was adopted within the analysis, as outlined in Section 18.3, to smooth the MC modelling $m_{Vh}^{(T)}$ shape systematics.

χ^2 Minimised Functional Form Smoothing - Algorithm Oversight

Following the above motivation and reasoning for the proposed best fit procedure, one issue does exist. The ratio $R(m_{Vh}^{(T)})$ has k bins in $m_{Vh}^{(T)}$, however the order of the fit function or number of terms, varies depending on whether $n = [1, 2]$. Consequently, for a given ratio $R(m_{Vh}^{(T)})$, the number of degrees of freedom for each fit varies according to $n_{\text{dof}} = k - n$.

Given that the skew of the χ^2 distribution $f(\chi^2, n_{\text{dof}})$ is dependent on n_{dof}, the probability of obtaining a $\chi^2/n_{\text{dof}} = \alpha$ from two fits with different degrees of freedom, is not identical. This is best illustrated by considering the p-value definition:

$$\int_{\chi^2_{\text{obs}}}^{\infty} f(\chi^2, n_{\text{dof}}) d\chi^2 = p\text{-value}, \tag{A.4}$$

where χ^2_{obs} is the minimised χ^2 value obtained from the fit, and the p-value represents the probability of obtaining a χ^2 value equal or greater than χ^2_{obs}. Figure A.2 shows $f(\chi^2, n_{\text{dof}})$ for a range of $n_{\text{dof}} = [5, 10, 15, 20]$ values in sub-figure A.2a, whilst sub-figure A.2b shows the variation of the p-value as a function of $\chi^2_{\text{obs}}/n_{\text{dof}}$, for $n_{\text{dof}} = 5$–35 in increments of 5. Sub-figure A.2a demonstrates that for small n_{dof}, the χ^2 distribution is skewed towards small χ^2 values, but the distribution slowly becomes symmetric as $n_{\text{dof}} \to \infty$.

Sub-figure A.2b therefore shows that for any fixed $\chi^2_{\text{obs}}/n_{\text{dof}}$ value, the probability of obtaining a result that is equal or greater than that observed, varies as a function of n_{dof}, due to the difference in skewness. Noting that p-value represents the probability that the observed fit result under the hypothesis that the functional form $f^n(m_{Vh}^{(T)})$ represents the parent distribution of the ratio, $\tilde{R}(m_{Vh}^{(T)})$, could be worse, means that a very small p-value indicates that it is highly unlikely that a statistical excursion could yield the observed result. Consequently one would rather conclude that it is more probable that the hypothesised functional form does not represent the parent distribution, and so an alternative form should be considered.

Therefore, when comparing the fit results of functional forms that have different degrees of freedom, the fit result with a χ^2_{dof} closest to unity, does not necessarily mean that the selected functional form best represents the parent distribution. Rather, a χ^2_{obs} that is slightly further from unity, but has a larger p-value, would be a more likely candidate for the true distribution. For example, as shown by sub-figure A.2b, for a fit with $n_{\text{dof}} = 10$ and $\chi^2/n_{\text{dof}} = 1$, an equally probable result can be obtained by a fit with $\chi^2/n_{\text{dof}} \geq 1.01$ that has 15 or more degrees of freedom ($n_{\text{dof}} \geq 15$).

Whilst this issue is an oversight in the procedure, the effect overall is extremely small. This because for a given ratio $R(m_{Vh}^{(T)})$, either a first order or second order functional form is fitted, meaning that the maximum variation of the number of degrees of freedom is $\Delta n_{\text{dof}} = 1$, which is paired with the fact that typically the ratios $R(m_{Vh}^{(T)})$ contain ≈ 20 or more $m_{Vh}^{(T)}$ bins. Therefore, small variations in the number of degrees of freedom induce only a very small change in the skewness of the χ^2 distribution, $f(\chi^2, n_{\text{dof}})$, that in turn only causes a small difference in the p-value for a fixed χ^2/n_{dof}.

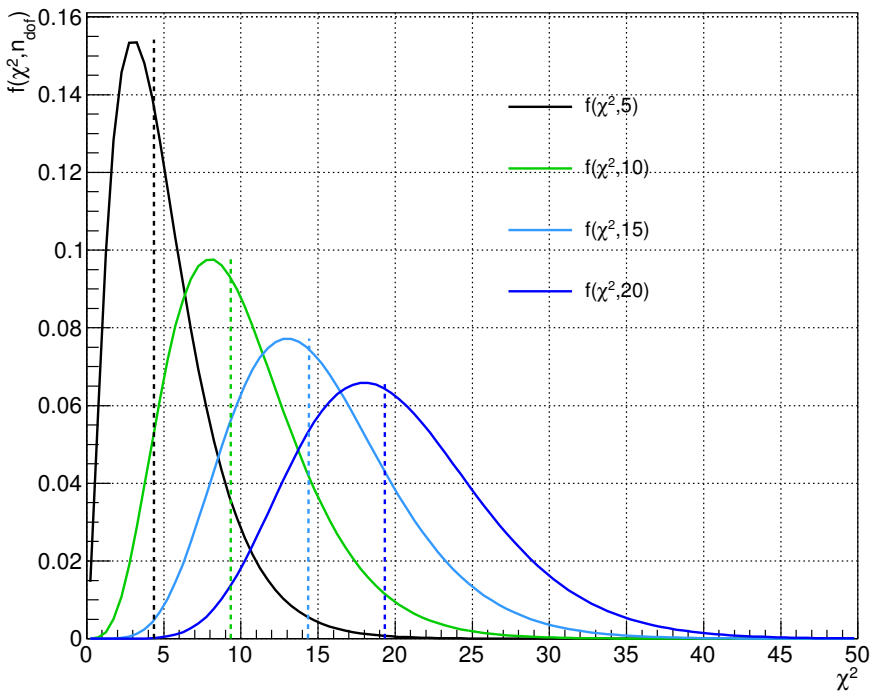

(a)

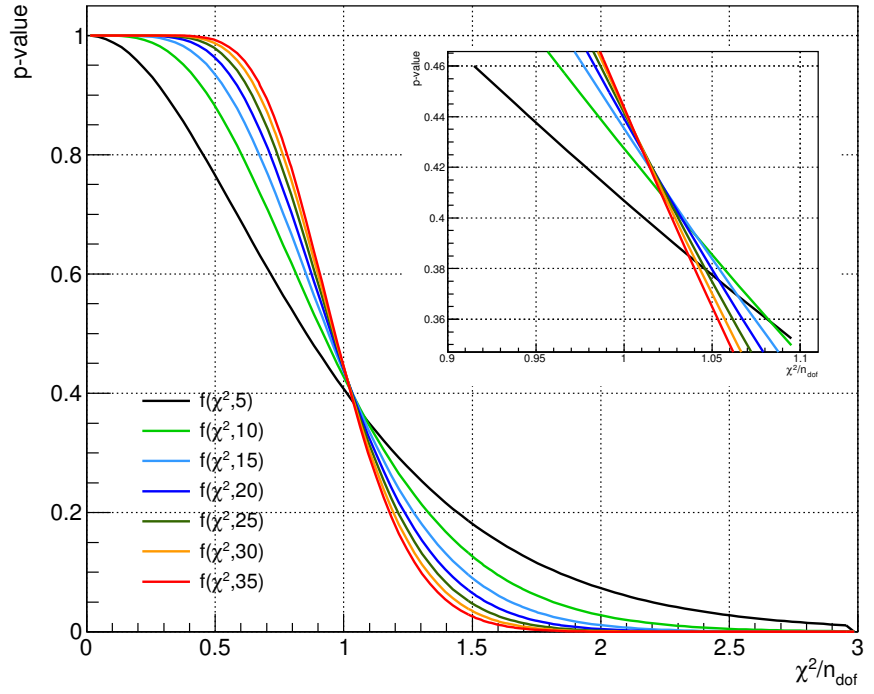

(b)

Figure A.2.: Comparison of $f(\chi^2, n_{\text{dof}})$ for $n_{\text{dof}} = [5, 10, 15, 20]$ along with the median value shown as a dotted vertical line (a), and the p-value as a function of χ^2/n_{dof} for $n_{\text{dof}} = [5, 10, 15, 20, 25, 30, 35]$ (b).

Appendix B.

Binned vs Smoothed Standard Model Modelling Uncertainties

The methodology outlined in Section 18.3, was one of multiple options considered when attempting to parameterise the variation of the $m_{Vh}^{(T)}$ templates due to modelling uncertainties in the 3 key background processes; $t\bar{t}$, V+Jets, and single top production. To recall, the analysis adopted a procedure whereby a function was fitted to the $h_i^{\text{var}}/h_i^{\text{nom}}$ ratio using a χ^2-minimisation process, in order to smooth out any statistical fluctuations. This procedure was compared to an alternative method, where the aforementioned binned ratio was used instead, and passed directly to the fit. These *binned* systematics would then be smoothed using the procedure outlined in section 17.4.1 instead.

To assess the impact of these two methodologies on the analysis, a control region only fit in the 2-lepton AZh channel was run using the χ^2 *smoothed* systematics, and the *binned* systematics. Figure B.2, shows the nuisance parameter pulls for these two fits. The black and red points correspond to the χ^2-*smoothed* methodology and *binned* systematics, respectively. In addition to this, an unconditional Asimov fit was also used in order to compare the expected sensitivity of the analysis under the two approaches, see figure B.3 for the exclusion curve. Due to the negligible difference between the binned and χ^2/n_{dof}-*smoothed* methods, both in the nuisance parameters and the exclusion performance of the analysis, a choice was made to use the χ^2/n_{dof}-*smoothed* systematics.

NP	Pull±σ (Smoothed)	
	Smoothed	Binned
norm_Zbb	1.27 ± 0.13	1.28 ± 0.13
norm_Zclbl	1.26 ± 0.12	1.26 ± 0.12
norm_Zjets_3pTag	1.60 ± 0.33	1.62 ± 0.34
norm_ttbar_3pTag_L2_T3	1.55 ± 0.31	1.57 ± 0.31
norm_ttbar_L2	0.97 ± 0.08	0.97 ± 0.08
LUMI_201516	−0.07 ± 0.99	−0.07 ± 0.99
MET_SoftTrk_ResoPara	−0.04 ± 0.99	−0.05 ± 0.99
MET_SoftTrk_ResoPerp	0.16 ± 0.98	0.15 ± 0.0.98
MET_SoftTrk_Scale	0.13 ± 0.87	0.12 ± 0.86
AZhTheory	0.00 ± 0.99	0.00 ± 0.99
VVNorm	−0.12 ± 0.99	−0.12 ± 0.99
EG_RESOLUTION_ALL	0.05 ± 0.81	0.05 ± 0.81
EG_SCALE_ALL	0.01 ± 0.86	0.01 ± 0.85
EL_EFF_ID_TOTAL_1NPCOR_PLUS_UNCOR	−0.12 ± 0.98	−0.12 ± 0.98
EL_EFF_Iso_TOTAL_1NPCOR_PLUS_UNCOR	−0.10 ± 0.97	−0.09 ± 0.97
EL_EFF_Reco_TOTAL_1NPCOR_PLUS_UNCOR	−0.01 ± 0.99	−0.01 ± 0.99
EL_EFF_Trigger_TOTAL_1NPCOR_PLUS_UNCOR	0.00 ± 0.99	0.00 ± 0.99
FATJET_JER	−0.22 ± 0.96	−0.22 ± 0.96
FATJET_JMR	0.25 ± 0.97	0.23 ± 0.97
FT_B_0_calo	0.28 ± 0.91	0.25 ± 0.92
FT_B_0_track	−0.23 ± 0.96	−0.24 ± 0.96
FT_B_1_calo	0.05 ± 0.97	0.02 ± 0.96
FT_B_1_track	−0.29 ± 0.91	−0.30 ± 0.92
FT_B_2_calo	−0.08 ± 0.99	−0.09 ± 0.98
FT_B_2_track	0.00 ± 0.99	0.00 ± 0.99
FT_Charm_0_calo	0.98 ± 0.67	0.98 ± 0.67
FT_Charm_0_track	−0.52 ± 0.87	−0.50 ± 0.89
FT_Charm_1_calo	0.14 ± 0.77	0.06 ± 0.75
FT_Charm_1_track	0.06 ± 1.00	0.08 ± 1.00
FT_Charm_2_calo	0.17 ± 0.96	0.12 ± 0.96
FT_Charm_2_track	0.09 ± 0.99	0.10 ± 0.99
FT_Charm_3_calo	0.01 ± 0.99	0.01 ± 0.99
FT_Charm_3_track	−0.02 ± 0.98	−0.02 ± 0.98
FT_Light_0_calo	0.16 ± 0.91	0.13 ± 0.90
FT_Light_0_track	−0.41 ± 0.90	−0.40 ± 0.91
FT_Light_1_calo	0.07 ± 0.97	0.08 ± 0.97
FT_Light_1_track	−0.02 ± 1.02	−0.01 ± 1.02
FT_Light_2_calo	−0.36 ± 0.94	−0.36 ± 0.94
FT_Light_2_track	0.02 ± 0.98	0.02 ± 0.98
FT_Light_3_calo	−0.14 ± 0.97	−0.16 ± 0.97
FT_Light_3_track	0.03 ± 0.99	0.03 ± 0.99
FT_Light_4_calo	−0.04 ± 0.98	0.04 ± 0.98
FT_Light_4_track	−0.27 ± 1.00	−0.27 ± 1.00
FT_EFF_extrap_calo	−0.12 ± 0.99	−0.11 ± 0.99
FT_EFF_extrap_from_charm_track	0.00 ± 0.99	0.00 ± 0.99
FT_EFF_extrap_track	0.12 ± 0.98	0.12 ± 0.98
JET_Comb_Baseline_Kin	−0.29 ± 0.91	−0.28 ± 0.91
JET_Comb_Modelling_Kin	−0.29 ± 1.05	−0.29 ± 1.05
JET_Comb_TotalStat_Kin	−0.29 ± 1.02	−0.29 ± 1.02
JET_Comb_Tracking_Kin	−0.19 ± 1.14	−0.19 ± 1.14
JER	0.03 ± 0.80	0.05 ± 0.80
JET_SR1_JET_1	0.58 ± 0.57	0.59 ± 0.57
JET_SR1_JET_2	−0.14 ± 1.40	−0.05 ± 1.52
JET_SR1_JET_3	−0.07 ± 0.82	−0.05 ± 0.84
MODEL_TTbar_Herwig_L2	0.41 ± 0.55	0.20 ± 0.36
MODEL_TTbar_Herwig_L2_T3	0.02 ± 0.89	0.0 ± 0.99
MODEL_TTbar_aMcAtNlo_L2	−0.10 ± 0.95	−0.21 ± 0.81
MODEL_TTbar_aMcAtNlo_L2_T3	0.01 ± 0.99	0.01 ± 0.99
MODEL_TTbar_rad_L2	0.08 ± 1.24	0.0 ± 1.03
MODEL_TTbar_rad_L2_T3	0.0 ± 1.00	0.0 ± 1.00
MODEL_Vjets_MadGraph	−0.12 ± 0.44	−0.14 ± 0.32
MUON_EFF_STAT	0.0 ± 0.99	0.0 ± 0.99
MUON_EFF_SYS	−0.08 ± 0.99	−0.07 ± 0.99
MUON_EFF_TrigStatUncertainty	0.0 ± 0.99	0.0 ± 0.99
MUON_EFF_TrigtUncertainty	0.0 ± 0.99	0.01 ± 0.99
MUON_ISO_STAT	0.0 ± 0.99	0.0 ± 0.99
MUON_ISO_SYS	0.05 ± 0.99	0.05 ± 0.99
MUON_TTVA_STAT	0.0 ± 0.99	0.0 ± 0.99
MUON_TTVA_SYS	0.0 ± 0.99	0.0 ± 0.99
NNLORW_L2	−0.15 ± 0.67	−0.15 ± 0.68
NNLORW_L2_T3	0.08 ± 0.99	0.08 ± 0.99
PRW_DATASF	−0.78 ± 0.67	−0.71 ± 0.68
StopNorm	0.0 ± 0.99	−0.01 ± 0.99
Zbb_ResMergedRatio	0.15 ± 0.94	0.14 ± 0.94
Zclbl_ResMergedRatio	−1.18 ± 0.74	−1.19 ± 0.74
ZlNorm	−0.30 ± 0.96	−0.28 ± 0.96
Zl_ResMergedRatio	−0.34 ± 0.95	−0.34 ± 0.94
ttbar_ResMergedRatio_L2	0.33 ± 0.92	0.33 ± 0.92
ttbar_topemuRatio_2L_L2	−0.18 ± 0.99	−0.18 ± 0.99
ttbar_topemuRatio_2L_L2_T3	−0.02 ± 0.99	−0.02 ± 0.99

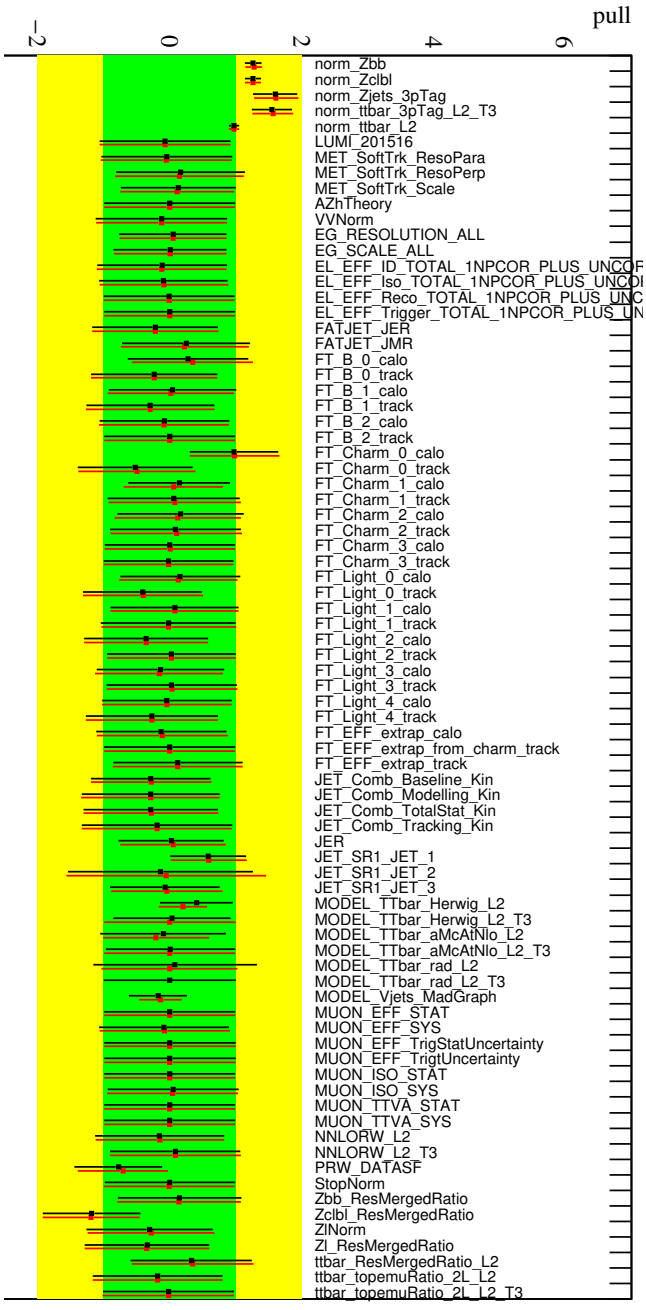

Figure B.2.: Comparison of the nuisance parameter pulls for the 2-lepton $A \to Zh$ channel using a control region only fit. Black points correspond to the fit run using parameterised systematics, whilst the red corresponds to the fit run using the binned. *Plot produced by Chikuma Kato (University of Tokyo (JP)), using inputs provided by the author*

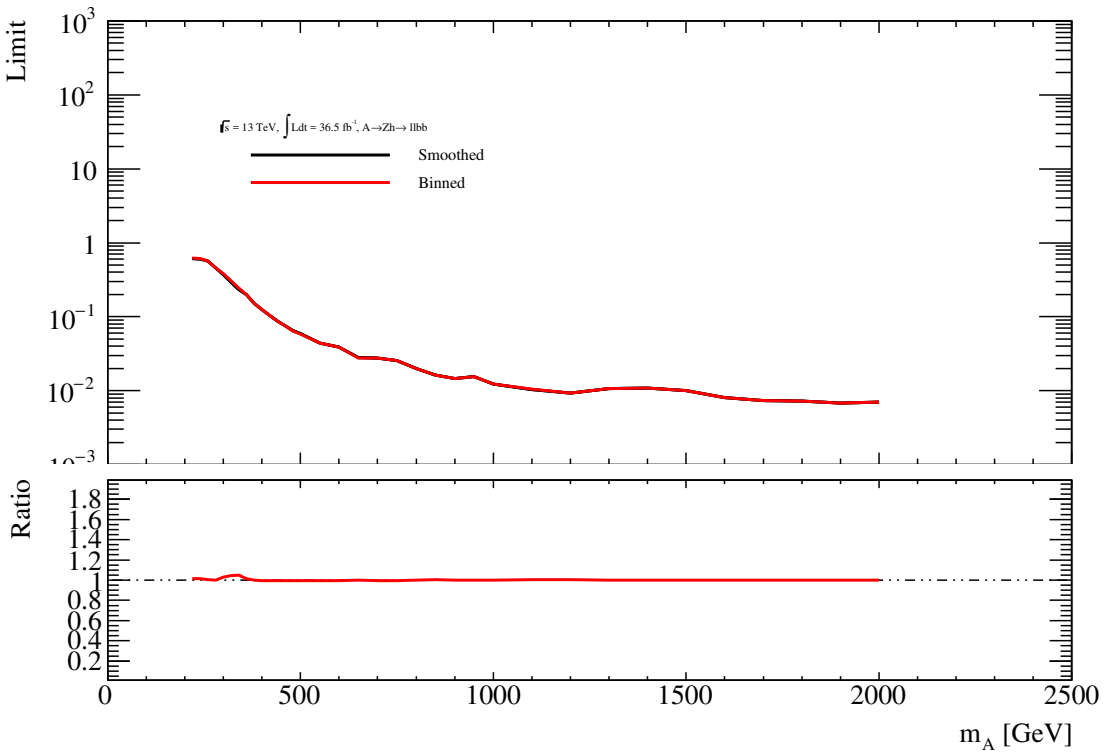

Figure B.3.: Comparison of the exclusion limits of $\sigma_{A\to Zh\to llbb} \times BR(h \to bb)$ for the 2-lepton $A \to Zh$ channel using a Asimov fit. *Plot produced by Chikuma Kato (University of Tokyo (JP)), using inputs provided by the author*

Bibliography

[1] ATLAS Collaboration, M. Aaboud et al., *Measurement of b-hadron pair production with the ATLAS detector in proton-proton collisions at* $\sqrt{s} = 8$ *TeV*, JHEP **11** (2017) 062, arXiv:1705.03374 [hep-ex].

[2] ATLAS Collaboration, *Search for heavy resonances decaying to a W or Z boson and a Higgs boson in final states with leptons and b-jets in 36.1* fb^{-1} *of pp collision data at* $\sqrt{s} = 13$ *TeV with the ATLAS detector*, Tech. Rep. ATLAS-CONF-2017-055, CERN, Geneva, Jul, 2017. http://cds.cern.ch/record/2273871.

[3] ATLAS Collaboration, *Search for new resonances decaying to a W or Z boson and a Higgs boson in the* $\ell\ell b\bar{b}$*,* $\ell\nu b\bar{b}$*, and* $\nu\nu b\bar{b}$ *channels in pp collisions at* $\sqrt{s} = 13$ *TeV with the ATLAS detector*, Tech. Rep. ATLAS-CONF-2015-074, CERN, Geneva, Dec, 2015. http://cds.cern.ch/record/2114846.

[4] T. e. a. Aoyama, *Tenth-Order Electron Anomalous Magnetic Moment — Contribution of Diagrams without Closed Lepton Loops*, Phys. Rev. **D91** (2015) no. 3, 033006, arXiv:1412.8284 [hep-ph]. [Erratum: Phys. Rev.D96,no.1,019901(2017)].

[5] D. e. a. Hanneke, *Cavity Control of a Single-Electron Quantum Cyclotron: Measuring the Electron Magnetic Moment*, Phys. Rev. **A83** (2011) 052122, arXiv:1009.4831 [physics.atom-ph].

[6] Super-Kamiokande Collaboration, Y. Fukuda et al., *Evidence for oscillation of atmospheric neutrinos*, Phys. Rev. Lett. **81** (1998) 1562–1567, arXiv:hep-ex/9807003 [hep-ex].

[7] SNO Collaboration, Q. R. Ahmad et al., *Measurement of the rate of* $\nu_e + d \to p + p + e^-$ *interactions produced by* ^8B *solar neutrinos at the Sudbury Neutrino Observatory*, Phys. Rev. Lett. **87** (2001) 071301, arXiv:nucl-ex/0106015 [nucl-ex].

[8] K. Garrett and G. Duda, *Dark Matter: A Primer*, Adv. Astron. **2011** (2011) 968283, arXiv:1006.2483 [hep-ph].

[9] Supernova Search Team Collaboration, A. G. Riess et al., *Observational evidence from supernovae for an accelerating universe and a cosmological constant*, Astron. J. **116** (1998) 1009–1038, arXiv:astro-ph/9805201 [astro-ph].

[10] Supernova Cosmology Project Collaboration, S. Perlmutter et al., *Discovery of a supernova explosion at half the age of the Universe and its cosmological implications*, Nature **391** (1998) 51–54, arXiv:astro-ph/9712212 [astro-ph].

[11] Particle Data Group, *Review of Particle Physics*, Chin. Phys. **C40** (2016) no. 10, 100001.

[12] D. J. Griffiths, *Introduction to elementary particles; 2nd rev. version*. Physics textbook. Wiley, New York, NY, 2008. https://cds.cern.ch/record/111880.

[13] CTEQ Collaboration, R. Brock et al., *Handbook of perturbative QCD: Version 1.0*, Rev. Mod. Phys. **67** (1995) 157–248.

[14] M. E. Peskin and D. V. Schroeder, *An Introduction to quantum field theory*. 1995. http://www.slac.stanford.edu/spires/find/books/www?cl=QC174.45%3AP4.

[15] R. K. Ellis, W. J. Stirling, and B. R. Webber, *QCD and collider physics*, Camb. Monogr. Part. Phys. Nucl. Phys. Cosmol. **8** (1996) 1–435.

[16] S. M. Bilenky and J. Hosek, *Glashow-Weinberg-Salam Theory of Electroweak Interactions and the Neutral Currents*, Phys. Rept. **90** (1982) 73–157.

[17] F. Englert and R. Brout, *Broken Symmetry and the Mass of Gauge Vector Mesons*, Phys. Rev. Lett. **13** (1964) 321–323.

[18] P. W. Higgs, *Broken Symmetries and the Masses of Gauge Bosons*, Phys. Rev. Lett. **13** (1964) 508–509.

[19] G. S. Guralnik, C. R. Hagen, and T. W. B. Kibble, *Global Conservation Laws and Massless Particles*, Phys. Rev. Lett. **13** (1964) 585–587. https://link.aps.org/doi/10.1103/PhysRevLett.13.585.

[20] S. P. Martin, *A Supersymmetry primer*, 1997. arXiv:hep-ph/9709356 [hep-ph].

[21] ATLAS Collaboration, *Observation of a new particle in the search for the Standard Model Higgs boson with the ATLAS detector at the LHC*, Phys. Lett. B **716** (2012) 1–29, arXiv:1207.7214 [hep-ex].

[22] CMS Collaboration, *Observation of a new boson at a mass of 125 GeV with the CMS experiment at the LHC*, Phys. Lett. B **716** (2012) 30–61, arXiv:1207.7235 [hep-ex].

[23] D. Eliezer and R. Woodard, *The problem of nonlocality in string theory*, Nuclear Physics B **325** (1989) no. 2, 389 – 469. http://www.sciencedirect.com/science/article/pii/0550321389904616.

[24] F. Sannino and K. Tuominen, *Orientifold theory dynamics and symmetry breaking*, Phys. Rev. **D71** (2005) 051901, arXiv:hep-ph/0405209.

[25] R. Foadi, M. T. Frandsen, T. A. Ryttov, and F. Sannino, *Minimal Walking Technicolor: Set Up for Collider Physics*, Phys. Rev. D **76** (2007) 055005, arXiv:0706.1696 [hep-ph].

[26] A. Belyaev, R. Foadi, M. T. Frandsen, M. Jarvinen, F. Sannino, et al., *Technicolor Walks at the LHC*, Phys. Rev. D **79** (2009) 035006, arXiv:0809.0793 [hep-ph].

[27] M. Schmaltz and D. Tucker-Smith, *Little Higgs review*, Ann. Rev. Nucl. Part. Sci. **55** (2005) 229–270, arXiv:hep-ph/0502182.

[28] M. J. Dugan, H. Georgi, and D. B. Kaplan, *Anatomy of a Composite Higgs Model*, Nucl. Phys. **B254** (1985) 299.

[29] K. Agashe, R. Contino, and A. Pomarol, *The Minimal composite Higgs model*, Nucl. Phys. **B719** (2005) 165–187, arXiv:hep-ph/0412089.

[30] D. Pappadopulo, A. Thamm, R. Torre, and A. Wulzer, *Heavy Vector Triplets: Bridging Theory and Data*, JHEP **09** (2014) 060, arXiv:1402.4431 [hep-ph].

[31] V. D. Barger, W.-Y. Keung, and E. Ma, *A Gauge Model With Light W and Z Bosons*, Phys. Rev. **D22** (1980) 727.

[32] R. Contino, D. Marzocca, D. Pappadopulo, and R. Rattazzi, *On the effect of resonances in composite Higgs phenomenology*, JHEP **10** (2011) 081, arXiv:1109.1570 [hep-ph].

[33] D. P. Kroese, T. Taimre, and B. I. Zdravko, *Handbook of Monte Carlo methods*. Wiley Series in Probability and Statistics. Wiley, Hoboken, NJ, 2011. https://cds.cern.ch/record/1346314.

[34] A. Buckley et al., *General-purpose event generators for LHC physics*, Phys. Rept. **504** (2011) 145–233, arXiv:1101.2599 [hep-ph].

[35] T. Gleisberg, S. Hoeche, F. Krauss, M. Schonherr, S. Schumann, F. Siegert, and J. Winter, *Event generation with SHERPA 1.1*, JHEP **02** (2009) 007, arXiv:0811.4622 [hep-ph].

[36] J. M. Campbell, J. W. Huston, and W. J. Stirling, *Hard interactions of quarks and*

gluons: a primer for LHC physics, Reports on Progress in Physics **70** (2007) no. 1, 89. http://stacks.iop.org/0034-4885/70/i=1/a=R02.

[37] J. C. Collins, D. E. Soper, and G. F. Sterman, *Factorization of Hard Processes in QCD*, Adv. Ser. Direct. High Energy Phys. **5** (1989) 1–91, arXiv:hep-ph/0409313 [hep-ph].

[38] Y. L. Dokshitzer, *Calculation of the Structure Functions for Deep Inelastic Scattering and e+ e- Annihilation by Perturbation Theory in Quantum Chromodynamics.*, Sov. Phys. JETP **46** (1977) 641–653. [Zh. Eksp. Teor. Fiz.73,1216(1977)].

[39] V. N. Gribov and L. N. Lipatov, *Deep inelastic e p scattering in perturbation theory*, Sov. J. Nucl. Phys. **15** (1972) 438–450. [Yad. Fiz.15,781(1972)].

[40] S. Höche, *Introduction to parton-shower event generators*, in *Proceedings, Theoretical Advanced Study Institute in Elementary Particle Physics: Journeys Through the Precision Frontier: Amplitudes for Colliders (TASI 2014): Boulder, Colorado, June 2-27, 2014*, pp. 235–295. 2015. arXiv:1411.4085 [hep-ph].

[41] S. Frixione and B. R. Webber, *Matching NLO QCD computations and parton shower simulations*, JHEP **06** (2002) 029, arXiv:hep-ph/0204244 [hep-ph].

[42] O. S. Bruning, P. Collier, P. Lebrun, S. Myers, R. Ostojic, J. Poole, and P. Proudlock, *LHC Design Report*. CERN Yellow Reports: Monographs. CERN, Geneva, 2004. https://cds.cern.ch/record/782076.

[43] R. Bruce, G. Arduini, S. Fartoukh, M. Giovannozzi, M. Lamont, E. Metral, T. Pieloni, S. Redaelli, and J. Wenninger, *Baseline LHC machine parameters and configuration of the 2015 proton run*, in *Proceedings, LHC Performance Workshop (Chamonix 2014): Chamonix, France, September 22-25, 2014*, pp. 100–106. 2015. arXiv:1410.5990 [physics.acc-ph].

[44] F. Marcastel, *CERN's Accelerator Complex. La chaîne des accélérateurs du CERN*, Oct, 2013. https://cds.cern.ch/record/1621583. General Photo.

[45] ATLAS Collaboration, *Improved luminosity determination in pp collisions at* $\sqrt{(}s) = 7$ *TeV using the ATLAS detector at the LHC*, Eur. Phys. J. **C73** (2013) 2518, arXiv:1302.4393 [hep-ex].

[46] A. Sidoti, *Minimum Bias Trigger Scintillators in ATLAS Run II*, JINST **9** (2014) no. 10, C10020. http://stacks.iop.org/1748-0221/9/i=10/a=C10020.

[47] ATLAS Collaboration, *The ATLAS Experiment at the CERN Large Hadron Collider*, JINST **3** (2008) S08003.

[48] ATLAS Collaboration, *Track Reconstruction Performance of the ATLAS Inner Detector at* $\sqrt{s} = 13$ *TeV*, Tech. Rep. ATL-PHYS-PUB-2015-018, CERN, Geneva, Jul, 2015. http://cds.cern.ch/record/2037683.

[49] ATLAS Collaboration, *ATLAS Insertable B-Layer Technical Design Report*, Tech. Rep. CERN-LHCC-2010-013. ATLAS-TDR-19, Sep, 2010. https://cds.cern.ch/record/1291633.

[50] S. Palestini, *The muon spectrometer of the ATLAS experiment*, Nucl. Phys. Proc. Suppl. **125** (2003) 337–345. [,337(2003)].

[51] A. D. Martin, W. J. Stirling, R. S. Thorne, and G. Watt, *Parton distributions for the LHC*, Eur. Phys. J. **C63** (2009) 189–285, arXiv:0901.0002 [hep-ph].

[52] ATLAS Collaboration, *Performance of the ATLAS Trigger System in 2015*, Eur. Phys. J. **C77** (2017) no. 5, 317, arXiv:1611.09661 [hep-ex].

[53] M. Ciuchini, E. Franco, S. Mishima, and L. Silvestrini, *Electroweak Precision Observables, New Physics and the Nature of a 126 GeV Higgs Boson*, JHEP **08** (2013) 106, arXiv:1306.4644 [hep-ph].

[54] G. D'Agostini, *Bayesian reasoning in high-energy physics: principles and applications*. CERN Yellow Reports: Monographs. CERN, Geneva, 1999. http://cds.cern.ch/record/395902.

[55] ATLAS Collaboration, *Search for new resonances decaying to a W or Z boson and a Higgs boson in the* $\ell^+\ell^- b\bar{b}$, $\ell\nu b\bar{b}$, *and* $\nu\bar{\nu}b\bar{b}$ *channels with pp collisions at* $\sqrt{s} = 13$ *TeV with the ATLAS detector*, Phys. Lett. **B765** (2017) 32–52, arXiv:1607.05621 [hep-ex].

[56] ATLAS Collaboration, *Search for a new resonance decaying to a W or Z boson and a Higgs boson in the* $\ell\ell/\ell\nu/\nu\nu + b\bar{b}$ *final states with the ATLAS detector*, Eur. Phys. J. **C75** (2015) 263, arXiv:1503.08089 [hep-ex].

[57] T. Lee, *A Theory of Spontaneous T Violation*, Phys. Rev. D. **8** (1973) 1226.

[58] J. F. Gunion and H. E. Haber, *The CP conserving two Higgs doublet model: The approach to the decoupling limit*, Phys. Rev. D. **67** (2003) 075019, arXiv:hep-ph/0207010.

[59] G. C. Branco, P. M. Ferreira, L. Lavoura, M. N. Rebelo, M. Sher, and J. P. Silva, *Theory and phenomenology of two-Higgs-doublet models*, Phys. Rept. **516** (2012) 1–102, arXiv:1106.0034 [hep-ph].

[60] LHC Higgs Cross Section Working Group Collaboration, *Handbook of LHC Higgs Cross Sections: 3. Higgs Properties*, arXiv:1307.1347 [hep-ph].

[61] N. Craig, J. A. Evans, R. Gray, C. Kilic, M. Park, et al., *Multi-Lepton Signals of Multiple Higgs Bosons*, JHEP **1302** (2013) 033, arXiv:1210.0559 [hep-ph].

[62] P. Fayet, *Supersymmetry and Weak, Electromagnetic and Strong Interactions*, Phys. Lett. **B64** (1976) 159.

[63] P. Fayet, *Spontaneously Broken Supersymmetric Theories of Weak, Electromagnetic and Strong Interactions*, Phys. Lett. **B69** (1977) 489.

[64] G. R. Farrar and P. Fayet, *Phenomenology of the Production, Decay, and Detection of New Hadronic States Associated with Supersymmetry*, Phys. Lett. **B76** (1978) 575–579.

[65] P. Fayet, *Relations Between the Masses of the Superpartners of Leptons and Quarks, the Goldstino Couplings and the Neutral Currents*, Phys. Lett. **B84** (1979) 416.

[66] S. Dimopoulos and H. Georgi, *Softly Broken Supersymmetry and SU(5)*, Nucl. Phys. **B193** (1981) 150.

[67] M. Joyce, T. Prokopec, and N. Turok, *Nonlocal electroweak baryogenesis. Part 2: The Classical regime*, Phys. Rev. **B53** (1996) 2958–2980, arXiv:hep-ph/9410282 [hep-ph].

[68] J. E. Kim, *Light Pseudoscalars, Particle Physics and Cosmology*, Phys. Rept. **150** (1987) 1–177.

[69] ATLAS Collaboration, *Search for a CP-odd Higgs boson decaying to Zh in pp collisions at $\sqrt{s} = 8$ TeV with the ATLAS detector*, Phys. Lett. **B744** (2015) 163–183, arXiv:1502.04478 [hep-ex].

[70] ATLAS Collaboration, *Search for a CP-odd Higgs boson decaying to Zh in pp collisions at $\sqrt{s} = 13TeV$ with the ATLAS detector*, Tech. Rep. ATLAS-CONF-2016-015, CERN, Geneva, Mar, 2016. http://cds.cern.ch/record/2141003.

[71] CMS Collaboration, CMS Collaboration, *Search for a pseudoscalar boson decaying into a Z boson and the 125 GeV Higgs boson in $l^+l^-b\bar{b}$ final states*, Phys. Lett. **B748** (2015) 221–243, arXiv:1504.04710 [hep-ex].

[72] ROOT Collaboration, K. Cranmer, G. Lewis, L. Moneta, A. Shibata, and W. Verkerke, *HistFactory: A tool for creating statistical models for use with RooFit*

and RooStats, 2012.

[73] G. Cowan, K. Cranmer, E. Gross, and O. Vitells, *Asymptotic formulae for likelihood-based tests of new physics*, Eur. Phys. J. **C71** (2011) 1554, arXiv:1007.1727 [physics.data-an]. [Erratum: Eur. Phys. J.C73,2501(2013)].

[74] R. Barlow and C. Beeston, *Fitting using finite Monte Carlo samples*, Computer Physics Communications **77** (1993) no. 2, 219 – 228. http://www.sciencedirect.com/science/article/pii/001046559390005W.

[75] J. S. Conway, *Incorporating Nuisance Parameters in Likelihoods for Multisource Spectra*, in *Proceedings, PHYSTAT 2011 Workshop on Statistical Issues Related to Discovery Claims in Search Experiments and Unfolding, CERN,Geneva, Switzerland 17-20 January 2011*, pp. 115–120. 2011. arXiv:1103.0354 [physics.data-an].

[76] A. Wald, *Tests of Statistical Hypotheses Concerning Several Parameters When the Number of Observations is Large*, Transactions of the American Mathematical Society **54** (1943) no. 3, 426–482. http://www.jstor.org/stable/1990256.

[77] A. L. Read, *Presentation of search results: the CL s technique*, Journal of Physics G: Nuclear and Particle Physics **28** (2002) no. 10, 2693. http://stacks.iop.org/0954-3899/28/i=10/a=313.

[78] J. Alwall, R. Frederix, S. Frixione, V. Hirschi, F. Maltoni, O. Mattelaer, H. S. Shao, T. Stelzer, P. Torrielli, and M. Zaro, *The automated computation of tree-level and next-to-leading order differential cross sections, and their matching to parton shower simulations*, JHEP **07** (2014) 079, arXiv:1405.0301 [hep-ph].

[79] R. D. Ball et al., *Impact of heavy quark masses on parton distributions and LHC phenomenology*, Nucl. Phys. **B 849** (2011) 296–363, arXiv:1101.1300 [hep-ph].

[80] T. Sjöstrand, S. Mrenna, and P. Z. Skands, *A Brief Introduction to PYTHIA 8.1*, Comput. Phys. Commun. **178** (2008) 852–867, arXiv:0710.3820 [hep-ph].

[81] ATLAS Collaboration, *Summary of ATLAS Pythia 8 tunes*, ATL-PHYS-PUB-2012-003 (2012) . https://cds.cern.ch/record/1474107.

[82] D. Eriksson, J. Rathsman, and O. Stal, *2HDMC: Two-Higgs-Doublet Model Calculator Physics and Manual*, Comput. Phys. Commun. **181** (2010) 189–205, arXiv:0902.0851 [hep-ph].

[83] H. E. Haber and O. Stal, *New LHC benchmarks for the $\mathcal{CP}$ -conserving two-Higgs-doublet model*, Eur. Phys. J. **C75** (2015) no. 10, 491, arXiv:1507.04281 [hep-ph]. [Erratum: Eur. Phys. J.C76,no.6,312(2016)].

[84] T. Gleisberg and S. Höche, *Comix, a new matrix element generator*, JHEP **12** (2008) 039, arXiv:0808.3674 [hep-ph].

[85] F. Cascioli, P. Maierhofer, and S. Pozzorini, *Scattering Amplitudes with Open Loops*, Phys. Rev. Lett. **108** (2012) 111601, arXiv:1111.5206 [hep-ph].

[86] S. Hoche, F. Krauss, M. Schönherr, and F. Siegert, *QCD matrix elements + parton showers: The NLO case*, JHEP **04** (2013) 027, arXiv:1207.5030 [hep-ph].

[87] K. Melnikov and F. Petriello, *Electroweak gauge boson production at hadron colliders through $O(\alpha_s^2)$*, Phys. Rev. **D74** (2006) 114017, arXiv:hep-ph/0609070.

[88] P. Nason, *A new method for combining NLO QCD with shower Monte Carlo algorithms*, JHEP **11** (2004) 040, arXiv:hep-ph/0409146.

[89] S. Frixione, P. Nason, and C. Oleari, *Matching NLO QCD computations with Parton Shower simulations: the POWHEG method*, JHEP **11** (2007) 070, arXiv:0709.2092 [hep-ph].

[90] S. Alioli, P. Nason, C. Oleari, and E. Re, *A general framework for implementing NLO calculations in shower Monte Carlo programs: the POWHEG BOX*, JHEP **06** (2010) 043, arXiv:1002.2581 [hep-ph].

[91] H.-L. Lai, M. Guzzi, J. Huston, Z. Li, P. M. Nadolsky, et al., *New parton distributions for collider physics*, Phys. Rev. D **82** (2010) 074024, arXiv:1007.2241 [hep-ph].

[92] T. Sjöstrand, S. Mrenna, and P. Z. Skands, *PYTHIA 6.4 Physics and Manual*, JHEP **05** (2006) 026, arXiv:hep-ph/0603175.

[93] J. Pumplin et al., *New generation of parton distributions with uncertainties from global QCD analysis*, JHEP **07** (2002) 012, arXiv:hep-ph/0201195.

[94] P. Z. Skands, *Tuning Monte Carlo Generators: The Perugia Tunes*, Phys. Rev. D **82** (2010) 074018, arXiv:1005.3457 [hep-ph].

[95] P. Golonka and Z. Was, *PHOTOS Monte Carlo: A Precision tool for QED corrections in Z and W decays*, Eur. Phys. J. **C45** (2006) 97–107, arXiv:hep-ph/0506026 [hep-ph].

[96] Z. Was, *TAUOLA the library for tau lepton decay, and KKMC / KORALB / KORALZ /... status report*, Nucl. Phys. Proc. Suppl. **98** (2001) 96–102, arXiv:hep-ph/0011305 [hep-ph].

[97] D. J. Lange, *The EvtGen particle decay simulation package*, Nucl. Instrum. Meth. **A462** (2001) 152–155.

[98] ATLAS Collaboration Collaboration, *Studies on top-quark Monte Carlo modelling with Sherpa and MG5_aMC@NLO*, Tech. Rep. ATL-PHYS-PUB-2017-007, CERN, Geneva, May, 2017. https://cds.cern.ch/record/2261938.

[99] P. Artoisenet, R. Frederix, O. Mattelaer, and R. Rietkerk, *Automatic spin-entangled decays of heavy resonances in Monte Carlo simulations*, JHEP **03** (2013) 015, arXiv:1212.3460 [hep-ph].

[100] L. Lonnblad, *Correcting the color dipole cascade model with fixed order matrix elements*, JHEP **05** (2002) 046, arXiv:hep-ph/0112284 [hep-ph].

[101] N. Lavesson and L. Lonnblad, *W+jets matrix elements and the dipole cascade*, JHEP **07** (2005) 054, arXiv:hep-ph/0503293 [hep-ph].

[102] T. Sjöstrand, S. Mrenna, and P. Z. Skands, *A Brief Introduction to PYTHIA 8.1*, Comput. Phys. Commun. **178** (2008) 852–867, arXiv:0710.3820 [hep-ph].

[103] ATLAS Collaboration, *Measurement of the Z boson transverse momentum distribution in pp collisions at $\sqrt{s}$ = 7 TeV with the ATLAS detector*, JHEP **09** (2014) 145, arXiv:1406.3660 [hep-ex].

[104] L. Altenkamp, S. Dittmaier, R. V. Harlander, H. Rzehak, and T. J. E. Zirke, *Gluon-induced Higgs-strahlung at next-to-leading order QCD*, JHEP **02** (2013) 078, arXiv:1211.5015 [hep-ph].

[105] B. Hespel, F. Maltoni, and E. Vryonidou, *Higgs and Z boson associated production via gluon fusion in the SM and the 2HDM*, JHEP **06** (2015) 065, arXiv:1503.01656 [hep-ph].

[106] R. V. Harlander, A. Kulesza, V. Theeuwes, and T. Zirke, *Soft gluon resummation for gluon-induced Higgs Strahlung*, JHEP **11** (2014) 082, arXiv:1410.0217 [hep-ph].

[107] S. Catani, Y. L. Dokshitzer, M. H. Seymour, and B. R. Webber, *Longitudinally invariant $k_\perp$ clustering algorithms for hadron hadron collisions*, Nucl. Phys. **B406** (1993) 187–224.

[108] M. Cacciari, G. P. Salam, and G. Soyez, *The anti-k_t jet clustering algorithm*, JHEP **04** (2008) 063, arXiv:0802.1189 [hep-ph].

[109] ATLAS Collaboration, *Performance of pile-up mitigation techniques for jets in pp collisions with the ATLAS detector*, Nucl. Instrum. Meth. **A824** (2016) 367–370, arXiv:1510.03823 [hep-ex].

[110] ATLAS Collaboration, *Jet Calibration and Systematic Uncertainties for Jets*

Reconstructed in the ATLAS Detector at $\sqrt{s} = 13$ *TeV*, ATL-PHYS-PUB-2015-015 (Jul, 2015) . https://cds.cern.ch/record/2037613.

[111] ATLAS Collaboration, *Jet energy measurement with the ATLAS detector in proton-proton collisions at* $\sqrt{s} = 7$ *TeV*, Eur. Phys. J. **C73** (2013) 2304, arXiv:1112.6426 [hep-ex].

[112] D. Krohn, J. Thaler, and L.-T. Wang, *Jet Trimming*, JHEP **02** (2010) 084, arXiv:0912.1342 [hep-ph].

[113] ATLAS Collaboration, *Identification of boosted, hadronically-decaying W and Z bosons in* $\sqrt{s} = 13$ *TeV Monte Carlo Simulations for ATLAS*, ATL-PHYS-PUB-2015-033 (Aug, 2015) . http://cds.cern.ch/record/2041461.

[114] ATLAS Collaboration, *Jet mass reconstruction with the ATLAS Detector in early Run 2 data*, Tech. Rep. ATLAS-CONF-2016-035, CERN, Geneva, Jul, 2016. http://cds.cern.ch/record/2200211.

[115] ATLAS Collaboration, *Electron efficiency measurements with the ATLAS detector using the 2015 LHC proton-proton collision data*, Tech. Rep. ATLAS-CONF-2016-024, CERN, Geneva, Jun, 2016. https://cds.cern.ch/record/2157687.

[116] ATLAS Collaboration, *Muon reconstruction performance of the ATLAS detector in proton - proton collision data at* $\sqrt{s}$ *=13 TeV*, Eur. Phys. J. **C76** (2016) no. 5, 292, arXiv:1603.05598 [hep-ex].

[117] ATLAS Collaboration, *Calorimeter clustering algorithms: Description and performance*, ATL-LARG-PUB-2008-002 (2008) . http://cds.cern.ch/record/1099735.

[118] ATLAS Collaboration, *Electron identification measurements in ATLAS using* $\sqrt{s}$ *= 13 TeV data with 50 ns bunch spacing*, ATL-PHYS-PUB-2015-041 (Sep, 2015) . http://cds.cern.ch/record/2048202.

[119] ATLAS Collaboration Collaboration, *Electron and photon reconstruction and identification in ATLAS: expected performance at high energy and results at 900 GeV*, Tech. Rep. ATLAS-CONF-2010-005, CERN, Geneva, Jun, 2010. https://cds.cern.ch/record/1273197.

[120] ATLAS Collaboration, *Electron efficiency measurements with the ATLAS detector using the 2012 LHC proton-proton collision data*, Tech. Rep. ATLAS-CONF-2014-032, CERN, Geneva, Jun, 2014.

http://cds.cern.ch/record/1706245.

[121] ATLAS Collaboration, *Electron reconstruction and identification efficiency measurements with the ATLAS detector using the 2011 LHC proton-proton collision data*, Eur. Phys. J. **C74** (2014) 2941, arXiv:1404.2240 [hep-ex].

[122] ATLAS Collaboration, *Concepts, Design and Implementation of the ATLAS New Tracking (NEWT)*, Tech. Rep. ATL-SOFT-PUB-2007-007, CERN, Geneva, Mar, 2007. https://cds.cern.ch/record/1020106.

[123] ATLAS Collaboration, *Performance of the ATLAS Inner Detector Track and Vertex Reconstruction in the High Pile-Up LHC Environment*, Tech. Rep. ATLAS-CONF-2012-042, CERN, Geneva, Mar, 2012. https://cds.cern.ch/record/1435196.

[124] R. O. Duda and P. E. Hart, *Use of the Hough transformation to detect lines and curves in pictures*, Commun. ACM **15** (Jan., 1972) 11–15. http://doi.acm.org/10.1145/361237.361242.

[125] ATLAS Collaboration, *Measurement of the muon reconstruction performance of the ATLAS detector using 2011 and 2012 LHC proton - proton collision data*, Eur. Phys. J. **C74** (2014) no. 11, 3130, arXiv:1407.3935 [hep-ex].

[126] N. Van Eldik, *The ATLAS muon spectrometer: calibration and pattern recognition.* PhD thesis, Amsterdam U., Amsterdam, 2007. https://cds.cern.ch/record/1044839. Presented on 22 Feb 2007.

[127] ATLAS Collaboration, *Reconstruction, Energy Calibration, and Identification of Hadronically Decaying Tau Leptons in the ATLAS Experiment for Run-2 of the LHC*, Tech. Rep. ATL-PHYS-PUB-2015-045, CERN, Geneva, Nov, 2015. https://cds.cern.ch/record/2064383.

[128] ATLAS Collaboration, *Expected performance of missing transverse momentum reconstruction for the ATLAS detector at* $\sqrt{s} = 13$ *TeV*, Tech. Rep. ATL-PHYS-PUB-2015-023, CERN, Geneva, Jul, 2015. https://cds.cern.ch/record/2037700.

[129] ATLAS Collaboration Collaboration, ATLAS Collaboration, *Optimisation of the ATLAS b-tagging performance for the 2016 LHC Run*, Tech. Rep. ATL-PHYS-PUB-2016-012, CERN, Geneva, Jun, 2016. https://cds.cern.ch/record/2160731.

[130] ATLAS Collaboration, *Expected performance of the ATLAS b-tagging algorithms in*

Run-2, Tech. Rep. ATL-PHYS-PUB-2015-022, CERN, Geneva, Jul, 2015. https://cds.cern.ch/record/2037697.

[131] ATLAS Collaboration, G. Aad et al., *Expected Performance of the ATLAS Experiment - Detector, Trigger and Physics*, arXiv:0901.0512 [hep-ex].

[132] G. Piacquadio and C. Weiser, *A new inclusive secondary vertex algorithm for b-jet tagging in ATLAS*, J. Phys. Conf. Ser. **119** (2008) 032032.

[133] G. Cowan, K. Cranmer, E. Gross, and O. Vitells, *Asymptotic formulae for likelihood-based tests of new physics*, Eur. Phys. J. **C71** (2011) 1554, arXiv:1007.1727 [physics.data-an]. [Erratum: Eur. Phys. J.C73,2501(2013)].

[134] *Missing Transverse Energy Trigger Signature Group* , https://twiki.cern.ch/twiki/bin/view/AtlasPublic/MissingEtTriggerPublicResults?r=r43. Accessed 18/09/17.

[135] ATLAS Collaboration, G. Aad et al., *Reconstruction of hadronic decay products of tau leptons with the ATLAS experiment*, Eur. Phys. J. **C76** (2016) no. 5, 295, arXiv:1512.05955 [hep-ex].

[136] ATLAS Collaboration, *Light-quark and Gluon Jets in ATLAS*, Tech. Rep. ATLAS-CONF-2011-053, CERN, Geneva, Apr, 2011.

[137] ATLAS Collaboration, *Monte Carlo Calibration and Combination of In-situ Measurements of Jet Energy Scale, Jet Energy Resolution and Jet Mass in ATLAS*, Tech. Rep. ATLAS-CONF-2015-037, CERN, Geneva, Aug, 2015. https://cds.cern.ch/record/2044941.

[138] ATLAS Collaboration, *Data-driven determination of the energy scale and resolution of jets reconstructed in the ATLAS calorimeters using dijet and multijet events at* $\sqrt{s} = 8\ TeV$, Tech. Rep. ATLAS-CONF-2015-017, CERN, Geneva, Apr, 2015. https://cds.cern.ch/record/2008678.

[139] ATLAS Collaboration, *Pile-up subtraction and suppression for jets in ATLAS*, Tech. Rep. ATLAS-CONF-2013-083, CERN, Geneva, Aug, 2013. https://cds.cern.ch/record/1570994.

[140] ATLAS Collaboration, *Jet global sequential corrections with the ATLAS detector in proton–proton collisions at* $\sqrt{s} = 8\ TeV$, ATLAS-CONF-2015-002, 2015. https://cds.cern.ch/record/2001682.

[141] ATLAS Collaboration, *Performance of large-R jets and jet substructure reconstruction with the ATLAS detector*, Tech. Rep. ATLAS-CONF-2012-065, CERN,

Geneva, Jul, 2012. https://cds.cern.ch/record/1459530.

[142] ATLAS Collaboration, *Performance of b-Jet Identification in the ATLAS Experiment*, JINST **11** (2016) P04008, arXiv:1512.01094 [hep-ex].

[143] ATLAS Collaboration, *Calibration of b-tagging using dileptonic top pair events in a combinatorial likelihood approach with the ATLAS experiment*, Tech. Rep. ATLAS-CONF-2014-004, CERN, Geneva, Feb, 2014. https://cds.cern.ch/record/1664335.

[144] ATLAS Collaboration, *Calibration of the performance of b-tagging for c and light-flavour jets in the 2012 ATLAS data*, Tech. Rep. ATLAS-CONF-2014-046, CERN, Geneva, Jul, 2014. https://cds.cern.ch/record/1741020.

[145] ATLAS Collaboration, *Luminosity determination in pp collisions at* $\sqrt{s} = 8$ *TeV using the ATLAS detector at the LHC*, Eur. Phys. J. C **76** (2016) no. 12, 653.

[146] ATLAS LUCID Collaboration, *Measurement of the luminosity with the new LUCID-2 detector in 2015*, Tech. Rep. ATL-COM-FWD-2016-008, CERN, Geneva, May, 2016. https://cds.cern.ch/record/2154368.

[147] ATLAS Collaboration, *Measurement of the Inelastic Proton-Proton Cross Section at* $\sqrt{s} = 13$ *TeV with the ATLAS Detector at the LHC*, Phys. Rev. Lett. **117** (2016) no. 18, 182002, arXiv:1606.02625 [hep-ex].

[148] ATLAS Collaboration, *Electron and photon energy calibration with the ATLAS detector using LHC Run 1 data*, Eur. Phys. J. **C74** (2014) 3071, arXiv:1407.5063 [hep-ex].

[149] ATLAS Collaboration, *Electron and photon energy calibration with the ATLAS detector using data collected in 2015 at* $\sqrt{s} = 13$ TeV, Tech. Rep. ATL-PHYS-PUB-2016-015, CERN, Geneva, Aug, 2016. https://cds.cern.ch/record/2203514.

[150] ATLAS Collaboration, *Early Inner Detector Tracking Performance in the 2015 data at* $\sqrt{s} = 13$ *TeV*, Tech. Rep. ATL-PHYS-PUB-2015-051, CERN, Geneva, Dec, 2015. https://cds.cern.ch/record/2110140.

[151] ATLAS Collaboration, *Monte Carlo Generators for the Production of a W or* Z/γ^* *Boson in Association with Jets at ATLAS in Run 2*, Tech. Rep. ATL-PHYS-PUB-2016-003, CERN, Geneva, Jan, 2016. https://cds.cern.ch/record/2120133.

[152] J. Butterworth et al., *PDF4LHC recommendations for LHC Run II*, J. Phys. **G43**

(2016) 023001, arXiv:1510.03865 [hep-ph].

[153] I. W. Stewart and F. J. Tackmann, *Theory Uncertainties for Higgs and Other Searches Using Jet Bins*, Phys. Rev. **D85** (2012) 034011, arXiv:1107.2117 [hep-ph].

[154] C. D. White, S. Frixione, E. Laenen, and F. Maltoni, *Isolating Wt production at the LHC*, JHEP **11** (2009) 074, arXiv:0908.0631 [hep-ph].

[155] M. Beneke, P. Falgari, S. Klein, and C. Schwinn, *Hadronic top-quark pair production with NNLL threshold resummation*, Nucl. Phys. **B855** (2012) 695–741, arXiv:1109.1536 [hep-ph].

[156] M. Cacciari, M. Czakon, M. Mangano, A. Mitov, and P. Nason, *Top-pair production at hadron colliders with next-to-next-to-leading logarithmic soft-gluon resummation*, Phys. Lett. **B710** (2012) 612–622, arXiv:1111.5869 [hep-ph].

[157] P. Bärnreuther, M. Czakon, and A. Mitov, *Percent Level Precision Physics at the Tevatron: First Genuine NNLO QCD Corrections to $q\bar{q} \to t\bar{t} + X$*, Phys. Rev. Lett. **109** (2012) 132001, arXiv:1204.5201 [hep-ph].

[158] M. Czakon and A. Mitov, *NNLO corrections to top-pair production at hadron colliders: the all-fermionic scattering channels*, JHEP **12** (2012) 054, arXiv:1207.0236 [hep-ph].

[159] M. Czakon and A. Mitov, *NNLO corrections to top pair production at hadron colliders: the quark-gluon reaction*, JHEP **01** (2013) 080, arXiv:1210.6832 [hep-ph].

[160] M. Czakon, P. Fiedler, and A. Mitov, *Total Top-Quark Pair-Production Cross Section at Hadron Colliders Through $O(\frac{4}{S})$*, Phys. Rev. Lett. **110** (2013) 252004, arXiv:1303.6254 [hep-ph].

[161] M. Czakon and A. Mitov, *Top++: A Program for the Calculation of the Top-Pair Cross-Section at Hadron Colliders*, Comput. Phys. Commun. **185** (2014) 2930, arXiv:1112.5675 [hep-ph].

[162] M. Botje, J. Butterworth, A. Cooper-Sarkar, A. de Roeck, J. Feltesse, et al., *The PDF4LHC Working Group Interim Recommendations*, arXiv:1101.0538 [hep-ph].

[163] A. D. Martin, W. J. Stirling, R. S. Thorne, and G. Watt, *Uncertainties on alpha(S) in global PDF analyses and implications for predicted hadronic cross sections*, Eur. Phys. J. **C64** (2009) 653–680, arXiv:0905.3531 [hep-ph].

[164] J. Gao, M. Guzzi, J. Huston, H.-L. Lai, Z. Li, P. Nadolsky, J. Pumplin, D. Stump, and C. P. Yuan, *CT10 next-to-next-to-leading order global analysis of QCD*, Phys. Rev. **D89** (2014) no. 3, 033009, arXiv:1302.6246 [hep-ph].

[165] R. D. Ball et al., *Parton distributions with LHC data*, Nucl. Phys. **B867** (2013) 244–289, arXiv:1207.1303 [hep-ph].

[166] M. Aliev, H. Lacker, U. Langenfeld, S. Moch, P. Uwer, et al., *HATHOR: HAdronic Top and Heavy quarks crOss section calculatoR*, Comput.Phys.Commun. **182** (2011) 1034–1046, arXiv:1007.1327 [hep-ph].

[167] P. Kant, O. Kind, T. Kintscher, T. Lohse, T. Martini, S. Molbitz, P. Rieck, and P. Uwer, *HatHor for single top-quark production: Updated predictions and uncertainty estimates for single top-quark production in hadronic collisions*, Computer Physics Communications **191** (2015) 74 – 89. http://www.sciencedirect.com/science/article/pii/S0010465515000454.

[168] S. Frixione, E. Laenen, P. Motylinski, B. R. Webber, and C. D. White, *Single-top hadroproduction in association with a W boson*, JHEP **07** (2008) 029, arXiv:0805.3067 [hep-ph].

[169] ATLAS Collaboration, *Evidence for the $H \to b\bar{b}$ decay with the ATLAS detector*, Tech. Rep. ATLAS-CONF-2017-041, CERN, Geneva, Jul, 2017. http://cds.cern.ch/record/2273847.

[170] M. Czakon, D. Heymes, and A. Mitov, *High-precision differential predictions for top-quark pairs at the LHC*, Phys. Rev. Lett. **116** (2016) no. 8, 082003, arXiv:1511.00549 [hep-ph].

[171] G. Cowan, *Statistical Data Analysis*. Oxford science publications. Clarendon Press, 1998. https://books.google.co.uk/books?id=ff8ZyW0nlJAC.

[172] ATLAS Collaboration, *Calibration of the b-tagging efficiency on charm jets using a sample of W+c events with 13 TeV ATLAS data*, Tech. Rep. ATL-COM-PHYS-2016-344, CERN, Geneva, Apr, 2016. https://cds.cern.ch/record/2146031.

[173] E. Gross and O. Vitells, *Trial factors for the look elsewhere effect in high energy physics*, The European Physical Journal C **70** (Nov, 2010) 525–530. https://doi.org/10.1140/epjc/s10052-010-1470-8.

[174] R. Brun and F. Rademakers, *ROOT – An object oriented data analysis framework*, Nucl. Instrum. Meth. A **389** (1997) no. 1, 81 – 86.